On the plastic deformation behaviour of nickel-based superalloys: low cycle fatigue and stress orientation effects

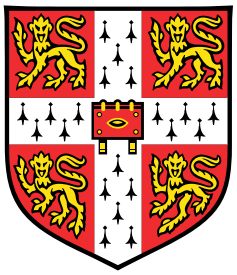

Fernando Daniel León-Cázares

Department of Materials Science and Metallurgy
University of Cambridge

This dissertation is submitted for the degree of
Doctor of Philosophy

Downing College July 2019

Declaration

This dissertation is submitted for the degree of Doctor of Philosophy at the University of Cambridge. It describes the research carried out in the Department of Materials Science and Metallurgy between January 2016 and July 2019, under the supervision of Prof. Cathie M.F. Rae. I hereby declare that except where specific reference is made to the work of others, the contents of this dissertation are entirely original and have not been submitted in whole or in part for consideration for any other degree or qualification in this, or any other university. This dissertation is my own work and contains nothing which is the outcome of work done in collaboration with others, with the exception of the operation of the TEM in Chapter 3 performed by Regina Schlütter and mechanical testing of the RR1000 samples also in Chapter 3 done by Rolls-Royce plc. This dissertation contains fewer than 60,000 words in length.

Part of this work has been published or is planned to be published soon in the literature (in order of submission):

- F.D. León-Cázares, R. Schlütter, T. Jackson, E.I. Galindo-Nava and C.M.F. Rae. A multiscale study on the morphology and evolution of slip bands in a nickel-based superalloy during low cycle fatigue. *Acta Materialia*, 182:47-59, 2020 (Chapter 3).

- F.D. León-Cázares, F. Monni, T. Jackson, E.I. Galindo-Nava and C.M.F. Rae. Stress response and microstructural evolution of nickel-based superalloys during low cycle fatigue: Physics-based modelling of cyclic hardening and softening. *International Journal of Plasticity*, in press, 2020 (Chapter 4).

- F.D. León-Cázares and C.M.F. Rae. A stress orientation analysis framework for glide behaviour of dislocations in face-centered cubic metals. *Manuscript in preparation* (Chapter 5).

- F.D. León-Cázares, F. Monni and C.M.F. Rae. Stress orientation dependence for the propagation of stacking faults and superlattice stacking faults in nickel-based superalloys. *Manuscript in preparation* (Chapter 6).

Additional work published during the course of the PhD:

- F.D. León-Cázares, C. Kienl and C.M.F. Rae. Three-Dimensional Reconstruction of Planar Deformation Features from Single Electron Micrographs. *Metallurgical and Materials Transactions A*, 51A:1163-1172, 2020.
- C. Kienl, F.D. León-Cázares and C.M.F. Rae. Deformation twinning during high temperature compression tests of the Ni-base superalloy ATI 718Plus. *Acta Materialia*, in press, 2020.

Fernando Daniel León-Cázares
July 2019

On the plastic deformation behaviour of nickel-based superalloys: low cycle fatigue and stress orientation effects

Fernando Daniel León-Cázares

This dissertation expands upon the current knowledge of plastic deformation in nickel-based superalloys, with a focus on dislocation mechanisms and the effect of microstructure. The two main topics treated are the evolution of the dislocation structure during low cycle fatigue and the effect of loading orientation on the propagation of stacking faults. A series of experimental and modelling techniques are employed throughout the thesis.

Low cycle fatigue is investigated with the motivation of understanding how slip bands form and develop prior to crack initiation. Electron microscopy techniques are used in alloy RR1000 to characterise these dislocation structures at different length scales in interrupted tests at room temperature and 700°C. The true slip line spacings and shear step lengths at the precipitate interfaces are measured for the first time ever with a new methodology, allowing for quantitative comparisons. Non-coplanar stacking faults are observed to be the main obstacles against which dislocations in a slip band pile up and accumulate in the form of mutipoles. The combination of these techniques provides a unique mechanistic and quantitative insight into the slip band and precipitate morphology evolution.

The characteristic response of these alloys, *i.e.* cyclic hardening followed by cyclic softening, is linked with the underlying evolution of the microstructure. A study on alloy 718Plus with different ageing heat treatments looks particularly at the influence from precipitate size and volume fraction. Microstructural characterisation is used as an input to a new physics-based mesoscale model that accounts for the prolonged precipitate shearing observed. Local accumulation of precipitate shearing near surface cracks is identified and regarded as an additional factor for fatigue failure.

Alternatively, the effect of loading orientation on the plastic deformation behaviour is investigated here in a more theoretical way. This variable is often oversimplified due to the complexity of some mechanisms, in particular those driven by dislocation reactions or splitting into Shockley partials. A novel orientation analysis framework is introduced as an alternative to simultaneously scrutinise the behaviour of multiple slip systems in a graphical and intuitive way. Due to the generality of this approach, this is developed for fcc crystals. Its application in the analysis of two simplistic twin nucleation models is performed to exemplify the use of the orientation maps generated. This framework opens the door to the study of many more deformation mechanisms in a new and more in-depth manner.

The orientation analysis framework is then expanded to the specific case of stacking faults in nickel-based superalloys, accounting for the presence of glide obstacles. The regions

where stacking fault propagation is promoted are developed analytically and validated with simulations from the literature for different precipitate morphologies and distributions. This theory is then extended to include thermally assisted superlattice stacking faults and microtwinning in a comprehensive way. Mechanistic maps that simultaneously consider stress, orientation and microstructure are developed for low and intermediate temperatures. The results found are in full agreement with data from the literature.

Acknowledgements

First and foremost, I want to thank my family, without whom my life would be very different from what it is today. To my parents, Gustavo and Lulú, for their constant guidance, support and love. Thanks for encouraging me to try my best to achieve my goals and for respecting every choice I have taken so far. To my brother, Gustavo (Bo), for the countless hours we have spent together doing all sorts of things. It has been an amazing experience sharing this stage of my life in Cambridge with you.

I want to express my sincere gratitude to my supervisor, Prof Cathie Rae, for welcoming me into the Rolls-Royce UTC and for guiding me through every stage of my PhD. I truly appreciate the freedom I had to try numerous new ideas, the advices given to tackle hard questions and the mentorship offered in this initial stage of my scientific career. I also want to thank my industrial supervisor, Tom Jackson, for his help in selecting the tests and the valuable discussions on fatigue in superalloys. I am also grateful to Dr Enrique Galindo Nava for his assistance in everything related to modelling and mathematics, for this opens the door to many new possibilities.

Many thanks to Dr Hon Tong Pang and Sue Rhodes for all the help provided in the lab, and to all the technical staff at the Department of Materials Science & Metallurgy. I also want to express my gratitude to my colleagues at the Rolls-Royce UTC from whom I have learnt a lot during the last 3 and a half years. All the discussions on the intricate mechanisms of plastic deformation will forever be remembered fondly.

And a huge thank you to all the people that have accompanied me during this journey in Cambridge; my flatmates, latin dancers, the Mexican society and everyone else who made this experience very enjoyable.

Finally, I want to thank those who have granted me the opportunity to pursue this academic degree. I am grateful to Consejo Nacional de Ciencia y Tecnología (CONACyT), Cambridge Trust, Roberto Rocca Education Program and Rolls-Royce plc for their financial support, and Rolls-Royce plc and Rolls-Royce Deutschland for providing the material used during this PhD.

Table of contents

List of figures

List of tables

Chapter 1

Introduction

The aerospace industry has evolved hugely over the last century, directly affecting the evolution of society in many aspects. In 2017 alone, over 4.1 billion passengers were transported in commercial airlines [1], and over the next years an annual compound 4.5% increase in the global passenger traffic is expected [2], as observed in Figure 1.1. To meet this demand, the worldwide fleet will grow by more than 20,000 engines by 2025 [3].

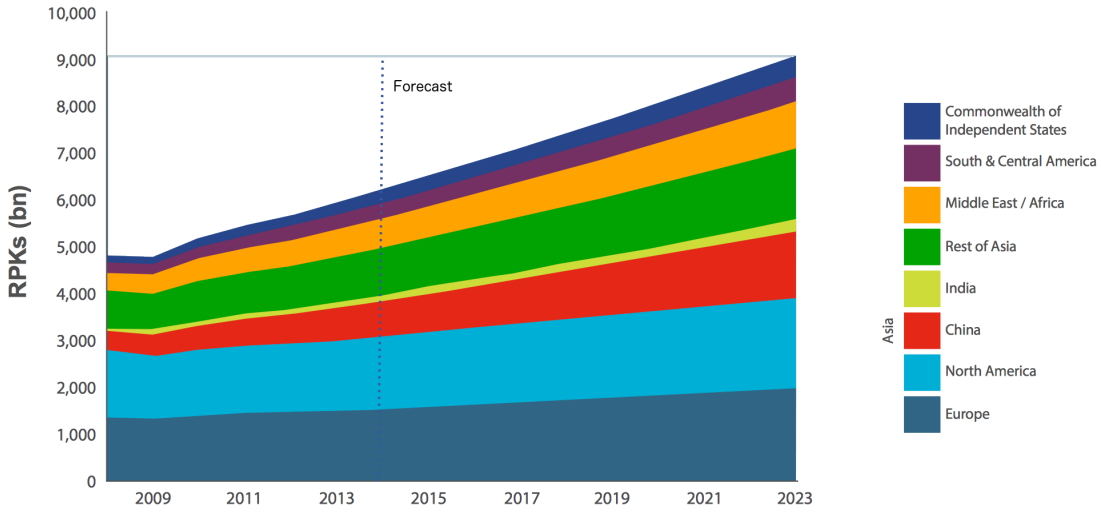

Fig. 1.1 - Aircraft traffic forecast by domicile from 2008 to 2023 in revenue passenger kilometres (RPKs). Adapted from [2].

This industry currently accounts for 2% of global CO_2 emissions [4], or 14% of emissions from all transport sources [1]. Also, from an economic point of view, fuel is estimated to account for 23.5% of all operating costs [5]. These factors drive the need to increase the efficiency of aircrafts. This is the reason why a typical engine contains titanium alloys, steels, aluminium alloys, reinforced plastics, ceramic coatings and composites, among

other materials [6]. The development of new materials with better mechanical and thermal properties allows the jet engine to run more efficiently while weighing less and being more durable.

This PhD dissertation focuses on the study of plasticity in nickel-based superalloys. Increasing the turbine entry temperature of the jet engine is essential for a higher efficiency [7]; these alloys are used in the hottest sections of the turbine due to their outstanding thermomechanical properties. Within the high pressure discs and blades, these materials must withstand large cyclic loads at high temperatures, thus becoming subject to a number of fatigue and creep deformation mechanisms that eventually result in crack formation and propagation. However, these mechanisms are not fully understood.

The two main topics treated in this thesis are: (i) low cycle fatigue deformation behaviour and (ii) the effect of loading orientation on the propagation of stacking faults. Multiple electron microscopy techniques and modelling approaches are used throughout the analyses. Whenever possible, physics-based mechanistic explanations are sought to explain the behaviours observed.

The first topic studied was that of low cycle fatigue, which is one of the main life limiting factors for turbine discs [8] due to crack growth during take off, when the highest stresses arise in these components. Note that the operating conditions vary depending on engine type and rating, compressor or turbine stage and flight profile being operated to. A turbine disc bore typically operates under 550 °C and the rim reaches temperatures of up to 600-700 °C. Besides, the most highly loaded features of these components will experience plasticity potentially throughout their service life [9]. Therefore, there is a real need to understand cyclic plasticity behaviour for a wide range of temperatures and stresses in nickel-based superalloys to improve component design and fatigue lifing. This justifies the relatively large strain amplitudes studied in Chapters 3 and 4.

The investigations are performed at the nano-, micro- and mesoscopic scales. Emphasis is placed on describing the slip bands, *i.e.* dislocation structures along which crack initiation is promoted [10], their formation process, morphology, distribution, interaction with the microstructure and evolution. Electron microscopy is employed to observe features of the slip bands at different length scales. A newly developed technique enables the first ever quantitative analysis of slip line spacings and shear step lengths, from which comparative studies are performed. This is all used to construct a mesoscopic model that links microscopic mechanisms with the macroscopic cyclic response of precipitate reinforced materials.

The interest in orientation began after stumbling upon an unexpected deformation phenomenon. Specifically, one of the characterisation techniques developed in this work revealed the importance of loading orientation due to three grains behaving very differently from the

rest. Whilst this initial observation is still not fully understood and is part of the future work, it sparked the curiosity that led to the development of a more general orientation analysis framework. Further details about this connection are discussed in Chapter 5.

The developed framework has many advantages over other approaches found in the literature, as it makes use of geometric constraints intrinsic to the fcc crystal structure that allow for the simultaneous analysis of all octahedral slip systems. Besides, it can be linked to orientation maps that graphically represent different dislocation behaviours. Overall, this novel and intuitive approach provides a better understanding of the effects of loading orientation.

While developing the aforementioned framework, a clear void in the literature was found regarding the effect of orientation on the propagation of stacking faults. An analysis on this topic became the first ever comprehensive theory to describe the effects of stress orientation on the formation of the many configurations of planar faults observed in nickel-based superalloys. Both the general framework and this particular work on stacking faults were developed simultaneously towards the end of the PhD, with promising results.

This thesis is organised as follows:

- Chapter 2 contains the literature review, which includes an introduction to nickel-based superalloys, typical compositions, phases and main plastic deformation mechanisms at low and intermediate temperatures. Known effects of loading orientation on some of these mechanisms are summarised. A section on low cycle fatigue covers previous findings on the morphology of slip bands, the evolution of the precipitate morphology and the typical macroscopic stress-strain responses found in multiple alloys. A brief section on the basics of mesoscopic modelling of plastic deformation is also given.

- Chapter 3 consists of a purely experimental multiscale study on the morphology and evolution of slip bands in superalloy RR1000 during low cycle fatigue. Samples from interrupted tests at two temperatures are analysed with different electron microscopy techniques. This chapter also introduces a newly developed characterisation methodology from which quantitative statistical analyses are drawn.

- Chapter 4 deals with a predictive model for the stress-strain response during low cycle fatigue. Efforts go into describing the cyclic hardening and cyclic softening typical of precipitate reinforced materials. Alloy 718Plus is chosen for its simpler microstructure, and the effects of precipitate size are investigated. Microstructural characterisation is also performed to feed the model.

- Chapter 5 introduces a general stress orientation analysis framework. Its main characteristics and advantages are described in detail, and its physical meaning explored for

the case of uniaxial loading. Analyses on simple twin nucleation mechanisms in fcc alloys are developed to exemplify the use of this framework.

- Chapter 6 develops in detail a theoretical analysis on the conditions for propagation of stacking faults. Different configurations are explored, both for athermal partial breakaway and segregation assisted faults. The ideas are directly compared against results from the literature in a wide variety of superalloys. Novel mechanistic maps for stress, orientation and microstructure are developed.

- Chapter 7 summarises the key findings of this dissertation. The final conclusions are drawn from the results of the individual chapters. A discussion is given regarding the main topics in which future work is recommended, and a series of concrete experiments and ideas to continue the research are outlined.

Chapter 2

Literature review

2.1 Nickel-based superalloys

"Superalloys" is the term used to refer to a group of materials engineered to have high strength and corrosion resistance at temperatures above the operation limit of steels [11]. Among these, a narrower classification is often made based on the element with the higher weight percent, *i.e.* nickel, iron-nickel or cobalt. This dissertation focuses on nickel-based superalloys.

2.1.1 Composition and phase stability

The complexity of superalloys arises from the fact that usually 10 or more elements in different concentrations are present in these alloys. Each element segregates to specific positions in the microstructure and modifies both the phase stability and the deformation mechanisms. Figure 2.1 shows some of the elements that are typically found in these alloys. Nonetheless, it is important to bear in mind that their concentrations vary significantly among alloys (as listed in Table 2.1), promoting the formation of different phases.

A continuous matrix γ composed of nickel atoms in a face-centred cubic (fcc) structure is present in all these alloys. The high solubility of nickel allows this phase to contain a significant amount of solid solution elements, *e.g.* Cr, Co, Mo and W. These substitutional atoms lower the stacking fault energy of the material [13] and provide a hardening effect due to the strain field formed around them as a consequence of their lattice misfit [14]. Additionally, this phase has a high stability compared to others [15], which is required for operation at high temperatures for prolonged times.

γ', a Ni_3Al intermetallic phase arranged in an ordered $L1_2$ structure, deposits in the form of precipitates coherent with the matrix. The Ni atoms, often replaced by Co or Pt, occupy

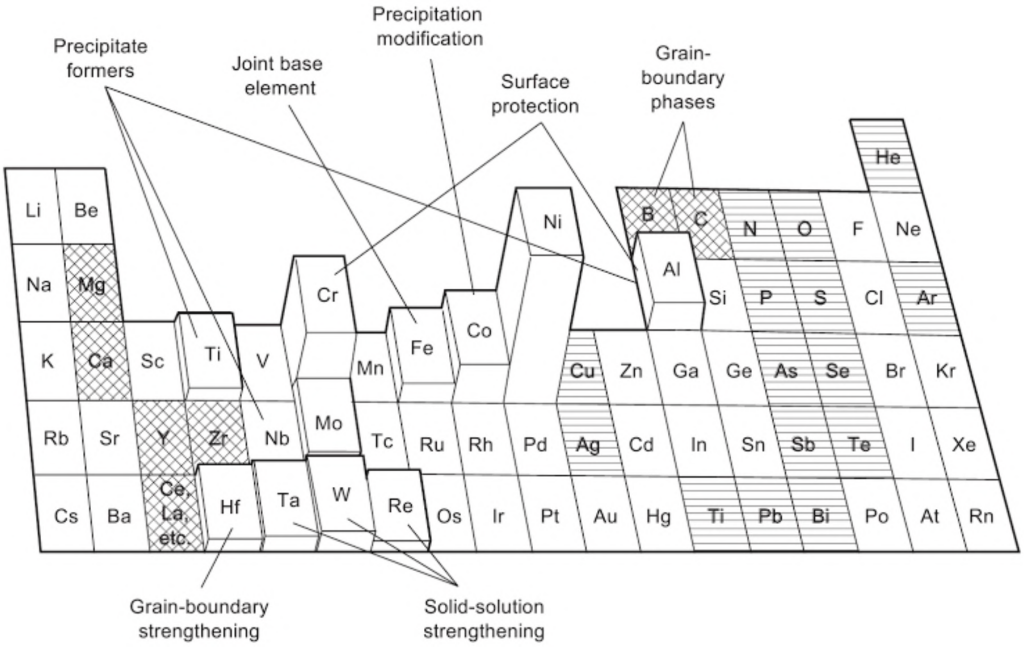

Fig. 2.1 - Main alloying elements used in nickel-based superalloys, where the height of the blocks indicates the relative amounts typically found. Cross-hatching and horizontal hatching denote beneficial and detrimental trace elements, respectively [12].

Table 2.1 - Compositions in wt% of some superalloys.

Alloy	Cr	Co	Mo	W	Nb	Al	Ti	Fe	Mn	Hf	Cu	C	B	Zr	Si	N	P	S	Ni
Alloy 690	29.5	-	-	-	-	-	0.28	10.48	0.26	-	-	0.018	-	-	0.24	-	-	-	Bal
Haynes 230	22.0	-	2.0	14.0	-	0.3	-	-	-	-	-	0.10	-	-	-	-	-	-	Bal
Haynes HR-120	25.0	3.0	2.5	2.5	0.7	0.1	-	33.0	0.7	-	-	0.05	0.004	-	0.6	0.2	-	-	Bal
Hastelloy X	22.0	1.5	9.0	0.6	-	0.25	-	18.5	-	-	-	0.10	-	-	-	-	-	-	Bal
Mar-M247LC	8.0	9.5	0.5	9.4	-	5.5	0.7	-	-	1.4	-	0.07	0.016	0.02	-	-	-	-	Bal
Nimonic 80A	19.5	-	-	-	-	1.4	2.4	-	-	-	-	0.06	0.003	0.06	-	-	-	-	Bal
Nimonic 90	19.5	16.5	-	-	-	1.5	2.5	-	-	-	-	0.07	0.003	0.06	-	-	-	-	Bal
Nimonic PE16	16.5	1.0	1.1	-	-	1.2	1.2	33.0	-	1.4	-	0.05	0.02	-	-	-	-	-	Bal
GH4742	14.0	9.95	5.12	-	2.6	2.54	2.52	-	-	1.4	-	0.06	-	-	-	-	-	-	Bal
GH4145/SQ	15.0	1.0	-	-	1.0	0.6	2.5	6.0	0.35	-	0.5	0.08	0.002	0.06	0.35	-	0.015	0.01	Bal
Inconel 792-5A	12.280	8.87	1.81	4.1	0.1	3.36	3.98	0.16	-	-	-	0.078	0.015	0.031	-	-	-	-	Bal
Udimet 720Li	16.0	15.0	3.0	1.25	-	2.5	5.0	-	-	-	-	0.025	0.018	0.05	-	-	-	-	Bal
TMW-4M3	13.5	25.0	1.8	1.2	-	2.3	6.2	-	-	-	-	0.02	0.02	0.03	-	-	-	-	Bal
Waspaloy	19.5	13.5	4.3	-	-	1.3	3.0	-	-	-	-	0.08	0.006	-	-	-	-	-	Bal

the $\left(0,\frac{1}{2},\frac{1}{2}\right)$-sites, whereas Al, Ti, V and Ta sit in the $(0,0,0)$-sites [15]. In this way, the number of Ni-Al bonds is maximised, avoiding the more energetically costly Al-Al. Figure 2.2 shows the unit cells of both the γ and γ' phases, and it can be seen how the only difference resides in the second sublattice.

The morphology of the γ' precipitates varies as a function of the ageing time, following the sequence shown in Figure 2.3: spheres, cubes, arrays of cubes and solid state dendrites [16]. Similarly, the volume fraction varies among different alloys as a function of composition

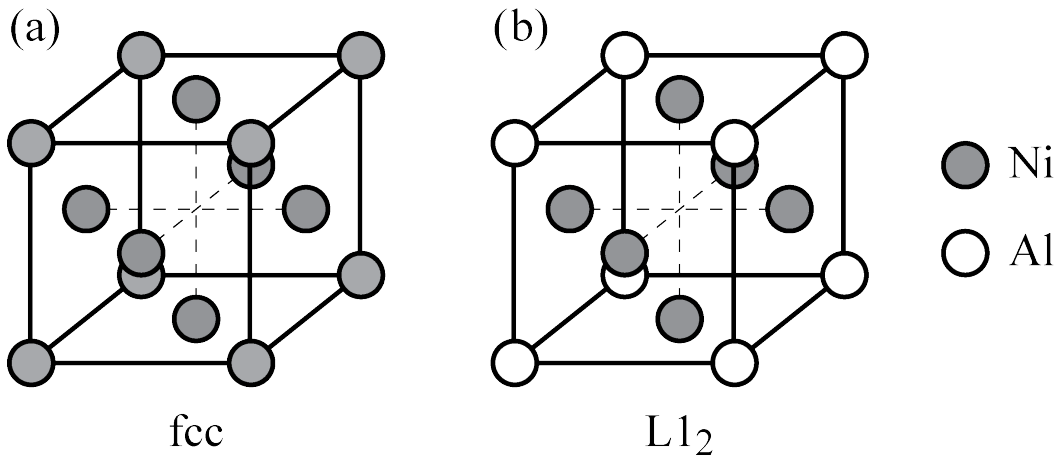

Fig. 2.2 - Unit cells of the (a) fcc and (b) $L1_2$ crystal structures [15].

and ageing temperature, ranging from solid solution to 75%. These huge differences promote a wide variety of deformation mechanisms, further detailed in Section 2.1.2.

Another strengthening phase is the body-centred tetragonal γ'', disc-shaped coherent precipitates characteristic of IN718. It forms mostly in nickel-iron superalloys with high niobium concentration [15]. Unlike γ' and γ'', other intermetallic precipitates are incoherent with the matrix, having a null strengthening contribution due to their low volume fractions [15]. Among these are the orthorhombic Ni_3Nb δ and the hexagonal Ni_3Ti phases, which are used to pin grain boundaries (where they preferentially deposit under some conditions) and improve the resistance to intergranular fracture [17].

Other phases that can form in this alloying system are the topologically close-packed (TCP) phases. These are complex crystal structures with a high and uniform atomic packing density that possess a certain degree of non-metallic bonding, and they are usually formed after long-term exposure at high temperatures in alloys with high concentrations of elements such as Cr, Mo, W and Re [15]. In general, these phases are avoided as they convey a detrimental effect to some properties. For instance, TCP phases act as crack initiation sites due to their brittle nature and they are also linked to a depletion of refractory elements in the matrix, softening the material [18].

Carbides and borides are also found in superalloys. *MC* precipitates in interdendritic regions and grain boundaries further decompose into $M_{23}C_6$ and M_6C at lower temperatures [15, 19]. Similar to the TCP phases, the formation of borides and carbides is associated with a depletion of metals at the matrix, which might have a detrimental effect on some properties. However, in some cases they are still purposely added into the alloys to improve creep life by inhibiting the grain boundary sliding phenomenon [15].

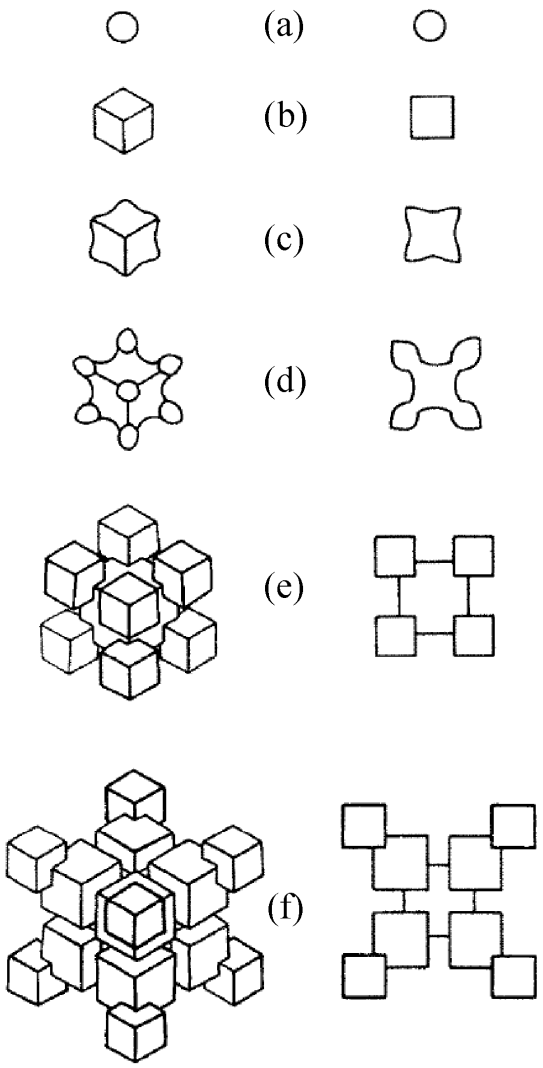

Fig. 2.3 - Schematic diagrams of the evolution of strain-induced faceted γ' shapes during ageing along projections $\langle 111 \rangle$ (left) and $\langle 001 \rangle$ (right) [16].

2.1.2 Deformation mechanisms

Several plastic deformation mechanisms have been identified in nickel-based superalloys under different conditions. Composition, phase distribution and morphology play an important role because they have an effect on the forces experienced by the dislocations. Temperature is critical as some of these mechanisms are diffusion-driven or thermally activated. Figure 2.4 qualitatively shows the ranges of stresses and temperatures where some dislocation behaviours may appear. The current section summarises the main plastic deformation mechanisms that have been observed in these alloys during monotonic loading, with an emphasis on low and intermediate temperatures.

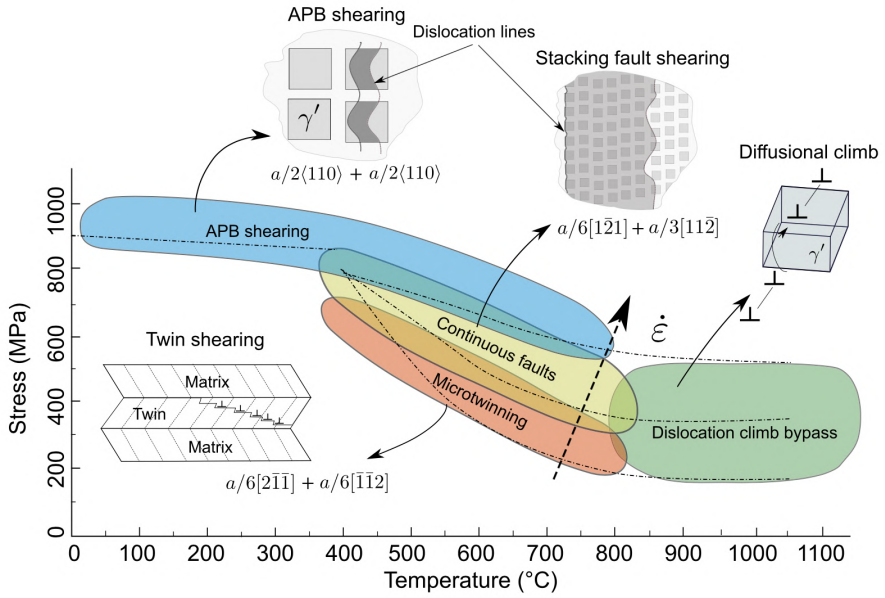

Fig. 2.4 - Mechanistic deformation map of a nickel-based superalloy illustrating the dependence on stress, temperature and strain rate [20].

Slip in the fcc γ matrix occurs mostly by glide of dislocations with a $\frac{a}{2}\langle 110\rangle$ Burgers vector along the octahedral $\{111\}$ planes, resulting in a total of 12 independent slip systems [21]. According to Frank's rule, each of these perfect dislocations may split into two closely spaced $\frac{a}{6}\langle 112\rangle$ Shockley partials bounding an intrinsic stacking fault. The geometric configuration of these slip systems is summarised in Thompson's tetrahedron [22] in Figure 2.5(a), where perfect dislocations are denoted by two roman letters and partials by one roman and one greek letters, *e.g.* AB and $A\delta$, respectively. Note that there is a specific sequential arrangement of the partials, shown in Figures 2.5(b) and (c): if a perfect dislocation is viewed from outside the tetrahedron and along the positive sense of the line, an intrinsic stacking fault requires placing the greek-roman partial on the viewer's left and the roman-greek partial on the right [23].

The dissociation width between the partials in these alloys is typically high due to their low stacking fault energy. Under some loading conditions it is possible for the partials to separate to a point where the interaction force between them becomes negligible and a decorrelated motion takes place. A stacking fault may then extend indefinitely if the leading partial continues to glide while the trailing one is pinned [24]. The extended planar defect may then act as an additional obstacle to other non-coplanar dislocations.

The low stacking fault energy also favours the planarity of slip, a property related to the ease of dislocations to cross slip [25, 26] also promoted by high lattice friction stresses and by the presence of short-range order [27–29]. According to the Friedel-Escaig mechanism,

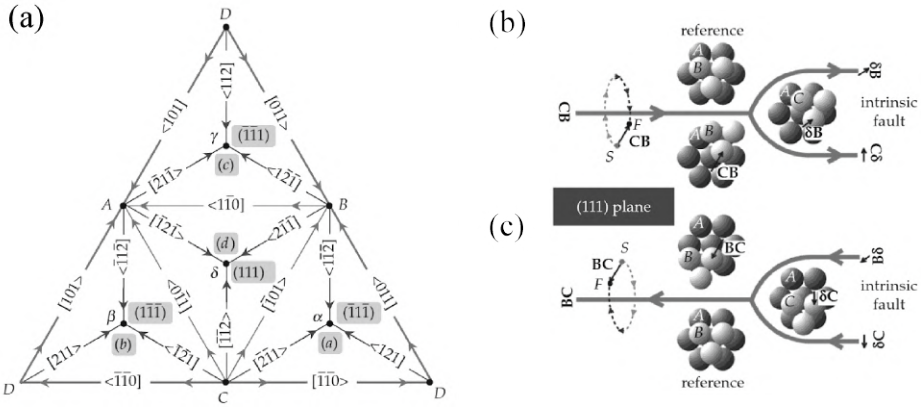

Fig. 2.5 - (a) Planar version of the Thompson tetrahedron with the perfect and partial dislocations. The views of dislocation *CB* from outside the tetrahedron to form an intrinsic stacking fault are also shown with the line vectors pointing (b) to the right and (c) to the left [23].

the partials of a screw segment must first form a constriction where they recombine to then split again and glide on the cross slip plane [30, 31], as illustrated in Figure 2.6. This enables dislocations to escape their original slip planes and distribute plastic deformation more homogeneously, but also promotes the annihilation of screw segments with opposite Burgers vector. The amount of cross slip and other interactions with the microstructure controls the formation of numerous dislocation structures [32–34].

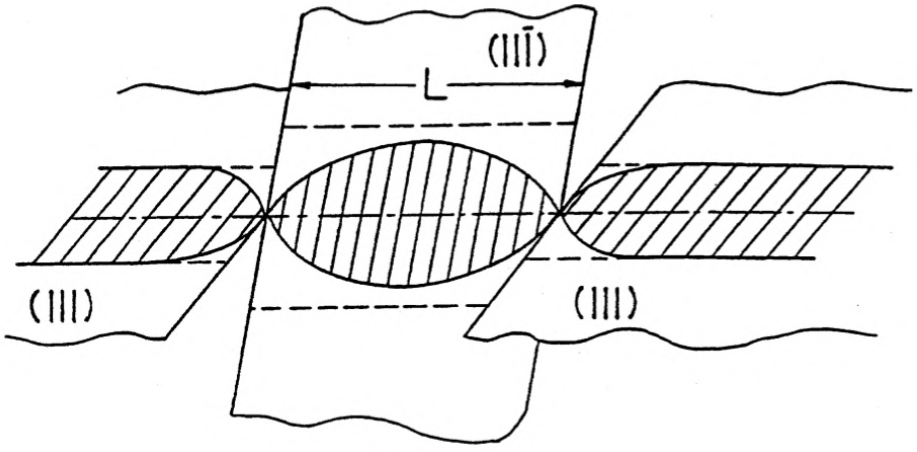

Fig. 2.6 - Schematic diagram of the Friedel-Escaig cross slip mechanism [31].

Glide of a perfect γ dislocation into the $L1_2$ structure is linked to the formation of an antiphase boundary (APB). This planar defect consists of a misconfiguration of the atomic stacking order, leading to an increase in the number of Ni-Ni and Al-Al bonds, and is associated with an additional energetic cost [15]. For this reason, the perfect dislocations

travel in pairs (also called superdislocations) when entering a γ' precipitate. The leading one leaves behind an APB and the original structure is restored by the trailing dislocation. This mechanism has been observed experimentally in superalloys, as shown in Figure 2.7, and also modelled within discrete dislocation dynamics frameworks [35, 36].

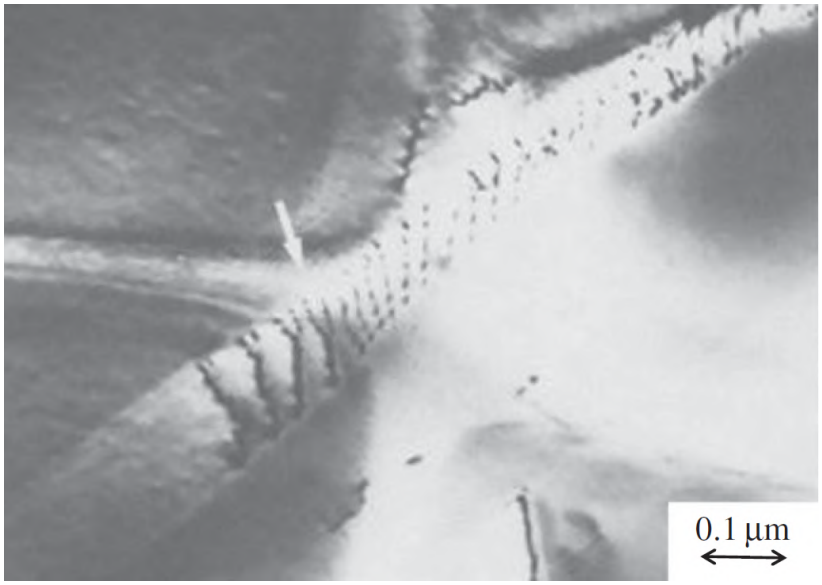

Fig. 2.7 - Individual dislocations in the γ matrix and coupling in pairs inside the γ' precipitates in Superalloy PWA 1480 loaded in tension at 705°C [37].

Depending on the size distribution and volume fraction of the precipitates, two shearing regimes have been identified: weak pair-coupling and strong pair-coupling. As shown schematically in Figure 2.8, the distance between the superpartials is larger than the particle diameter in the former, whereas in the latter coupled dislocation pairs are seen within a single particle. Alternatively, the Orowan bypassing mechanism dominates over particle shearing for sufficiently large precipitates, leading to the formation of dislocation loops [38]. The different mechanisms previously described may operate concomitantly in nickel-based superalloys with multimodal γ' size distributions [39, 40].

Additionally, cross slip of screw segments onto a {001} cube plane is promoted for short distances ($\sim$ 20 Å) in the $L1_2$ crystal structure [41]. This occurs because the APB energy in the octahedral plane is higher than that in the cubic plane, as shown experimentally for various alloys [31, 42]. The resulting dislocation segments in the cube plane are denominated Kear-Wilsdorf locks, and they contribute to the exhaustion rate of mobile dislocations that confers additional strength to the material. This mechanism is thermally activated, and has been thought to be the reason behind the anomalous yielding effect in nickel-based superalloys [15, 42], *i.e.* a higher yield stress at higher temperatures.

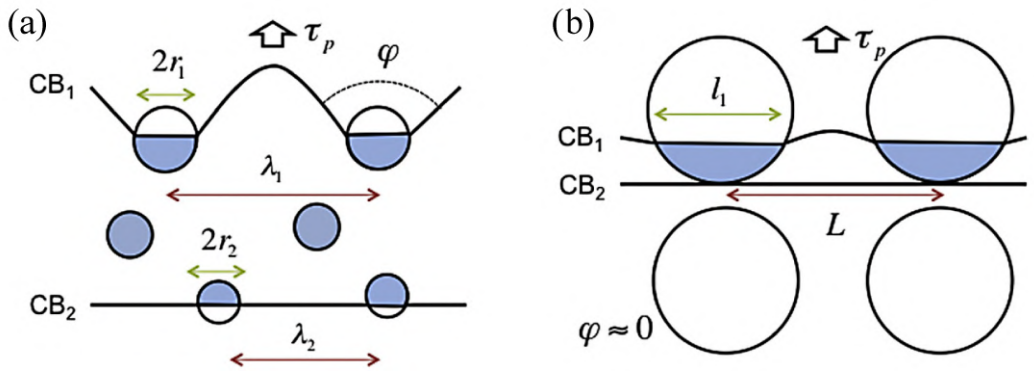

Fig. 2.8 - Schematic representation of the dislocation configurations in the (a) weak pair-coupling and (b) strong pair-coupling regimes [40]. CB_1 and CB_2 are the leading and trailing dislocations, respectively.

At intermediate temperatures and low strain rates, plastic deformation is dominated by the formation of superlattice faults in the γ' precipitates: superlattice intrinsic stacking faults (SISFs) and superlattice extrinsic stacking faults (SESFs) develop in one or two adjacent slip planes, respectively. These planar faults are the result of $\frac{a}{6}\langle 112\rangle$ partial dislocation glide, which gives rise to anisotropy in the tensile/compressive behaviour [43]. The temperature and time dependences for the formation of these defects come from two diffusion-controlled mechanisms. Firstly, local atomic reordering is required to transform the initially formed high energy defect into a superlattice fault [44]. Secondly, the segregation of γ-forming elements ahead of the stacking faults lowers the energy of the defects, which also lowers the shear resistance for the leading dislocations [45]. Contrary to their behaviour in the precipitates, no elemental segregation has been observed in stacking faults in the fcc matrix [46].

A number of mechanisms have been proposed for the creation of these defects, but no experimental evidence has been found for most of them. Vorontsov *et al.* [47] proved via the high resolution TEM in Figure 2.9 that the leading end of the SISFs and SESFs have a different character to that of the extended fault and are bound by closely spaced partials gliding in two adjacent planes. Moreover, the morphology of these defects also varies in the matrix. They may appear either isolated within the precipitates or as extended bands running through both phases [47, 48]. A more complex dislocation arrangement is that of a stacking fault ribbon, where the SISF-APB-SESF alternating character schematically shown in Figure 2.10 results from the cooperative motion of partial dislocations [49, 50].

Another deformation mechanism driven by partial dislocations is the formation and storage of microtwins [44, 51], typically found at lower stresses than those for superlattice faults [20]. An example of such structure is given in Figure 2.11. Unlike macroscopic

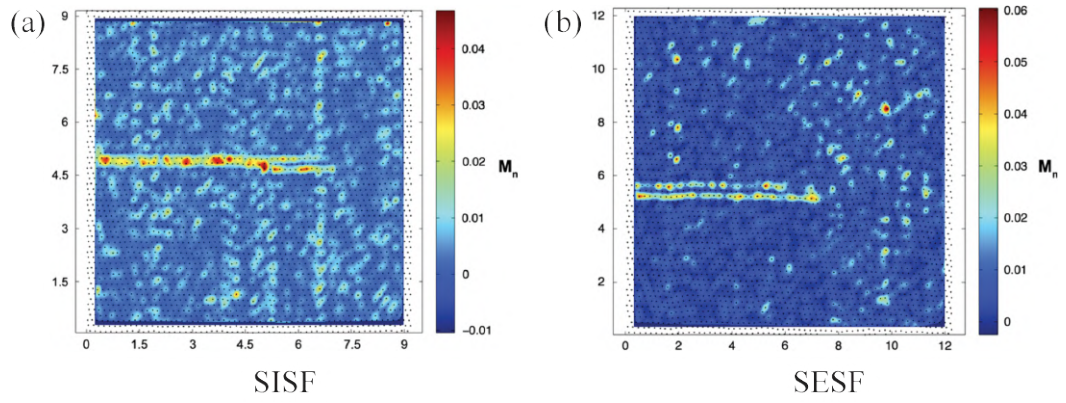

Fig. 2.9 - High resolution TEM showing the centre of symmetry parameter M_n of the atoms at the leading end of a (a) SISF and a (b) SESF [47].

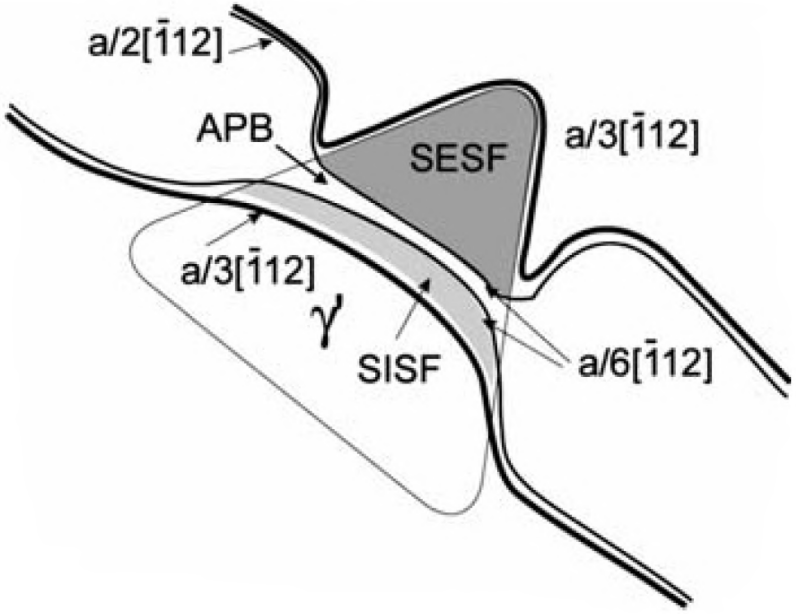

Fig. 2.10 - Schematic diagram of the γ' shearing mechanism by an $a\langle 11\bar{2}\rangle$ ribbon during primary creep [50].

deformation twins in other fcc alloys, the thickness of the microtwins in nickel-based superalloys varies between 4 and 50 atomic planes [52]. Similar to other planar faults in γ', segregation of γ-forming elements has been found in the fault and ahead of the leading end [20], which may facilitate their growth.

The microtwin deformation mechanism is driven by glide of $\frac{a}{6}\langle 112\rangle$ Shockley partials on adjacent planes, although there is still controversy regarding how they nucleate [27]. According to the Kolbe model [44], this cooperative motion of dislocations forms a pseudo-twin (with an orthorhombic structure in the $L1_2$ phase). Subsequently, the original crystal

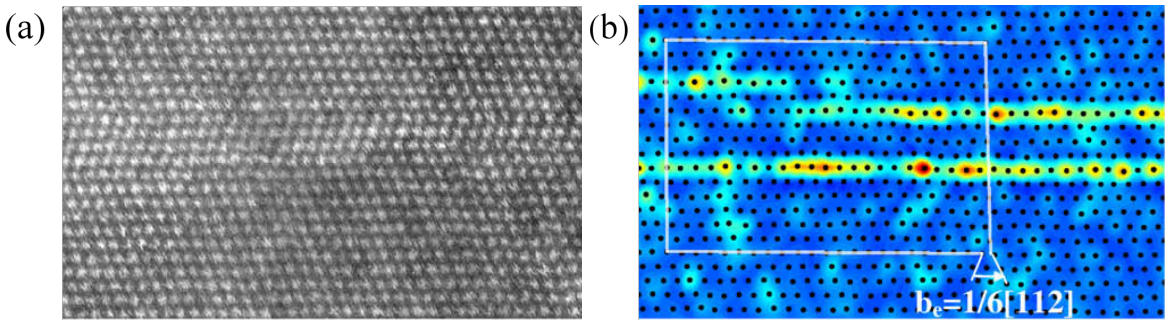

Fig. 2.11 - (a) HAADF image of two $\frac{a}{6}[112]$ dislocations at the microtwin interface, causing a change in thickness from 4 to 6 layers, and (b) its corresponding RGB coloured-coded image based on central symmetry parameter highlighting the microtwin interface [52].

structure is restored by a diffusion driven thermally activated reordering process over atomic distances, further studied by Kovarik *et al.* [52]. A schematic diagram of this microtwinning mechanism is depicted in Figure 2.12.

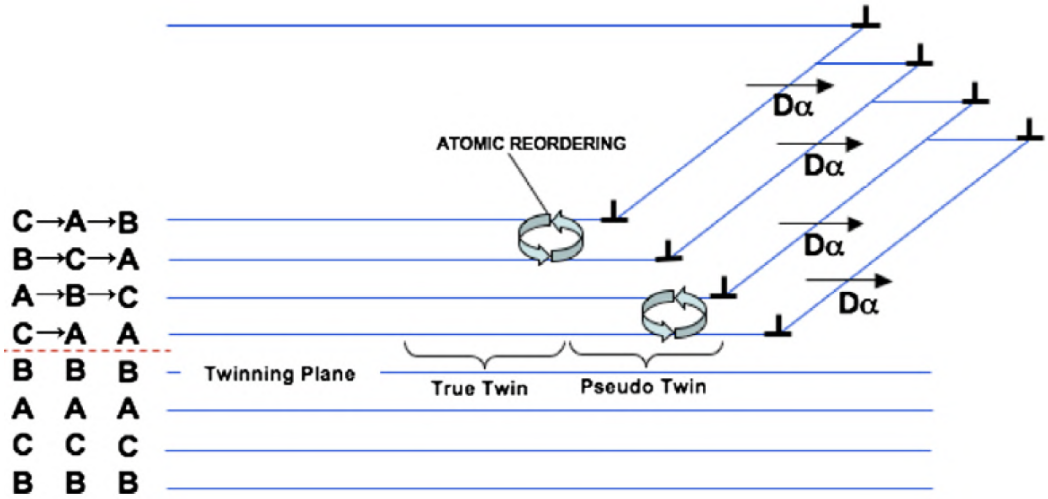

Fig. 2.12 - Schematic diagram of the Kolbe mechanism for microtwinning by passage of $\frac{a}{6}\langle 112\rangle$ partials on adjacent planes [52].

2.1.3 Effects of loading orientation

A material may exhibit very different deformation behaviours depending both on the stress magnitude and orientation. These variations are imperceptible for polycrystalline alloys with random textures from a macroscopic point of view due to the combined effect of thousands

of grains. However, clear distinctions appear upon analysing single crystals or individual grains in a polycrystalline alloy.

All the possible orientations of an fcc crystal can be mapped using stereographic projections of vectors within a unit cell, as shown in Figure 2.13(a). Due to symmetry, the fundamental sector in Figure 2.13(b) suffices to represent all these orientations by mapping only one direction from each family of vectors with the same Miller indices.

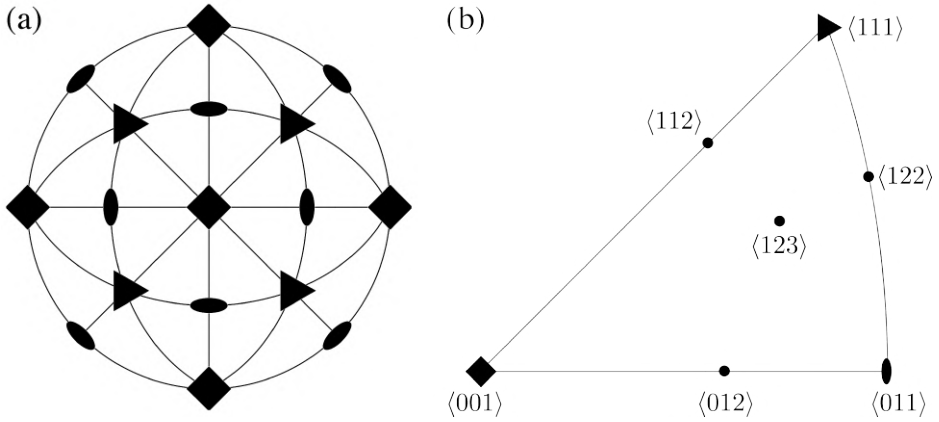

Fig. 2.13 - (a) Stereographic projection of the $\langle 001 \rangle$, $\langle 011 \rangle$ and $\langle 111 \rangle$ directions in the fcc unit cell and (b) its fundamental sector. The same symbols are used for each family of directions, and additional vectors are shown in (b).

The variations in behaviour arise as the forces experienced by dislocations of different slip systems depend on the orientation of the stress tensor. Consider first the case of uniaxial loading. The most important geometric parameter linking the tensile stress σ_0 and the shear stress pushing the dislocation τ is the Schmid factor m_S, defined as

$$m_S = \frac{\tau}{\sigma_0} = \cos\xi \cos\varphi, \tag{2.1}$$

where ξ and φ are the angles between the applied force and the slip plane normal and slip direction, respectively [53]. The relevant geometry is schematised in Figure 2.14(a). The maximum value of the Schmid stress $\frac{a}{2}\langle 110 \rangle$ perfect dislocations is plotted in Figure 2.14(b). At the edges of this plot multiple slip is more predominant, as the maximum Schmid factor is shared between two slip systems, coplanar along the line from [011] to [111] and non-coplanar elsewhere.

The effect of loading orientation becomes more complicated upon considering the forces acting on the Shockley partials, for which the maximum Schmid stress is plotted in Figure 2.14(c). An important feature of this plot is that the force is stronger on the leading partial on one side of the inverse pole figure, and on the trailing partial on the other [54, 55].

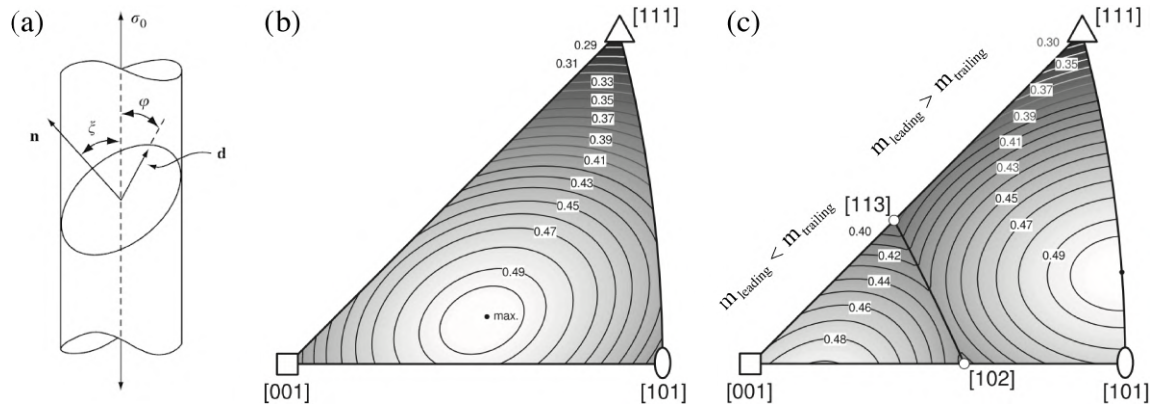

Fig. 2.14 - (a) Schematic diagram of the relevant angles for the calculation of the Schmid factor for uniaxial tension [53], where **n** is the normal to the slip plane and **d** the slip direction. Contour plots of the maximum Schmid factor for (b) perfect $\frac{a}{2}\langle 110\rangle$ dislocations and (c) $\frac{a}{6}\langle 112\rangle$ Shockley partials [54].

Douin *et al.* [56] developed the mechanistic map shown in Figure 2.15 based on the stress that a dissociated dislocation experiences, accounting for the presence of cuboidal precipitates. This was obtained via simulating the motion of the individual partials, allowed to travel only through the matrix. The behaviours observed for different stress orientations (with their corresponding labels) are: immobile dislocation (0), glide of the leading partial only (1), glide of decorrelated partials (2*) and glide of correlated partials (2). This map offers an explanation for the propagation of stacking faults under an applied stress.

Posterior studies of the same kind have shown a similar behaviour for materials with spherical precipitates which may be bypassed via Orowan looping [24, 57]. The simulation of a dislocation gliding through a more complex microstructure with variable precipitate sizes and spacings has shown that there is a critical channel width below which stacking fault propagation is promoted, and another one at which the leading partial is also stopped [58].

Twinning in fcc metals has also a very important dependence on loading orientation. Multiple studies in different alloys have shown that it occurs preferentially close to a $\langle 001\rangle$ orientation for compression [59–61] and near a $\langle 111\rangle$ for tension [54, 62–65]. This has been rationalised as an effect of the stress on the individual partials, promoting twinning when the leading partial experiences a stronger force compared to the perfect dislocation [61, 62]. Whilst this explains its propagation, there is still a debate towards the appropriate twin nucleation mechanism (or mechanisms) and its orientation dependence. The reader is referred to a recent study by De Cooman *et al.* [66] that summarises many of these in a comprehensive way.

Creep at intermediate temperatures in nickel-based superalloys also shows different behaviours depending on the orientation of the load. Moreover, a clear tension-compression

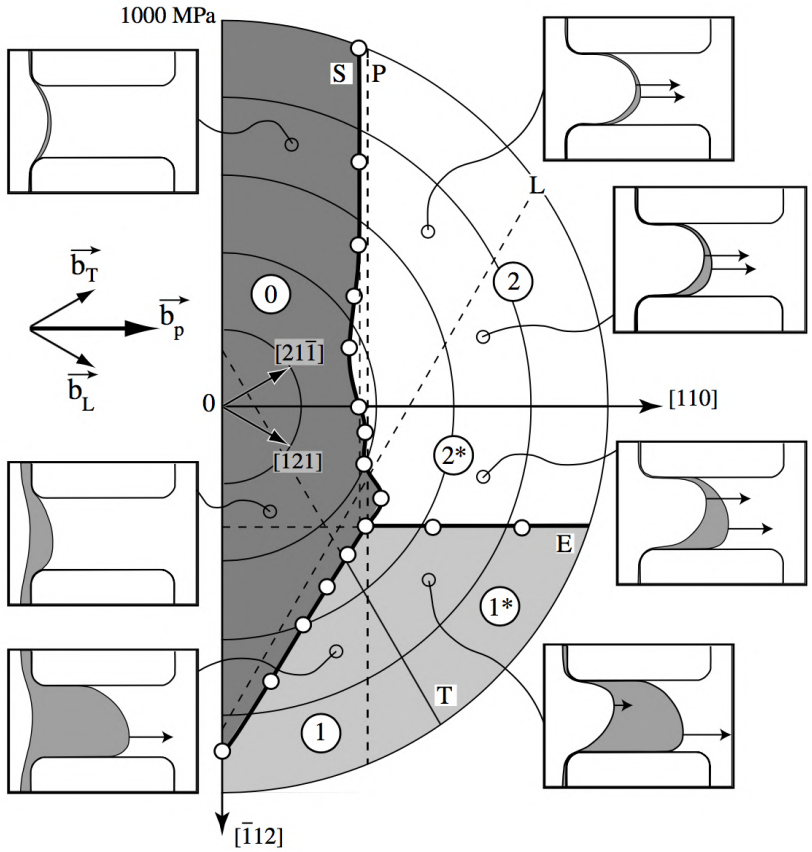

Fig. 2.15 - Regions for the different behaviours of a $\frac{a}{2}\langle 110\rangle$ dissociated dislocation moving in the $(1\bar{1}1)$ plane as a function of the stress. The numbers "0", "1" and "2" indicate the number of partials that move through the channel, and the insets show examples of simulations with arrows representing the velocities of the partials. The Burgers vectors of the partials are drawn for reference. [56].

asymmetry is observed in the macroscopic strain response, mostly linked to the aforementioned nature of the $\frac{a}{2}\langle 110\rangle$ slip systems [43, 67, 68]. The types of planar faults that develop for different orientations varies widely as a consequence of this. For instance, creep tests performed in single crystals of alloy PWA1480 with the load along a $\langle 001\rangle$ axis showed predominantly the presence of SISFs for tension and SESFs for compression [69].

2.2 Low cycle fatigue of nickel-based superalloys

2.2.1 Cyclic deformation mechanisms and related phenomena

Fatigue damage in metals occurs due to the accumulation of slip irreversibilities that gradually induce changes in the local atomic arrangement, the morphology of the microstructure and the surface topography. All these evolve with increasing cycles until the formation of cracks is energetically favoured; these continue to grow until failure. Thus, understanding these irreversibilities is of great importance in describing the fatigue behaviour. Multiple mechanisms introduce slip irreversibilities, some of them highlighted by Mughrabi [25, 70, 71], such as

- annihilation of dislocations;
- formation of dislocation dipoles;
- emergence of dislocations at the surface;
- cross slip of dislocations;
- surface roughening due to random to-and-fro dislocation glide;

The cyclic deformation in metals results in a series of dislocation structures that differ based on the composition of the alloys. Microstructural parameters such as the stacking fault energy, the phase composition and the friction stress, among others, directly affect the way in which dislocations move back and forth according to the loading direction. Besides, the applied stress, strain rate and temperature define also which mechanisms are favoured. Thus, a wide variety of phenomena, described in this section, have been seen during fatigue tests for different conditions and alloys.

Slip bands

Pure fcc metals and alloys with a wavy slip behaviour, below a stress threshold, lead to a cyclic stress saturation characterised by the formation of persistent slip bands (PSB) with a ladder structure surrounded by a matrix of dipolar veins, as shown in Figure 2.16. The rungs in these structures are formed by edge dislocation dipoles from which more edge segments bow out, forming screw dislocations which then glide along the channels depositing new edge dislocations in the walls [25, 72]; simultaneously, dislocations of different sign, both edge and screw, continuously annihilate. The term “persistent” is used for these structures as they reappear at their original location after being polished [73], which indicates that they develop along the whole grains and not only at the surface.

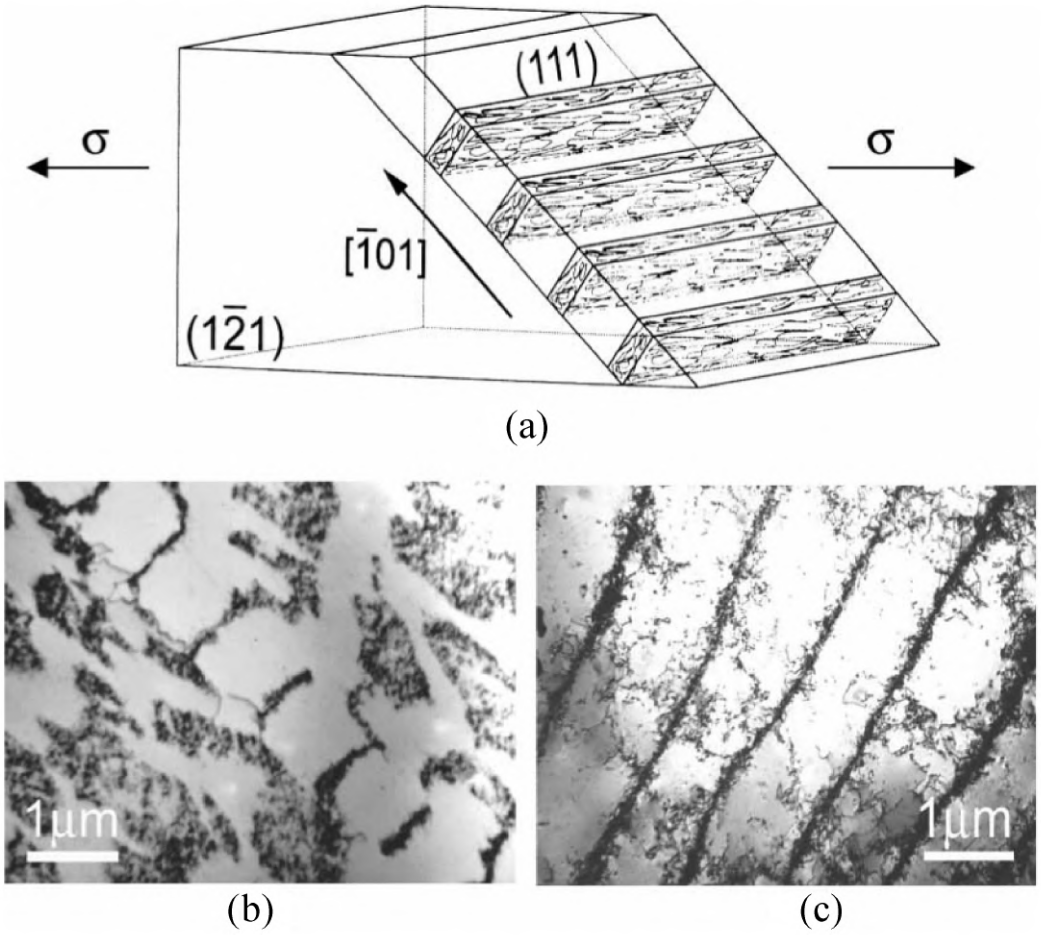

Fig. 2.16 - PSB in a copper single crystal oriented for single slip: schematic illustration (a) and TEM micrographs of the dislocation structure in foils parallel to the (1$\bar{2}$1) plane (b) and parallel to the primary slip plane (c) [26].

When cyclically deformed, nickel-based superalloys and other alloys with a planar slip behaviour develop slip bands rather than PSBs, although a ladder structure similar to a PSB has been found in Nimonic 80A [74], Inconel 713LC [75] and Waspaloy [76] deformed at room temperature. Slip bands are complex dislocation structures that develop along nearby parallel $\{111\}$ planes, where the plastic strain is highly localised and along which crack initiation is promoted. The dislocation dynamics that take place in the slip bands are considerably less well understood than those in PSBs, although some similarities have been observed between the two, *e.g.* the mobility of the dislocations is hindered by the presence of point defects, dislocation debris and prismatic loops [10, 26, 76].

The formation of slip bands has been analysed with different methods, although this process is still not fully understood. Fisher *et al.* [77] proposed more than sixty years ago

that slip bands have their origin in bursts of rapid slip by the generation of dislocation loops from Frank-Read sources. The resulting pile up of dislocations expands in a non-circular shape due to the difference in the forces screw and edge dislocations experience [78], and extend until they reach barriers, which might be of the Lomer-Cottrell type [79, 80] or grain boundaries, among others. The slip lines are formed through this process very rapidly, in times in the order of 10^{-4} to 10^{-5} seconds [81]. Based on the Peach-Koehler equations for forces acting on dislocations, different models have successfully predicted in varied ways the number and position of dislocations in a pile up under different conditions [82–87]. However, the sole activation of the Frank-Read sources explains only the formation of a slip line. Furthermore, if no irreversibilities are present, the dislocation pile ups can annihilate when loading on reversal as seen by Pettinari-Sturmel during an *in situ* TEM analysis of a γ single crystal [88].

A double cross slip process, originally proposed by Koehler [89], has been identified as the mechanism responsible for the lateral widening of the slip lines which ultimately results in the formation of the slip bands [90–94]. According to this model, screw segments in a blocked pile up may cross slip and glide in the conjugate plane until the resultant forces again favour it to cross slip back onto the original plane orientation, by which a Koehler source is formed [93, 95]. Further plastic straining results then in the generation of additional dislocations in a new primary slip system close to the original one. Loading on reversal may activate some of the sources in the opposite direction, which eventually leads to the formation of the dipole structure typical of slip bands [91, 96]; a schematic representation of this process is shown in Figure 2.17.

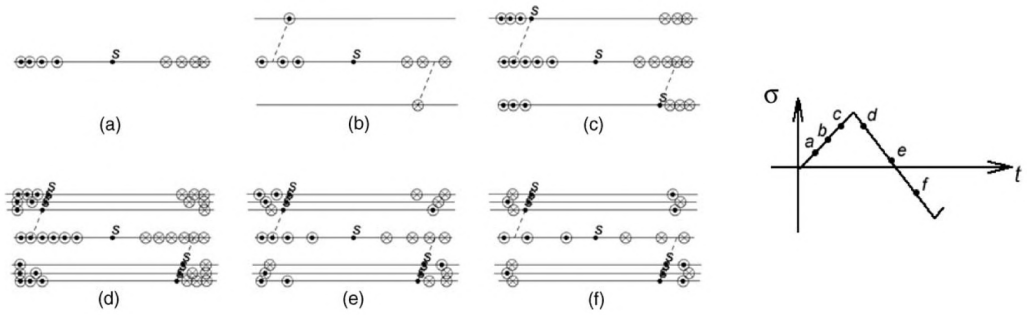

Fig. 2.17 - Schematic representation of the double cross slip process and dipole formation during cyclic loading [91]. (a) Formation of dislocation pile up, (b) cross slip, (c) cross slip back onto a primary slip plane forming new dislocation sources, (d) formation of new dislocation pile ups at additional activated planes, (e) annihilation of dislocations when the applied stress is removed, and (f) activation of the sources in the opposite direction when loaded in reversal.

The evolution of the slip bands is directly related to the development of slip steps at the surface of the material, which ultimately result in the formation of intrusions and extrusions that promote the formation of cracks. However, this topography shows only the number of dislocations that have reached the surface and their specific location and orientation, which is not enough to understand the complex interactions that happen at the grain interiors. Numerous discrete dislocation dynamics analyses have been performed to address this, mostly in precipitate-free materials. These have, among other things, proven that cross slip is necessary for slip bands to form [94, 95] and accumulate dislocation dipoles [91], although a deep understanding of how the composition and microstructure affect their morphology has not been achieved yet. Wang *et al.* [94], in a simulation for a monotonic loading with a high strain rate, also demonstrated an interesting phenomenon in which double cross slip connects: (i) slip lines among a slip band, (ii) neighbouring slip lines by which the slip band thickens, and (iii) neighbouring slip bands at a larger length scale. A similar effect is observed in Waspaloy in Figure 2.18, where thin bands conglomerate to form a thicker slip band.

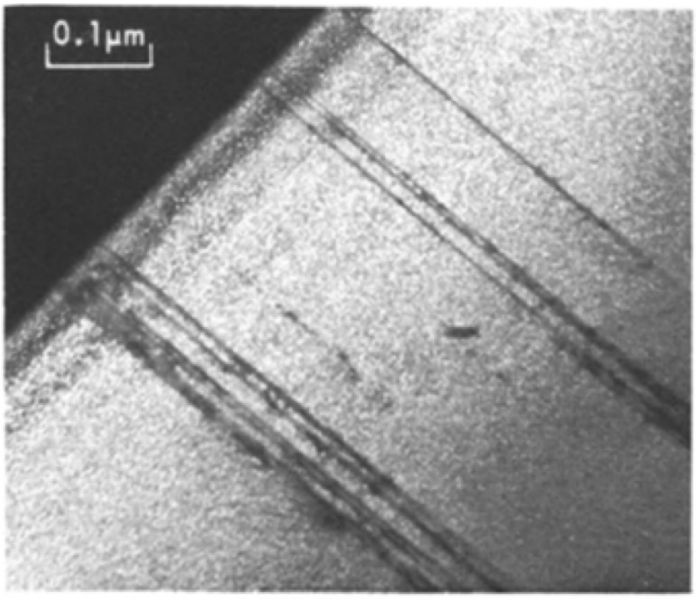

Fig. 2.18 - Dark field TEM micrograph of a slip band in an underaged Waspaloy fatigued at a 0.5% plastic strain at room temperature [97].

Shin and coauthors [98, 99] performed a similar analysis but in a precipitation-hardened material. They modelled the particles as a series of barriers to dislocation motion which soften gradually with each dislocation passing through them. Even when this approach was not specifically developed for intermetallic precipitates, and thus it does not consider the formation of antiphase boundaries, it might be able to capture some effects of the softening process due to particle shearing (more details of this process are given in Section 2.2.2). In

these studies, the shearable precipitates increase the amount of slip localisation as it becomes easier for dislocations to glide along planes where the facets have already been softened, while the non-shearable particles promote the formation of Orowan loops, increasing the back-stress and forcing dislocations to spread further away.

The evolution of the slip band morphology, *i.e.* parameters such as the band width, slip band spacing, extrusion height and local dislocation density, is not yet fully understood, and controversy is still found in the literature. Material and operation variables directly affect the mechanisms responsible for the slip band characteristics, and, to the knowledge of the author, no systematic study has been done in covering a wide variety of conditions. Moreover, the effects that have been reported are in many cases difficult to interpret as many internal variables in a fatigue test can be modified by only changing one input parameter. For example, if the slip band width increases with larger precipitate sizes within a set of experiments, it might be difficult to say whether these two lengths are directly linked or if the thickness variation occurs due to the different stress or plastic strain response obtained because of the variation in the yield stress.

In alloys such as SAE 304 [100] and AISI 316L [101] stainless steel, the slip band structure is formed after a large number of cycles (between 100 and 1000 cycles for different conditions). However, the strain localisation in nickel-based superalloys occurs during the first cycle [102]. The low stacking fault energy in nickel-based superalloys promotes the formation of well defined slip bands even during monotonic loading, with an increase in the number of slip bands for higher strain amplitudes [103]. Additionally, multiple slip is favoured for high levels of deformation to the point where slip bands form with two or three different {111} orientations [104], and interactions between dislocations gliding in these planes might result in an increased cyclic hardening [105]. Regarding their evolution, a variation towards shorter slip band spacings has been seen during the first few cycles (between 1 and 10 cycles) [106, 107], until a saturation state which might be related to the peak stress in fatigue tests is reached [104, 108].

Thickening of the slip bands with the number of cycles has occasionally been reported [97], although these results could occur due to stress concentrations near the crack surface [109]. In general, it appears that the slip band width mostly depends on the material composition and microstructure. A strong dependence on the stacking fault energy has been found, which seems congruent with the fact that this parameter controls the ease of dislocations to cross slip. A low stacking fault energy is associated with a lower density of defects [10] and with hindered cross slip activity, which ultimately results in much thinner slip bands. The presence of shearable precipitates also decreases their thickness [10], although it is not clear how the particle size and volume fraction affect it. Ho *et al.* [76] showed

that the slip band width is an increasing function of both the γ' size and the grain size in Waspaloy, the first parameter having a higher influence. A dislocation dynamics simulation [93] predicted a quadratic dependence on the grain size, although this does not reproduce other experimental measurements; another study [98] reproduces the mentioned precipitate size effect.

The slip band width appears to be independent of the strain amplitude [76, 107]. Alternatively, the strain rate might only affect the required stress to form the slip bands, but not their morphology [94, 110], whereas the temperature (within the range where dislocation glide dominates the deformation behaviour) might have a slight effect on the thickness due to the variation in the stacking fault energy.

The slip band spacing arises from the need of the material to accommodate the imposed plastic deformation. This parameter has been proposed to be a function of the maximum stress response in a test, either with a linear or a quadratic dependence [29, 104, 111]. However, these relations seem to reproduce the data only within a certain range of the experimental results. Other functional dependencies in terms of the plastic strain have been used to fit data from several experiments [97, 111], although these are merely empirical relations which ignore the mechanisms behind slip band formation. Physics-based equations for slip band spacing was proposed by Venkataraman *et al.* [112] by means of a minimum energy configuration from the dislocation structure of a pile up and as an instability transition following the disintegration of a vein structure [113, 114]. Nonetheless, no proper experimental study has validated these results. To the knowledge of the author, modelling of these parameters in more complex microstructures has not been attempted.

The effect of other operation parameters on the slip band spacing in nickel-based superalloys has rarely been discussed. Valsan and coauthors [115] performed a study on Nimonic PE16, in which they observed an increase in this distance for higher temperatures, within the range from 450 to 650°C. However, the difference observed might to be due to the difference in the stress response; a similar conclusion could be reached for their analysis on the strain rate effect. Furthermore, larger precipitate sizes were associated with a decrease in the slip band spacing in NimonicPE16 [116, 117], whereas a study made in Waspaloy showed no obvious dependence for different γ' and grain sizes [76]. Overall, it seems that this spacing is a function of the response of the material rather than a parameter intrinsically related to the material properties.

Precipitate shearing

Dislocations that glide in a plane do not always glide back when the direction of the stress is reversed due to slip irreversibilities, which include dislocation cross slip, annihilation or

trapping in the form of dipoles. These have no effect on the atomic ordering in the matrix or inside the precipitates due to the periodicity of the crystal lattice, but form a step at the interface between these two phases. Gradual shearing of the precipitates within a slip band occurs during cyclic deformation due to the random to-and-fro glide of dislocations. An example of this in superalloy Nimonic PE16 is shown in Figure 2.19.

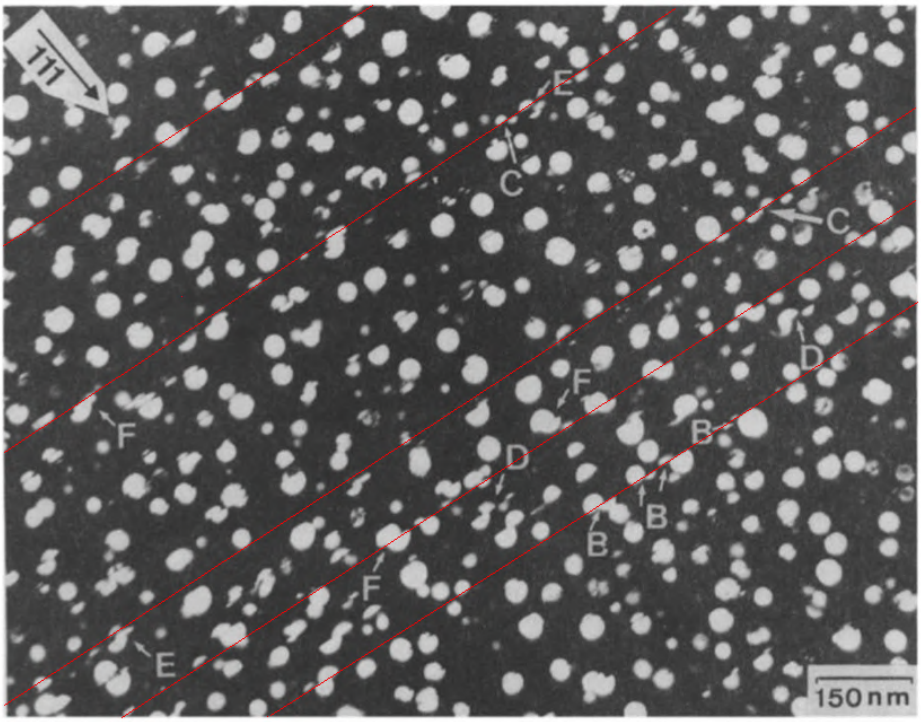

Fig. 2.19 - Dark field TEM micrograph of a Nimonic PE16 sample deformed to 200 cycles at room temperature showing sheared γ' particles [117]. Some slip bands where precipitates are clearly sheared are marked in red.

The precipitate cross section that the dislocations have to traverse when gliding in a slip line is decreased due to the shearing process. For this reason, the cause of cyclic softening has been attributed to this mechanism [105, 116, 118–120]. Note in Figure 2.19 that the shear step lengths vary in each plane, so that different particle configurations arise. For example, the two sheared halves can be partially (B) or completely (C) separated; and in some cases the top half of a γ' precipitate can even deposit on the bottom half of the neighbouring particle, restoring some of the precipitate cross sectional area (D) [117].

Alternatively, a "disorder hypothesis" has also been proposed, according to which the random motion of dislocations continuously scrambles the atoms along the slip bands, eliminating the local ordering of the precipitate structure [121]. This would also result in macroscopic cyclic softening due to the loss of antiphase boundary, although the kinetics of

this process are different and would also be highly influenced by the atomic diffusivity of the solute species.

Precipitate-free deformation bands

In some fatigue tests, deformation bands along which no precipitates can be found have been reported; however, the formation mechanisms and conditions for their occurrence are not yet fully clear. Similarly to the precipitate shearing mechanism, γ'-free deformation bands have been linked to cyclic softening, as dislocations can glide more easily along that region [97, 116, 122]. Materials in which they have been identified include Waspaloy [97], Nimonic PE16 [116, 117] and an experimental nickel-based superalloy [122], as well as other thermodynamic systems where the microstructure contains shearable precipitates, such as Al-Li [123–125], Al-Zn-Mg [126] and Al-Ag [127]. Very little is mentioned in the literature regarding their morphology, although it seems that they are always thicker than the precipitates dissolved [116]. An example of a microstructure with precipitate-free bands is shown in Figure 2.20.

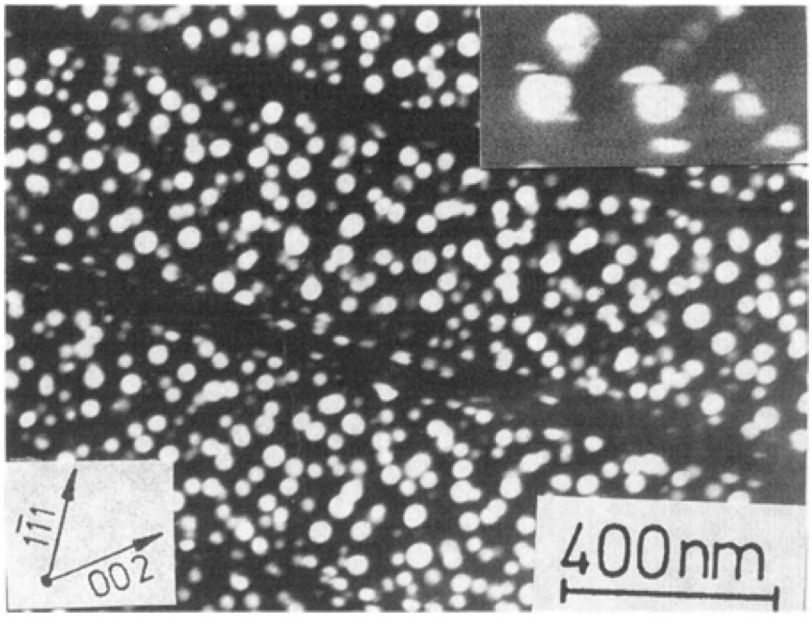

Fig. 2.20 - Dark field TEM micrograph of an overaged Nimonic PE16 sample deformed at a strain amplitude of 0.6% at room temperature showing γ'-free deformation bands. A magnified view of the sheared precipitates is shown in the inset [116].

An important characteristic of these deformation bands is that precipitates reappear if subjected to an adequate heat treatment, meaning that the chemical composition of the band does not vary after they have been formed [117, 127]. Sundararaman and coauthors [117]

proposed a model in which these bands originate due to the fragmentation of the precipitates by dislocations gliding in the octahedral plane and cross slipping in the cube plane, all of this within the slip bands. The particles would be cut into very small particles and redistributed until no precipitates are left along the deformation band. However, it seems improbable that the depletion occurs only due to mechanical processes without any dissolution of the precipitates [128].

Alternatively, Brechet *et al.* [123] proposed a simple model of particle dissolution from an energetic analysis considering the change in the area/volume ratio of the precipitates due to the shearing process. A similar approach by the same author [128] that also considers re-precipitation due to the solute enrichment in the matrix, pointed out that the precipitate depletion could result in a negative strain rate sensitivity within a range of strain amplitudes, a pseudo-Portevin-Le Chatelier effect also accompanied by serrations in the flow stress curve. This phenomenon has been experimentally seen in alloys containing shearable precipitates, *e.g.* in Al-Li alloys a 'genuine' Portevin-Le-Chatelier effect was ruled out as there should be a very low interaction between dislocations and lithium atoms [128].

Dynamic strain ageing

In nickel-based superalloys, the serrations in the stress-strain curve and the negative strain rate sensitivity have also been attributed to the presence of dynamic strain ageing (DSA), also called Portevin-Le-Chatelier effect. This is a temperature and strain rate dependent mechanism that consists in the jerky movement of dislocations due to their pinning and unpinning, occurring due to the diffusion of solute atoms around arrested dislocations, momentarily hindering their movement [33, 129, 130]. From an activation energy point of view, interstitial solutes have been identified as responsible for the appearance of serrated flow in the temperature region from 250 to 350°C, whereas substitutional solutes control this mechanism from 400 to 650°C [131, 132]. Mannan [132] summarised some of the consistent DSA effects that appear during low cycle fatigue tests, such as

- serrated stress-strain response;
- increase in the work hardening and work hardening rate;
- increase in the localisation of plastic strain;
- decrease in the strain rate sensitivity, even to negative values under certain conditions.

DSA effects have been reported in a wide variety of nickel-based superalloys under different temperature and strain rate regimes, although less data are reported for the latter.

Examples of these include solid solution alloys such as Alloy 690 [133], Hastelloy X [131] and Haynes 230 [134, 135], as well as γ'-strengthened alloys, some of which are Waspaloy [111], Nimonic PE16 [115], TMW-4M3 [136] and 720Li [137]. It is hard to state the conditions for the occurrence of DSA as it is also strongly dependent on the composition and its effects appear at varied temperatures, ranging from 200°C [133] up to 760°C [134] in different alloys.

Furthermore, the interpretation of the effects of the Portevin-Le Chatelier mechanism have been mostly derived from the macroscopic stress response of the materials (flow stress serrations, strain rate sensitivity), and very little work has been done looking at the microscopic effects, such as the true interactions between dislocations and solute atoms [130]. In general, no systematic study has identified whether the reported effects arise due to DSA or other mechanisms such as the pseudo-Portevin-Le Chatelier effect previously described.

Precipitation and evolution of second phase particles

Carbides, nitrides and carbonitrides already present in the alloys prior to deformation have been found to further precipitate and grow during cyclic loading at high temperatures. In the case of carbides (which have been studied more extensively and appear to precipitate dynamically in larger amounts), this process requires the diffusion of carbon and other elements to occur according to the reactions [138]

$$MC + \gamma \rightarrow M_{23}C_6 + \gamma', \tag{2.2}$$

$$MC + \gamma \rightarrow M_6C + \gamma' \tag{2.3}$$

and

$$M_6C + M' \rightleftarrows M_{23}C_6 + M'', \tag{2.4}$$

where M, M' and M'' denote different elements, *e.g.* Hf, Ta, Nb and Ti. Reactions 2.2 and 2.3 represent the gradual precipitation and coarsening of $M_{23}C_6$ and M_6C by means of the MC carbide decomposition, which is a major source of carbon below 980°C in most nickel-based superalloys [19, 138], whereas equation 2.4 denotes the interaction between the first two. Preferential sites for the precipitation of carbides are grain boundaries [111, 122, 139], twin boundaries [111, 139], slip bands [29, 111, 139], dislocations [131, 140] and the interfaces between the matrix and other types of carbides [19]. In the case of dislocations, the formation of second phase particles is due to the local reduction in strain energy around them, this effect being higher for edge segments [141].

It has been said that the contribution of the carbides to the yield stress is negligible due to their low volume fractions [15, 40], although the effect of the dynamic precipitation during cyclic loading to the flow stress is still controversial with some authors arguing in its favour [141, 142]. Similar to DSA, carbide precipitation on dislocations effectively immobilizes them, promoting the formation of new dislocations [141, 142]. Similarly, carbides in the matrix represent an obstacle to dislocation movement as shown in Figure 2.21. Moreover, the second phase particles are also associated with higher back stresses [143, 144]. On the contrary, the formation of carbides comes with the depletion of carbon in the γ matrix, which may weaken the material by a decrease in the solid solution strengthening [19].

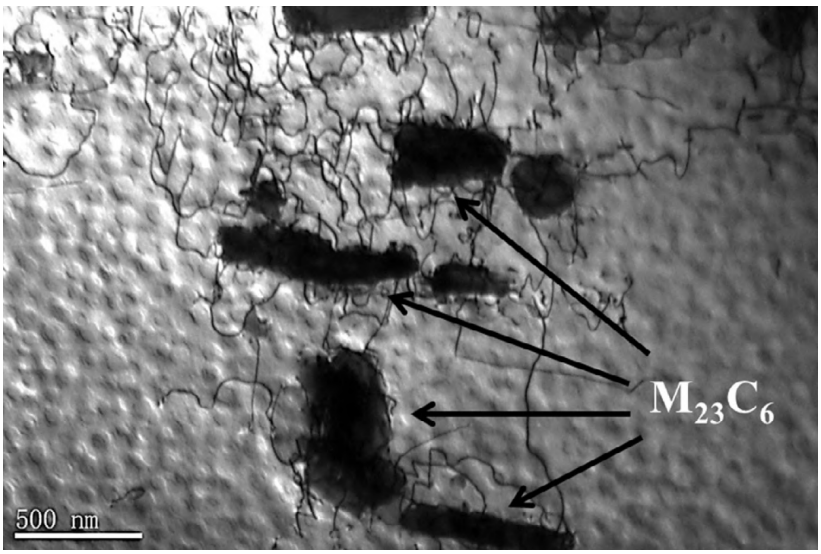

Fig. 2.21 - $M_{23}C_6$ carbides preventing the movement of dislocations in a superalloy GH4037 gas turbine blade operated in-service for about 1600 hours [19].

As expected from considering the diffusion kinetics, larger carbides can be found at higher temperatures and for longer times. In a similar way, γ' coarsening has been identified in several nickel-based superalloys fatigued at high temperatures [29, 111, 139, 141]. This has been associated in the literature with cyclic hardening, although depending on the precipitate size this could also soften the material (growth of overaged particles) based on the precipitate strengthening theory detailed in Section 2.1.2. It must be highlighted that this mechanism should be time dependent, rather than strain rate dependent.

Homogeneous deformation

As an alternative to the high localisation of strain previously described, homogeneous dislocation distributions have also been identified under some deformation conditions. Large precipitate sizes further promote the formation of Orowan loops, developing higher internal

stresses and hindering dislocation glide in those planes [98, 116]. Under certain deformation conditions, high γ' volume fractions of cuboidal precipitates confine the deformation to the γ-channels, resulting in the formation of wavy deformation bands [145]. This transition from planar to wavy slip behaviour has been shown extensively in different γ' strengthened nickel-based superalloys [97, 104, 105, 116, 146]; an example of this is shown in Figure 2.22.

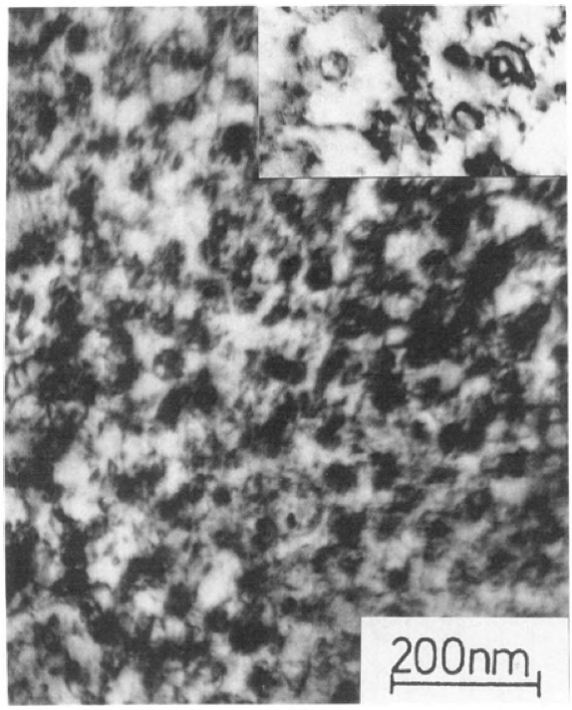

Fig. 2.22 - Homogeneous distribution of dislocations in an overaged sample of Nimonic PE16 cyclically deformed at a strain amplitude of 2.6%. A high density of dislocations as well as Orowan loops can be seen in the inset [116].

With increasing temperatures the slip bands become more diffuse until they can no longer form [29, 111], resulting in a dislocation structure consisting of Orowan loops around the γ' precipitates and dislocation tangles homogeneously distributed. Additional cross slip of the otherwise planar slip bands enables dislocations to move along the matrix avoiding the stronger precipitates [147]. This homogeneous deformation might occur due to different phenomena, *e.g.* the variation in the stacking fault energy promotes cross slip and the increased vacancy diffusion results in more dislocation climb, as has been reported in a wide variety of alloys [29, 109, 136, 148, 149]. Besides, the addition of heavy atoms such as rhenium at high temperatures further promotes slip homogenisation due to the increase in the lattice misfit, resulting in denser dislocation networks at the precipitate interfaces [150].

Deformation homogenisation is also promoted for large strains in microstructures containing precipitates. Similar to the temperature effect, there appears to be a transition from planar to wavy slip due to variations in the strain amplitude of the cyclic loading [146]. This phenomenon could arise from the necessity of the material to accommodate the additional plastic deformation, forcing dislocations to cross slip and develop additional slip bands.

2.2.2 Cyclic stress-strain response

Over the last fifty years a wide variety of studies have explored the fatigue behaviour of nickel-based superalloys. However, the priority in the scientific community has been to understand the crack initiation and propagation phenomena, rather than the evolution of the macroscopic stress response. Mostly empirical equations have been used to describe this due to the complexity of the dislocation mechanisms that take place at different stages of the fatigue process.

The cyclic stress-strain curves obtained from many tests vary a lot and trends are not easy to identify. In order to address this issue, a summary of different tests is presented in Tables 2.2 and 2.3 for solid solution and γ'-strengthened alloys, respectively. This summary includes tests performed from room temperature to about 800°C to capture the transition between different deformation regimes, although higher temperatures were not included as they have mostly been done in single crystal alloys, which lie beyond the scope of the present work.

Table 2.2 - Microstructure and operation conditions of fatigue tests in solid solution nickel-based superalloys where the cyclic stress response is reported. Values in italic are the changing variables in the corresponding work.

Alloy	Grain size	Temperature	Strain rate		Strain ratio	Strain amplitude	Ref.
			Linear	Sinusoid			
	[μm]	[°C]	[%/s]	[Hz]		[%]	
Alloy 690	53	*RT, 204*		0.15	-1	*0.2 - 0.5*	[133]
Haynes HR-120	-	*RT - 982*	0.4		-1	*0.2 - 1.15*	[142]
Hastelloy X	*77	*RT - 704*	0.04		-1	0.3	[131]
Haynes 230	60	*RT - 982*		*0.003 - 0.33*	*-1, 0*	*0.15 - 0.8*	[134]

- Values not reported
* Average value
RT: Room temperature

Many difficulties arise when comparing fatigue data from the literature, *e.g.* microstructures not fully characterised and missing data. Furthermore, as seen in Tables 2.2 and 2.3, some of the tests have been done under different loading modes; for instance, using a constant total or plastic strain amplitude control. Similarly, some experiments were performed with a constant strain rate, whereas others employed a sine wave for the displacement. These differences, although not expected to affect the trends of the stress curves and microstructure evolution, may introduce variations in the operating deformation mechanisms at different stages of the tests.

The most common behaviour seen in these alloys consists of a short cyclic hardening stage (of around 20 cycles) followed by softening until crack initiation. Examples of this are shown in Figure 2.23, where an increasing stress for larger strain amplitudes can be

Table 2.3 - Microstructure and operation conditions of fatigue tests in γ'-strengthened nickel-based superalloys where the cyclic stress response is reported. Values in italic are the changing variables in the corresponding work.

Alloy	Grain size	γ' precipitate		Temperature	Strain rate		Strain	Strain amplitude		Ref.
		Size	Fraction		Linear	Sinusoid	ratio	Total	Plastic	
	[μm]	[nm]	[-]	[°C]	[%/s]	[Hz]		[%]	[%]	
**Experimental alloy	-	-	-	650		0.5	-1	*0.3 - 0.8*		[122]
Mar-M247LC	-	500	-	*760 - 982*		0.05	-1	*1.2 - 1.64*		[149]
Waspaloy	60	*8*	-	RT	-		-1		*0.24 - 0.83*	[97]
		25								
		50								
		90								
Waspaloy	*125*	**6.5*	-	*RT - 800*		0.33	-1		*0.075 - 0.15*	[111]
	16	*B: 300 + 90*								
Nimonic 80A	60	*< 5*	-	RT		0.2	-1		*0.025 - 3*	[104]
		13								
		20								
		B: 100 + 13								
Nimonic 90	300	-	-	RT	0.3		-1	*0.4 - 1.1*		[151]
Nimonic 90	130	*S*	0	RT	0.3		-1	*0.5 - 1.1*		[105]
		11.35	0.14							
		27.15	0.14							
		60.35	0.14							
Nimonic PE16	-	*12.5*	-	RT	0.4		-1	0.57		[152]
		21								
		30								
Nimonic PE16	30	*10*	0.07	RT	0.4		-1	*0.6, 2.6*		[116]
		21	0.07							
		30	0.07							
Nimonic PE16	65	*S*	0	650	0.3		-1	*0.25 - 1*		[146]
		18	0.11							
		35	0.11							
Nimonic PE16	65	*S*	0	*450 - 650*	*0.003 - 3*		-1	0.6		[115]
		18	0.11							
GH4742	-	-	-	650	0.6 - 1.4		-1	*0.3 - 0.7*		[153]
GH4145/SQ	110	B: 80 + 20	-	538	0.4		-1	*0.35 - 0.95*		[154]
Inconel 792-5A	3000	B: 600 + 200	-	*RT, 900*	0.2		-1	*0.16 - 1.2*		[155]
Udimet 720Li	11	T: *5500 + 120 + 50	0.18, -, -	*RT - 650*	0.5		-1	*0.4 - 1.2*		[137]
TMW-4M3	8.7	T: *1500 + *65 + *7	0.17, -, -	*400 - 725*	0.8 - 1.2		0	*0.4 - 0.6*		[136]

- Values not reported
* Average value
** Composition of the experimental alloy given
RT: Room temperature
S: Solutionized
B: Bimodal precipitate size distribution
T: Trimodal precipitate size distribution

clearly seen. Additionally, a difference in the behaviour of the peak stress is observed when comparing Figures 2.23(a) and (b), where there is a clear shift towards a lower cycle number at high strain amplitudes.

This cyclic behaviour is very different from that in other fcc materials, which typically show cyclic hardening until stress saturation (*e.g.* pure copper [26, 156], brass [157], mild steel [158], structural carbon steel [159]) or only cyclic softening (*e.g.* γ''-strengthened superalloy Inconel 718 [160–163]). Other materials that show the aforementioned hardening/softening behaviour are alloying systems with coherent shearable precipitates, such as Al-Cu [164], Cu-Co [165], Al-Zn-Mg [126].

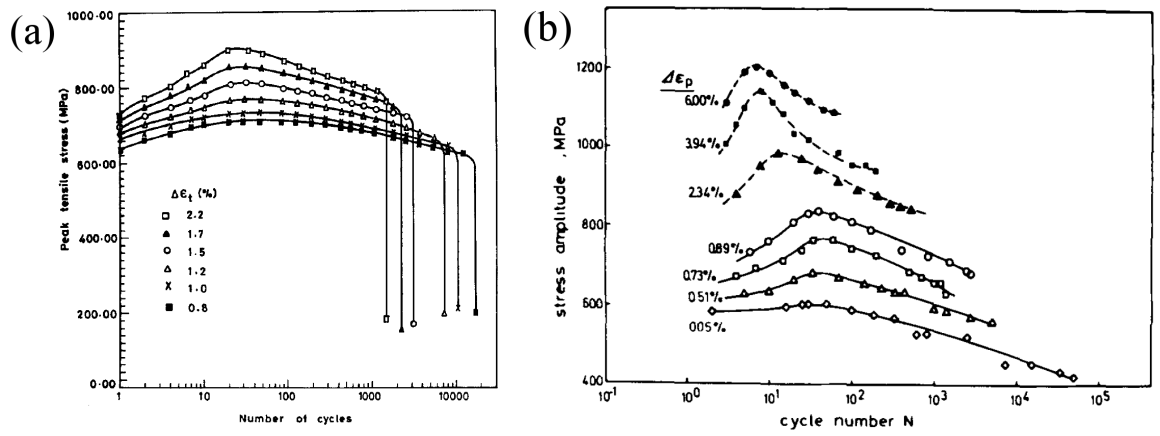

Fig. 2.23 - Room temperature cyclic stress-strain curve of (a) Nimonic 80A [104] and (b) Nimonic 90 [151] for different strain amplitudes.

Many mechanisms have been proposed to explain the observed responses, but no consensus has been reached regarding which one dominates for each condition. The stress hardening mechanisms that have been mentioned are:

- accumulation of dislocations at the slip bands [29];
- build-up of Orowan loops around large precipitates [166];
- dynamic strain ageing [115, 131, 133, 136, 137];
- carbide precipitation on dislocations [141, 142];
- growth of underaged precipitates [29].

Alternatively, mechanisms responsible for the cyclic softening include:

- precipitate shearing [105, 116, 119, 120, 152];
- precipitate disordering [108, 152, 164];
- precipitate dissolution [123, 152];
- formation of precipitate-free deformation bands [97, 116, 117];
- loss of coherency between the matrix and the precipitates [167];
- microtwin formation [133];

- formation of planar dislocation structures from a more homogeneous deformation behaviour [100, 101];
- growth of overaged precipitates [167];
- growth of carbides at high temperatures [142];
- grain growth during cyclic loading at high temperatures for long times [122].

In general, it is agreed that hardening of the materials is due to dislocation interactions between them or with other microstructural features. The accumulation of dislocations has been studied mostly in metals with wavy slip that form a cell subgrain structure [168, 169], although similar processes are expected to occur in planar slip materials. It results from the balance of dislocation formation and annihilation; the former happens as a necessity for the material to accommodate the plastic strain, and the latter is a dynamic recovery process that includes includes annihilation of screw segments due to cross slip or of edge-type dislocations by climb at high temperatures [169, 170]. The combination of these processes is expected to reach a saturation stage [165], although the dislocation density and the number of cycles to reach this point varies with the deformation conditions.

Cyclic softening in nickel-based superalloys has been mostly associated to the first three mechanisms mentioned: precipitate shearing, disordering and dissolution, although there is controversy regarding which amongst these dominates the process [152]. All these processes soften the material by effectively decreasing the precipitate cross sectional area that the dislocations have to traverse, but they differ mostly in the kinetics driving this change. Moreover, the formation of γ'-free deformation bands may further decrease the strength of the material, although it cannot be responsible for all the softening as their appearance has not been spotted in many alloys.

The softening rate is usually lower in solid solution alloys than in precipitate-strengthened materials, an example of which is shown in Figure 2.24. In the former, the softening process has been associated with other phenomena. At low temperatures and large strain amplitudes, the appearance of deformation microtwins has been associated with a decrease in the dislocation density [133], although their formation and evolution during the fatigue test has not been observed. On the other hand, the growth of overaged particles, carbides and the grain size may be responsible for the softening observed at high temperatures in both solid solution and precipitate-containing alloys. Softening in solutionized alloys has also been attributed to the observed *in situ* dynamic precipitation of small γ' particles during cyclic loading under certain deformation conditions [115, 146], which might be subsequently sheared. A mathematical model that considers dynamic formation of GP zones

in supersaturated aluminium alloys has been proposed to occur via the contributions of vacancies and dislocations [171], although it has not been applied in superalloys.

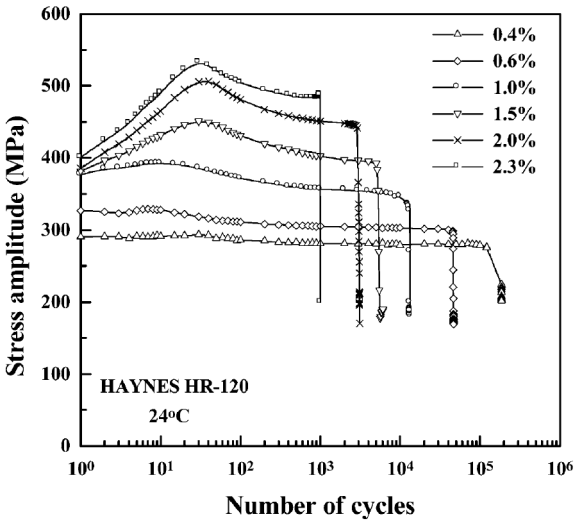

Fig. 2.24 - Cyclic stress-strain curve of the solid solution alloy Haynes HR-120 deformed at room temperature for different strain ranges [142].

Larger precipitate sizes in underaged materials seem to increase the yield stress of the alloy, with small changes in the evolution of the cyclic stress-strain response. This can be seen in Figure 2.25(a). However, there is a clear deviation in both the hardening and softening rate for larger precipitates. This behaviour, evidenced in Figure 2.25(b), has been associated with the transition towards a more homogeneous deformation for very large precipitates. The storage of dislocations in Orowan loops around large precipitates is an additional source of hardening that further increases the kinematic hardening [172–175].

A systematic study of the precipitate size effect in a Cu-2at%Co alloy performed by Mughrabi [165], shown in Figure 2.26, revealed the existence of a saturation stage following the cyclic softening. Furthermore, a residual stress contribution from the precipitates can be identified at saturation, meaning that the softening process does not remove all the hardening provided by the second phase particles [165]. Tests in many nickel-based superalloys have shown a similar behaviour, with a softening rate that decreases with the number of cycles, although a steady stress amplitude is rarely reached. This could be due to crack initiation taking place before this stage is reached.

An intermediate temperature regime, from approximately 200 to 600°C, can be seen in different solid solution and γ'-strengthened alloys. This is characterised by a higher hardening rate comprising a larger number of cycles, and it has been linked to the presence of dynamic strain ageing [115, 131, 133, 136, 137]. Thus, it is possible that the softening

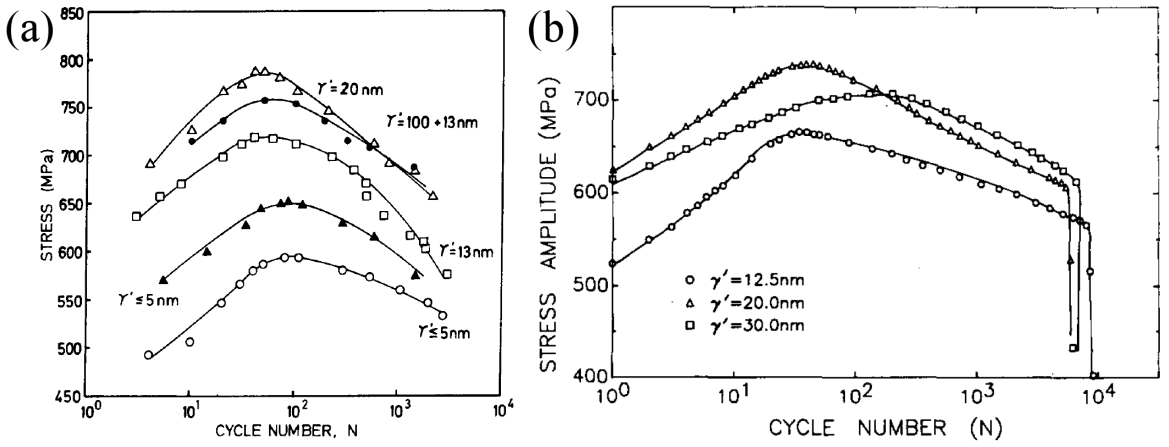

Fig. 2.25 - Cyclic stress-strain curve of (a) Nimonic 80A [104] and (b) Nimonic PE16 [152] deformed at room temperature for different γ' sizes.

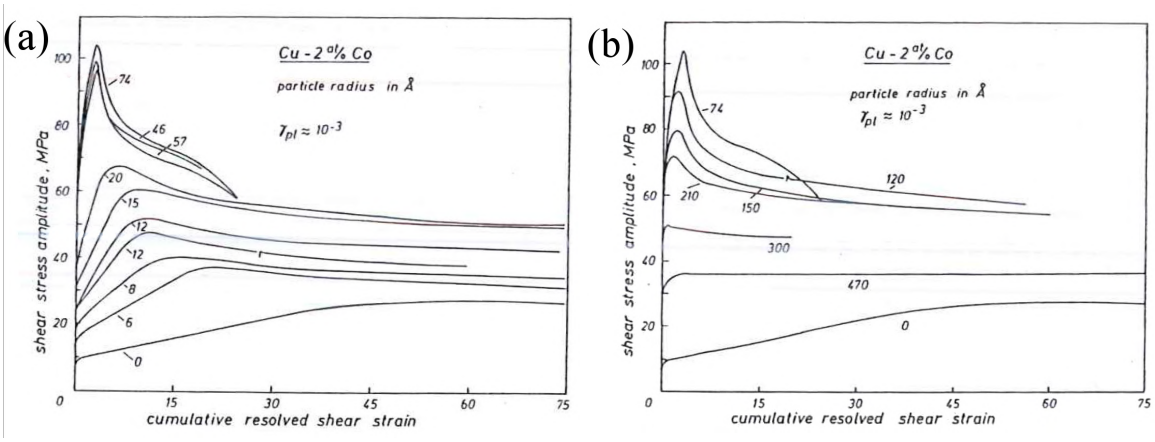

Fig. 2.26 - Cyclic stress-strain curve of a Cu-2at%Co alloy with (a) underaged and (b) overaged precipitates cycled at room temperature [165].

mechanisms still operate at these temperatures, although the increased hardening dominates the overall behaviour of the material.

At even higher temperatures the trend reverts and the peak stress shifts again towards a smaller number of cycles. It is not clear whether this transition is only linked to the disappearance of dynamic strain ageing or also because of the activation of other mechanisms such as dislocation climb or carbide precipitation and coarsening. Furthermore, at very high temperatures (above 900°C) a constant stress amplitude, sometimes following a slight softening stage, is seen [149, 155, 167]. This might occur due to a transition towards more

homogeneous deformation with no precipitate shearing. Examples of the temperature effect in some alloys are shown in Figure 2.27.

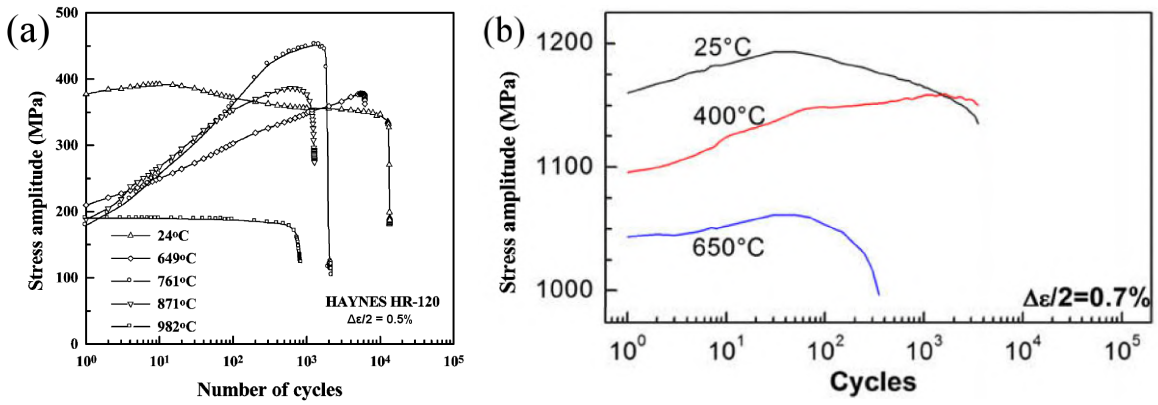

Fig. 2.27 - Cyclic stress-strain curve of (a) Haynes HR-120 [142] and (b) 720Li [137] cyclically deformed at different temperatures.

2.3 Mesoscale modelling: Kocks-Mecking formulation

Many modelling approaches have been postulated to account for the role of dislocations in plastic flow for different modes of continuous deformation. At the mesoscale (typically between $10^{-8}-10^{-5}$ m), mathematical descriptions are formulated by considering the average values of the variables with little regard to individual dislocation behaviours or arrangements. The Kocks-Mecking model [81, 176, 177] is based on the assumption that a single internal variable, *i.e.* the average dislocation density ρ, can be used to determine the kinetics of plastic deformation. The dislocation density is also linked to the macroscopic stress response σ via the Taylor equation

$$\sigma = M\alpha\mu b\sqrt{\rho}, \tag{2.5}$$

where M is the Taylor factor, μ the shear modulus, b the Burgers vector and α a constant of order unity accounting for the strength of the dislocation/dislocation interactions [177].

The evolution of the dislocation density as a function of the plastic strain ε_p is

$$\frac{d\rho}{d\varepsilon_p} = \frac{d\rho^+}{d\varepsilon_p} - \frac{d\rho^-}{d\varepsilon_p}, \tag{2.6}$$

where $d\rho^+/d\varepsilon_p$ and $d\rho^-/d\varepsilon_p$ are the dislocation storage and annihilation rates, respectively. The storage of dislocations is an athermal contribution and it depends on the mean free path of the dislocations Λ in the form

$$\frac{d\rho^+}{d\varepsilon_p} = \frac{M}{b\Lambda}. \tag{2.7}$$

This accounts for the spacing of different microstructural parameters that act as obstacles to dislocation glide Λ_i, and for dislocation/dislocation interactions, separated by a distance Λ_d, as

$$\Lambda^{-1} = k_1\Lambda_d^{-1} + \sum_i \Lambda_i^{-1}, \tag{2.8}$$

where $\Lambda_d = 1/\sqrt{\rho}$ and k_1 is a material dependent parameter called dislocation storage coefficient [176]; empirical approximations for this term have been given via experimental datasets in pure materials [176–179].

Alternatively, dynamic recovery arises from the collapse of dislocations with opposite signs, both edge dipoles by climb and screw dislocations by cross-slip at an average separation lower than a critical distance that depends on the composition and glide behaviour of the dislocations [170]. Thus, the annihilation term in equation (2.6) is highly dependent on

temperature and strain rate, and it increases proportionally to the dislocation density, *i.e.*

$$\frac{d\rho^{-}}{d\varepsilon_p} = Mk_2\rho, \tag{2.9}$$

where k_2 is the dynamic recovery coefficient. Additional modelling on this parameter has also been performed [169, 180], although, similarly to the case of k_1, most of the literature focuses on pure materials, which deform in a more homogeneous way than nickel-based superalloys.

One of the advantages of this model is that it can be used for tests with non-constant temperatures and strain rates, as the response of the material is a function of the immediate dislocation density. However, fatigue modelling at the mesoscopic scale requires additional considerations as dislocations travel in opposite directions during the tensile and compressive loading stages, which results in phenomena such as the Bauschinger effect. This has been addressed by considering a supplementary internal variable, the density of dislocations partially recoverable upon reversal loading ρ_r, with an evolution that depends on microstructure and operation conditions [181].

Estrin [182], among other authors, has further extended the model to consider additional microstructures, including alloys with shearable and non-shearable precipitates, solute atoms and grain size effects. These and other modifications are essentially done by considering additional stress contribution terms in equation (2.5) or supplementary obstacles to dislocations in equation (2.8), although obvious variations in the values of k_1 and k_2 come associated with these changes.

Precipitates in particular have a big influence on the stress response of the material and they are relevant to the study of nickel-based superalloys. According to Ashby's theory [183], non-shearable particles are a source of geometrically necessary dislocations (GNDs), required for compatibility at the matrix/precipitate interface, which give rise to internal stresses due to the misfit and difference in shear moduli [172, 184]. The number of dislocations per particle, their influence to the flow stress and their contribution to the Bauschinger effect have been modelled within Kocks-Mecking frameworks for different alloying systems [185–187]. However, shearable precipitates have been addressed to a lesser extent, and the evolution of the particle morphology has not been incorporated into these models.

The formation of dislocation structures has been considered in the case of cell formation by acknowledging that there is a heterogeneous distribution of dislocations consisting of walls (high ρ) and cell interiors (low ρ) [188]. This is similar to treating the material as a composite with two different phases, with the difference that their volume fractions may vary with straining and they do not have well defined interfaces, so that dislocations constantly

move from one region to the other [81]. Within the composite model, equation (2.5) can be rewritten as

$$\sigma = M\alpha_1\mu b\sqrt{\rho_1} + M\alpha_2\mu b\sqrt{\rho_2}, \tag{2.10}$$

where the subindices 1 and 2 correspond to the different dislocation regions, and the α coefficients are not the same due to their different dislocation interactions and effects on the stress response.

Chapter 3

Morphology and evolution of slip bands

3.1 Introduction

Fatigue in metals has been studied for over 180 years [189]; the term *"fatigue"* itself dates back to 1854 [190]. For the majority of this time an empirical approach was used to identify trends in the behaviour of materials upon different loading conditions. The well known Coffin-Manson power law for the prediction of fatigue life as a function of plastic strain during low cycle fatigue is an example of this. Whilst these are useful to describe the behaviour of tested materials, research on the physics behind deformation and damage phenomena provide a clearer picture of how and why these occur.

The morphology of the slip bands that develop during low cycle fatigue has been characterised to some extent in a number of nickel-based superalloys. However, a lot less is known regarding how these evolve. Due to the destructive nature of the techniques, microscopy studies reveal the deformation structure only after the test has stopped. These inconveniences can be partially circumvented by characterising samples from interrupted tests, so that direct comparisons can be made between behaviours after a different number of cycles.

A combination of electron microscopy techniques is used here to investigate multiple aspects of the slip bands, including their formation, propagation, dislocation arrangements, interaction with γ' precipitates and, most importantly, the evolution of all these. Two imaging modes are used within the SEM to analyse the heterogeneity of slip across grains and the morphology of sheared precipitates. TEM is employed to observe the dislocations structures in detail. A new methodology is also introduced to measure slip band parameters such as slip line spacing and shear step length through an orientation analysis. Statistics of these parameters are obtained and compared for different conditions. The combination of these techniques provides a unique mechanistic and quantitative insight into the slip band and precipitate morphology evolution.

3.2 Material and methods

The material examined in this study is the powder processed polycrystalline nickel-based superalloy RR1000, supplied by Rolls-Royce plc. The composition of this alloy is given in Table 3.1. The heat treatment consisted of a supersolvus solutioning at 1170°C for two hours, fan air cooling close to -1°C/s, ageing at 760°C for 16 hours and static air cooling. Six dog bone shaped samples with the geometry shown in Figure 3.1 were machined, and their 14 mm gauge lengths polished and shot peened.

Table 3.1 - Chemical composition of alloy RR1000 (wt%).

Ni	Cr	Co	Mo	Al	Ti	Ta	Hf	Zr	C	B
bal	15	18.5	5	3	3.6	2	0.5	0.06	0.027	0.015

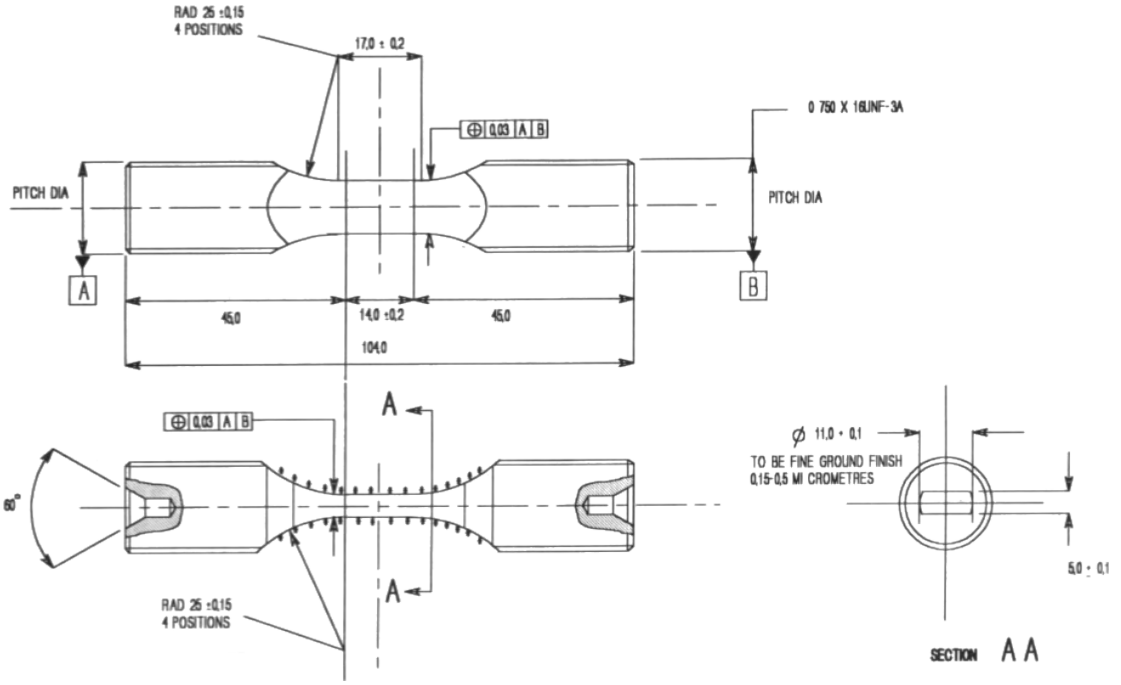

Fig. 3.1 - Geometry of the RR1000 low cycle fatigue samples with all dimensions in millimetres.

Interrupted fatigue tests were performed by Rolls-Royce plc at room temperature and 700°C for 1, 40 and 500 cycles in a servo-hydraulic test frame with a side contact extensometer and a furnace surrounding the specimen. A fully reversed strain control was used with an amplitude of $\Delta\varepsilon/2 = 0.6\%$, a constant strain rate of $0.5\%\text{s}^{-1}$ and dwell times of one second at the minimum and maximum strains. The tests started with a tensile load and ended after a

compression stage. The maximum and minimum stresses per cycle were recorded for each cycle, together with the cyclic stress-strain response.

SEM samples were then cut parallel to the loading direction for every condition expecting some slip bands to be close to an edge-on orientation. Samples were also cut from an undeformed material to look at the initial microstructure and dislocation arrangement. All samples were hot mounted in bakelite, ground and polished with diamond suspensions and colloidal silica following standard procedures.

Electron Channeling Contrast Imaging (ECCI) was performed under the circular backscatter detector of a FEI NOVA NanoSEM with a tension of 30 kV and a working distance of 5 mm. Multiple grains of each sample were imaged in this mode by tilting the stage within a $\pm 1^{\circ}$ to get close to a two-beam condition. This technique was used to get an overview of the main deformation mechanisms taking place at different temperatures and number of cycles, as well as to appreciate the variability found among different grains for each condition. Furthermore, the backscattered electron detector was also used to measure the grain size via the circular intercept method as per the ASTM standard E112-13 with six circles of 700 μm diameter.

Transmission electron microscopy (TEM) was also performed in specimens tested at 20°C and 700°C for 1 and 40 cycles to look at the dislocation interactions taking place within the slip bands. Slices of the material were cut parallel to the loading direction, spark eroded and electropolished with a solution of 10% perchloric acid in methanol. All the images were taken in a JEOL 200CX TEM in bright field mode. Multiple consecutive sections of some slip bands were imaged at a high magnification and then stitched together with an image processing software by manually adjusting the brightness and contrast of the individual images.

A preferential γ' etchant described in Table 3.2 was applied to a set of SEM samples after standard sample preparation to characterise the microstructure and to look at the morphology of the sheared precipitates under the secondary electron through-lens detector of the SEM with a voltage of 15 kV. Secondaries and tertiaries were independently imaged at 10 kX and 50 kX, respectively, by manually outlining the edges of the holes and performing the particle analysis in the ImageJ software package.

3.2.1 Slip line characterisation technique from γ'-etched samples

A slip band in a γ'-etched sample appears as a series of holes sheared along parallel planes, as in Figure 3.2(a). All the shear steps within a slip band appear to happen forward and backward along only one direction, leaving markings on the etched sample surface from which the orientation of slip can be deduced. The methodology introduced in this section

Table 3.2 - Chemical composition of the γ' etchant.

	Compound	Quantity	Details
Part I	H_2O	150 ml	The preparation was done in two steps
	HCl	150 ml	following the indications in [191]. The
	MoO_3	2.5 g	samples were submerged in the Part II etchant
Part II	HNO_3	15 ml	for 10 seconds.
	H_2O	25 ml	
	Part I	30 ml	

was used to access the true slip line spacings and shear displacements produced at the scale of individual slip planes in grains chosen at random from the samples fatigued at 20°C and 700°C for 40 and 500 cycles.

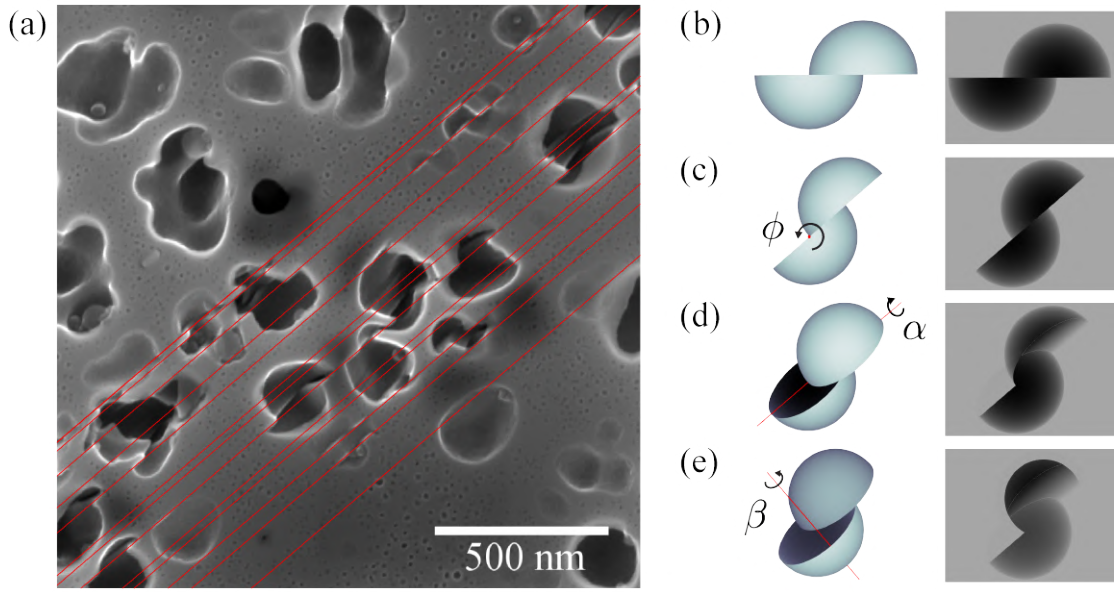

Fig. 3.2 - (a) Secondary electron micrograph of a γ'-etched sample fatigued for 500 cycles at 20°C showing sheared precipitates. Red lines are drawn along the lines where the active slip planes intersect the sample surface. Models of a precipitate sheared and the hole it would leave in the matrix after being etched away are shown after consecutively applying (a) a shear step of length s and rotations by angles (c) ϕ, (d) α and (e) β.

This technique consists in measuring within the SEM characteristic lengths from the shear steps left in the etched holes to obtain the angles of the consecutive rotations that a sheared particle would need to undergo to produce the shape of a hole as observed in a micrograph. The axes of the rotations by angles ϕ, α and β are the normal to the sample surface, the slip line projection and the normal to the slip plane, respectively. Figure 3.2(b-e) schematically shows the sequence of these rotations and angles for a precipitate and a precipitate hole.

To define the directions and angles required to describe the orientation and real distances of interest, consider three orthogonal right-handed coordinate systems: (x,y,z) with the x and y axes aligned with the sides of the micrograph, (x',y',z') resulting from the rotation along the z axis by angle ϕ so that the active slip markings are parallel to x', and (x'',y'',z'') with $x''=x'$, y'' parallel to the slip plane normal and positioned at the centre of the precipitate on the shear plane. These coordinate systems can be seen in Figure 3.3 along with other parameters described in this section.

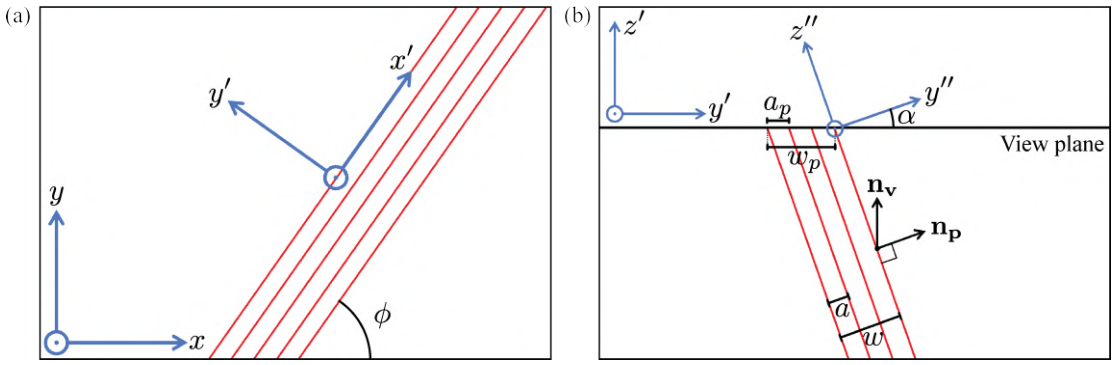

Fig. 3.3 - Schematic representations of the different coordinate systems (blue), slip line and slip line projections (red) and some of the slip band parameters as seen from (a) the direction of the electron beam and (b) a lateral view with the slip band edge-on.

Sheared holes show the presence of elliptical marks. These are the projections onto the viewing plane of the circular cross sections along which shearing of the precipitates occur. Assuming an initial perfect sphericity, it would be possible to unequivocally determine the value of the angle α by measuring the ratio between the major and minor radii of the ellipse, $r_{x'}$ and $r_{y'}$ respectively, as

$$\alpha = \arcsin\left(\frac{r_{y'}}{r_{x'}}\right). \tag{3.1}$$

These features are drawn for a precipitate as an example in Figure 3.4(a).

To calculate β consider a vector in the third coordinate system $\mathbf{s}=(s_p,0,s_{z''})$ defining the direction and magnitude of a shear step. It is possible to directly measure s_p as the centre-to-centre distance between both halves of the sheared hole. Due to the in- and out-of-plane component of the shear direction, the segments along the slip line of the top and bottom halves of the hole l_1 and l_2 will not have the same length. The z''-coordinates of such segments before shearing occurred can be calculated from

$$z''_i = \frac{1}{2}\sqrt{d^2 - l_i^2}, \tag{3.2}$$

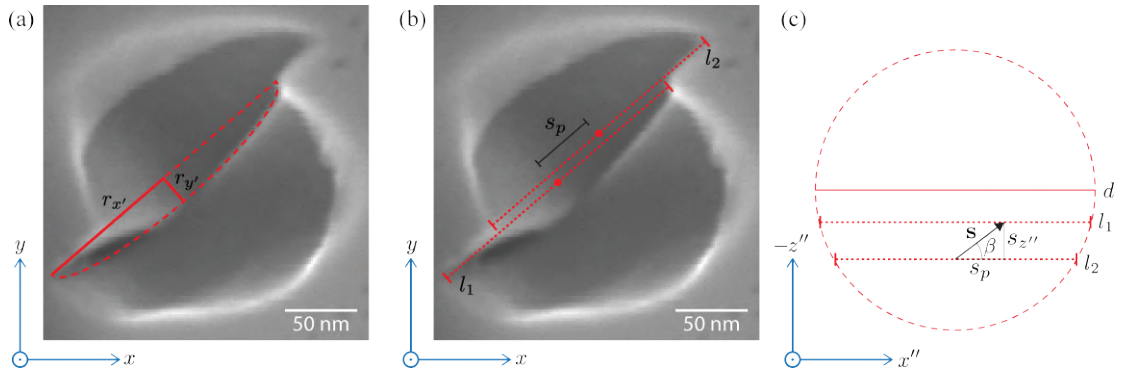

Fig. 3.4 - Lengths required to calculate (a) α and (b) β from a precipitate hole. (c) Precipitate cross section on the slip plane where shearing occurs in the direction $\mathbf{s}$.

where d is the diameter of the cross section at the shear plane. This distance can be detected and measured even tenths of nanometers under the surface in cases where more than half of the precipitate was positioned below the specimen surface thanks to the high voltage of the electron beam. Moreover, $s_{z''} = |z''_2 - z''_1|$ and

$$\beta = \arctan\left(\frac{s_{z''}}{s_p}\right). \tag{3.3}$$

Figure 3.4(b) shows an example of the aforementioned lengths. A schematic diagram of the cross section on the slip plane is drawn in Figure 3.4(c) before shearing occurs, showcasing the origin of β.

The angles α and β are the only parameters required to access the true morphology of the slip bands and shearing distances at the multiple slip lines observed. The y'' axis is relevant as both the slip band width w and slip line spacing a lengths lie along this direction. From Figure 3.3(b) it can readily be seen that

$$a = a_p \cos\alpha \tag{3.4}$$

where a_p is the projection of a onto the (x', y') plane, and $w = \sum_i a_i$ for each slip band. Similarly, the true shear step lengths s at each slip line are

$$s = \frac{s_p}{\cos\beta}. \tag{3.5}$$

With these parameters, an estimate of the local plastic shear strain for each slip band $\gamma_{p,SB}$ can also be obtained as $\gamma_{p,SB} = \sum_i s_i / w$. The height profile $h(y'')$ parallel to the Burgers vector of the slip band can also be reproduced as a piecewise step function from the shearing distances

and slip line spacings with the form

$$h(y'') = \sum_{i=1}^{n} s_i H\left(y'' - \sum_{j=1}^{i-1} a_j\right), \tag{3.6}$$

where n is the number of slip lines in the band, $H(x)$ is the Heaviside step function and $y'' = 0$ is the position of the first slip line in the band.

The Schmid factor m_S can also be calculated if the direction of unidirectional loading $\mathbf{n_\sigma}$ is known. The components of the active slip system in the (x,y,z) coordinate system can be extracted by accounting for the rotation matrices

$$R_1 = \begin{bmatrix} \cos\phi & \sin\phi & 0 \\ -\sin\phi & \cos\phi & 0 \\ 0 & 0 & 1 \end{bmatrix} \tag{3.7a}$$

$$R_2 = \begin{bmatrix} 1 & 0 & 0 \\ 0 & \cos\alpha & \sin\alpha \\ 0 & -\sin\alpha & \cos\alpha \end{bmatrix} \tag{3.7b}$$

via

$$\mathbf{n_p} = R_1^{-1} R_2^{-1} \begin{bmatrix} 0 \\ 1 \\ 0 \end{bmatrix} \tag{3.8}$$

and

$$\mathbf{n_s} = R_1^{-1} R_2^{-1} \begin{bmatrix} \cos\beta \\ 0 \\ \sin\beta \end{bmatrix}, \tag{3.9}$$

where n_s is the unit vector in the direction of the shear steps. The Schmid factor is then $m_S = (\mathbf{n_\sigma} \cdot \mathbf{n_p})(\mathbf{n_\sigma} \cdot \mathbf{n_s})$. Even though information regarding the crystal is obtained with this technique, it is impossible to fully determine the orientation of other slip planes as two mirrored Thompson's tetrahedrons may contain a slip system with the orientation found.

SEM micrographs with a resolution between 1 and 4.2 nm/pixel were used, and all the length measurements were taken between pixels with a similar intensity at a level where the brightness gradient was high. The loading direction was set horizontally in every micrograph to calculate the Schmid factor of the active slip system. The slip line spacings were measured once between every pair of slip markings, whereas the shear distances were taken to be the average of as many measurements as could be taken from the micrograph on multiple precipitate holes along a slip line, which typically varied between 1 and 6. Most of these

measurements were done in the secondary γ' because the in- and out-of-plane shearing makes it harder to measure slip in the smaller tertiaries, but these were still considered whenever the magnitude and direction of the displacement could be identified. Moreover, when slip steps along the matrix/precipitate interface could be observed but they were smaller than a pixel and thus could not accurately be measured, they were recorded as the pixel size in the current micrograph.

Note that the applicability of this method depends upon the original size and morphology of these particles, the error being less for larger and more spherical precipitates. Additionally, the analysis of a larger number of precipitate holes which show the required features results in a higher statistical accuracy.

3.3 Results

3.3.1 Microstructure

The material analysed here has an ASTM grain size number of 6.15 (mean planar diameter of 43 ± 4 μm) as calculated by the circular intercept method. Annealing twins on multiple slip systems populate the material. The resulting secondary and tertiary precipitates are morphologically different. Rounded tertiaries populate the regions between the more flowery secondaries. Table 3.3 summarises the results from two micrographs for each precipitate family accounting for 909 secondaries and 2774 tertiaries in total, and the intercept size distributions are shown individually in Figure 3.5. The equivalent diameter of these intercepts d_{eq} that would result in the same measured area for each precipitate is used here to characterise the size distribution. The circularity $C = 4\pi A/P^2$ (calculated from the individual areas A and perimeters P measured) is also given for each precipitate family.

Table 3.3 - γ' characterisation. The error bars correspond to the standard deviations of the measurements and the calculated errors in the volume fractions.

Family	Volume fraction [-]	Mean d_{eq} [nm]	Circularity
Secondary	0.37 ± 0.04	223 ± 73.4	0.81 ± 0.12
Tertiary	0.06 ± 0.05	10.8 ± 4.1	0.96 ± 0.04

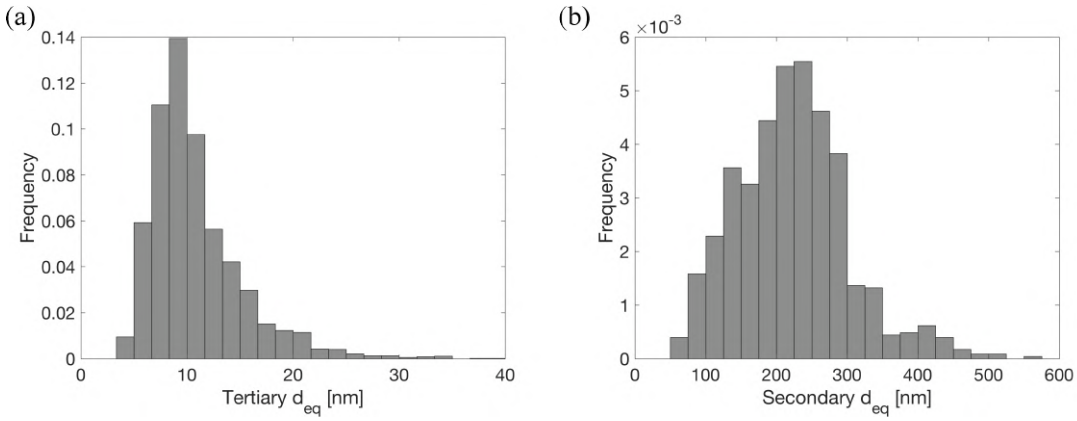

Fig. 3.5 - Normalised (a) tertiary and (b) secondary γ' intercept size distributions with bin widths of 1.67 nm and 25 nm, respectively. The first bin of the tertiary precipitates is empty as it is smaller than the resolution used for the characterisation.

3.3.2 Mechanical testing

The LCF tests performed at each temperature gave very similar results, with the sample loaded for 40 cycles at 20°C showing the highest variation in stress for the first cycle but still closely following the trend of the other curves, as seen in Figure 3.6(a).

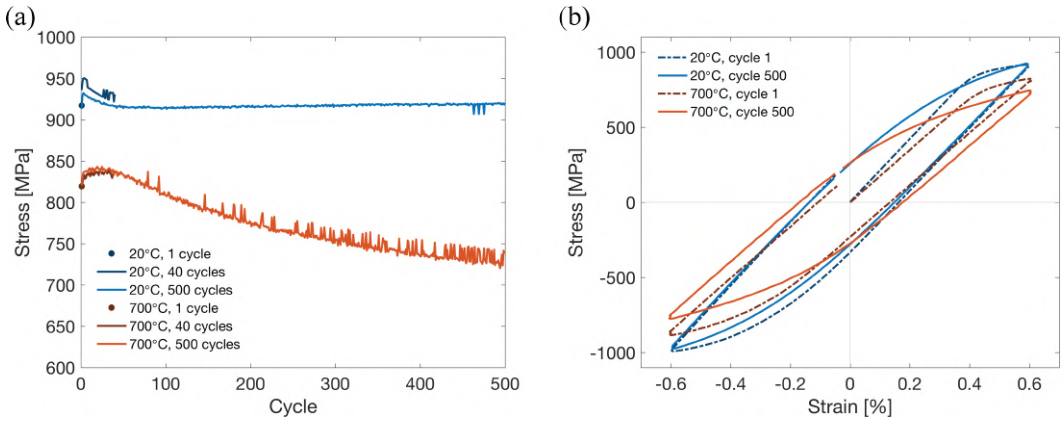

Fig. 3.6 - (a) Evolution of the maximum stress per cycle for the six samples tested in LCF and (b) first and last stress-strain hysteresis curves of the samples tested for 500 cycles at 20°C and 700°C.

At both temperatures there is an initial hardening stage followed by cyclic softening. The peak stress occurs during the first 10 cycles at 20°C and between 20 and 40 cycles at 700°C. Afterwards, the softening rate decreases in both cases but only at 20°C does it reach a saturation stage which continues until the end of the test after 500 cycles.

Figure 3.6(b) shows the hysteresis curves during the first and last cycles of the 500 cycles samples for each temperature. The plastic deformation experienced per cycle at different temperatures was similar when accounting for the hardening and softening regimes. After 500 cycles the cumulative plastic strain at 20°C is only 3.6% larger than that at 700°C.

3.3.3 ECCI

The only sign of deformation in the undeformed sample is the presence of stacking faults on multiple slip planes. These have a length of a few micrometers and extend mostly through both matrix and precipitates, although in some instances their contrast disappears within secondary γ' particles. The density of stacking faults varies between grains, some having almost none and others showing many aligned with 2, 3 or 4 slip planes. No significant differences are observed between the stacking faults before and after deformation for the conditions tested.

Slip bands can be observed in all the deformed samples. Even though the technique does not easily allow resolution of the individual active slip planes, bands formed of many of these appear as stripes with a higher intensity. In most cases, the slip bands in the primary slip system traverse the whole grain or the majority of it. Additionally, a clear contrast gradient can be seen along the length of many slip bands, indicating a variation in the dislocation density.

The deformation at room temperature is for the most part confined within slip bands, while minimum dislocation contrast is observed in the thicker regions in-between. After just one cycle at room temperature, most grains show little or no deformation with ECCI. A few well defined slip bands with a spacing of over 5 μm can be spotted within some grains, without any evidence of secondary slip. After 40 and 500 cycles, the material has more slip bands, which also look thicker and have a higher intensity. In some grains they appear in very small numbers, but in most cases multiple bands with the same orientation can be seen. Other grains show secondary slip and only in one case a third slip system contained a well defined slip band. Overall, there are no apparent differences between the deformation behaviour in both samples after considering all the grains imaged in this way. Figures 3.7 (a)-(c) and (d)-(f) showcase ECCI micrographs in samples tested at 20°C and 700°C, respectively.

While the deformation is similar at 700°C, some differences become apparent when looking at a large number of grains, such as the higher volume fraction of slip bands. The sample fatigued for one cycle has more grains where slip bands have formed, although qualitatively these look similar to those in the 20°C test. Upon further cyclic loading it once more becomes difficult to spot differences between the samples fatigued for 40 and 500 cycles. More slip bands appear in most grains, although some still show none. Secondary slip is

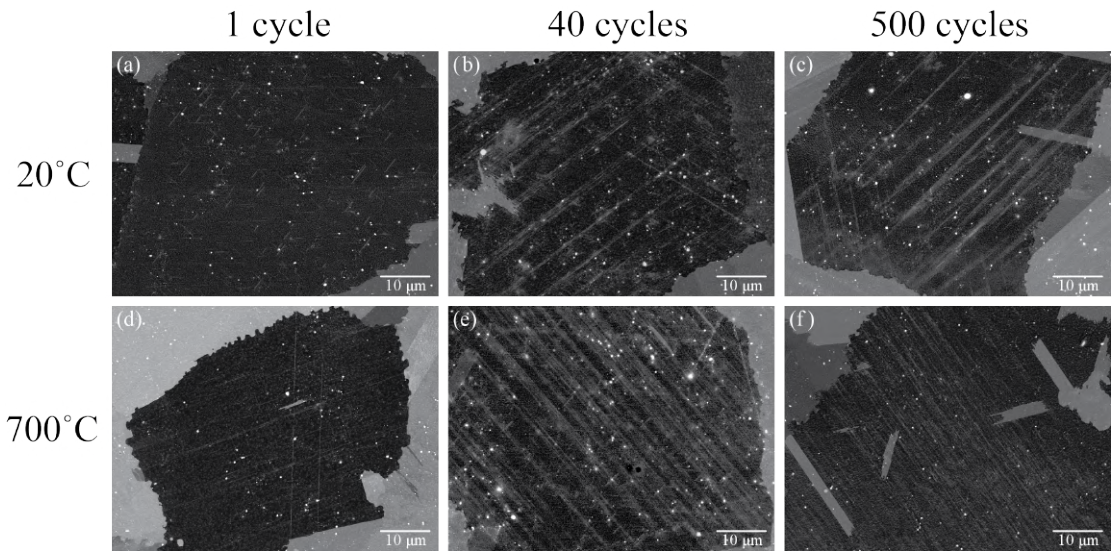

Fig. 3.7 - ECCI micrographs of samples fatigued at 20°C and 700°C for 1, 40 and 500 cycles.

scarcer at this temperature and no tertiary slip activation is observed. Instead, more and more slip bands develop along a single slip plane orientation in heavily deformed grains, to the point where high contrast fills most of the area in some regions of the ECCI micrographs in the form of thin parallel lines. An example of this more homogeneous deformation behaviour can be seen in Figure 3.8.

3.3.4 Slip band shearing statistics

Slip bands in γ'-etched samples, such as that in Figure 3.2(a), clearly show shearing of precipitates along the slip lines, which extend over the whole region imaged. Shear steps are typically observed in all the precipitates along a slip line, but their lengths vary. Thus, reporting the average length per slip line gives a good indication of the overall behaviour at a section of the band rather than the measurements at individual precipitates.

The samples fatigued at both temperatures for one cycle show small amounts of shearing and slip bands are hard to spot. Three bands found for each condition show a maximum of four parallel slip lines. This indicates that although some slip bands form during the first fatigue cycle, as will be shown by TEM later, more cyclic deformation is required to promote precipitate shearing along most of their slip lines. Due to the scarcity of slip bands in these conditions, no statistical analysis was performed in samples fatigued for one cycle.

The analysis on the statistics of slip band shearing was performed for a number of grains for each condition, accounting for one or more slip bands within each grain. Table 3.4 summarises the number of grains and slip bands characterised for each loading condition,

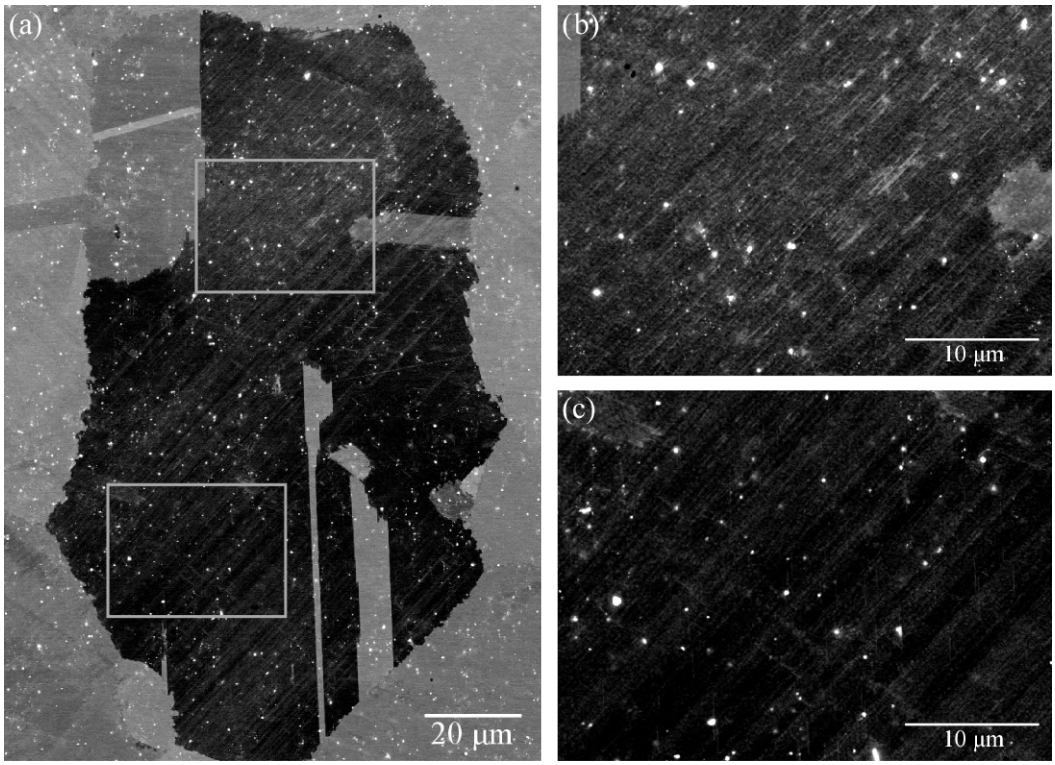

Fig. 3.8 - (a) ECCI micrograph of a grain with more homogeneous deformation from a sample fatigued at 700°C for 40 cycles. The regions inside the boxes are shown at a higher magnification in (b) and (c).

as well as the number of measurements performed for the statistical analysis of slip line spacings a, shear step lengths s and slip band widths w. These statistics do not include the samples fatigued for only one cycle because of the small numbers of slip bands and slip lines found within them.

Table 3.4 - Number of features considered in the analysis.

Temperature	Number of cycles	Grains	a measurements	s measurements	Slip bands
20°C	500	6	133	54	7
	40	4	69	44	4
	1	1	1	1	1
700°C	500	3	103	104	13
	40	6	257	264	5*
	1	1	3	4	1

* Plus 3 regions of homogeneous deformation

In some cases it is not possible to access the true distances within a slip band due to variability in the precipitate morphology and experimental error. The measurements of α

show an increase in its standard deviation SD_α towards larger angles due to the relatively low circularity of the secondary γ'. For some orientations close to $\alpha = 0°$, *i.e.* the slip plane perpendicular to the specimen surface, the elliptical markings disappear as the minor radius becomes as small as the pixel size, in which case SD_α should be small ($< 3°$) but is reported here as zero. Alternatively, the standard deviation SD_β increases with bigger values of both α and β. The orientations of the grains analysed altogether with the aforementioned trends can be seen in Figure 3.9.

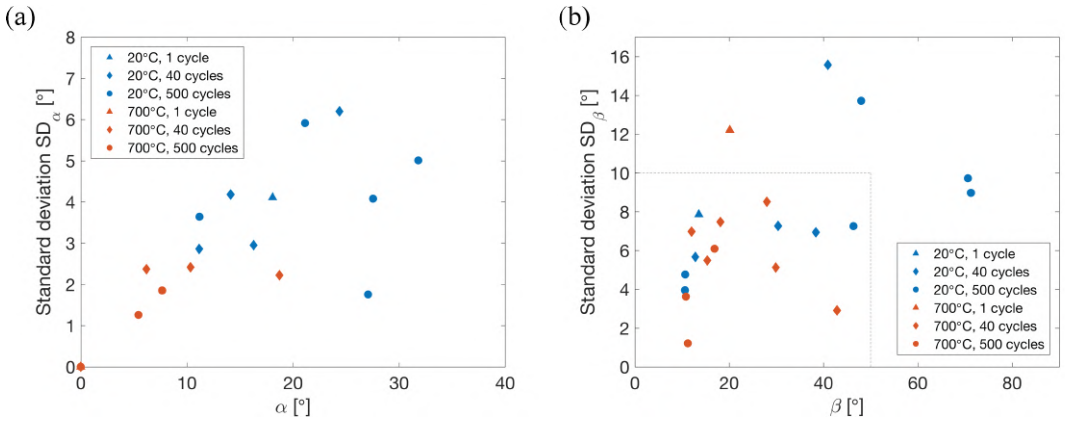

Fig. 3.9 - Angles (a) α and (b) β and their standard deviations for the grains analysed. The samples outside the dashed box were ignored for the *s*-analysis.

The lower values of α for the samples deformed at room temperature are just a consequence of randomly selecting the imaged grains. This does not bias the results as the Schmid factors of the grains tested at both temperatures ranged between similar values. In total, 86% of the grains have a Schmid factor bigger than 0.4, and the minimum value found is 0.3. These are all, as expected, within the range of the maximum Schmid factor for all possible orientations (0.27 to 0.5).

The slip line spacings in all the grains analysed are considered in the present work, whereas the shear step lengths could not be measured for some crystal orientations. Values of β further away from the ideal $\beta = 0°$ make the measurements of s more difficult and inaccurate as their in- and out-of the viewing plane components grow bigger. Similarly, those grains where $SD_\beta > 10°$ cannot be properly measured. Thus, the grains that lie outside the dashed square in Figure 3.9(b) are not considered in the following *s*-statistics. This limits the number of grains that can be analysed from an SEM specimen but does not systematically affect the results because the samples were cut parallel to the loading direction.

In some micrographs two or more nearby slip bands can be seen. However, considering that they consist only of slip lines that are closely spaced, it is not always clear where one slip band ends and a new one begins. Consequently, a limit is set here to an arbitrary value of

$a = 400$ nm, above which only 18 spacings were measured. Conversely, three of the grains analysed for the 700°C and 40 cycles sample show the presence of closely spaced slip lines throughout the whole micrograph, over a distance perpendicular to the slip plane of over 4 μm. These are regions of homogeneous deformation like those observed with ECCI. As no differences were found in the shear step length and slip line spacing measurements between these and other samples, these grains are included in the following analysis except for the slip band width results.

The histograms of the slip line spacing in Figure 3.10 show no significant variation with the number of cycles at room temperature, and only a small increase at 700°C. The latter most likely arises from the huge scatter seen in the measurements as it is extremely unlikely that a slip line could completely disappear and precisely reverse all the shearing events, *i.e.* the number of slip lines should either increase or remain constant. Alternatively, the active slip planes seem to be more spread out at higher temperatures. The average slip line spacings $\bar{a}$ at 20°C and 700°C are 45.3 nm and 74.6 nm, respectively. These values consider all the slip line measurements performed at those temperatures for 40 and 500 cycles.

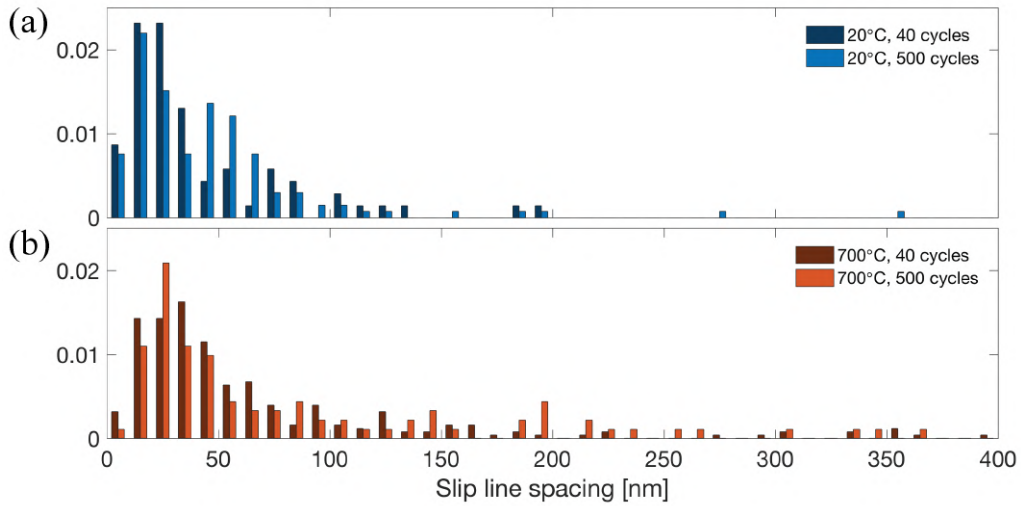

Fig. 3.10 - Histograms of the slip line spacings a at (a) 20°C and (b) 700°C. The values are normalised accounting only for the values recorded lower than 400 nm and the bin width is 10 nm.

Regarding the slip band width, not many measurements were taken due to the length scale at which the technique works, making it difficult to draw definitive conclusions. The values recorded are shown in Figure 3.11 together with the number of slip lines each band contained. Even though there is a big spread, which might arise due the different orientations imaged and variations in the microstructure, it is seen again that the plastic deformation is more localised at 20°C.

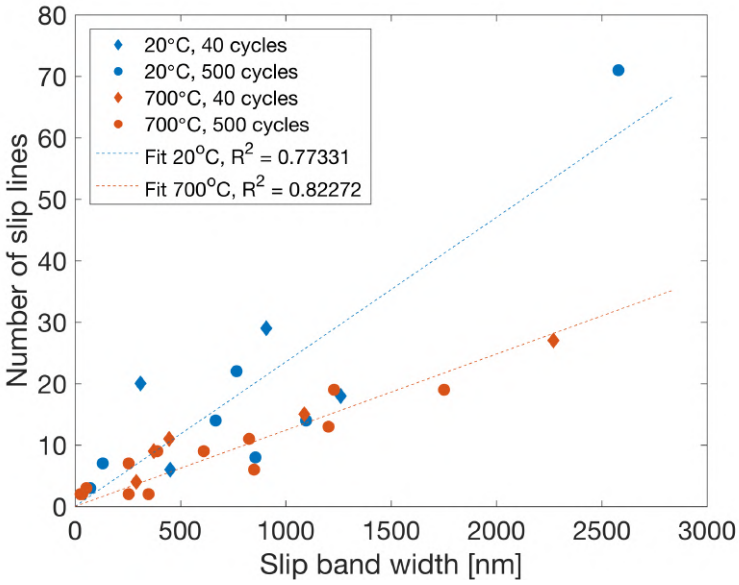

Fig. 3.11 - Number of slip lines as a function of the slip band width. Linear fits and their R^2 values are included for each temperature.

Considering all the slip bands measured, the mean widths at 20°C and 700°C are 827 and 684 nm, respectively. However, a closer look into Figure 3.11 shows that there is a big difference at room temperature between the widest band and the rest, and if this outlier was ignored a mean width of 652 nm would be obtained. Moreover, the slip band width is plotted against the Schmid factor in Figure 3.12 to look at orientation effects but no visible trend can be extracted; similar results were obtained when plotting the Schmid factor against other parameters.

When looking at the results of the shear step lengths, the first thing to notice is that most distributions are centred around $s = 0$, meaning that the combined effect of multiple slip lines within a slip band tends to be neutral, having some slip lines concentrating the shearing in one or the other direction. As seen in Figure 3.13(a), in about half of the grains the average shear distance per slip line is smaller than 2 nm, and in the rest this value stays mostly under 4 nm. The outlier, with a mean shear step length of 11 nm, is actually one with homogeneous deformation. In this grain 88% of the slip lines show precipitates sheared in one direction. The second highest value belongs to a grain with one slip band measured, and both belong to the sample loaded for 40 cycles at 700°C. If one considers the widths as in Figure 3.13(b), no overall trend is seen but it is clear that a few slip bands concentrate the majority of the deformation.

While overall the plastic strain tends to remain close to zero due to the nature of the fully reversed fatigue tests, the shear steps do change in magnitude. However, by measuring this

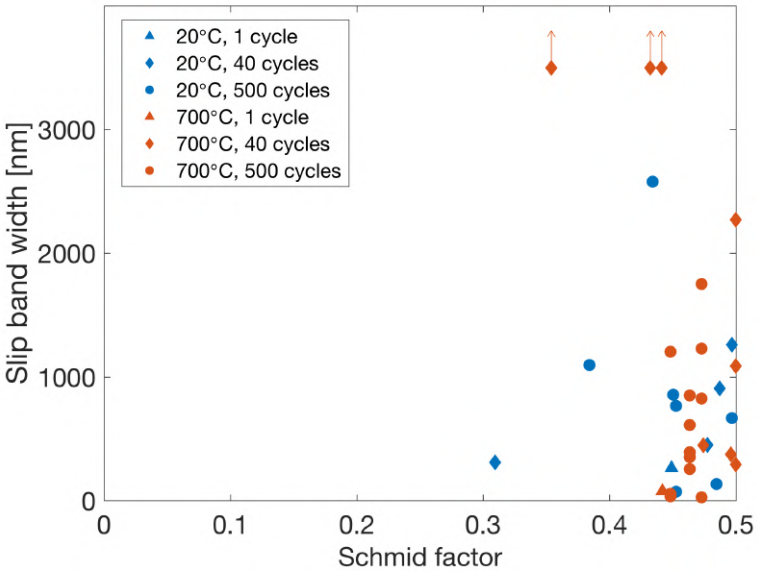

Fig. 3.12 - Slip band width as a function of the Schmid factor. The marks with arrows pointing upwards represent the three grains that showed homogeneous deformation.

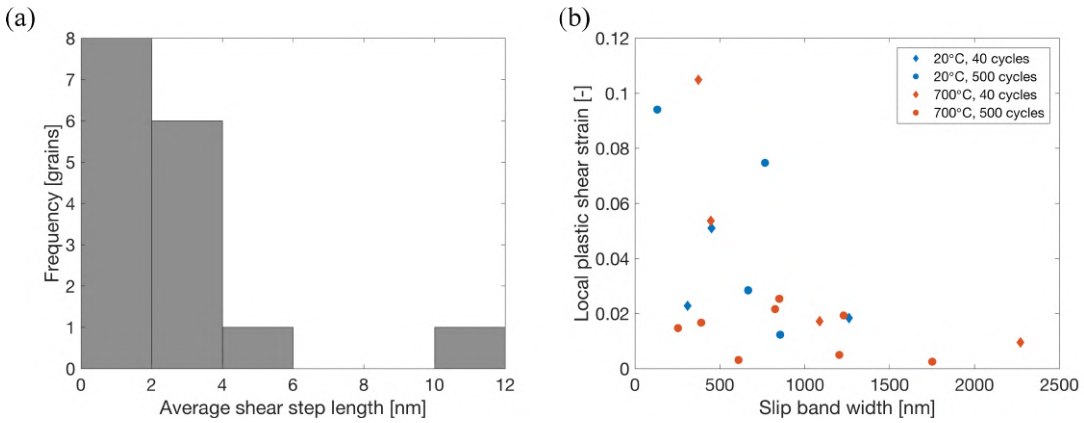

Fig. 3.13 - (a) Histogram of the average shear step length per grain considering magnitude and direction. (b) Distribution of the slip band plastic shear strains as a function of their widths.

distance it is not possible to know how many slip irreversibilities took place along that slip plane. These are events in which a dislocation glides in one direction but then is unable to glide back. Mechanisms that produce slip irreversibilities include cross slip, dislocation annihilation, formation of dipoles and emergence of dislocations at a crystal surface, among others [25, 70, 71].

Differt *et al.* [192] proposed a way of estimating the number of irreversibilities per slip line $2z$ from the probability distribution P of the number of slip steps $\Delta n = s/b$ when

considering multiple active planes. The model assumes that the same number of dislocations glide along each slip line, as well as a history-independent probability for the generation of a slip irreversibility. Deviations of this may arise due to the heterogeneous nature of slip and the spatial variability of the precipitate morphology, which would favour precipitate shearing along slip lines that have been previously cut. Nonetheless, this approach is derived in Appendix A and equation (A.5) is used here as the fitting function for the results of each condition shown in Figure 3.14 in an effort to give a better insight into the physics of the precipitate shearing phenomenon. The parameter z is related to the mean shear step length through equation (A.6).

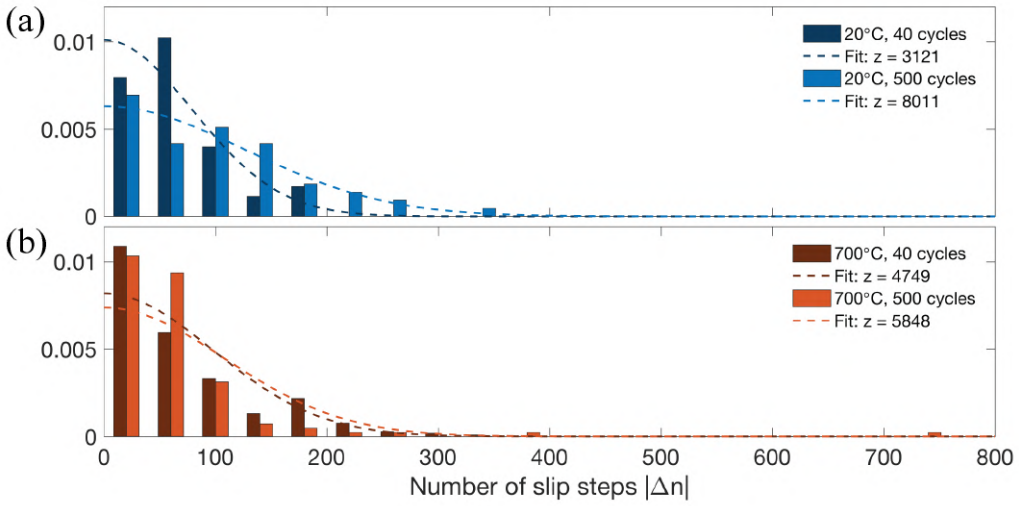

Fig. 3.14 - Histograms of the number of slip steps in each slip line at (a) 20°C and (b) 700°C. The values are normalised and the bin width is equal to 40 steps. The maximum likelihood estimation to a Bessel function of the first kind are shown in dashed lines for each condition.

At both temperatures the estimated number of slip irreversibilities increases with more cycles as expected. Figure 3.15 shows that this evolution slows down after the first 40 cycles of the test. At a higher temperature the expected number of slip irreversibilities should be higher because of the increased cross slip activity. This behaviour is observed for the first 40 cycles, although the opposite is true after 500 cycles. This can be explained by accounting for the volume fraction of the material filled with slip bands, which is further discussed in Section 3.4. Moreover, the 95% confidence interval of the maximum likelihood estimates are too spread and there is a chance that the real evolution of the slip irreversibility accumulation is not properly captured by the curves in Figure 3.15.

The evolution of the height profile of a slip band is then related to its slip line spacings and shear step lengths. Reconstructions of the estimated profiles for the slip bands analysed are given in Figure 3.16 following equation (3.6), where the horizontal and vertical axes

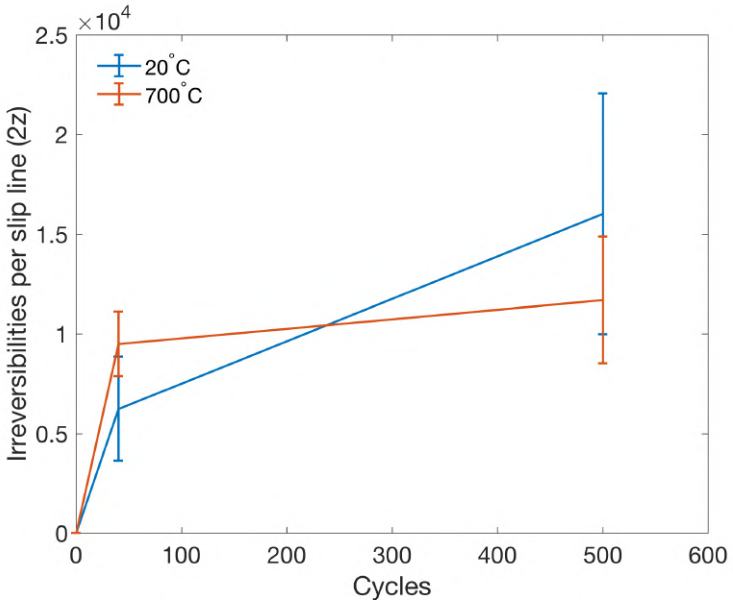

Fig. 3.15 - Calculated number of slip irreversibilities as a function of the number of cycles. The error bars correspond to the 95% confidence limits of the maximum likelihood estimates.

are aligned with the normal to the slip plane and the shear direction, respectively. These showcase, as previously described, the small local plastic strain left in the slip bands even after 500 cycles.

The results described in this section are, to the knowledge of the authors, the first to ever quantify slip at the level of individual slip planes and in the directions relevant to the slip band. The methodology described in Section 3.2.1 enables the measurement of the real shear step lengths and slip line spacings. The profiles from Figure 3.16 are analogous to others obtained via Atomic Force Microscopy [107, 193], but measured in the direction of the Burgers vector and performed in the bulk rather than on the surface, offering new insights into the deformation behaviour of nickel-based superalloys.

3.3.5 TEM

The TEM micrographs show the dislocation structures in more detail. In grains with small amounts of deformation, primarily in the samples fatigued for one cycle, single dislocations can be seen. However, the predominant features observed are stacking faults on multiple slip systems. The majority of these are a few microns long and extend through both phases, with some holes most likely around the precipitates. The density of stacking faults also varies considerably, even within neighbouring regions of the same grain. An example of such an area without heavy deformation is given in Figure 3.17 (a). Both of these types of defects

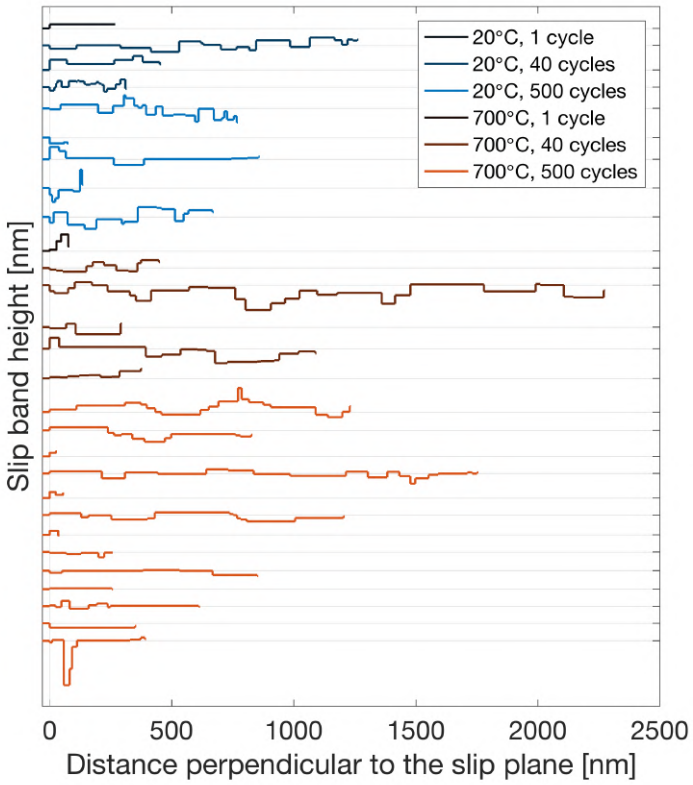

Fig. 3.16 - Slip band height profiles along their widths and in the direction parallel to the Burgers vector of the active slip system. The first slip line is considered in all the cases to be located at $y'' = 0$ and the aspect ratio between distances along the plot axes is 1:1.

were present in the material before the cyclic loading. It is possible that some of the stacking faults propagate upon loading as the partials bounding them may overcome glide obstacles, although the same stress would later be applied in the reverse direction. The question of how these stacking faults evolve during fatigue remains open.

The sample fatigued for one cycle at room temperature presents the smallest number of heavily deformed bands with a high dislocation density, although most grains contain multiple parallel shear bands. In some instances only one or two nearby active slip planes extend over tens of microns, probably forming the precursors of more intensely deformed slip bands, *i.e.* with a higher dislocation density distributed over more planes such as those analysed in γ'-etched specimens. Among these, dislocation loops and double loops can occasionally be seen around secondary precipitates, such as those in Figure 3.17 (b). Nonetheless, no more than two concentric loops are ever observed.

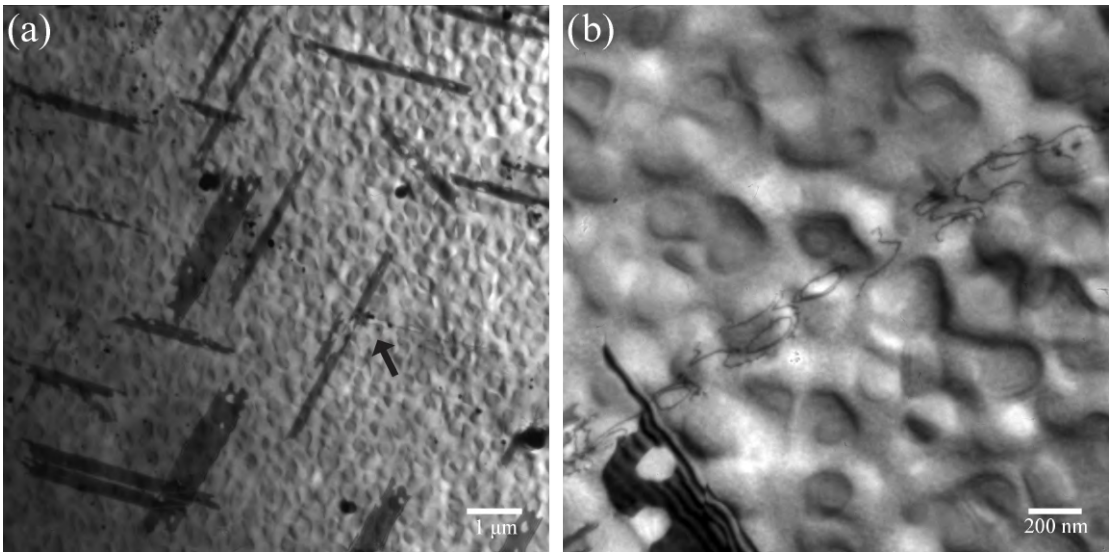

Fig. 3.17 - TEM micrographs of regions with little deformation in the sample fatigued at 20°C for 1 cycle. (a) Stacking faults and single dislocations in multiple orientations. The arrow points to a slip line that seems to end at the intersection with a stacking fault. (b) Slip line showing dislocation loops and double loops.

A thicker and more developed slip band in the same sample can be seen in Figure 3.18(a). Even though the dislocation density varies abruptly within the single band, the same active slip planes for the most part can be seen on both sides of the dark region where the huge number of dislocations completely obscures the electron beam. This property is shared with the slip bands imaged for every condition. The slip lines sometimes become completely invisible in some regions but then show up again with the same spacing. This indicates that dislocations travel on such planes but only accumulate at some points where glide is impeded by obstacles. Overall, they tend to either continue for the whole length of the grain or for most of it before gradually disappearing towards one end of the band.

Slip bands with a higher dislocation density over more slip planes do not contain dislocation loops, but rather show pile ups. With the accumulation of multiple dislocations in a single slip plane, the resulting high stresses may provoke the collapse of the loops. Furthermore, when these pile ups form in nearby slip planes they align with each other in such a way that the dislocations line up with each other to minimise the energy, as seen in Figure 3.18(d).

Non coplanar stacking faults appear to be the main obstacles against which pile ups are initially formed within the slip bands. Examples of this are shown in Figure 3.18(b)-(d), but other instances were also observed both at 20°C and 700°C. These barriers can however be overcome by some of the dislocations, which are then free to glide in the regions with a lower

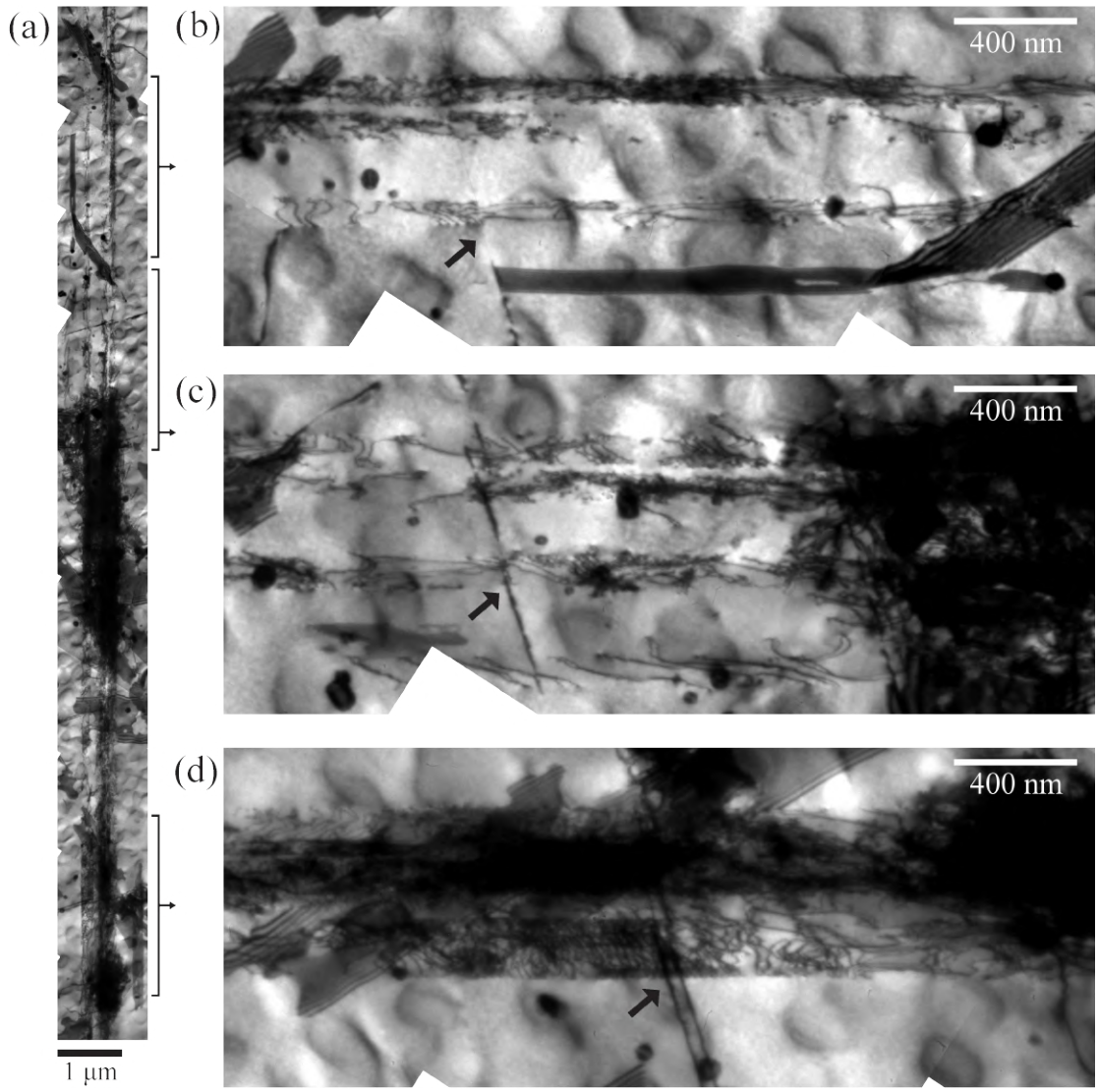

Fig. 3.18 - (a) TEM micrograph of a slip band from a sample fatigued at 20°C for 1 cycle. The areas indicated by the brackets are shown at higher magnifications and rotated 90° counterclockwise in (b)-(d). The arrows point at interactions between dislocation pile ups in the slip band and non-coplanar edge-on defects.

dislocation density. A change in the line vector of the dislocations that bypass the stacking fault is seen in many cases; *e.g.* in Figure 3.18(b). The intermittent contrast of these defects indicates the presence of dislocations along some regions of the faults.

Another feature that can be observed in the sample fatigued for one cycle is the presence of cross slip in between the active planes of a slip band. An example of this is shown in an edge-on view of a slip band in Figure 3.19. This is additional evidence for double cross slip

as the mechanism responsible for the thickening and intensification of the slip bands from the very beginning of the fatigue process.

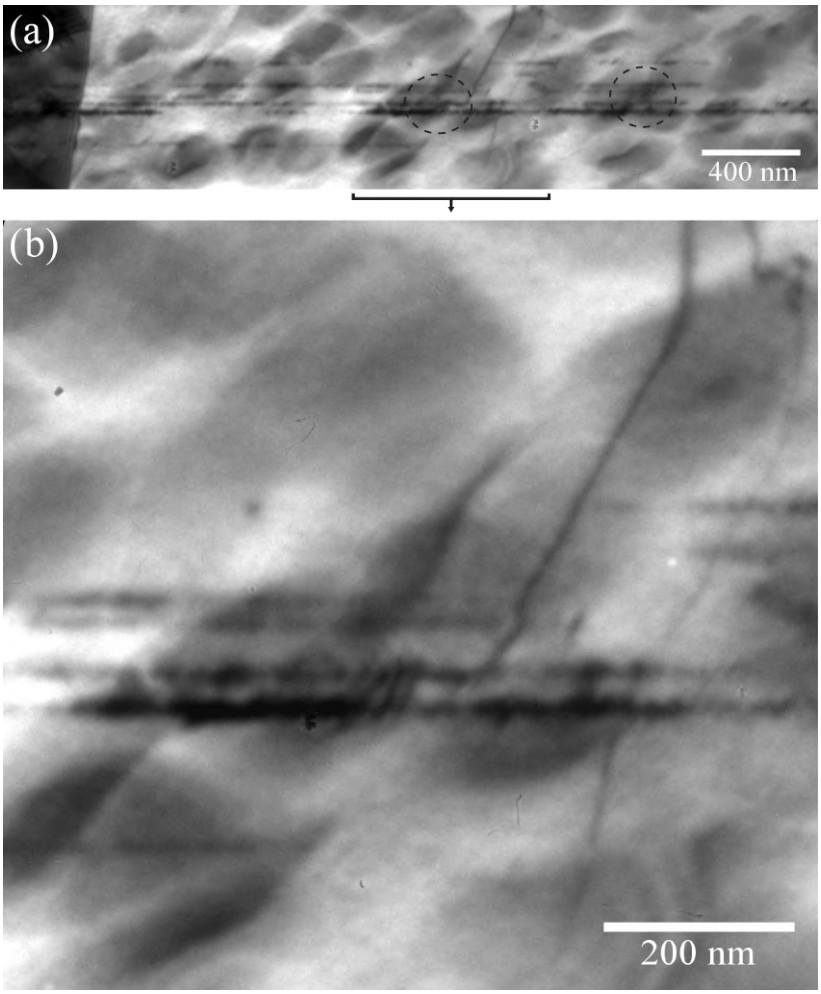

Fig. 3.19 - (a) TEM micrograph of an edge-on slip band from a sample fatigued at 20°C for 1 cycle where double cross slip events can be seen (enclosed by the dashed ellipses). The region indicated by the bracket is shown at a higher magnification in (b).

TEM in samples fatigued for 40 cycles at 20°C shows considerably more well developed slip bands. Yet, these also present varied thicknesses and slip densities even within the same grain. Some of the slip bands in this condition are heavily deformed and it becomes difficult to distinguish their features using this technique, as seen in Figure 3.20(a). Dark regions with a large dislocation density are seen along different sections of the slip band, mostly located at intersections with non-coplanar stacking faults and bands, and extending to both sides. This is clearly linked to the nature of the cyclic loading, as further discussed in section 3.4.

Even though most of the deformation seems to be carried by a single slip plane orientation, secondary slip can often be seen in the form of very thin bands with only a few active slip

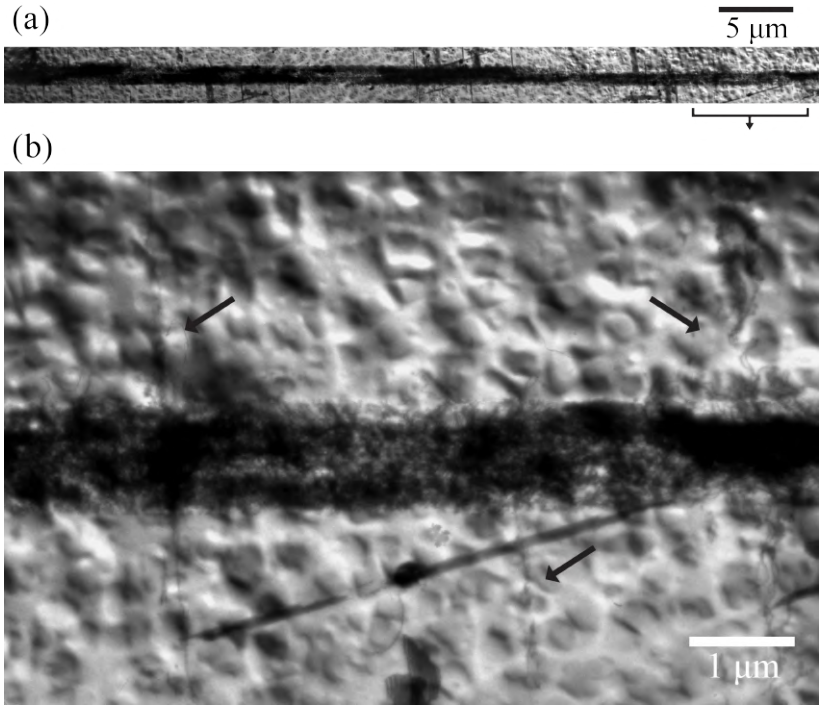

Fig. 3.20 - (a) TEM micrograph of a slip band from a sample fatigued at 20°C for 40 cycles. The region indicated by the bracket is shown at a higher magnification in (b). The arrows point towards secondary slip bands, only two of which have crossed the primary slip band.

planes that may or may not travel across the primary slip bands. This is shown at a higher magnification in Figure 3.20(b). Inside grains at preferential orientations or under higher strain amplitudes, these secondary slip bands may thicken and increase their dislocation density to form deformation structures such as that imaged with ECCI in Figures 3.7 (b) and (c).

More slip bands can be seen at 700°C after one cycle, compared to 20°C. These show on average activation of more slip planes, albeit with low dislocations densities. Similar features to those found at lower temperatures are seen, such as the presence of dislocation loops and the interactions between slip bands and non-coplanar stacking faults. Figure 3.21 shows an example of a slip band found in this condition. The formation of pile ups on nearby planes with aligned dislocations is similar to that described at 20°C. Note that by using different **g** vectors in Figures 3.21(b) and (c), the former in a two-beam condition and the latter just slightly off, it is seen that the region within the slip band with the highest dislocation density is located around the traversing stacking fault. Dislocations with a different Burgers vector are also present in this area.

Overall, after 40 cycles at 700°C the plastic deformation looks considerably less localised than at the lower temperature, in agreement with the slip line spacing statistical analysis.

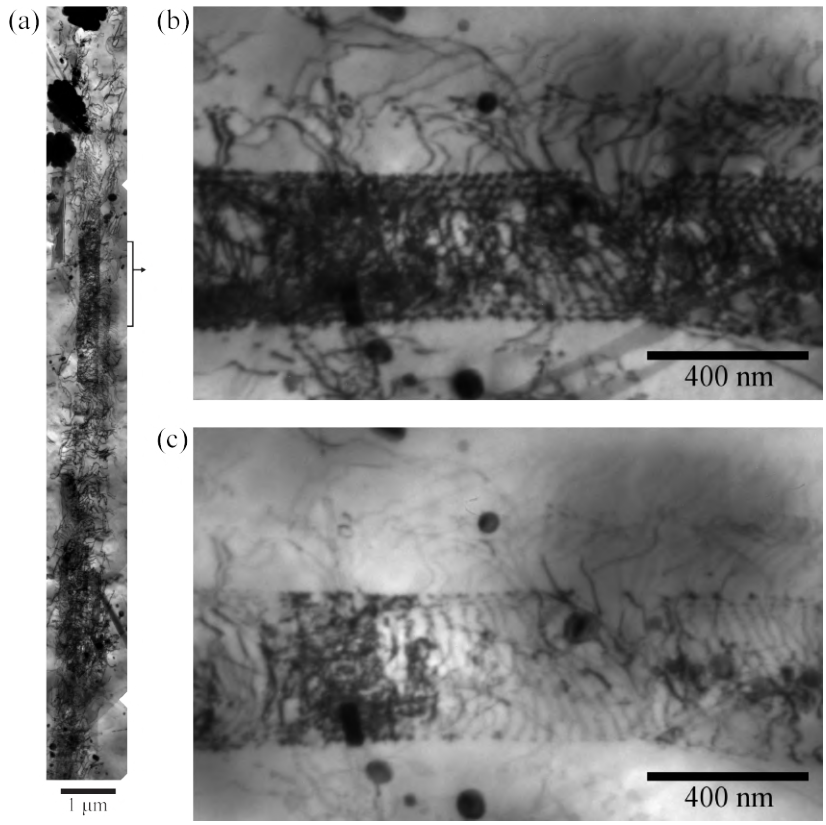

Fig. 3.21 - (a) TEM micrograph of a slip band from a sample fatigued at 700°C for 1 cycle. A region around a non-coplanar stacking fault is imaged in with two different beam conditions, (b) in a two-beam condition and (c) slightly off.

More slip bands populate the grain volume, but their dislocation density never reaches the levels seen at 20°C. Figure 3.22 shows a slip band imaged under two different two-beam conditions that suggests that most of the deformation is accommodated by a single slip system. Dislocations with a different Burgers vector are clear only close to the grain boundaries and to a lesser extent around the intersections between the slip bands and the non-coplanar stacking faults. This is to be expected as the stress states in these regions can vary considerably from that at the grain interior. This behaviour is also observed in neighbouring slip bands within the same grain.

Regions with more homogeneous deformation such as that in Figure 3.23 are also seen in this condition. At high magnifications possible by using the TEM, the planarity of slip can be resolved in the form of multiple parallel active slip planes. Qualitatively, these dislocation structures look very similar to those of thinner slip bands. Note that narrow bands free of dislocations can still be seen in some regions of the material. This agrees with the observations performed with ECCI, and suggests that the plastic deformation may spread and

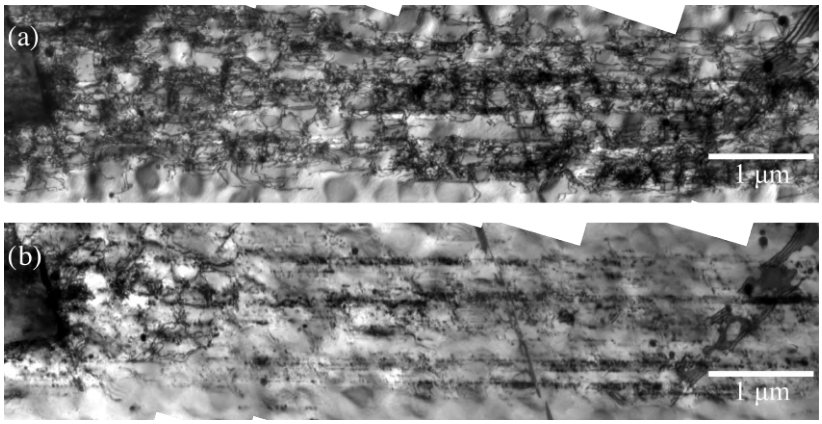

Fig. 3.22 - TEM micrographs of a slip band from a sample fatigued at 700°C for 40 cycles with two different beam conditions.

cover the majority of a grain via the creation of new slip bands, the thickening of existing ones, or a combination of both.

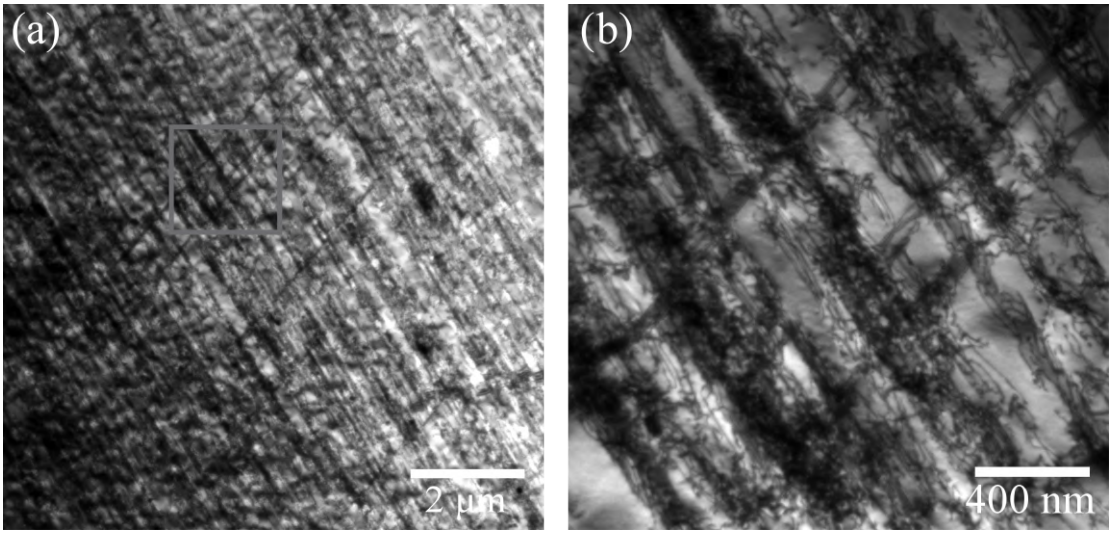

Fig. 3.23 - (a) TEM micrograph of a region with a homogeneous deformation from a sample fatigued at 700°C for 40 cycles. The region inside the box is shown at a higher magnification in (b).

3.4 Discussion

3.4.1 Deformation behaviour

Plastic deformation in RR1000 has been observed to develop mainly in the form of slip bands. There are morphological differences between these bands at room temperature and 700°C, but they show similar operating mechanisms and features. SEM in γ'-etched samples and TEM reveal that most of the dislocations gliding within a slip band share the same Burgers vector and distribute heterogeneously along the active slip planes. The presence of stacking faults in similar number densities and sizes (with a typical length of $\sim 3\mu m$) in samples with and without plastic deformation suggests these result from spontaneous dissociation during heat treatment and rules out a significant contribution of superlattice faults to plastic deformation. Dislocation climb was not observed either, and although it may appear during tests at 700°C, its contribution is deemed inconsequential due to the planarity of slip observed in all the samples. The elastic behaviour of the material appears to dominate over the viscous component for the strain rate of $0.5\%s^{-1}$ with dwell times of 1 second selected here.

Plastic deformation in these conditions seems to be completely confined to the octahedral slip planes. A study by Mello *et al.* [194] showed that activation of cubic slip may occur during low cycle fatigue above 550°C in RR1000, and proposed a mechanism for alternating zig-zagged slip along {111} cross slip planes in the matrix. No evidence of such dislocation behaviour is found in the present work, even though no full orientation characterisation of the grains was done. A possible cause for this is the lower strain amplitude imposed here. Similarly, this is the main reason why secondary slip is scarce.

A schematic picture sequence of the evolution of a slip band and the precipitates it shears is shown in Figure 3.24. The origin of the slip band was not identified in these observations, but any dislocation source may activate the initial slip plane. From the first cycle double cross slip of dislocations can result in the formation of Koehler sources [89] in neighbouring parallel planes a few nanometers apart, which results in an effective thickening of the band. Repeated generation of sources via this mechanism appears to reach a steady state before 40 cycles in terms of slip band width and dislocation density. The degradation of the precipitates due to shearing may however continue upon further cyclic loading due to the random nature of the slip irreversibilities. The individual steps in this sequence are discussed in detail in this section.

After just one cycle it is evident that a slip line may extend over several microns and cover all or the majority of a grain. Orowan looping and shear via dislocation pairs are observed during the early stages of a slip band, but as the dislocation density increases the resulting stress results in the collapse of the loops. A similar phenomenon was identified by Brechet

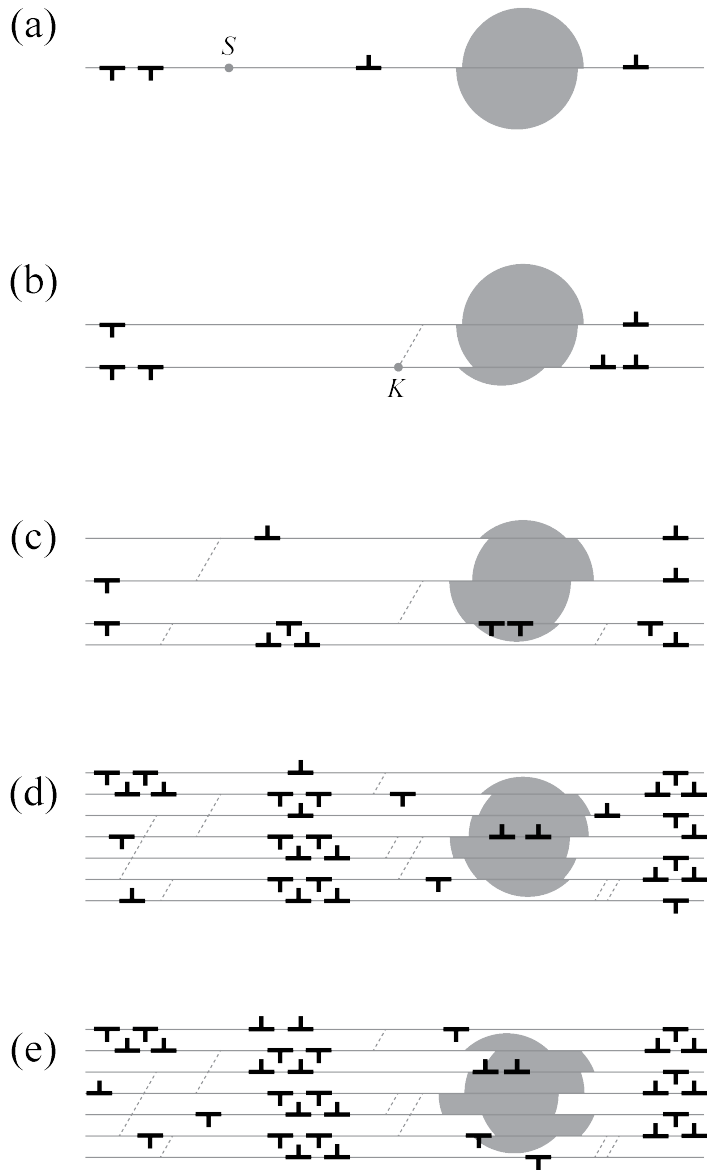

Fig. 3.24 - Schematic representation of the formation and evolution of a slip band and a precipitate. (a) Activation of the initial slip plane from a dislocation source *S* and (b) generation of a Koehler source *K* in a neighbouring plane via double cross slip during the first loading stage. Fatigue cycles produce (c) activation of more slip planes, slip band thickening and formation of dislocation multipoles until (d) a steady state in slip band width and dislocation density is reached. (e) Further cyclic loading results in continued degradation of the precipitates due to the back-and-forth motion of dislocations and slip irreversibilities.

and Louchet [195] in a precipitate strengthened Al-Li alloy. Additionally, dislocations and slip accumulation along individual slip planes distribute heterogeneously as determined by TEM and the SEM slip statistical analysis, respectively.

The role of double cross slip as the mechanism responsible for the activation of nearby slip planes is supported by the experimental evidence found. Multiple dislocations in the cross slip plane may interconnect two or more slip lines, as shown in Figure 3.19. It is not possible to resolve whether this mechanism preferentially originates from the constriction of the partials at a point in the γ/γ' interface or just within the matrix. Cross slip could also take place at the intersection with a non-coplanar stacking fault but only if both planes involved share the Burgers vector of the dislocations in the slip band.

A slip band will continue to thicken as more nearby slip planes become active via double cross slip until it reaches a steady state before 40 cycles, as negligible variation in slip band widths is seen between samples fatigued for 40 and 500 cycles. A low stacking fault energy typically results in thinner bands, but the widths obtained in this study are larger than most reported values in nickel-based superalloys ($<$ 200 nm) [10, 76]. The big secondary γ' precipitates in RR1000 are most likely responsible for this behaviour. As seen in Figure 3.5, the mean slip bands recorded are just bigger than the largest secondary precipitates. This may arise as a way for the material to accommodate more plastic deformation in the matrix around these.

The rate at which new slip bands form is not clear. It has been reported that slip bands in nickel-based superalloys tend to develop during the first cycle and further intensify their plastic strain with additional cyclic deformation [102, 194]. However, the strain amplitudes used in those studies were higher than those chosen for this work and others [106, 107]. The mobility of dislocations within the slip bands formed during the first cycle may decrease as the dislocation density increases, becoming unable to accommodate the plastic deformation in subsequent cycles. As a result, more slip bands would need to be formed during the early stages of the fatigue process.

Upon reaching the steady state as observed by ECCI with no significant differences after 40 cycles, progressive precipitate degradation continues with the back-and-forth motion of dislocations. This is a consequence of mechanisms promoting slip irreversibility, *e.g.* the constant creation and annihilation of dislocations, cross slip events and the emergence of dislocations at a free surface [25, 70, 71]. The accumulation of slip irreversibilities per slip line plotted in Figure 3.15 is shown to increase monotonically with the number of cycles, as expected from the model employed. However, large error bars arise from the number of measurements taken. Larger data sets giving a higher statistical significance would be required to draw decisive conclusions, but the current results give a strong indication of what is really happening in the material.

The main obstacle against which pile ups develop in this alloy are non-coplanar stacking faults. These hinder dislocation glide as they displace the slip plane in the direction perpen-

dicular to its normal by one third of the interplanar spacing d_{111}. These obstacles appear to be more effective than the precipitates. However, this lattice displacement may be overcome with a high enough stress such as that produced on the leading dislocation of a pile up, as shown in Figure 3.18(b). These defects act as semipermeable membranes where dislocations accumulate on many parallel slip planes within a slip band.

Referring to Thompson's tetrahedron [22], the character of a dislocation at the interface with such a fault may be either pure screw or mixed with a 60° angle between its line and Burgers vectors. In the first scenario, shown in Figure 3.25(a), a dislocation may cross slip and either glide in the conjugate plane or cross slip back onto the primary orientation but on the other side of the stacking fault. This transmission mechanism would be induced by a large shear stress produced in the leading dislocation of a pile up.

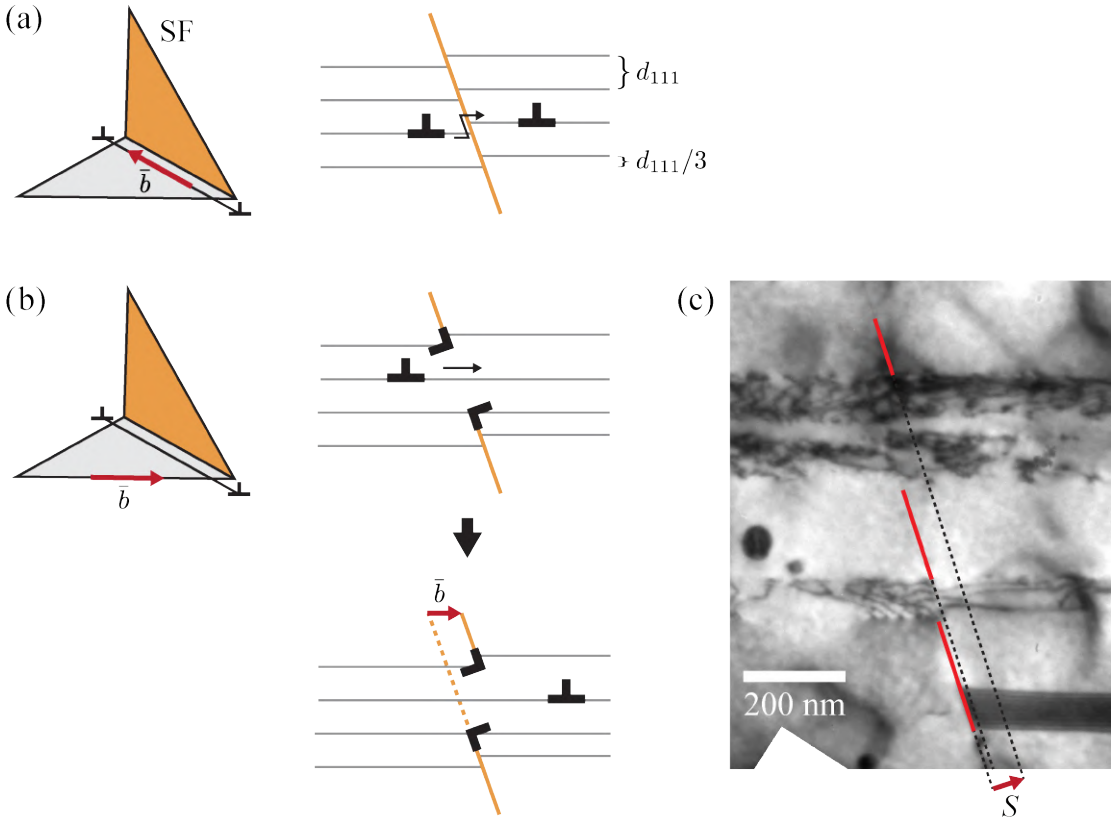

Fig. 3.25 - Two faces of Thompson's tetrahedron with the dislocation considered (left) and view along the line vector of the mechanisms proposed for non-coplanar stacking fault bypassing (right) for (a) a screw segment and (b) a dislocation with a 60° character. (c) Region from TEM micrograph in Figure 3.18(b) highlighting the stacking fault segments (red) and the shear displacement S observed.

If the piling dislocations have a 60° character instead, then climb would be needed to achieve the out-of-plane movement, requiring a large number of vacancies that may not

be readily available at this strain rate and even less so at room temperature. Alternatively, a high stress may induce a realignment of the slip planes by the nucleation of partials on the conjugate plane with opposite Burgers vectors that locally remove the stacking fault, as illustrated in Figure 3.25(b). Upon glide through this narrow gap, one end of the stacking fault would be displaced by one Burgers vector. A misalignment of both ends would then only occur for the dislocations with an edge component. A closer look at the stacking faults from Figures 3.18(b) and (c) shows such displacements where dislocations have bypassed them, as highlighted for the former in Figure 3.25(c). The step length S drawn in this micrograph must have been produced by ~ 300 dislocations that sheared the stacking fault.

Pile ups in nearby planes arrange themselves in organised structures with regular spacings, which is predicted by linear elasticity theory to occur only for dislocations with an edge character (pure screw segments would either cross slip and annihilate or just repel each other). Initially, these low energy dislocation structures such as that in Figure 3.18(d) are clearly not entirely formed of dislocation dipoles, as they have a net Burgers vector different from zero that makes them push against the stacking fault. Similarly, dislocations with an opposite Burgers vector gliding in the opposite direction may form these low energy structures on the other side of the stacking fault, as seen in Figure 3.21.

With more cycles these regions with a high dislocation density may develop more stable configurations as they accumulate dislocation dipoles and multipoles. Nonetheless, plastic deformation is unlikely to occur in these regions as the mobility of the dislocations in them will be lower. This phenomenon is analogous to the classical theory of persistent slip bands, in which edge segments that manage to escape the rungs filled with dipoles bow out until they encounter the next obstacle and the deposited screw segments glide freely laterally [72]. The main difference in this case is that the barriers are clear microstructural features with an irregular spacing against which the dislocations pile up, rather than self-forming structures composed of dipoles. This rationale may be extended in a similar way to interactions with non-coplanar slip bands, which will appear more frequently for higher strain amplitudes.

The main difference due to temperature spotted with the three techniques used is the distribution of slip lines. A larger separation between these is seen at 700°C, which is rationalised here as a consequence of cross slip being a thermally activated mechanism. A similar argument as that used by Essmann and Mughrabi [170] suggests that below a critical separation in the direction normal to the slip plane, the screw segments will tend to cross slip and annihilate, further hindering plastic deformation. The orientation dependence of cross slip [30, 196, 197] may then be responsible in part for the scatter in the mean slip line spacings. Furthermore, for any single band there is also a variation in the spacings that arises from spatial variations in the precipitate distribution and the random nature of the double

cross slip events during the formation process. However, the mean values are independent of slip band width, suggesting that the thickening process of a band might occur when it must accommodate more plastic deformation and it is not possible to activate new slip planes inside it.

At a larger scale, this impacts directly the fraction of material that develops slip bands. Having more widely spaced slip lines at 700°C implies that more regions in a grain must nucleate slip bands to accommodate the imposed macroscopic strain, accounting for the similar thicknesses at both temperatures. Not developing bands in secondary slip systems, as confirmed qualitatively with ECCI, further increases the need to form more slip bands in the primary system. The extreme cases observed of slip bands filling the totality of some grains exemplify this behaviour. The low Schmid factors of these slip systems, shown in Figure 3.12, are unexpected. Localisation of slip might have a dependence on non-Schmid components of the stress tensor, or alternatively be influenced by stress incompatibilities with neighbouring grains.

The height profiles in Figure 3.16 and the calculated mean displacements per slip line show that overall the plastic strain left in the slip bands after the tests ended is relatively low. This is achieved by the combination of shear steps in opposite directions. The randomness of the sequence of shear steps is investigated by the probability of finding, for a given slip line with shear direction $\mathbf{n_s}$, neighbours shearing the secondary precipitates in the same direction. Ignoring the top and bottom slip lines of each slip band (and of each micrograph with homogeneous deformation), they can fall into three categories: (i) both neighbours shear in the same direction $\mathbf{n_s^{(1)}} = \mathbf{n_s^{(2)}} = \mathbf{n_s}$, (ii) in the opposite direction $\mathbf{n_s^{(1)}} = \mathbf{n_s^{(2)}} = -\mathbf{n_s}$ or (iii) they are opposite to each other $\mathbf{n_s^{(1)}} = -\mathbf{n_s^{(2)}}$, where $\mathbf{n_s^{(1)}}$ and $\mathbf{n_s^{(2)}}$ are the shearing directions of the neighbouring slip lines. As seen in Figure 3.26, categories (i) and (ii) cover around 25% of the cases each, which points towards a fully random behaviour. Deviations from this value appear towards larger shear step lengths, but this is attributed to the sample sizes being too small. Ignoring the magnitude of the shear displacements, the results for each category are (i) 23 %, (ii) 28% and (iii) 49%. Thus, no obvious trend is observed and the clustering of slip lines in a specific pattern is ruled out.

The outlier grain with 88% of the slip lines pointing in one direction exhibits a very different behaviour. Even though the fatigue tests were interrupted after a compressive stage and thus some macroscopic plastic deformation is left within the material, it is unlikely that the shearing asymmetry arises only during the last loading stage because many of the lines would still show the previous shearing in both directions. One possible cause is that slip irreversibilities have a higher probability of occurring when loaded in tension than in compression (or vice versa), which would make the shearing happening during that stage

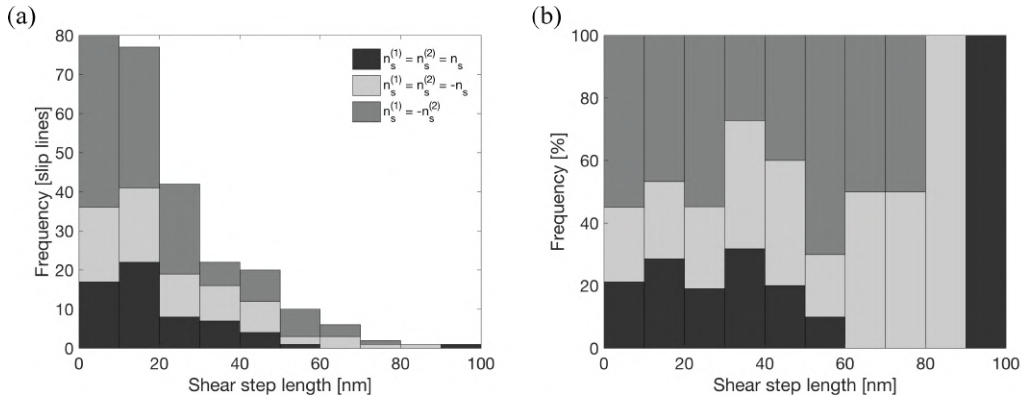

Fig. 3.26 - (a) Histogram of all the shear step lengths divided into three categories depending on the direction of shear of the neighbouring slip lines. The normalised results are plotted in (b).

more likely to accumulate over many cycles. This again could happen for some loading orientations accounting for the probability of cross slip [196]. Additional studies in slip reversibility are required.

3.4.2 Slip line characterisation technique

The methodology developed in this work proved valuable for accessing the true morphology of the slip bands. The resolution of the secondary electron through-lens detector in the SEM was able to capture shear step lengths as small as 1 nm long. The main source of error in the calculation of the slip orientation comes from the low sphericity of the secondary precipitates. This is specially true in the calculation of β as it is more affected by deviations from a circular cross section. This is reflected in the higher standard deviation this parameter shows. Excluding some slip bands from the shear step length statistical analysis helps to minimise these errors. Moreover, this is a systematic error and, as such, the trends are still expected to represent what happens in the material under the different conditions.

The shear steps generate a series of extrusions and intrusions upon reaching the sample surface [198], which have been quantitatively studied by means of atomic force microscopy (AFM) [103, 107, 193, 199] and high resolution digital image correlation (HR-DIC) [194, 200–202]. The information extracted from these techniques is similar to that assessed in the current study, but they cannot access the true three-dimensional displacements within the bulk of the material.

Advantages of the characterisation technique developed here are the higher resolution that allows for the quantification of slip at individual planes, the true three-dimensional data acquired and its applicability in the bulk of the material, affected neither by environ-

mental effects nor image stresses at the free surface. AFM enables the quantification and measurement of steps, but at the surface of the material where image stresses are expected to alter the deformation behaviour. Also, this technique does not consider the direction of the displacements, *i.e.* the Burgers vector of the relevant slip system. HR-DIC cannot capture the behaviour of plastic deformation at the nanometre length scale as it assumes a continuous strain tensor rather than localised slip at individual planes. These discontinuities have recently been incorporated into a Heaviside-DIC [203], but its resolution is still lower than that achieved in this work. HR-DIC at high temperatures has been performed in nickel-based superalloys by using a stable oxide layer as the speckle pattern to track the deformation [202], but the evolution of such layer under some conditions limits its applicability.

Disadvantages of the introduced technique include its low speed and manual recording of the measurements taken, as well as its limitation to alloys with large precipitates. This could be improved by automating the task via image processing, but the contrast variability in a micrograph makes this difficult, especially for the calculation of α and β. Determining these angles could be facilitated by performing electron backscattered diffraction (EBSD) prior to applying the γ' etchant. Slip line spacings and shear step lengths can then be measured for precipitates as small as 20 nm.

3.5 Conclusions

The current work makes use of a combination of electron microscopy techniques to provide a deeper understanding of the low cycle fatigue deformation behaviour at low and intermediate temperatures of polycrystalline nickel-based superalloy RR1000. The main findings of the current chapter are:

- Plastic deformation at both temperatures is mainly accommodated within slip bands that start developing from the first cycle of the fatigue process. Features in these dislocation structures include extended slip lines with inhomogeneous dislocation densities, dislocation dipoles and multipoles, pile ups at non-coplanar stacking faults and double cross slip as the mechanism for activation of new slip lines.

- The heterogenisation of the dislocation density within the slip bands arises as a consequence of their interaction with non-coplanar defects, mainly stacking faults, which act as permeable membranes to dislocation glide.

- At room temperature the plastic deformation in the slip bands is more localised. Cross slip as a dislocation annihilation mechanism for slip in nearby planes fully explains this behaviour. At higher temperatures this results in active slip planes further away

from each other, and the lower local plastic strain attained forces more slip bands to develop across the grains to the point where they may get too close and fill the entirety of some grains.

- The only quantitative difference found between the slip bands in samples fatigued for 40 and 500 cycles is the average shear step length per slip line, which increases as the test continues. This has deep implications in the damage accumulation process that takes place during low cycle fatigue, where the strengthening effect of the secondary precipitates is continuously degraded due to the shearing process.

Chapter 4

Physics-based modelling of the cyclic response

4.1 Introduction

The cyclic stress-strain response during uniaxial fatigue is associated with a large number of interacting mechanisms that depend on the deformation conditions and the chemistry and microstructure of the material. The formation and evolution of dislocation structures, and the continuous degradation of the precipitates, constitute complex phenomena that affect the macroscopic response in ways that have not yet been fully understood. Physical modelling and experimental validation are used in this chapter to investigate these issues.

This chapter introduces a simple one-dimensional physics-based model for the description of the hardening/softening cyclic behaviour observed in nickel-based superalloys. An alloy with a monomodal precipitate size distribution is used as a natural step to begin to understand this behaviour in a simpler microstructure. Special attention is paid to the effect of γ' size on the formation of heterogeneous dislocation structures as a source of work hardening and precipitate shearing as the main mechanism responsible for cyclic softening. Thus, classical precipitate hardening theory is revisited to include the dynamics of microstructure degradation due to repeated shearing.

The philosophy proposed for the model is that of linking the macroscopic stress evolution with the mechanisms controlling deformation at the microscopic and mesoscopic scales. The evolution of the microstructure is considered, so that it is possible to relate different phenomena that depend upon the same microstructural parameters. This is inspired by the findings discussed in Chapter 3. However, a different alloy with a unimodal precipitate size distribution is used for experimental validation due to a need to attain simplicity in this first

modelling approach. The model is also applied to data from the literature for alloy Nimonic PE16 to further validate the model.

4.2 Material and Methods

The material examined in this study is the polycrystalline nickel-based superalloy 718Plus, supplied by Rolls-Royce Deutschland. The composition of this alloy is given in Table 4.1. 718Plus was selected due to its slow γ' precipitation kinetics [204], which allow for a solutioning heat treatment followed by rapid cooling to avoid the nose of the TTT diagram and obtain a single phase material.

The initial shape of the material was a slice of supersolvus hammer forged billet with a diameter of 230 mm and thickness of 56 mm. Electrical discharge machining was used to cut cylinders with a diameter of 11 mm from the centre of the billet. These were subjected to one of four different heat treatments, denoted solutionised (S), underaged (UA), peak aged (PA) and overaged (OA). The solvus temperatures have been reported to be 967°C for γ' and 1012°C for the η/δ precipitates [205]. Thus, all heat treatments started with a supersolvus solutioning step at 1020°C for two hours followed by water quenching. Following the precipitation and coarsening curves given by Zickler *et al.* [206] for this alloy, ageing was done at 775°C for 10 (UA), 38 (PA) and 72 (OA) hours, followed by water quenching. Fatigue samples with the dimensions shown in Figure 4.1 were then machined from the specimens, removing the oxide layers formed during the heat treatments.

Table 4.1 - Chemical composition of alloy 718Plus (wt%) [207].

Ni	Cr	Co	Mo	W	Al	Ti	Nb	Fe
bal	18	9.1	2.7	1	1.45	0.75	5.4	9.5

Interrupted fatigue tests were performed at room temperature for 500 cycles in an Instron 8862 - 100kN servo hydraulic machine with a clip-on extensometer. Fully reversed triangular strain control was used with an amplitude of $\Delta\varepsilon/2 = 0.83\%$ and a constant strain rate of $0.3\%\text{s}^{-1}$, starting with a tensile load and ending after a compression stage. The cyclic stress-strain responses for all the cycles were recorded.

Two samples with a thickness of 4 mm were cut perpendicular to the loading axis from the middle part of the gauge length for each condition. These were hot mounted in bakelite, ground and polished with diamond suspensions and colloidal silica according to standard procedures. The γ'-etchant from Table 3.2 was applied for 20 seconds to one sample from each condition.

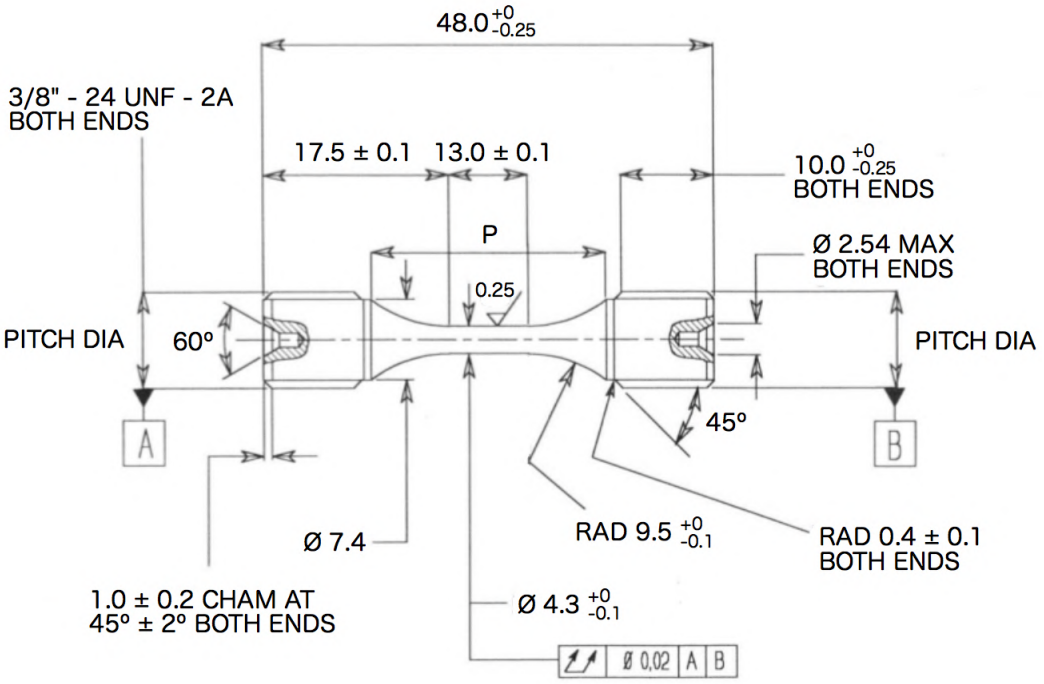

Fig. 4.1 - Geometry of the 718Plus low cycle fatigue samples with all dimensions in millimetres.

Scanning electron microscopy was performed in a ZEISS GeminiSEM 300. The secondary electron through-lens detector was used on unetched samples to characterise the γ' volume fraction and precipitate size distribution with the ImageJ software package by first applying the operations of smooth, threshold regional gradient [208] and watershed in micrographs taken at different magnifications for each ageing condition. This detector was also employed for the etched samples to observe shear steps in the precipitates. While crack initiation is outside the scope of this study, the higher plastic strains developed in this region are of particular interest for an analysis on the evolution of the microstructure, so these regions were also imaged.

The circular backscattered electron detector was used to measure the grain size via the circular method intercept following the ASTM standard E112-13 with six circles of 700 μm diameter in the unetched samples. Electron channeling contrast imaging (ECCI) was performed in over 20 grains at a low magnification (<1000X) for each condition to identify differences in the spread of the slip bands.

An estimation of the density of active slip planes is used to calculate the amount of slip each of these accommodates. The quantification of the volume fraction occupied by slip bands is preferred over that of their widths and spacings for simplicity. The variability in these lengths makes it difficult to determine where one slip band ends and the next

one starts, specially for grains with a more homogeneous plastic deformation behaviour. Besides, the true distances cannot be accessed with this technique. Measuring the slip band fraction at the grain length scale from the differences in the ECCI contrast circumvents these issues. However, quantifying the slip band volume fraction from the intensity profile along a line perpendicular to the band is very inconsistent. The inhomogeneous distribution of dislocations along a given plane makes two profiles from parallel lines vary considerably even when closely spaced. Contrast changes due to small carbides, embedded polishing media or even the γ' precipitates also affect these profiles.

Fast Fourier transform (FFT) filtering, possible thanks to the planarity of slip in this alloy, is used to circumvent these obstacles. The following analysis was performed in 10 grains from each sample in ECCI micrographs at a 5000X magnification with a resolution of 20 nm/pixel. Parallel bands produce in a FFT image a perpendicular bright sharp line that goes through the centre, as shown in Figure 4.2(a) for a crystal with slip bands in two different slip plane orientations. Traces of a horizontal and vertical line appear due to the squared shape of the enclosed region, but these can be ignored. In Figure 4.2(b), filtering out the lines linked to the active slip plane orientations and performing an inverse fast Fourier transformation (IFFT) results in an image with most of the features of the original micrograph, but without the slip bands. The opposite is done in Figures 4.2(c) and (d), filtering out from the FFT image everything but a rectangle of width ~ 3 pixels along these lines before applying an IFFT. This eliminates the inhomogeneities that were initially randomly distributed and produces a contrast that changes almost uniquely in the direction perpendicular to the selected plane orientation, making the measurements considerably more consistent. The intensity profiles along the red lines from Figures 4.2(c) and (d) are plotted in Figures 4.2(e) and (f), respectively. The volume fractions of slip bands are measured from the ratio of points with an intensity higher than a set threshold, shown with the dashed lines. This value is manually selected to be below the contrast observed in the bands.

4.3 Results

The initial stress-strain hysteresis curves for the different samples are shown in Figure 4.3(a). The yield stress shows the expected trend, with the PA condition stronger than the rest. A big difference in plastic strain amplitude can be seen from the first cycle. This varies from 0.62% for the S sample to $\sim 0.43\%$ for the rest, due to its considerably lower yield stress. This must be accounted for for a comparative analysis between the different conditions.

The evolution of the cyclic stress amplitude from Figure 4.3(b) shows hardening followed by softening for all the samples, although with different characteristics. Precipitate shearing

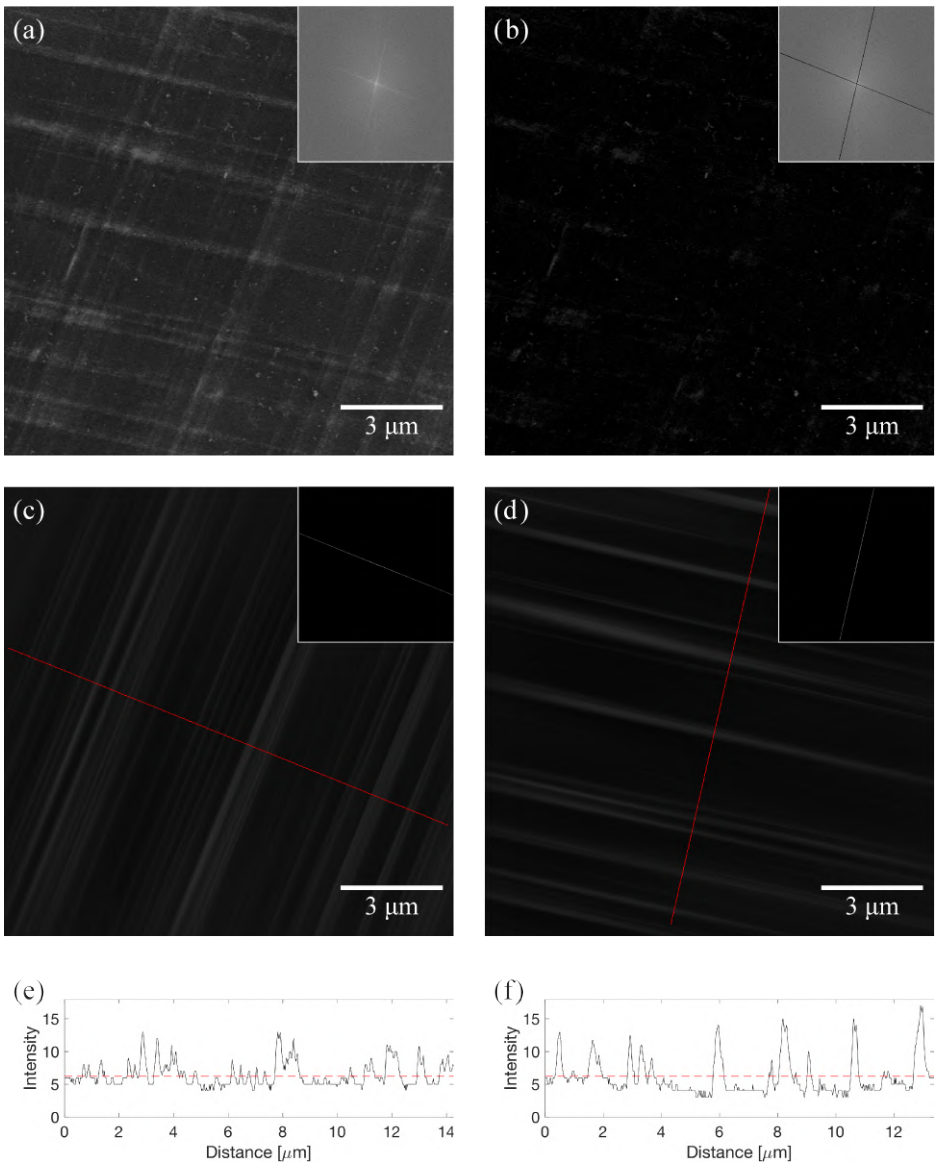

Fig. 4.2 - Methodology for the measurement of the slip band volume fractions. (a) Original ECCI micrograph showing a crystal with slip bands in two different orientations. (b) Image produced by filtering out the pixels along the lines with a high contrast from the previous FFT and then applying an IFFT. (c) and (d) result from filtering out from the initial FFT everything but the pixels within a rectangle aligned with a line with high contrast. The intensity profiles along the red lines are shown in (e) and (f), with the selected thresholds shown as dashed lines. All the FFTs are shown in the top right corner of their respective figures, where the black pixels are those filtered out before performing the IFFTs.

cannot be the only mechanism responsible for cyclic softening as this is also observed in the S sample, in agreement with LCF in solid solution alloys [131, 133, 134, 142]. Regardless, shearing might have a considerable effect on it as discussed in Section 2.2.2. The cyclic

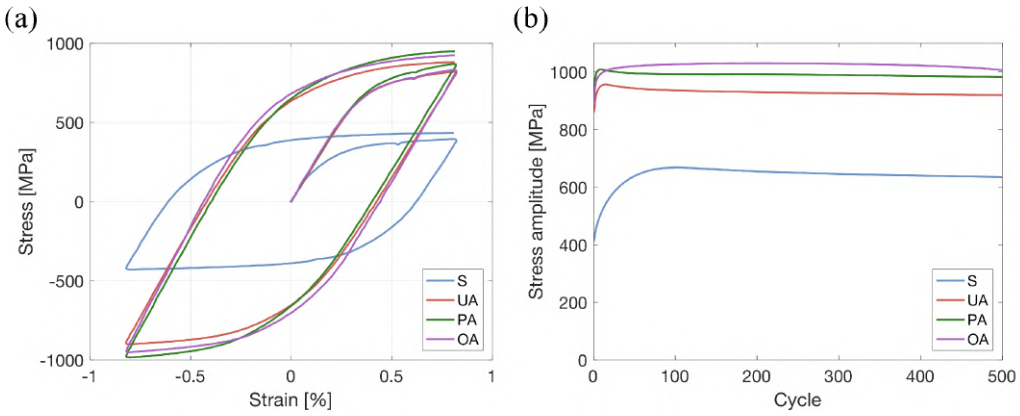

Fig. 4.3 - (a) First complete stress-strain hysteresis curve and (b) evolution of the cyclic stress amplitude of the 718Plus samples.

behaviours of the UA and PA samples are very similar, reaching the maximum stress after 14 and 9 cycles, respectively, and the following pronounced softening rate gradually decreases during the next hundred cycles. Alternatively, the OA condition hardens during the initial ~ 240 cycles and reaches a stress amplitude larger than the other samples. The softening that follows has the smallest slope among all, but increases towards the end of the test.

The ASTM grain size number of the material analysed is 5.86 (mean planar diameter of 47 ± 2 μm), and the grain boundaries are nonserrated. Annealing twins are very common throughout all the samples. No sign of δ/η precipitates is observed in any of the heat treated samples, as expected from the solutioning step [17].

The number of precipitates counted, area fraction and mean diameter of the precipitate intercepts d_{eq} are summarised in Table 4.2 for the three ageing conditions, together with other relevant data. Normalised histograms with the correspondent precipitate intercept sizes are given in Figure 4.4, fitted to lognormal probability distributions as done in previous studies [209, 210]. The mean and standard deviation of the logarithmic values of the distributions are also given in Table 4.2. No sign of γ' precipitates was found in the solutionised sample, neither in etched nor in unetched samples. The presence of precipitates smaller than 4 nm that could have formed during water cooling cannot be ruled out due to the resolution of the SEM, but even if this was the case, their contribution to the yield stress of the material would be negligible due to their weak cross sections.

Representative ECCI micrographs for each ageing condition are shown in Figure 4.5. Plastic deformation is in general accommodated in slip bands that extend through the entirety of a grain. Unlike alloy RR1000 at room temperature, 718Plus does not contain stacking faults. Multiple slip dominates throughout all samples. Most grains for all conditions show slip bands in two different slip plane orientations, but some contain bands in one or three

Table 4.2 - γ' characterisation. The error bars correspond to the standard deviations of the measurements and the calculated errors in the volume fractions.

Sample	Count	Area imaged [μm^2]	Volume fraction [-]	Mean d_{eq} [nm]	Circularity	Lognormal fit
UA	4939	0.9	0.2 ± 0.02	14.1 ± 4	0.89 ± 0.08	2.59 ± 0.34
PA	6010	3.8	0.23 ± 0.02	27.5 ± 7	0.86 ± 0.09	3.28 ± 0.27
OA	2603	3.2	0.21 ± 0.02	38 ± 11.2	0.83 ± 0.1	3.59 ± 0.31

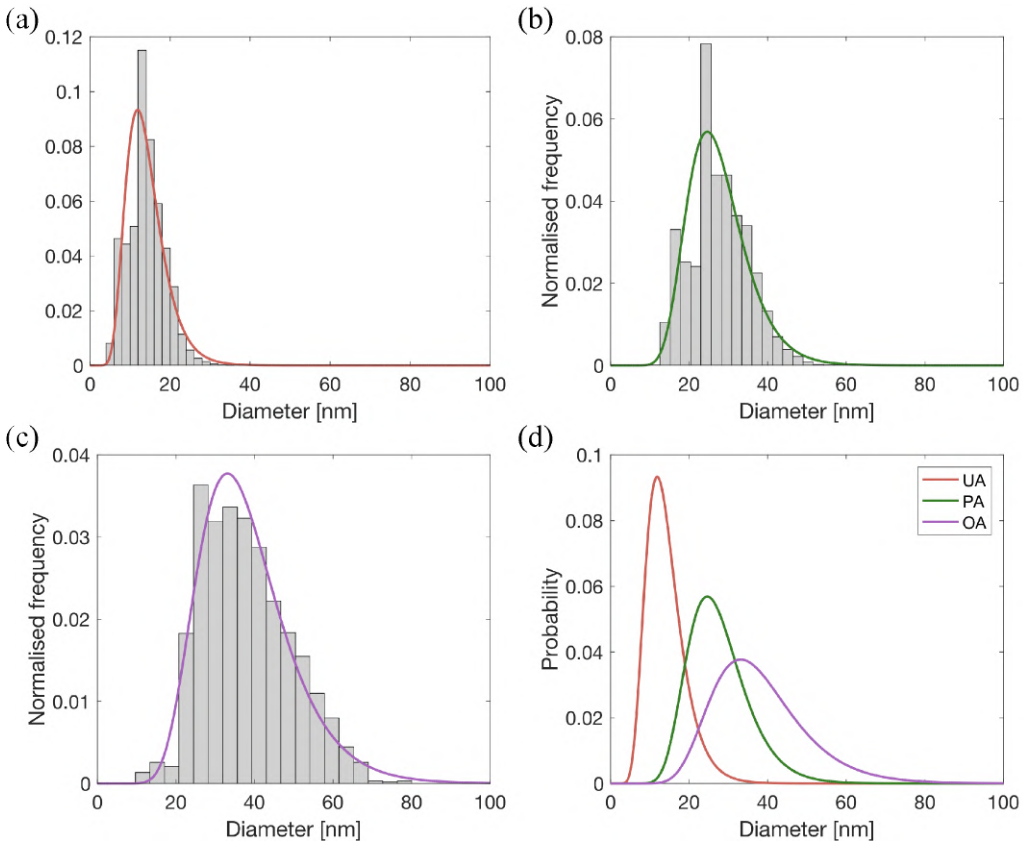

Fig. 4.4 - Normalised histograms of the precipitate intercept size in the (a) underaged, (b) peak-aged and (c) overaged samples, fitted to lognormal distributions. These probability distributions are plotted together in (d) for comparison.

orientations. Figure 4.6 shows the fraction of grains with each observed behaviour, counting a minimum of 24 grains per condition.

The volume fraction of slip bands in the primary slip system as a function of precipitate size obtained via the FFT filtering is reported in Figure 4.7, where the high standard deviations highlight the large variability observed between grains. The S condition has the highest volume fraction, although a direct comparison with the other samples must be done with caution due to the larger plastic strain per cycle this specimen was subjected to. The absence of precipitates may however have an effect regardless of this, as these have been observed

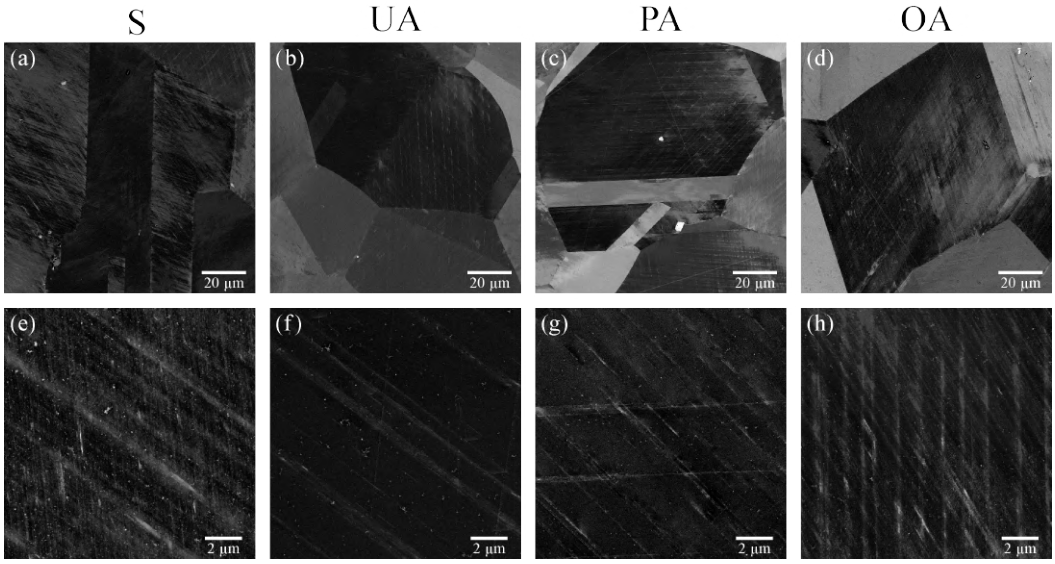

Fig. 4.5 - ECCI micrographs of samples from the four ageing conditions at a magnification of (a-d) 600X and (e-f) 5000X.

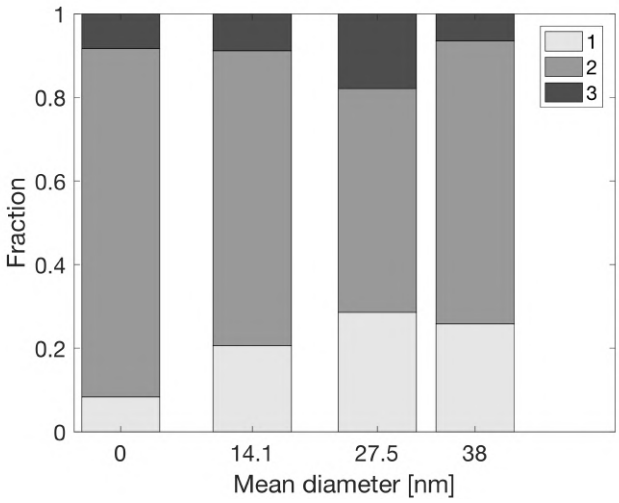

Fig. 4.6 - Fraction of grains with slip bands in 1, 2 and 3 different slip plane orientations for each ageing condition.

to promote slip localisation [10, 165]. Longer ageing times result in a higher quantity of slip bands too. This behaviour in the spread of plastic deformation agrees with experimental studies on Waspaloy [76] and dislocation dynamics simulations with the incorporation of shearable precipitates [98]. Note that the difference from the UA to the PA condition is rather small, but a considerable increase is observed for the OA condition.

While this quantitative analysis shows the overall trend of the ECCI observations, more differences in the slip localisation can be discerned. Some of the grains in the S condition

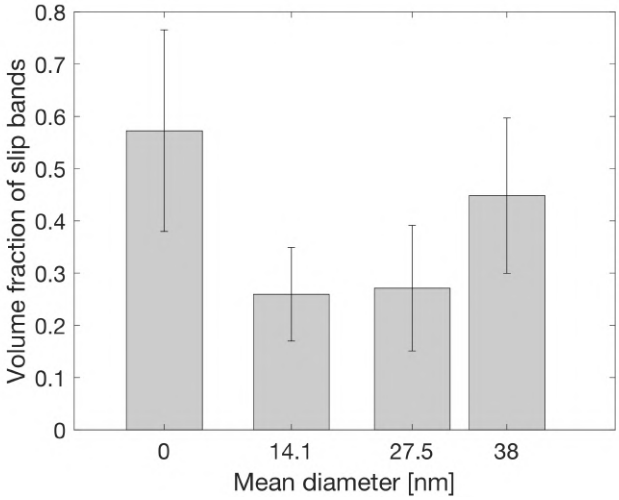

Fig. 4.7 - Volume fraction of slip bands in the primary slip system for the different ageing conditions. The error bars denote the standard deviation in the measurements.

show a homogeneous distribution of slip similar to that showcased in RR1000, where parallel bands fill almost the entirety of the volume. On top of this, clear slip bands develop in a secondary orientation. This behaviour is also observed to a lesser degree in the OA sample. Examples of this can be seen in Figures 4.5(e) and (h). Conversely, all the imaged grains in the UA and PA conditions show localisation of plastic deformation in clearly spaced distinct slip bands.

Signs of γ' shearing are observed in the three precipitate reinforced microstructures, as shown in Figure 4.8 in γ'-etched samples. The slip bands look similar to those in RR1000, with closely spaced continuous slip lines along which precipitates are sheared. However, there is a large in- and out-of-plane component of the displacement vectors in all the micrographs due to the samples being cut perpendicular to the loading axis. Halves of sheared precipitates are commonly observed because of this. Measurements of the slip line spacing with the methodology described in Section 3.2.1 were only obtained in the OA and PA samples, giving an average of 20.1 nm and 23.8 nm, respectively. The slip bands in the UA sample were spotted but the slip lines could not be traced due to the small precipitate size and the limited resolution of the through-lens detector in the SEM.

Surface cracks are observed in all samples. Examples of the precipitate morphology in the regions nearby are shown in Figure 4.9. Clear signs of higher amounts of plastic deformation are observed in all cases. Sheared precipitates populate slip bands in the vicinity of the cracks for the PA and OA conditions. In the former in particular, multiple nearby parallel bands show more shearing than their counterparts in the bulk. In the UA sample, precipitate-free deformation bands appear close to the crack and ahead of the crack tip, hinting towards

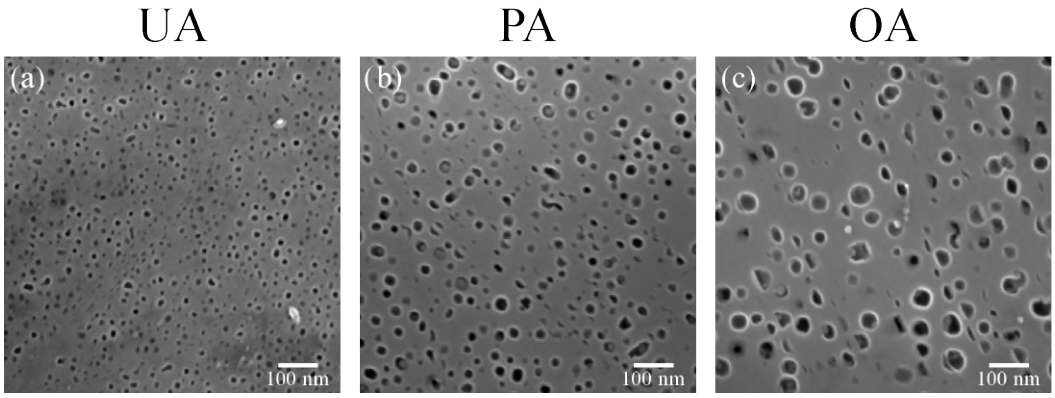

Fig. 4.8 - Secondary electron micrographs of slip bands in the (a) UA, (b) PA and (c) OA γ'-etched samples.

their dissolution at high cumulative plastic strains. No γ' is observed in these regions even at higher magnifications. Cracks in the S condition are present too, but no special feature around these is observed due to the absence of precipitates throughout the whole sample.

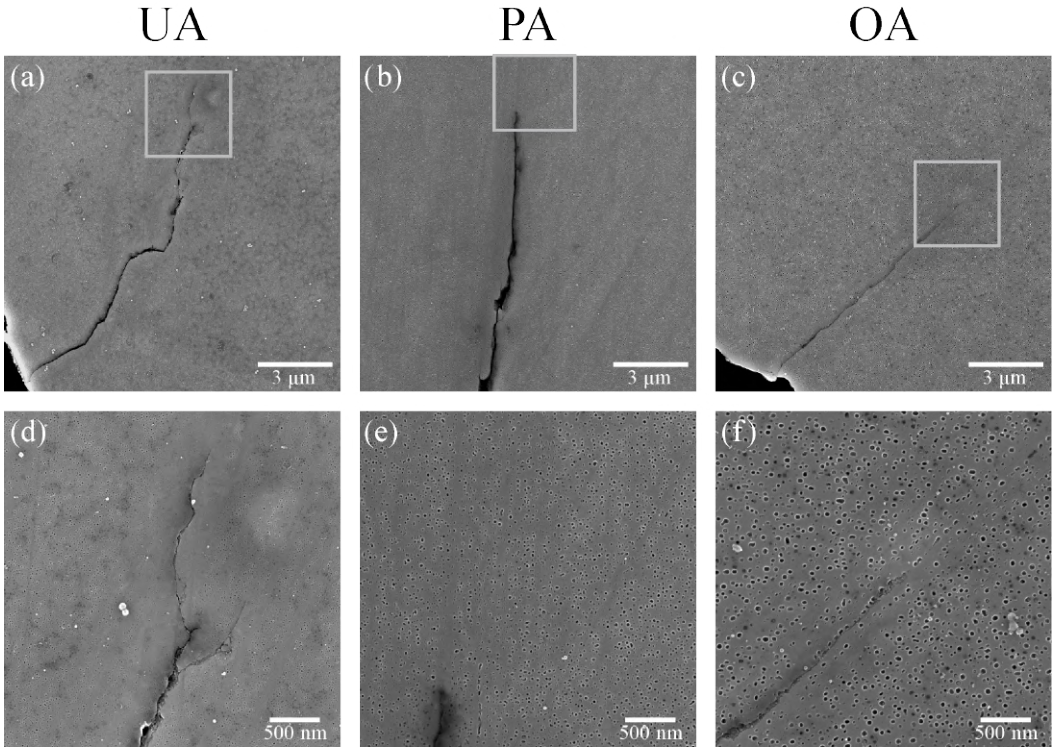

Fig. 4.9 - Secondary electron micrographs of surface cracks in the UA, PA and OA γ'-etched samples. The enclosed regions in (a-c) are shown at a higher magnification in (d-f).

4.4 Discussion and modelling

Slip bands are the main dislocation structure formed during low cycle fatigue in superalloy 718Plus for all ageing conditions tested. While not recorded extensively in this study, the shear behaviour shares similarities with that observed in RR1000 regardless of the large difference in precipitate size and volume fraction, such as the heterogeneous character of steps along a given slip plane.

The main difference observed is the degree of slip localisation. Consider first the S condition. As mentioned before, a direct comparison with the other samples must be done with caution due to the difference in plastic strain, but similar trends are expected to appear regardless of this. With the activation of a source, dislocations will generate and glide freely until back stresses force them to double cross slip onto nearby slip planes. The absence of obstacles means that dislocations will redistribute freely across the material, resulting in more homogeneous structures. On the contrary, dislocations in precipitate reinforced materials are more likely to glide on an already active plane as the precipitates become weaker with continuous shearing along these planes, rather than double cross slipping onto a pristine plane. While the effect of a single dislocation may be negligible, pile ups may contribute significantly to microstructure degradation even for low plastic strains in monotonic loading.

The slip line spacings measured are comparable in length to the γ' diameter (about half the distance as those in RR1000), so that most of the precipitates are sheared only at one or two planes. When required, shorter double cross slip events can preferentially redistribute the plastic deformation in the matrix. The weaker cross sections in underaged materials are easily sheared by dislocations, with a high slip localisation. For longer ageing times, as the individual precipitates become stronger, dislocations encounter harder barriers and are forced to spread more. This results in the activation of more slip bands across entire grains, as observed in the OA condition.

4.4.1 Cyclic deformation behaviour modelling

The macroscopic stress σ required to exert a certain amount of plastic deformation ε into an alloy stems from a combination of mechanisms. In this work, the different contributions considered are those of (i) a stress σ_0 due to the combined effects of grain boundaries and solid solution in the γ matrix, (ii) γ' precipitates σ_P, (iii) isotropic hardening σ_D due to the accumulation of dislocations, and (iv) kinematic hardening σ_K from the long-range internal stresses produced by heterogeneous deformation [211]. Congruently with models found in

the literature [144, 185, 186], the superposition of these contributions follows the form

$$\sigma = (\sigma_0 + \sigma_P + \sigma_D) \cdot \operatorname{sign} \dot{\varepsilon} + \sigma_K, \tag{4.1}$$

where $\operatorname{sign} \dot{\varepsilon}$ denotes the direction of loading. This common simplification in mesoscopic models avoids dealing with stress inhomogeneities and the deformation constraints imposed on the individual grains within a polycrystal to focus on the behaviour of the material as a whole, albeit losing detail at shorter length scales. The total strain $\varepsilon_t = \varepsilon_e + \varepsilon_p$ has an elastic $\varepsilon_e = \sigma/E$ and a plastic ε_p components, and the plastic strain rate $\dot{\varepsilon}_p$ can be further described with Orowan's equation [212]

$$\dot{\varepsilon}_p = M^{-1} b \rho_m v, \tag{4.2}$$

where M is the Taylor factor, b the Burgers vector, ρ_m the mobile dislocation density and v the average velocity of these dislocations.

The contribution of the γ' phase to the yield stress is calculated as a function of the precipitate diameter r and the antiphase boundary energy γ_{APB} from classical precipitation hardening theory [38, 213, 214]. Two regimes, weak and strong pair-coupling, are modelled from the forces felt by two dislocations gliding on the same slip plane. The contribution to the critical resolved shear stress due to weakly paired dislocations τ_{wc} follows equation

$$\tau_{wc} = \frac{d\gamma_{APB}}{2b^2 L} \left(\frac{d\gamma_{APB}}{\mu} \right)^{1/2}, \tag{4.3}$$

where μ is the shear modulus and L the mean precipitate spacing. An additional term $-f$ typically appears inside the square root in equation (4.3), which arises from considering that the trailing dislocation has already entered a γ' at the critical point for precipitate shearing. This has been shown to introduce errors for alloys with small precipitates [210] and is therefore avoided in the current derivation. For larger precipitates, strong pair-coupling is given by

$$\tau_{sc} = \frac{W\mu b}{\pi L} \left(\frac{\pi d\gamma_{APB}}{W\mu b^2} - 1 \right)^{1/2}, \tag{4.4}$$

where W is a dimensionless constant used to account for uncertainties in the model and fit the results. The reader is referred elsewhere [15] for a more detailed derivation of these equations. The precipitate spacing

$$L = \left(\frac{\pi}{6f} \right)^{1/2} d \tag{4.5}$$

can then be substituted into equations (4.3) and (4.4). The active mechanism will be that which requires the lowest stress to occur, *i.e.* $\sigma_P = M \min(\tau_{wc}, \tau_{sc})$.

Kinematic hardening is promoted by the presence of a secondary phase due to the incompatibilities that arise upon deforming a material with elastic inclusions [172, 211]. An empirical Armstrong-Frederick equation proven effective in the modelling of precipitate-strengthened materials [144, 215, 216] is cast in its differential form

$$d\sigma_K/c_2 = c_1 d\varepsilon_p - \sigma_K |d\varepsilon_p|, \tag{4.6}$$

where c_1 and c_2 are fitting constants. Upon disposing of the absolute value via the use of $\operatorname{sign}\dot{\varepsilon}$, integration of equation 4.6 leads to

$$\sigma_K = c_1 \operatorname{sign}\dot{\varepsilon} + (\sigma_{K0} - c_1 \operatorname{sign}\dot{\varepsilon}) \exp[-c_2 \operatorname{sign}\dot{\varepsilon}(\varepsilon_p - \varepsilon_{p0})], \tag{4.7}$$

which is solved each time the load is reversed with σ_{K0} and ε_{p0} the values of σ_K and ε_p at that point (both set equal to zero at the beginning of the first cycle), respectively. The physical interpretations of c_1 and c_2 lie beyond the scope of the current study, and linking these to the precipitate evolution represents an additional challenge that must be tackled separately.

4.4.2 Cyclic hardening

The dislocation density acts as the main internal variable to determine the gradual hardening due to plastic straining. However, due to the slip localisation observed in this alloy, not all the volume shows an increase in the dislocation density. Thus, the evolution of the slip band volume fraction f_{SB} is incorporated. While this variable could be described as the slip band width over the slip band spacing, the large variability of these parameters makes it to more convenient to directly use the measured fraction.

This composite material description makes it possible to split the total dislocation density ρ into

$$\rho = f_{SB}\rho_{SB} + (1 - f_{SB})\rho_0, \tag{4.8}$$

where the subindex *SB* stands for a local variable at the slip bands and ρ_0 is the initial dislocation density, which remains unchanged in the interband regions. Equations (4.2) and (4.8), accounting only for mobile dislocations, lead to the decomposition of the plastic strain ε_p in a similar fashion. Even when dislocations in the interband region have an effect on the flow stress in planar slip materials, their density and mobility are much lower than those within the slip bands [33, 97]. Thus, the macroscopic plastic strain is dictated by the local

strain at the slip bands

$$\varepsilon_p = f_{SB}\varepsilon_{SB,p}. \tag{4.9}$$

This equation relates the microscopic strain produced by the slip bands with the macroscopic plastic behaviour. Using the local plastic strain at the slip bands as a variable in the model is an effective way of linking the different mechanisms related to the cyclic stress evolution. Yet, it is clear that this is a simplification of the problem as in reality strain compatibility requires, due to geometrical constraints, the simultaneous operation of five independent slip systems to avoid fracture. The remaining part of the model is built upon the assumption that most of the plastic deformation occurs within the slip bands and only for stresses above the onset of macroscopic plastic deformation.

A Kocks-Mecking framework for the evolution of the dislocation density as a function of the macroscopic strain is incorporated by accounting for the composite model. This has the form

$$\frac{d\rho_{SB}}{d\varepsilon_p} = \frac{\partial\rho_{SB}}{\partial\varepsilon_{SB,p}}\frac{d\varepsilon_{SB,p}}{d\varepsilon_p}, \tag{4.10}$$

where the first term in the right-hand side of this equation is related to the evolution of the dislocations due to the local plastic strain, while the second term refers to the amount of strain localisation at the slip bands. A Kocks-Mecking equation [81] can describe the local behaviour

$$\frac{d\rho_{SB}}{d\varepsilon_{SB,p}} = k_1\sqrt{\rho_{SB}} - k_2\rho_{SB}, \tag{4.11}$$

where k_1 and k_2 are the dislocation storage and dynamic recovery coefficients. Thus, even with a low macroscopic plastic strain, the slip bands may accommodate large amounts of deformation [10], which has a direct effect on the dislocation creation and annihilation.

Combining equations (4.9), (4.10) and (4.11), the evolution of the dislocation density can be expressed as

$$\frac{d\rho_{SB}}{d\varepsilon_p} = (k_1\sqrt{\rho_{SB}} - k_2\rho_{SB})\left(\frac{1}{f_{SB}} - \frac{\varepsilon_p}{f_{SB}^2}\frac{df_{SB}}{d\varepsilon_p}\right). \tag{4.12}$$

The first parenthesis on the right-hand side of equation (4.12) determines the saturation of the isotropic hardening due to a gradual increase in the dislocation density. The second parenthesis links the localised deformation with the macroscopic strain via the volume fraction of slip bands; the first term converts the local variable to a global dislocation density and the second term acts as an additional source of dislocations due to the generation of new slip bands. The latter must have a larger effect during the first loading stage as the slip bands develop, and its effect becomes negligible once saturation of f_{SB} is reached.

Modelling the evolution of f_{SB} to reproduce this behaviour cannot be achieved solely as a dependence on ε_p due to the cyclic nature of the load. Instead, this is done with a variable

$$q = \max\left(|\varepsilon_p|, q\right) \tag{4.13}$$

that records the maximum plastic strain that has been attained at any point during the fatigue test. This provides a physical meaning to the behaviour observed in other models, such as that of Maciejewski and Ghonem [144], who have used a similar variable on an empirical model for isotropic hardening. The volume fraction of slip bands is then assumed to follow equation

$$f_{SB} = f_{SB0}\sqrt{q}, \tag{4.14}$$

where f_{SB0} can be fitted to the values measured. A similar dependence can be imposed on experimental data of slip band spacings reported in the literature [104]. This description is phenomenological rather than mechanistic and it reproduces the behaviour observed, but further modelling is required to explain the physical basis and parametric dependences of f_{SB0}.

Equations (4.13) and (4.14) explain why in total strain amplitude controlled tests an increase in the number of slip bands is observed for a higher number of cycles. Cyclic softening results in higher plastic strains than those obtained during the first cycles, promoting the formation of additional slip bands. However, this happens only after the amount of softening is enough to counteract the hardening effect of the dislocations. Similarly, more slip bands form in grains closer to the fatigue crack, as the local plastic strain is highly localised in those areas [109].

The dislocation density at the slip bands can be extracted from the previous analysis by solving the differential equation (4.12). Mughrabi's composite model for heterogeneous dislocation distributions [188], originally developed for the cell structure deformation mechanism in wavy slip materials, is not employed here as it assumes that both regions are loaded in series. Instead, a standard Taylor equation

$$\sigma_D = M\alpha_{SB}\mu b\sqrt{\rho} \tag{4.15}$$

is used to estimate the work hardening contribution to the flow stress, where the geometrical factor α depends on the type and arrangement of dislocations [217].

4.4.3 Cyclic softening

Precipitate shearing due to the accumulation of slip irreversibilities has been identified as one of the main mechanisms leading to the softening of the material in superalloys [166]. This loss in strength occurs due to a decrease in the effective area of antiphase boundary [119, 120]. The dislocation/particle interactions appear to be complex as not only the area between the top and bottom halves of the sheared precipitate decreases, but also the shape of this cross section changes. In reality, this should have an effect on variables inherent to the calculation of precipitate strengthening, such as the bowing angle. For simplicity, a model based on the reduction of the precipitate cross sectional area A_{APB} is proposed from the seminal ideas by Differt *et al.* [192] (further detailed in Appendix A). The following assumptions are also considered:

- All the slip bands have the same morphology, consisting of m_{sl} slip lines equally spaced by a distance a. This is schematically shown in Figure 4.10.
- All the slip lines carry dislocations with a Burgers vector positive during the tensile stages of the fatigue process and negative during the compressive stages.
- The shearing process in each precipitate occurs in the direction of its nearest neighbour, situated at a distance $L_{eff} = L$.

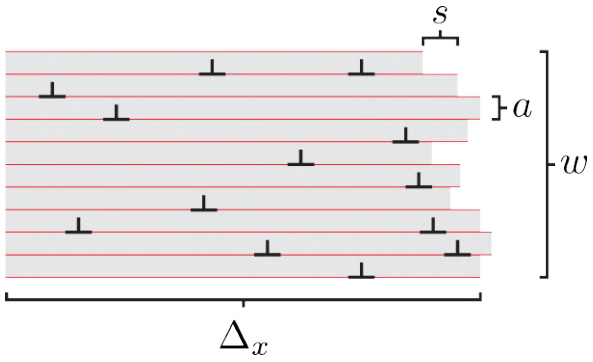

Fig. 4.10 - Schematic representation of a slip band of width w, consisting of m_{sl} slip lines, shown in red, equally spaced by a distance a, showing some dislocations and a slip profile at the right due to slip irreversibilities.

Upon shearing, the mean cross sectional sectional area of the precipitates $\overline{A_{APB}}$ decreases, but the interparticle distance L remains constant. A softening curve arises from substituting d in equations (4.3) and (4.4) with an associated reduced precipitate diameter $\overline{d_{APB}} = 2\sqrt{\overline{A_{APB}}/\pi}$. This takes into account the physical evolution of the precipitate degradation

phenomenon. A link between the reduction in $\overline{A_{APB}}$ and the cumulative local plastic strain $\varepsilon_{SB,p,cum}$ is required to incorporate this dependence into the model.

As shown in Figure 4.10, the movement of dislocations inducing plastic strain occurs at individual slip planes. From Orowan's equation (equation (4.2)), a description for the local plastic strain in a representative volume $V = wl\Delta x$ can be given as

$$\varepsilon_{SB,p} = M^{-1} b \Delta x \rho_{SB,m}\,, \tag{4.16}$$

where the subindex m stands for mobile dislocations. Assuming that all the dislocations in this volume have the same length l, the mobile dislocation density can be expressed as

$$\rho_{SB,m} = \frac{m_{sl} n_p l}{V}, \tag{4.17}$$

where n_p is the average number of dislocations gliding per plane; thus, combining equations (4.16) and (4.17) gives

$$n_p = \frac{a}{b} M \varepsilon_{SB,p}\,. \tag{4.18}$$

Introducing a factor p that denotes the fraction of dislocations that undergo an irreversibility process after glide, the average number of irreversible steps per plane can be calculated as $n_{p,irr} = p n_p$. This irreversibility factor may depend on the immobile dislocation density, which promotes both dislocation trapping and annihilation, but is assumed here to remain constant throughout the tests for simplicity. Then, the expected number of irreversible steps in each direction per slip line z at any point of a deformation process is

$$z = \frac{ap}{2b} M \varepsilon_{SB,p,cum}. \tag{4.19}$$

For a test with a constant plastic strain amplitude, this is very similar to equation (A.1), although equation (4.19) has the advantage that it can be applied to fatigue tests where the stress or strain amplitude does not remain constant during the whole process.

The methodology proposed by Differt *et. al.* [192] (detailed in Appendix A) estimates the probability function of the number of irreversible slip steps in a single plane Δn, so that an average shear step length $\bar{s}$ can be calculated. However, considering the whole probability distributions of this variable results in a more complete description of the shearing process, *i.e.* using $P(s)$ instead of only $\bar{s}$. From equation (A.5), and knowing that $s = b\Delta n$, this takes the form

$$P(s) = \exp(-2z)\, I_{s/b}(2z), \tag{4.20}$$

where $I_{s/b}$ is the modified Bessel function of the first kind.

Let us now consider how each shear step modifies the cross sectional area A_{APB} of a precipitate along that slip plane. This is the area that the dislocations have to cross, and it is delimited by the distance L_{APB} schematically shown in Figures 2.19(a) and (b).

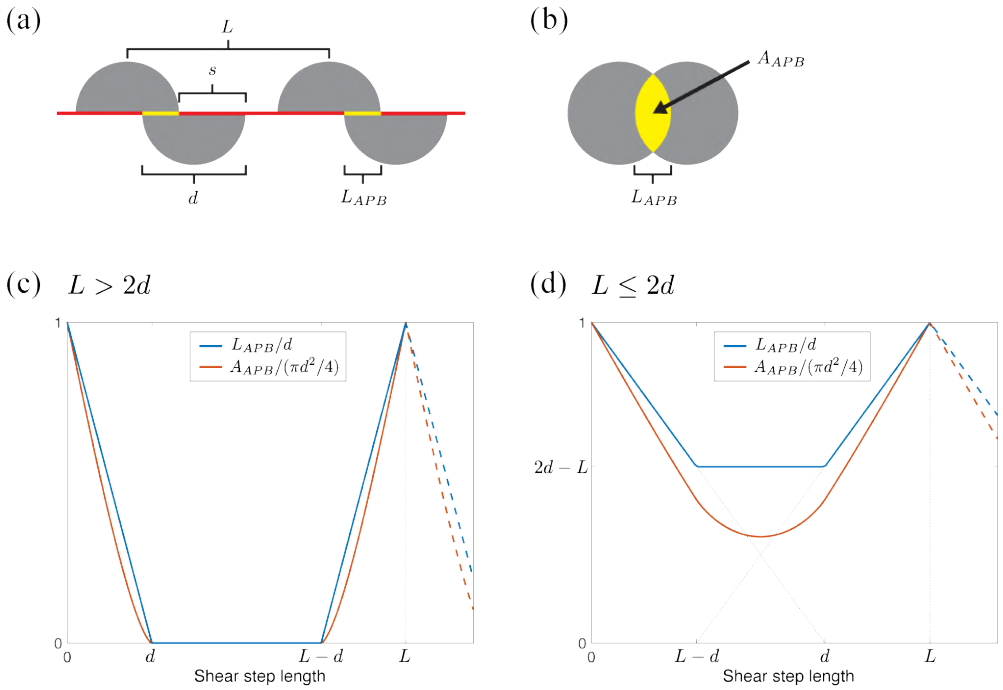

Fig. 4.11 - (a) Lateral view and (b) top view of the sheared precipitate configuration, and the normalised L_{APB} and A_{APB} as a function of the shear step length for microstructures with (c) $L > 2d$ and (d) $L < 2d$. The periodic boundaries at $s = L$ are represented by the dashed black lines.

For $L > 2d$, one can see that as s increases, the distance L_{APB} decreases linearly from its initial value $L_{APB} = d$ until it vanishes when $s = d$. However, once $s = L - d$ the bottom half makes contact with the top half of the precipitate next to it, restoring part of the previously lost antiphase boundary. This behaviour has been observed before [117], as well as in RR1000 in Chapter 3. Once $s = L$, these fully overlap and L_{APB} takes its initial value. If s keeps increasing after this the whole process repeats; thus, an effective slip step length can be defined from this symmetry as

$$s_{eff} = \mathrm{mod}\,(s, L). \tag{4.21}$$

The area where two equal circles shifted by distance s intersect can be described by the relation

$$A_{int}(s) = \frac{d^2}{2}\cos^{-1}\left(\frac{s}{d}\right) - \frac{s}{2}\sqrt{d^2 - s^2}. \tag{4.22}$$

Thus, A_{APB} follows a similar trend to L_{APB}, although it decreases from its initial value following equation (4.22) rather than linearly. Both curves, normalised to their initial values, are schematically shown in Figure 2.19(c).

These values behave differently when $L \leq 2d$ (higher volume fractions) as the bottom half of a precipitate will start contacting the neighbouring particle before being totally separated from its original top half, which is represented in Figure 2.19(d). The plateau displayed in this curve originates from adding the two smaller L_{APB} segments formed at both ends of each particle. The resulting equations for these parameters as a function of the effective slip step length, for any L/d ratio, can be expressed from geometric considerations as

$$L_{APB}(s_{eff}) = \max\left(-s_{eff}+d,\, s_{eff}-L+d,\, 2d-L,\, 0\right) \tag{4.23}$$

and

$$A_{APB}(s_{eff}) = A_{int}(s_{eff}) + A_{int}(L-s_{eff}). \tag{4.24}$$

Upon combining these geometric parameters with the probability function $P(s)$, the individual probabilities of each $|s| > L$ must to be mapped into the domain of s_{eff} due to periodic symmetry, as shown in Figure 4.12 for s_{eff}. An associated $P(A_{APB})$ is immediately obtained from this, and as these are discrete distributions, the mean values $\overline{A_{APB}} = A_{APB}P(A_{APB})$ and $\overline{d_{APB}}$ can be calculated. Substituting d in equations (4.3) and (4.4) with $\overline{d_{APB}}$, and combining it with equation (4.19), leads to the evolution of σ_P as a function of the local cumulative plastic strain. Note that the initial value of L remains constant throughout a simulation.

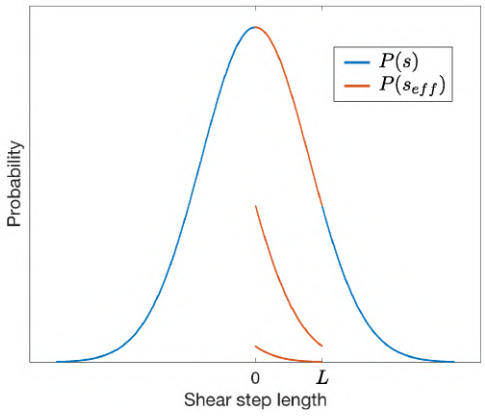

Fig. 4.12 - Schematic representation of the mapping of the probability of s into the domain of s_{eff}.

4.4.4 Aplication of the model

While some of the parameters in the model would be expected to vary for the different heat treatments, a single value is used for all four conditions. While this introduces errors in the simulations, this is preferred over overfitting every curve. Furthermore, this allows the variables characterised to show their effects on the evolution of the cyclic stress response. Table 4.3 contains the values used for all the input parameters of the model.

Table 4.3 - Input parameters for the simulations.

Parameter	718Plus	Nimonic PE16
M [-]	3.06	3.06 [218]
α [-]	0.2	0.2 [188, 217]
b [nm]	248	248 [40]
μ [GPa]	82.7	66.4 [219]
γ_{APB} [J/m^2]	0.16	0.15
W [-]	0.4	0.7
σ_0 [MPa]	110	270
c_1 [MPa]	340	250
c_2 [-]	500	110
k_1 [μm^{-1}]	150	250
k_2 [-]	5.6	7.9
ρ_0 [m$-$2]	10^{10}	10^{10}
d [nm] *	0, 14.1, 27.5, 38	12.5, 21, 30
f [-]	0.215	0.07
f_{SB0} [-] *	7.2, 4, 4.3, 6.3	4.3
a [nm]	21.7	21.7
p [-]	0.4	0.3

* Values for each ageing condition

Material parameters α, ρ_0 and b are selected from values typically reported in the literature. The value of α varies between 0.1 and 0.4 depending on many factors and may even evolve during a test, and a value of 0.2 appears often for heterogeneous dislocation patterns [188, 217]. The initial dislocation density ρ_0 does not significantly affect the results, and the variation in Burgers vector between different superalloys is negligible, so these parameters were set from the beginning. Values extracted from experimental characterisation are d, f, a and f_{SB0}. This last value is set for each sample so that the plastic strain observed in the hystereses curves gives the measured f_{SB} using equation (4.14).

As all the precipitate reinforced samples were heat treated at the same temperature, the γ' volume fraction is expected to be equal. The small variation measured was thus neglected. The yield stresses were then calculated from the difference between the solutionised and

the aged samples by choosing appropriate values of γ_{APB} and W. Note that precipitate hardening in these samples is considerably lower than that reported in this alloy at room temperature for the conventional δ/η-subsolvus heat treatment [207, 220, 221] (1124 MPa [221]). The calculated initial precipitate strengthening contribution of alloy 718Plus as a function of precipitate size and its evolution in terms of the local cumulative plastic strain are shown in Figure 4.13. As expected, larger precipitates take longer to lose their effect as more dislocations are required to shear them completely. This explains the softening rates observed in multiple alloys. The overaged samples do not harden upon straining as the mean precipitate cross section decreases but the initial value of the precipitate spacing remains constant throughout the simulation.

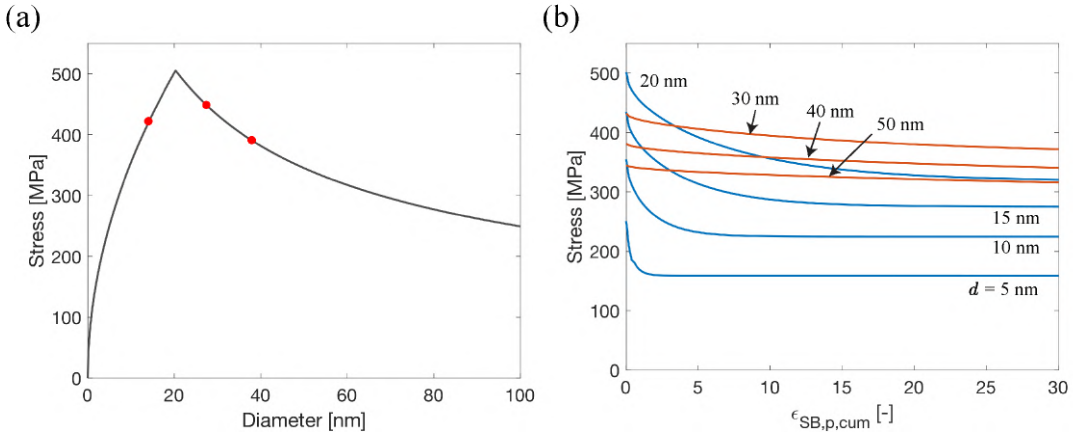

Fig. 4.13 - (a) Precipitate contribution to the yield stress as a function of diameter, where the red dots correspond to the UA, PA and OA samples in this study. (b) Evolution of this contribution as a function of the local cumulative plastic strain for different precipitate sizes. The blue and red lines correspond to underaged and overaged samples, respectively.

The kinematic hardening coefficients, the Kocks-Mecking parameters and the irreversibility factor p are used to fit all the curves produced. Figure 4.14 shows a comparison between the experimental and the simulated cyclic response in all samples. Trends in the cyclic plastic behaviour of the different ageing conditions are reproduced. As mentioned before, modelling of softening in the S sample is not done here due to the absence of precipitates. All other simulated curves show the hardening and softening behaviours expected.

The crossover between the curves of the PA and the OA samples is of particular interest. This is a consequence of two factors. Firstly, the lower softening rate in the latter due to precipitate size. Secondly, a higher volume fraction of slip bands in this condition. While ρ_{SB} saturates at the same value for all samples, ρ becomes larger for the OA condition, increasing the isotropic hardening. Another effect of the higher f_{SB} is that each band must accommodate a lesser amount of plastic deformation per cycle, so that the cyclic hardening

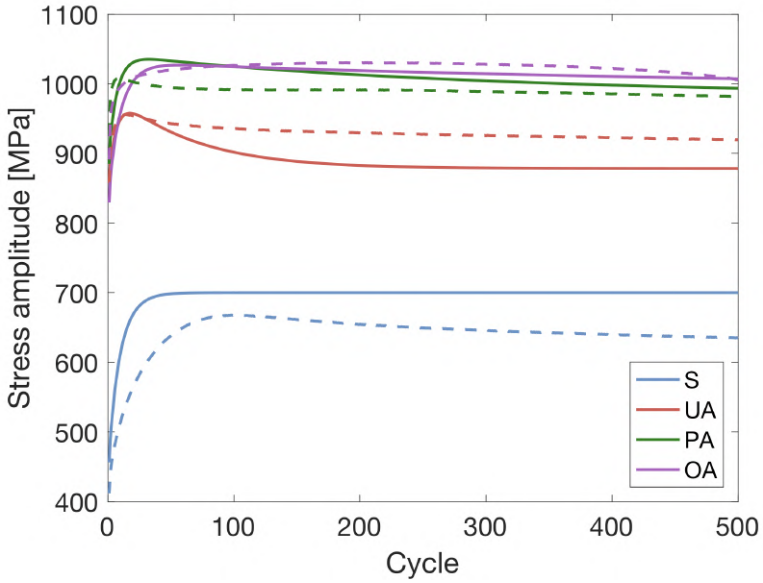

Fig. 4.14 - Experimental (dashed lines) and simulated (solid lines) evolution of the cyclic stress amplitude of the 718Plus samples.

behaviour becomes slower. Thus, the maximum stress amplitude in the S and OA samples is reached after a higher number of cycles compared to the other materials.

Figure 4.15 shows the first and last cyclic stress-strain hysteresis curves for the precipitate strengthened samples. A close agreement between experiments and simulations is observed. The largest difference appears in the OA sample, which hardens more slowly in the simulation. The larger f_{SB} is not enough in this case to significantly increase the hardening rate. The Kocks-Mecking parameter k_1 should be larger for this sample to better match the experimental curve.

The shape of the hysteresis curves also changes with the number of cycles. Hardening rates for each cycle only change in the model due to the saturation of isotropic hardening, whereas the experimental curves are more related to slight increase in the kinematic hardening. Nonetheless, the variation during the 500 cycles does not greatly influence the plastic strain attained per cycle, which is a variable of major importance for both the hardening and softening contributions to the overall stress.

The model is also applied to experimental results from the literature in superalloy Nimonic PE16 fatigued at room temperature, with data from Sundararaman *et al.* [152] and Singh *et al.* [116]. These were selected because the tests performed vary both precipitate size and total strain amplitude, and characterisation of the precipitate size and volume fraction is also given. The input parameters of these simulations are shown in Table 4.3. A similar logic is

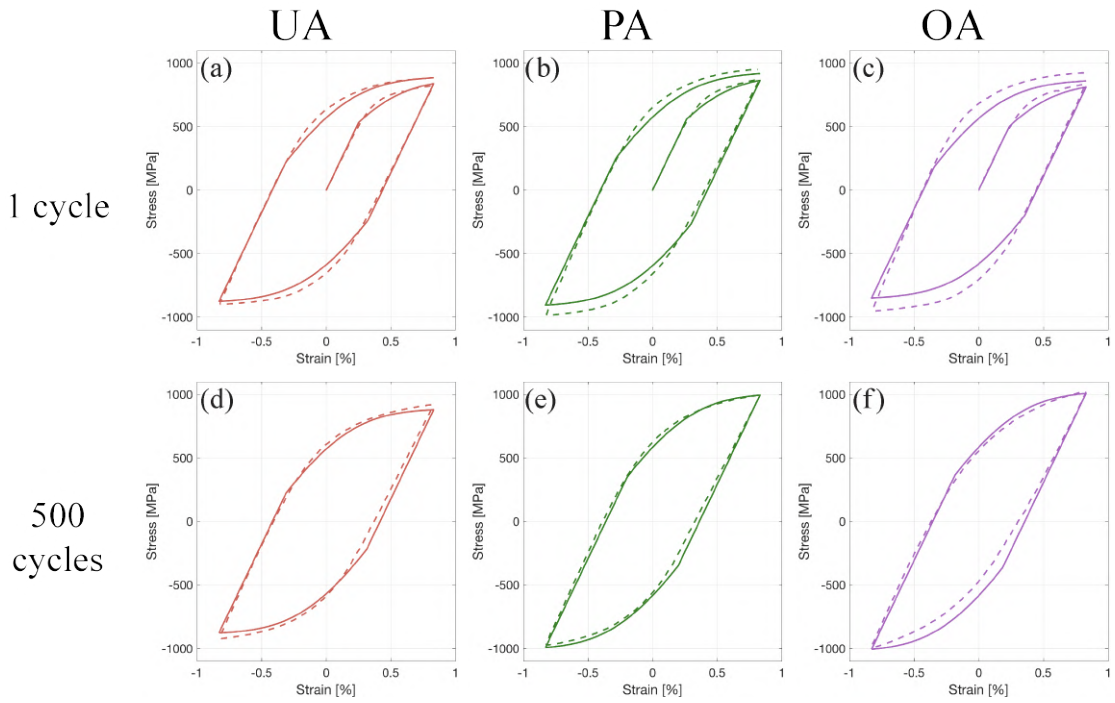

Fig. 4.15 - Experimental (dashed lines) and simulated (solid lines) stress-strain hysteresis curves of samples UA, PA and OA for cycles (a-c) 1 and (d-f) 500.

followed to select the values used, with the exception of f_{SB0} and a, for which no information exists. For convenience, these are chosen to match the values in alloy 718Plus.

Figure 4.16(a) shows the curves for the evolution of the stress amplitude in materials with different ageing times. Note that the horizontal scale is logarithmic as these tests ran until failure for close to 10000 cycles. These are also carried out at a lower strain amplitude of 0.57%. The behaviours seen are similar to those described before; a crossover between the peak-aged and overaged conditions appears again and is also reproduced in the simulations. Unlike for 718Plus, the same volume fraction of slip bands is used for all alloys, so this behaviour is purely due to the slower softening rate for larger precipitates.

Low cycle fatigue tests with different total strain amplitudes are shown in Figure 4.16(b) for the peak-aged condition, with simulation results that resemble the experimental curves. Another feature of the hardening model is showcased here. The macroscopic plastic strains these samples experience from the first cycle are different, those resulting in more slip bands being developed for higher amplitudes. Even though the local dislocation densities saturate at the same value for all tests, isotropic hardening does not. This agrees with classical work hardening theory, as a higher f_{SB} implies that mobile dislocations will run into more forest dislocations. The trends followed by the maximum stress are fully reproduced,

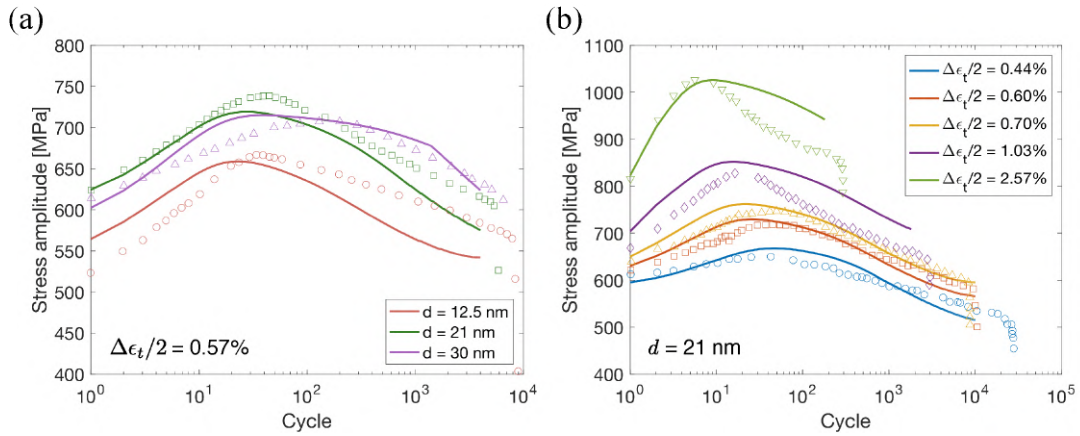

Fig. 4.16 - Experimental (markers) and simulated (solid lines) evolution of the cyclic stress amplitude of alloy Nimonic PE16 for (a) different precipitate sizes [152] and (b) strain amplitudes [116].

shifting towards larger stresses and lower number of cycles for higher strain amplitudes. This behaviour has been observed in other nickel-based superalloys [97, 104, 151].

4.4.5 Final remarks

The model is able to reproduce trends of the macroscopic stress-strain response. Yet, its most important feature is accounting for the evolution of the dislocation structure and microstructure evolution by employing phenomenological and physics-based equations. While fitting of some parameters is needed to match simulations with experiments, there is a physical meaning to every variable in the isotropic hardening and precipitate shearing models. This allows for a direct comparison between ageing conditions of the effect of parameters such as precipitate size and heterogeneity of slip.

While there are a number of fitting parameters in the model, many of these are borrowed from existing models (*e.g.* W, c_1, c_2, k_1, k_2). Other physical descriptions have been developed for these phenomena elsewhere, but they include even more fitting parameters. Not being the primary scope of the current work, these are not further detailed. Alternatively, the slip localisation and precipitate shearing parts of the model rely only on one (f_{SB0}) and two (a and p) fitting parameters, respectively, all of which detailed more in depth.

A discussion needs to be had regarding the effect of precipitate shearing on the cyclic softening behaviour. While this is held in this model as the only mechanism responsible, it is evident that other phenomena have an influence too. This is clear from the results of the S sample and others from the literature [105, 115, 133, 142]. With the characterisation performed in RR1000 and 718Plus, the most reasonable explanation for this is the evolution

of the dislocation structure. Slip bands may develop during the initial cycles. Whilst this is partially captured with the saturation of the dislocation density in the isotropic hardening, a subsequent relaxation process towards a more stable dislocation substructure within the slip bands is plausible. What generates this behaviour remains an open question.

On the other hand, it is also clear that precipitate size has an important effect on the cyclic softening process in multiple alloys. The model of gradual reduction in the effective precipitate cross section gives the expected behaviour, with a softening rate that gradually slows down. The saturation of this process after many cycles is modelled here based on the recombination of sheared precipitates. Due to the periodicity of the shearing process, there is always a remaining antiphase boundary contribution $\overline{A_{APB,sat}}$ [117, 165]. This saturation limit of the softening process can be expressed as

$$\overline{A_{APB,sat}} = \lim_{z\to\infty} \sum_{A_{APB}=0}^{\pi d^2/4} A_{APB}\, P(A_{APB}) = \frac{1}{L}\int_0^L A_{APB}\, ds_{eff} = \frac{2}{3}\frac{d^3}{L}, \tag{4.25}$$

which in terms of the γ' volume fraction becomes

$$\overline{A_{APB,sat}} = \left(\frac{2f}{3\pi}\right)^{1/2} d^2. \tag{4.26}$$

These results arise from a geometric analysis by considering the periodicity of the A_{APB} function. If the assumption that a precipitate half will travel in the direction of its nearest neighbour is false, *i.e.* $L_{eff} > L$, then the initial softening rate will remain the same but the saturation stress will decrease. It suffices to substitute L with a corresponding mean distance L_{eff} in equations (4.21) and (4.25) to produce this change.

This saturation variable $\overline{A_{APB,sat}}$ might have a connection with the precipitate dissolution observed in the UA sample near a crack. If precipitates within a slip band are sheared excessively so that the remaining particles are very small, nucleation theory dictates that dissolution may become energetically favourable. It does not make sense talking about a critical radius as the shape of the sheared precipitate segments are not spherical, but a balance between their area and volume should determine the condition for this process to begin. A similar plastic strain induced phase transition was observed and modelled by Brechet *et al.* in a Al-Li alloy. The energetics for dissolution due to chemistry are left beyond the scope of the current study, but equation (4.26) constitutes a prediction of its parametric dependence on microstructure. The formation of precipitate-free deformation bands is predicted to be considerably more dependent on γ' size than volume fraction, explaining their appearance only for the UA condition. Additional dislocation behaviours that may promote precipitate

dissolution are a reduction of slip line spacing at high strains and γ' shearing on multiple non-parallel slip planes.

The mesoscopic model is used here to predict the behaviour of a polycrystal, but similar ideas can be adapted at other length scales. Crystal plasticity could offer a more complete description of the distribution of slip bands within individual grains accounting for crystal orientation effects. A more accurate description for the softening behaviour can also be added to dislocation dynamics frameworks to further investigate the process of slip localisation during low cycle fatigue.

Of particular importance is the incorporation of the ideas on the evolution of the microstructure to the description of fatigue damage. An empirical parameter for the prediction of crack initiation is the cumulative plastic strain [222–224], which is also related to precipitate shearing. While this might not be directly responsible for crack nucleation, the process can be thought of as a feedback loop. Slip localisation produces local softening, which further promotes slip along the sheared planes. This is also associated with the formation of extrusion and intrusions that precede crack nucleation [91, 107, 198, 225]. The high stresses ahead of the crack tip induce high plastic strains that locally soften the material even more and promote more slip localisation. Damage accumulation takes place over multiple cycles along severely damaged slip bands, resulting in crack nucleation and short crack propagation.

4.5 Conclusions

Scanning electron microscopy characterisation in alloy 718Plus and a newly developed physics-based mesoscopic model of cyclic deformation are used here to investigate the cyclic hardening and cyclic softening behaviours of nickel-based superalloys during low cycle fatigue. Whilst fitting in the model is used to approximate the shape of the hysteresis curves and cyclic stress evolution, this is kept to a minimum by using the same values of Kocks-Mecking and kinematic hardening parameters for samples with different ageing conditions. This reduces the predictive power of the model but offers in return better insights into the effects of slip localisation and precipitate degradation on the stress response of the material.

The main findings of this study are:

- The presence of shearable precipitates increases the degree of localisation of plastic deformation, but slip bands spread more homogeneously across the grains for larger particles. This, together with the higher number of dislocations required to shear a precipitate, are deemed responsible for the slower softening rates observed in overaged samples.

- A composite model for isotropic hardening based on slip localisation within slip bands is able to link the plastic strain heterogenisation at the grain length scale and the stress saturation variation as a function of strain amplitude at the macroscopic level.
- A physics-based description of the cyclic softening behaviour developed as an extension of classical precipitate hardening theory is able to reproduce the effects of precipitate size and volume fraction.
- Higher degrees of plastic deformation are observed near surface cracks, with evidence of increased local precipitate degradation. This results in the formation of precipitate-free deformation bands for the underaged condition. The presence of these features is linked here to the saturation limit of the sheared precipitate cross sectional area from geometric principles.

Chapter 5

Stress orientation analysis framework

5.1 Introduction

Historically, little attention has been paid to the effect of non-Schmid stresses on various dislocation mechanisms in fcc crystals. While the Schmid stress dictates for the most part the glide behaviour of a dislocation, it has been shown across different length scales that the Escaig stress (also referred to as co-slip stress) plays a crucial role in phenomena such as homogeneous and heterogeneous dislocation nucleation [226, 227], dislocation drag [228], stacking fault propagation [229] and cross slip [196]. Because of how different these mechanisms are, this stress has been analysed using different arbitrary nomenclatures and coordinate systems, which makes it difficult to transfer the acquired knowledge across different areas of study. The incorporation of non-Schmid stresses into a more comprehensive framework is then required to understand the orientation dependence of plastic deformation as a whole.

The Escaig stress is that component resolved on the slip plane of a given dislocation but in the direction perpendicular to its Burgers vector [30], such that it exerts no force on it. However, for a dissociated $\frac{a}{2}\langle 110\rangle\{111\}$ dislocation, the Escaig stress pushes both Shockley partials with the same force but in opposite directions, thus expanding or contracting the intrinsic stacking fault width. Its effect on the separation between the partials is small in materials with a high stacking fault energy for shear stresses below 500 MPa [230]. Considering that most fcc engineering alloys used during the first half of the 20th century fall into this category, it is understandable why the Escaig stress was ignored in most early metallurgical studies. On the other hand, the Escaig stress has a big influence on low stacking fault energy materials, such as austenitic stainless steels, nickel-based superalloys and advanced TWIP and TRIP steels, and formation of extended stacking faults is promoted

with stresses as low as 250 MPa. Thus, it is necessary to account for its effect in any stress activated mechanism that is affected by a change in the stacking fault width.

Previous research in this area includes the derivation of models to describe the behaviour of a single dissociated dislocation under applied Schmid and Escaig stresses, accounting for stacking fault constrictions [231], effects of dislocation character [229], friction stresses [230], cross slip activation energies [30, 196, 197, 232] and effects of a stress field generated by nearby dislocations [233], among others. The techniques used in these models include mostly molecular dynamics and line tension approximations performed at a microscopic length scale on individual slip systems. A systematic way of translating the results of these studies into orientation dependent macroscopic effects on the plastic deformation is missing. The current work addresses this issue by introducing a new intuitive orientation analysis framework with a graphical representation for the stress states of the individual slip planes.

The initial motivation to develop this study was born from the orientation analysis performed in Chapter 3. Looking at Figure 3.12, the highest Schmid factor of the three grains encountered with homogeneous distributions of slip are lower than the rest. This is counterintuitive, as less plastic deformation would be expected to occur in these grains. Upon stumbling upon the concept of Escaig stress, an analogous plot of the slip band width as a function of the Escaig factor (further described in this chapter) came as a natural idea to complement the analysis. This is shown in Figure 5.1. The dislocations in the aforementioned grains have in reality a high shear stress but directed perpendicular to their Burgers vector. Whilst a full analysis of this phenomenon has been left for future work (more on this in Chapter 7), this sparked the curiosity that led to the development of the orientation framework introduced in this chapter.

5.2 Stress orientation framework

Following the setup adopted by Baudouin *et al.* [230], consider an orthonormal right-handed coordinate system oriented with respect to a $\frac{a}{2}\langle 110\rangle\{111\}$ dislocation so that the x-axis coincides with its Burgers vector and the z-axis is perpendicular to its slip plane. The angle θ between the Burgers vector $\overline{b} = [b,0,0]$ and the line vector $\overline{l} = [l\cos\theta, l\sin\theta, 0]$ dictates the character of the dislocation, ranging from 0° (screw segment) to 90° (edge segment). If the dislocation dissociates into Shockley partials, their Burgers vectors will point at angles of $\pm 30^\circ$ from $\overline{b}$. For such a dissociated dislocation viewed from outside Thompson's tetrahedron, an intrinsic stacking fault is achieved by placing the partials in a specific order [22, 23], in this case given by $\overline{b_1} = \left[\frac{b}{2}, \frac{-b}{2\sqrt{3}}, 0\right]$ and $\overline{b_2} = \left[\frac{b}{2}, \frac{b}{2\sqrt{3}}, 0\right]$, where

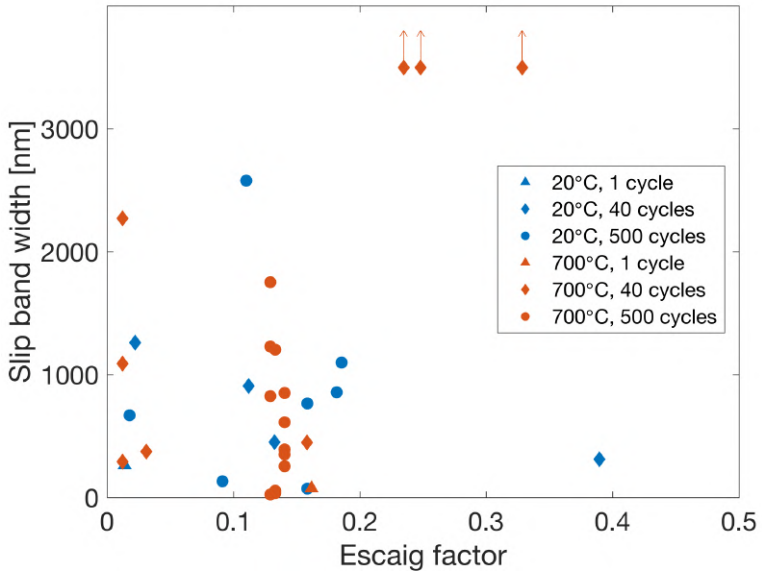

Fig. 5.1 - Slip band width as a function of the Escaig factor. The marks with arrows pointing upwards represent the three grains that showed homogeneous deformation.

the subindices $_1$ and $_2$ refer to the leading and trailing partials, respectively. Figure 5.2 shows the arrangement proposed for such a dislocation and its Shockley partials.

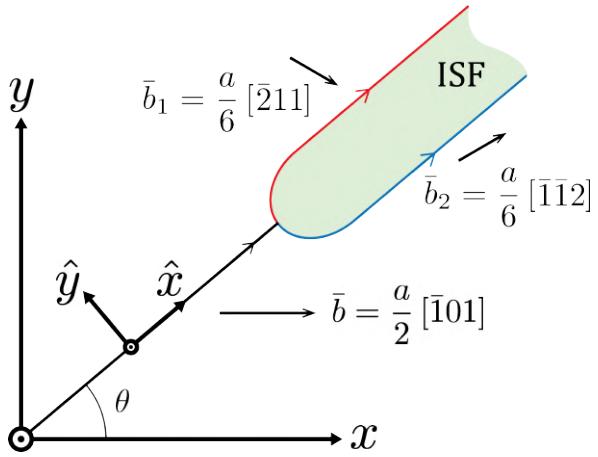

Fig. 5.2 - Coordinate systems for a perfect dislocation, its Shockley partials and the intrinsic stacking fault in-between. The arrows along the dislocations represent the line vectors.

If we consider a homogeneous applied stress field within this coordinate system with the general form

$$\overline{\overline{\sigma}} = \begin{bmatrix} \sigma_{xx} & \tau_{xy} & \tau_{xz} \\ \tau_{xy} & \sigma_{yy} & \tau_{yz} \\ \tau_{xz} & \tau_{yz} & \sigma_{zz} \end{bmatrix}, \tag{5.1}$$

then glide of the perfect dislocation depends only on the magnitude of the Schmid stress $\tau_S = \tau_{xz}$, and occurs in the $\hat{y}$ direction (if it is positive). The Peach-Koehler equation from linear isotropic elasticity theory predicts a force on the dislocation $\overline{F_{PK}} = (\overline{\overline{\sigma}} \cdot \overline{b}) \times \overline{l}$ with magnitude $F_{PK} = b\tau_S$ and direction perpendicular to $\overline{l}$. In this scenario, none of the other stress components affect the evolution of the dislocation. However, if we consider a dissociated dislocation, then τ_{yz} will exert forces with the same magnitude but opposite direction on both partials. The resulting forces in this case are

$$F_{PK1} = \frac{b}{2}\tau_S - \frac{b}{2\sqrt{3}}\tau_E \tag{5.2a}$$

$$F_{PK2} = \frac{b}{2}\tau_S + \frac{b}{2\sqrt{3}}\tau_E \tag{5.2b}$$

where $\tau_E = \tau_{yz}$ is the Escaig stress. Note that the sum of both forces adds up to the force felt by the perfect dislocation, *i.e.* $F_{PK1} + F_{PK2} = F_{PK}$. This means that even when the dislocation is dissociated, in many cases it can still be analysed as a perfect dislocation as the second terms in equations (5.2a) and (5.2b) cancel out.

The importance of the Escaig stress comes into play when analysing its effect on the stacking fault width. Consider an infinitely long straight dislocation dissociated into partials in a frictionless and otherwise perfect fcc crystal. Other than the Peach-Koehler forces, the partials will also experience attraction due to the stacking fault binding them together and repulsion due to the interaction force between them. The total forces per unit length felt by the partials in the direction $\hat{y}$ perpendicular to their line vectors are

$$F_1 = F_{PK1} + F_{int} - \gamma_{ISF} \tag{5.3a}$$

$$F_2 = F_{PK2} - F_{int} + \gamma_{ISF} \tag{5.3b}$$

where $F_{int} = A_s/d$ is the interaction force [230],

$$A_s = \frac{2 - \nu - 2\nu\cos 2\theta}{8\pi(1-\nu)}\mu b_p^2, \tag{5.4}$$

d is the intrinsic stacking fault width (unlike in Chapters 3 and 4 where it referred to precipitate diameters), μ the shear modulus, $b_p = b/\sqrt{3}$ the Burgers vector of a partial dislocation, ν the Poisson's ratio and γ_{ISF} the intrinsic stacking fault energy. If there is no stress applied, a stable separation distance between the partials $d_0 = A_s/\gamma_{ISF}$ is predicted.

If the stress applied is non-zero, the force balance $F_1 = F_2$ gives a new stable stacking fault width [230]

$$d_E = \frac{A_s}{\gamma_{ISF} + \frac{b}{2\sqrt{3}}\tau_E}. \tag{5.5}$$

This indicates that a positive Escaig stress will reduce the separation between the partials. Furthermore, the stacking fault width will extend to infinity whenever $\tau_E \leq -\frac{2\sqrt{(3)}}{b}\gamma_{ISF}$. Note that in the literature the Escaig stress is often defined in the opposite way (so that a positive τ_E increases d), but the orientation chosen in this work matches that of the more widely used Thompson's notation.

Following a very similar analysis, Byun [229] reported that the stacking fault width will never vary for an edge dislocation, although he made a crucial mistake by completely ignoring any stress contribution in the direction of the line vector. Even though equation 5.5 was published half a decade ago [230], Byun's character dependence is still widely and incorrectly used as an assumption in stacking fault and twinning analyses [55, 66]. In reality, linear isotropic elasticity predicts the stacking fault width of an edge segment to be larger than that of a screw by a factor of $(2+\nu)/(2-3\nu)$ (~ 2.09 for a typical value of $\nu = 0.3$) and the complete decorrelation of the partials to occur at the same stress for any dislocation character.

5.3 Orientation maps

For the next part of the analysis consider a plot of τ_S vs. τ_E in which the stress state of all the $\frac{a}{2}\langle 110\rangle\{111\}$ slip systems are included, hereby denoted stress orientation maps. Due to the high symmetry of the fcc unit cell, there are two geometric constraints regarding the coordinates of the twelve points, regardless of the stress tensor. Firstly, the three slip systems of each $\{111\}$ plane fall within a circle of radius $\tau = ||\overline{\overline{\sigma}}\,\overline{n}||$ centred at the origin, where $\overline{n}$ is the unit vector normal to the slip plane. Secondly, the points in each circle are spaced 120° apart just like the three coplanar Burgers vectors. Figure 5.3(a) shows some of these maps for the case of uniaxial tensile loading considering both the Schmid factor m_S and an analogous Escaig factor $m_E = \tau_E/\sigma_0$, where σ_0 is the applied tensile stress. Note that in some plots, as those for the vertices of the inverse pole figure, two or more points share the same coordinates. It must be emphasised that these maps are not stereographic projections of any kind, but just a geometric representation of the stress in all the slip planes combined.

Consider two dissociated dislocations with stress states situated at points (τ_S, τ_E) and $(-\tau_S, \tau_E)$, as those in Figure 5.4. A negative Schmid stress reverts the direction of motion of a dislocation and swaps the leading with the trailing partial, but leaves the stacking fault

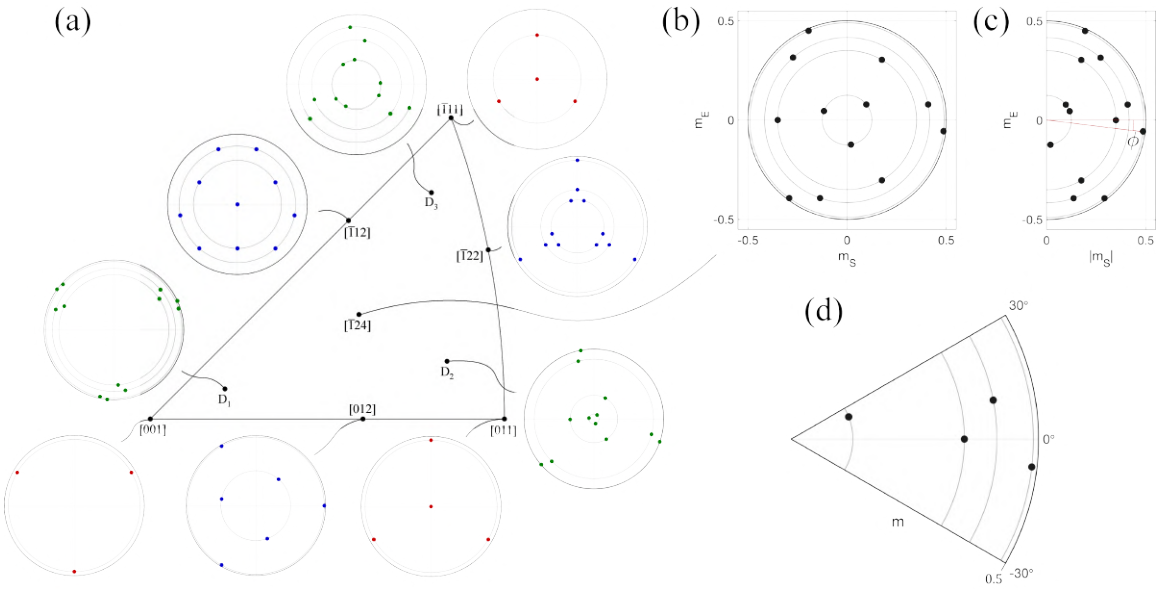

Fig. 5.3 - (a) Fundamental sector of an fcc unit cell with maps of the Schmid and Escaig factors of the 12 $\frac{a}{2}\langle 110\rangle\{111\}$ slip systems for multiple orientations of uniaxial tensile loading. The maps correspond to orientations at the vertices (red), at the edges (blue) and at points situated 10° away from the vertices (green). The four grey circles in each map, one for every slip plane, contain their respective three slip directions. To facilitate visualisation, the gridlines cross each other at (0,0) and the black circles have a radius of 0.5. (b) The map for orientation $[\bar{1}24]$ is plotted separately for reference, together with its corresponding (c) $|m_S|$ half map and (d) reduced map over the domain of ϕ.

width unchanged. Thus, a map with the absolute value $|m_S|$ is sufficient to represent the behaviour of the 12 slip systems, as shown in Figures 5.3(b) and (c). Furthermore, if no distinction is made between the direction of the Burgers vectors and the 24 slip systems are considered, mapping into such a half map makes the stress states of every pair of parallel slip directions collapse into one single point, as long as the right handedness of the coordinate system is preserved.

Compare now the first stress state proposed with that which arises upon loading reversal *i.e.* $(-\tau_S, -\tau_E)$, from Figure 5.4. In this case, both the direction of motion of the dislocation and the effect of the Escaig stress on the stacking fault width are reverted. This effect most likely has an effect during cyclic loading, as it implies that partials will glide with a different separation during, for instance, tensile and compressive stages, being more likely to cross slip in one of them. Graphically, a stress reversal results in a point inversion around the origin. Thus, it can immediately be seen that the deformation behaviour of crystals loaded in tension along a $\{011\}$ or $\{111\}$ direction will resemble that of one compressed along a $\{001\}$ axis. These orientation effects on the stacking fault width during cyclic loading may

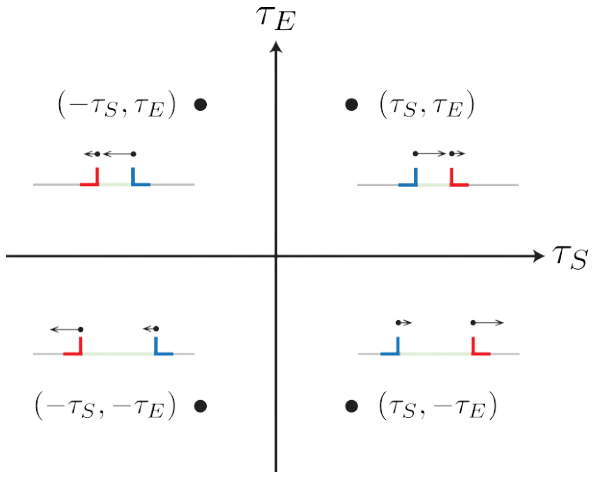

Fig. 5.4 - Schematic diagram of the forces felt by the partial dislocations under four different stress states: (τ_S, τ_E), $(-\tau_S, \tau_E)$, $(\tau_S, -\tau_E)$ and $(-\tau_S, -\tau_E)$. The leading and trailing partials in each case are coloured in red and blue, respectively, and the arrows represent the direction and magnitude of the individual forces.

explain the homogeneous plastic deformation behaviour observed in the three RR1000 grains discussed in Figure 5.1. Whilst a lower Schmid factor would be expected to induce less plasticity due to lower shearing rates, a higher magnitude of the Escaig factor may facilitate cross slip, enabling the formation of slip lines on additional planes. This is currently only a potential explanation of the observed phenomenon and effects of strain compatibility due to the polycrystalline nature of the sample must also be considered. Ideas on how to tackle this investigation are further detailed in Chapter 7.

Another advantage of these maps is that they allow for a quick inspection of the stress state in each partial, a description preferred by some authors [54, 55]. The Burgers vectors of the leading and trailing partials were initially chosen to point at -30° and 30° from the x-axis, and these constraints are preserved in the stress plots. The Schmid factors of the partials that compose each perfect dislocation, m_{S1} and m_{S2}, are then the projections onto axes that point at these angles. Note that the lines joining the point with the highest Schmid factor and the two coplanar slip directions have in the orientation map slopes of $\pm\sqrt{3}$, as they share the same partials. Similarly, the polar coordinates (with radius m and angle φ) for each slip system can be easily observed. This description is also widely used in the literature [56, 57, 234]. Table 5.1 contains the conversion formulae between the variables from different nomenclatures.

Overall, the stress state of a given slip plane can be defined by an angle ϕ from the τ_S axis to a line going from the origin to the point with the highest Schmid factor in a map such as that in Figure 5.3(c). Due to symmetry and the constraints previously described, ϕ can

Table 5.1 - Conversion formulae between variables used in different descriptions of the stress state of a dislocation.

	$(m_S\ ,\ m_E)$	$(m\ ,\ \varphi)$	$(m_{S1}\ ,\ m_{S2})$
$(m_S\ ,\ m_E)$	-	$m = \sqrt{m_S^2 + m_E^2}$ $\varphi = \arctan\left(\frac{m_E}{m_S}\right)$	$m_{S1} = \frac{1}{2}(\sqrt{3}m_S - m_E)$ $m_{S2} = \frac{1}{2}(\sqrt{3}m_S + m_E)$
$(m\ ,\ \varphi)$	$m_S = m\cos(\varphi)$ $m_E = m\sin(\varphi)$	-	$m_{S1} = m\cos(\varphi + 30^\circ)$ $m_{S2} = m\cos(\varphi - 30^\circ)$
$(m_{S1}\ ,\ m_{S2})$	$m_S = \frac{1}{\sqrt{3}}(m_{S1} + m_{S2})$ $m_E = -m_{S1} + m_{S2}$	$m = \frac{2}{\sqrt{3}}\sqrt{m_{S1}^2 - m_{S1}m_{S2} + m_{S2}^2}$ $\varphi = \arctan\left(\frac{\sqrt{3}(-m_{S1}+m_{S2})}{m_{S1}+m_{S2}}\right)$	-

only vary between -30° and 30°. An orientation map restricted to this domain will contain only one point per slip plane, as seen in Figure 5.3(d). This sort of plot simultaneously captures the stress state of every $\frac{a}{2}\langle 110\rangle\{111\}$ and $\frac{a}{6}\langle 112\rangle\{111\}$ slip system in a unique and unambiguous manner. Regions for the appearance of plasticity mechanisms with an orientation dependence may then be drawn within this domain. The regions for angles higher than 30° and lower than -30° will also contain only one stress state each, but the use of the domain given by ϕ is deemed more intuitive.

Physically, an angle $\phi = -30^\circ$, giving the hereby called Λ-configuration, favours glide of the same leading partial in two coplanar slip systems and appears during tensile loading along an orientation on the line from $\langle 011\rangle$ to $\langle \bar{1}11\rangle$ or upon $\langle 001\rangle$ compression. Upon reversing the loading direction, a Y-configuration with $\phi = 30^\circ$ results in a higher Schmid factor for the trailing partial.

Figure 5.5(a) shows the value of the angle ϕ for the slip plane with the highest Schmid factor for all possible uniaxial tensile loading orientations. A clear transition can be seen when moving away from a $\langle 001\rangle$ axis, from promoting glide on the trailing partial to the leading one. This transitions occurs as the stress state in the slip plane rotates between two consecutive $\langle 112\rangle$ directions because of the specific routes the atoms must take in order to generate an intrinsic stacking fault, illustrated in Figure 5.5(b). The fundamental difference between the two types of $\langle 112\rangle$ directions in an fcc crystal must be incorporated into any type of mechanistic modelling driven by Shockley partials, which is often ignored [20, 43]. This description can also be extended to the four slip planes; the corresponding m_i values and ϕ_i angles $(i = 1,2,3,4)$ are plotted in Figure 5.6.

Angle ϕ is then a more intuitive parameter than others found in the literature. It can be used together with the orientation maps to determine the effects of orientation on both the microscopic dislocation behaviour and the macroscopic deformation response.

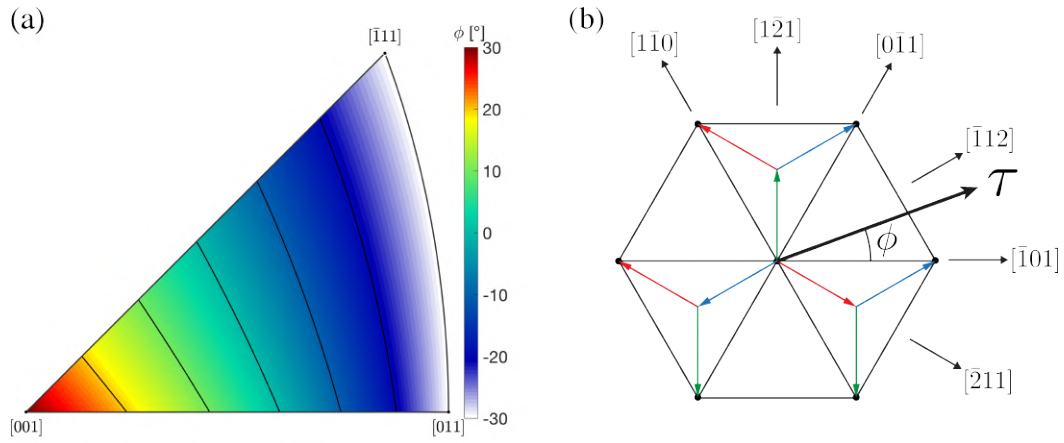

Fig. 5.5 - (a) Inverse pole figure showing the value of the angle ϕ of the slip plane with the highest shear stress. (b) Schematic diagram of the atomic configuration on the (111) plane, where the atoms would sit on the corners of the triangles. The coloured arrows show the routes an atom in the middle point can take to get to the 6 neighbouring positions, generating an intrinsic stacking fault after being swiped by the leading partial. ϕ is in this context the angle between the shear stress in this plane and the slip direction closest to that orientation.

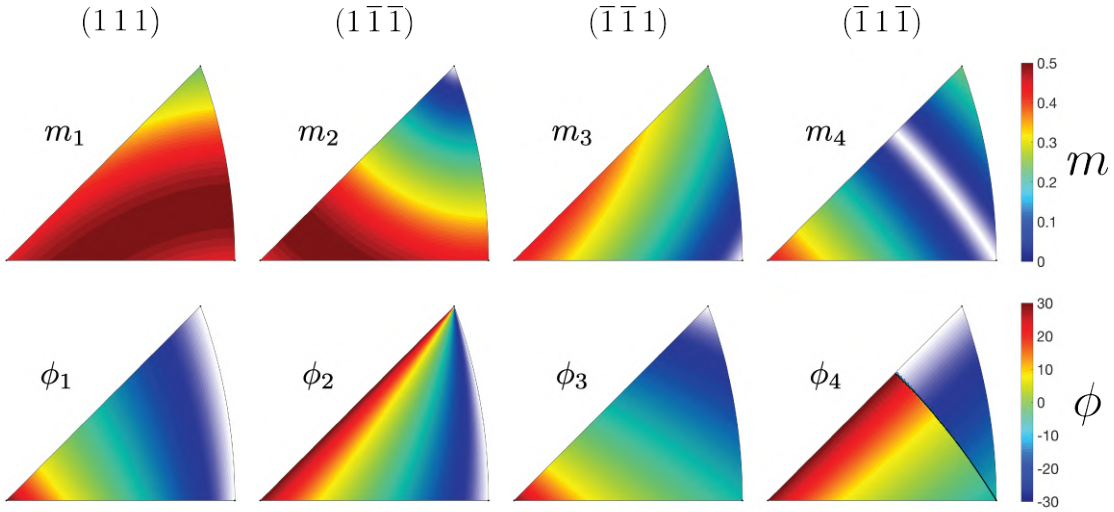

Fig. 5.6 - m_i values and ϕ_i angles of the four slip planes $(i = 1,2,3,4)$ for all the orientations of uniaxial tensile loading.

5.4 Deformation twinning

From the results by Gutierrez-Urrutia and Raabe [63, 64] it can be seen that the planarity of slip decreases monotonically with ϕ within the domain of this parameter as a consequence of two reasons: planar fault propagation and probability of cross slip. Stacking faults and

twins are promoted for lower angles. Simultaneously, perfect dislocations will cross slip more easily for higher angles due to the reduced stacking fault width.

Twinning in fcc alloys has been reported extensively in materials with a low stacking fault energy. This deformation mechanism accommodates plastic deformation by glide of leading partials with an identical Burgers vector on adjacent $\{111\}$ planes. The intrinsic character of a stacking fault becomes extrinsic when two adjacent planes have been sheared by these dislocations, and upon further twinning the stacking sequence reverts from ABCABC to ACBACB, forming again an fcc structure in between two twin boundaries.

A clear orientation dependence has been observed both in single crystals and in individual grains in polycrystals. Uniaxial loading tests have shown that twinning is promoted close to a $\langle 011 \rangle$ or $\langle 111 \rangle$ orientation during tension [54, 59, 63–65, 235–237] and $\langle 001 \rangle$ during compression [59–61], *i.e.* for orientations with a low value of ϕ on the octahedral slip plane with the highest resolved shear stress. Note that Figure 5.5(a) is effectively the same as that in reference [62], where it is argued that the ratio $\frac{m_S}{m_{S1}}$ is highly correlated to the likelihood of mechanical twins to develop. With the conversion formulae previously described, this is effectively $\frac{m_S}{m_{S1}} = \frac{2}{\sqrt{3}-\tan\phi}$. The use of angle ϕ then enables a better understanding of the orientation effects in each slip plane. A similar criterion is used by Cai *et al.* [61], although their ratio combines Schmid factors from slip planes in different slip systems.

This explains the propagation of twins for these orientations, but it remains unclear how they form in the first place. A realistic twin nucleation mechanism must account for the generation of identical Shockley partials on adjacent planes and for the immobilisation of the trailing partials. A number of twin nucleation mechanisms proposed have recently been summarised by De Cooman *et al.* [66]. Two of these are analysed in this section under the light of the orientation framework introduced.

The Copley-Kear-Byun partial dislocation breakaway mechanism [229, 238] has been proposed on the sole basis of stacking fault widening as a result of the stress applied. This can be thought of as generating an infinitely long stacking fault from equation (5.5) with a large negative Escaig stress. Upon narrowing down the orientation domain to that of angle ϕ, such a boundary is reflected along the -30° axis. As shown in Figure 5.7, this twin nucleation mechanism is more likely to appear for Y-configurations, as a slip system located at an angle $\varphi = -90°$ produces the largest separation of the partials for any given resolved shear stress. As mentioned before, twinning has experimentally been observed for the opposite configuration, deeming this twinning nucleation mechanism unrealistic.

Another twin nucleation mechanism that avoids introducing more complicated dislocation reactions is that proposed by Li *et al.* [239], where the required partials are emitted from a dislocation source or a grain boundary [240]. Initially, it is assumed that a leading partial is

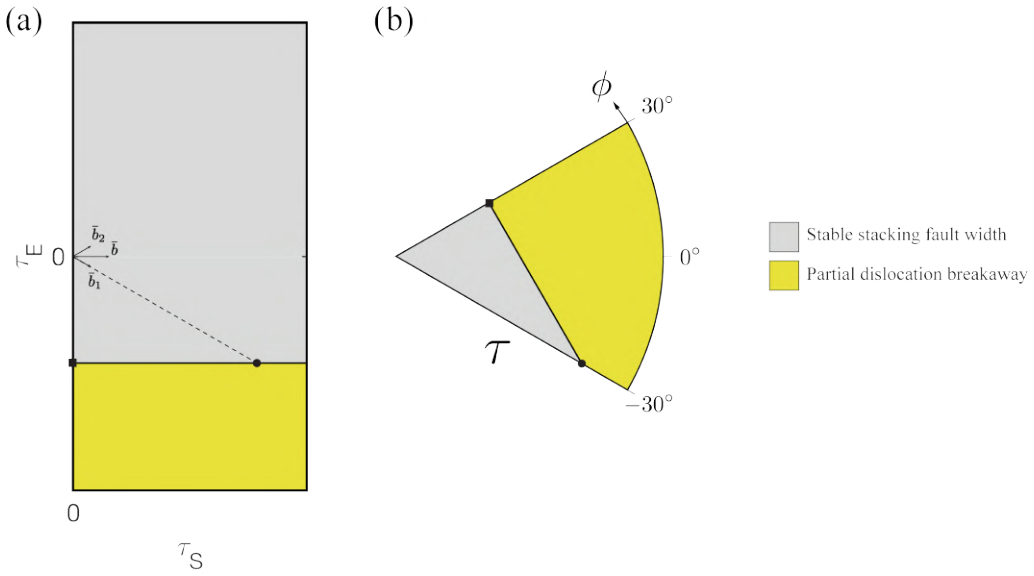

Fig. 5.7 - Orientation dependence of the Copley-Kear-Byun partial dislocation breakaway mechanism [229, 238] for the extension of a stacking fault as a twin nucleus. (a) Schematic plot with aspect ratio 1:1 of the stress orientations where each regime would appear and (b) reduced map within the domain of ϕ. Two points are marked before and after reflecting the boundary along the -30° axis for reference.

emitted and it glides away from such boundary. This is then followed by one of two options: (i) the emission of a trailing partial on the same slip plane, or (ii) the emission of another identical leading partial (denoted twinning partial) on an adjacent plane. The former results in perfect dislocation glide, whereas the latter forms an extrinsic stacking fault and later a twin if the process is repeated on adjacent planes.

The initial model did not incorporate the interaction forces between both dislocations [239]. However, a more recent implementation by McCabe *et al.* [240] arrived at the conclusion that these take the same value in both scenarios regardless of the Burgers vector of the second partial nucleated. This contradicts the results from the linear isotropic elasticity theory, and is in reality a mistake which arises from the way in which they derive the repulsion force by forcing the leading partial to be stationary when the second partial nucleates; this has been incorporated into more models [20] and thus needs to be verified.

Ignoring the image stresses due to the grain boundary, the condition $\mathrm{C1_t}$ for nucleation of a leading partial $F_1 > 0$ reads

$$\mathrm{C1_t}: \tau_E < \sqrt{3}\tau_S - \frac{2\sqrt{3}}{b}\gamma_{ISF} \tag{5.6}$$

and is analogous to C2. Accounting for the corresponding interactions between the dislocations, the forces on the trailing partials are

$$F_{2s} = F_{PK2} - \frac{A_s}{d_s} + \gamma_{ISF} \tag{5.7}$$

for perfect dislocation glide and

$$F_{2t} = F_{PK1} - \frac{A_t}{d_t} + (\gamma_{ISF} - \gamma_{ESF}) \tag{5.8}$$

for twinning nucleation, where γ_{ESF} is the extrinsic stacking fault energy, A_t/x is the interaction force between two parallel dislocations separated by a distance x on the same slip plane and with the same Burgers vector,

$$A_t = \frac{4 - 2\nu - 2\nu\sin(\pi/6 + 2\theta)}{8\pi(1-\nu)}\mu b_p^2 \tag{5.9}$$

and d_s and d_t are the intrinsic stacking fault widths at the moment of nucleation of the trailing partial and the twinning partial, respectively. Twinning nucleation via this mechanism will be promoted when $d_t < d_s$, which can be found by individually solving equations (5.7) and (5.8) with $F_{2s} = 0$ and $F_{2t} = 0$, resulting in

$$\mathrm{C2_t}: \ \tau_E < -\frac{\sqrt{3}(A_t - A_s)}{A_t + A_s}\tau_S - \frac{2\sqrt{3}(A_t\gamma_{ISF} - A_s(\gamma_{ISF} - \gamma_{ESF}))}{b(A_t + A_s)}. \tag{5.10}$$

These conditions are schematically plotted in a full map and in the domain of ϕ in Figures 5.8(a) and (b), respectively. These delimit the region where twin nucleation is to be expected. Similar to the Copley-Kear-Byun breakaway mechanism, Li's criterion for the nucleation of a twinning partial appears in the lower part of a τ_S vs. τ_E plot. Again, this would be more likely to occur for Y-configurations regardless of the angle of the twinning condition, which contradicts experimental evidence.

Twin nucleation via both mechanisms discussed here is not supported by this orientation analysis. This conclusion arises naturally from performing a simultaneous analysis on the stress states of the three slip systems that belong to the primary slip plane. All previous studies of this kind focused on a single slip system under specific conditions, yet this work showcases why this is not possible if a complete orientation dependence is to be obtained. A more complex dislocation mechanism that results in the formation of sessile trailing partials would appear more plausible as a twin nucleation mechanism. The use of the current framework could be extended to such mechanisms proposed in the literature.

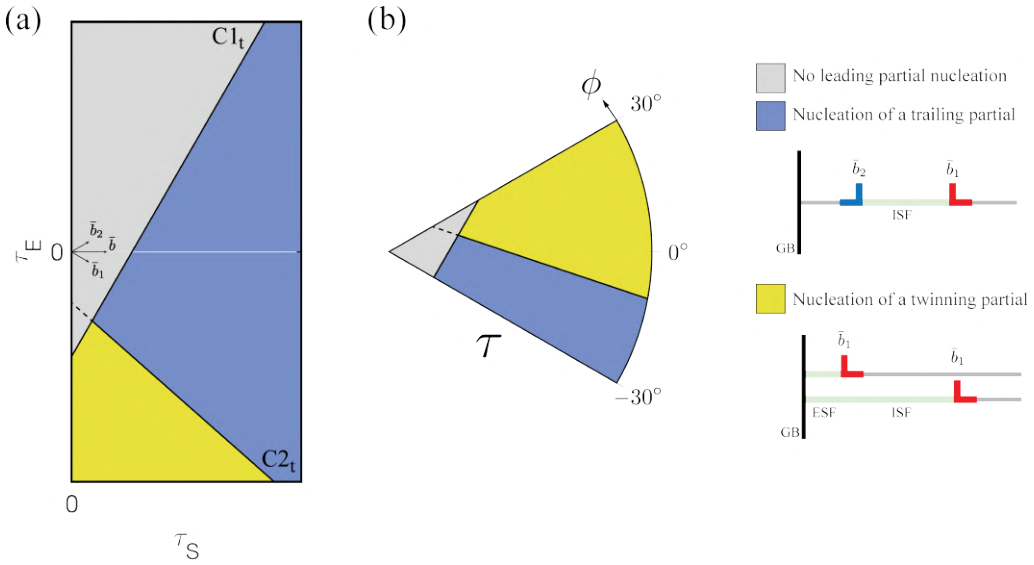

Fig. 5.8 - Orientation dependence of Li's criterion [239] for the nucleation from a grain boundary of a trailing partial bounding an intrinsic stacking fault or a twinning partial on an adjacent plane giving rise to an extrinsic stacking fault. (a) Schematic plot with aspect ratio 1:1 of the stress orientations where each regime would appear and (b) reduced map within the domain of ϕ.

5.5 Conclusions

There exists a set of geometrical constraints that links the stresses that may be attained by the $\frac{a}{2}\langle 110\rangle$ and $\frac{a}{6}\langle 112\rangle$ slip systems on a given octahedral plane in the fcc crystal structure. The orientation analysis framework built from this allows for a simple and intuitive way of studying dislocation mechanisms driven dislocations with those Burgers vectors. The main advantages it offers are:

- The orientation maps, graphical interpretations rationalised with a set of geometrical constraints that simultaneously capture the relevant shear stresses felt by all the slip systems.
- A one parameter description via angle ϕ that determines the orientation effects of the stress on a given octahedral slip plane.

Properties of the orientation maps and the physical meaning of key configurations have been explored in detail.

Such orientation analyses facilitate the scrutiny of complex deformation mechanisms. The Copley-Kear-Byun and Li's twin nucleation mechanisms were proven to contradict experimental data by linking the required shear stresses pushing the dislocations with a

macroscopic uniaxial load. It is only when accounting for the three coplanar slip systems in the most stressed slip plane that the real dependences on ϕ are obtained.

Chapter 6

Orientation dependence for the formation of stacking faults

6.1 Introduction

Stacking faults in nickel-based superalloys have many different roles. Their behaviour discussed in Chapter 3 as obstacles for dislocation glide within slip bands during low cycle fatigue is only one example. They may also hinder plasticity during monotonic loading, accommodate deformation themselves, or develop into twins when propagating on multiple adjacent planes. Nonetheless, it is not well understood how they form and evolve with temperature and deformation in materials with a complex microstructure.

To complicate things, many diverse configurations of stacking faults have been observed in nickel-based superalloys. The characteristic contrast of these defects may appear in the precipitates, the matrix or both. If one includes the superlattice faults typical at intermediate temperatures, then the number of available routes for dislocations to accommodate plastic deformation in the material becomes too large to rationalise in a simple manner. While experimental characterisations of some of these faults have elucidated the specific dislocation configurations, predictions of which types of faults will dominate for a given arbitrary condition are still impossible.

The stress orientation analysis framework introduced in Chapter 5 is used here to elaborate a comprehensive theory that includes many of these stacking fault configurations via the introduction of physical obstacles. Orientation dependent yield criteria for the propagation of intrinsic stacking faults are developed in a general way and compared to simulations from the literature. An analysis on two typical precipitate morphologies elucidates the origin of the differences in athermal stacking fault configurations. The model is then extended via

deductive reasoning to include superlattice stacking faults. Finally, mechanistic maps with a dependence on stress, orientation and microstructure are developed.

6.2 Athermal stacking fault propagation

The first instance analysed is athermal fault propagation, which in this context includes intrinsic stacking faults (ISF) in the fcc matrix and complex intrinsic stacking faults (CISF) in the $L1_2$ precipitates. Their extrinsic counterparts formed by glide of an identical Shockley partial in an adjacent plane, the extrinsic stacking fault (ESF) and complex extrinsic stacking fault (CESF), also belong to this category but are not included in this study.

Continuing the development of the orientation analysis framework from Chapter 3, consider the infinitely long dislocation in the system of coordinates introduced in Figure 5.2 under the influence of an applied stress. Even though equation (5.5) results in a stable stacking fault width, this force balance does not imply that both partials will stop moving once it is reached. This will happen if and only if $\tau_S = 0$; otherwise, the partials will continue to move with the same direction and velocity. In order for the stacking fault to reach a true stable and immobile width, *i.e.* $F_1 = F_2 = 0$, at least one more force in the form of an obstacle is required.

Additional forces opposing dislocation glide can appear in two forms: as friction forces, treated as homogeneous and continuous forces that act along every segment of the dislocation, or as an obstacle or series of obstacles that inhibit dislocation motion either when they come into contact with the dislocation or, more realistically, by introducing a stress gradient into the crystal. Friction forces have been treated to some extent in the past [230], but a deeper physical understanding is offered in this work. Besides, their use in this model is treated in a different way.

The Peierls stress is the friction or shear stress that needs to be overcome for dislocations to glide within a unit cell. However, some hardening mechanisms such as solid solution strengthening τ_{ss} (and in some instances grain boundary strengthening τ_{HP}) are also usually modelled as continuous forces that oppose dislocation movement, and thus can be added as contributions to a global drag. The friction forces per unit length on the partials F_{f1} and F_{f2} cannot be the same as those on perfect dislocations F_f. Moreover, molecular dynamics simulations suggest that the friction stress is also dependent on the dislocation character [228], meaning that the magnitude of the individual forces on the partials are not necessarily the same. Considering the glide of a dissociated dislocation with a small stacking fault width $d \sim d_0$, it can readily be seen that $F_f = F_{f1} + F_{f2}$. Even though $F_{f1} = F_{f2}$ and $F_f = F_{f1} + F_{f2}$

would be reasonable assumptions to make to attain simplicity, a better understanding of this model results from not merging these two variables into a single one.

An individual obstacle behaves in a similar way to the friction forces, with the difference that it does not act uniformly along the dislocation. This will tend to produce more dislocation bowing as glide is opposed only at certain locations. Precipitates, individual forest dislocations and twin boundaries are examples of discrete obstacles, and the conditions for a dislocation to bypass them usually depend upon their intrinsic characteristics and spatial distribution. The opposing force can appear in the form of a discontinuous barrier or as a stress gradient, *e.g.* the energetic cost of generating an antiphase boundary when shearing a coherent precipitate and the coherency stress induced by the lattice misfit of that same defect, respectively. Lastly, if these obstacles were considered at a larger length scale, they could be taken as an additional contribution to the friction forces. Think, for instance, of the resistance from cutting a non-coplanar dislocation compared to the latent hardening in a large region filled with forest dislocations of that same slip system.

Consider now the dissociated infinitely long dislocation but this time in a crystal with friction and with the leading partial pushing against an obstacle, so that a new force balance arises

$$F_{PK1} + F_{int} - \gamma_{ISF} - F_{f1} - R = 0 \tag{6.1a}$$

$$F_{PK2} - F_{int} + \gamma_{ISF} \pm F_{f2} = 0, \tag{6.1b}$$

where R is the reaction force exerted by the obstacle and the $\pm$ sign accounts for the two possible directions in which the trailing partial could move. Solving this system of equations results in a force $R = b\tau_S - F_{f1} \pm F_{f2}$ and the new range for a stable stacking fault width

$$d_\sigma = \frac{A_s}{\gamma_{ISF} + \frac{b}{2}\tau_S + \frac{b}{2\sqrt{3}}\tau_E \pm F_{f2}}. \tag{6.2}$$

This result shows how the Schmid stress can have an effect on d when considering the presence of obstacles, but unlike the Escaig stress, τ_S will only decrease its value. This result is important by itself as it implies that recombination of the partials, possibly followed by cross slip or by other dissociation reactions, becomes more probable when a dislocation is blocked.

The most favourable scenario for the decorrelation of partials is that with a stress state that promotes the formation of an infinitely long stacking fault, which will occur only when two conditions are met: (C1) that the trailing and (C2) leading partials will always have the force to surpass the obstacles in the -$\hat{y}$ and $\hat{y}$ directions, respectively. The "always" in both conditions means that they must happen even after the partials are completely decorrelated,

i.e. when $d \to \infty$ and $F_{int} = 0$. These conditions can be written as

$$\text{C1}: F_{PK2} + \gamma_{ISF} + F_{f2} \leq -R_1 \tag{6.3}$$

and

$$\text{C2}: F_{PK1} - \gamma_{ISF} - F_{f1} \geq R_1, \tag{6.4}$$

where R_1 is the critical force for the leading partial to bypass an obstacle. Note that in this way, the trailing partial behaves as the leading one but glides in the opposite direction. A closer look into these conditions shows that for $F_{f1} \leq F_{f2}$, whenever C1 holds true, then C2 does too.

If C1 is false, then the trailing partial will eventually start trying to move in the $\hat{y}$ direction until it encounters obstacles. At this point, nothing in the analysis prevents the leading partial from continuing to move. A semi-infinite stacking fault can arise if two conditions are met: (C2) that the leading partial will always have the force necessary to overcome the obstacles, and (C3) that the trailing partial will never reach the force R_2 necessary to overcome the obstacles that have previously been surpassed by the leading one, *i.e.*

$$\text{C3}: F_{PK2} + \gamma_{ISF} - F_{f2} < R_2. \tag{6.5}$$

If only C2 is false, then the leading partial will eventually become blocked and the resulting finite stacking fault will be immobile. On the other hand, if only C3 is false, then the trailing partial will at some point surpass the obstacles and the stacking fault will become mobile.

If both conditions C2 and C3 are false, then the outcome will depend on which of the two events occurs first. Adding the interaction force with its corresponding sign to both conditions and turning them into equalities makes it possible to determine the critical widths at which the stacking fault will become blocked

$$d_{blocked} = \frac{A_s}{-F_{PK1} + \gamma_{ISF} + R_1 + F_{f1}} \tag{6.6}$$

or become mobile

$$d_{mobile} = \frac{A_s}{F_{PK2} + \gamma_{ISF} - R_2 - F_{f2}}. \tag{6.7}$$

Combining them and rearranging the terms results in a new condition

$$\text{C4}: \tau_S > \frac{1}{b}\left(R_1 + R_2 + F_{f1} + F_{f2}\right) \tag{6.8}$$

for the resulting stacking fault to be mobile.

Immediately after the width d_{mobile} has been reached, the force in the leading partial will still be bigger than that in the trailing one, thus continuing to extend the stacking fault. This will stop whenever the leading partial cannot surpass the obstacles any longer ($d = d_{blocked}$) or when both dislocations feel the same force and start moving in a correlated way. This last condition will occur at a separation of

$$d_{correlated} = \frac{A_s}{\gamma_{ISF} + \frac{b}{2\sqrt{3}}\tau_E + \frac{R_1 - R_2 + F_{f1} - F_{f2}}{2}}. \tag{6.9}$$

A closer inspection shows that $d_{correlated} < d_{blocked}$ whenever condition C4 is met, meaning that the overall correlated motion of partials will happen with a stacking fault width given by equation (6.9). As expected, if $R_1 = R_2$ and $F_{f1} = F_{f2}$, then the mobile stacking fault width will be d_E. Moreover, the condition for the uncorrelated motion of partials in the $\hat{y}$ direction becomes

$$\text{C5}: \ \tau_E \leq -\frac{\sqrt{3}}{b}\left(2\gamma_{ISF} + R_1 - R_2 + F_{f1} - F_{f2}\right). \tag{6.10}$$

Finally, a condition with the form

$$\text{Cd}: \ \tau_S > \frac{1}{b}\left(R + F_f\right), \tag{6.11}$$

considering the force for obstacle surpassing by a perfect dislocation R, is similar to condition C4. However, $R_1 + R_2$ is most likely different to R for most of the obstacles due to the difference between the tensions of a partial and a perfect dislocation [241].

With this set of conditions it is possible to estimate the behaviour of the dislocation under any stress state. By rearranging all of them in the form of equations one gets a series of straight lines that subdivide a map of τ_S vs. τ_E into five main dislocation regimes, as shown in Figure 6.1.

Even though there are five lines, some of the features of the figure have more constraints due to the nature of the conditions. For instance, the gradients of the inclined lines are fixed at $\sqrt{3}$ and $-\sqrt{3}$ as they act as forces opposing the movement of the partials. Additionally, the boundaries of conditions C2, C3, C4 and C5 coincide at point P with coordinates given by relations (6.8) and (6.10), while C1 and C2 coincide at point Q with coordinates $\left(\frac{F_{f1} - F_{f2}}{b}, -\frac{\sqrt{3}\left(2\gamma_{ISF} + 2R_1 + F_{f1} + F_{f2}\right)}{b}\right)$. Thus, γ_{ISF} affects both points by shifting them towards lower values of τ_E, making stacking fault propagation more difficult.

Maps like this one have been generated by simulations of individual partials for the case of Frank-Read sources [234], narrow channels [24, 56], precipitate shearing [57] and precipitate arrays [58], but the current analytical approach generalises the dislocation

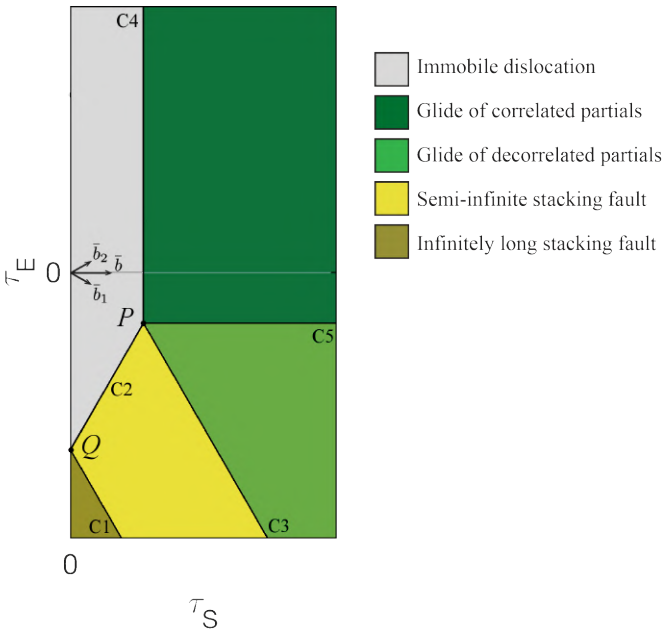

Fig. 6.1 - Schematic plot of the different glide regimes for a dissociated $\frac{a}{2}\langle 110\rangle\{111\}$ dislocation with an aspect ratio of 1:1. Important features include the boundaries defined by conditions C1-C5 and points P and Q where they intercept each other.

behaviour. Moreover, the infinitely long stacking fault regime has never been described, most likely due to the large stresses at which it would appear.

Another implication of this analysis is that none of the conditions depend on the interaction force between the partials. This factor was ignored in previous models just for simplicity [56, 57], but the current derivation shows that the elasticity related parameter A_s has no effect on the boundaries between different regimes. Nonetheless, it affects the stacking fault width in the regions of immobile dislocations and glide of correlated partials, given by equations (6.6) and (6.7), respectively. Considering the anisotropic elasticity of the crystal would add another orientation dependence for the dissociation width [242], without any effect on the boundaries plotted.

Orientation maps such as those in Figure 5.3 can then be superimposed onto a plot with the different glide regimes to determine the behaviour that each slip system will show. Note that this is only possible if the obstacles offer the same resistance in every direction, which would not be the case if R_1 had an orientation dependence, *e.g.* for arrays of non-spherical precipitates with a preferential orientation. Moreover, dislocation structures formed after yield may not offer the same glide resistance in different slip systems due to latent hardening [243].

Consider now the angle

$$\theta_P = -\arctan\left(\frac{\sqrt{3}(2\gamma_{ISF}+R_1+F_{f1}-R_2-F_{f2})}{R_1+R_2+F_{f1}+F_{f2}}\right) \tag{6.12}$$

between the horizontal axis and a line from the origin to point P in Figure 6.1. This is in general the parameter determining the likelihood for an fcc crystal to develop deformation stacking faults compared to perfect dislocation glide. If this has a value lower than $-30°$, then it is impossible to promote stacking fault propagation without first reaching the glide of correlated partials regime in a coplanar slip system. This conclusion arises by considering the constraints previously described of the coordinates of the different slip systems on the orientation maps. Furthermore, the minimum resolved shear stress for stacking fault propagation in this condition is that of P. Inspection of equation (6.12) shows that the key parameters for promotion of stacking faults are a low stacking fault energy and a high trailing partial glide resistance R_2+F_{f2}.

6.2.1 Obstacle surpassing mechanisms

Overall, most obstacle surpassing mechanisms depend on the line tension T of the dislocation as the radius of curvature ρ it will adopt is inversely proportional to the force applied F through the relation $\rho = T/F$. This tension, which can be thought of as the self-energy per unit distance of the dislocation, is proportional to μb^2, but it also depends on the character and even on whether it belongs to a perfect dislocation or is a completely isolated partial [241]. Modelling of this parameter has been performed before in a more complete way [241], although for simplicity it is here assumed to be $T = \alpha\mu b^2/2$ in accordance to other approaches in the literature, where α is a dimensionless parameter close to one.

In nickel-based superalloys, perfect dislocations can either shear or loop around the $L1_2$ coherent precipitates typically found, and the preferred mechanism depends on factors such as the precipitate size distribution and volume fraction f, the antiphase boundary energy γ_{APB} and the elastic properties of the material. Shearing leaves behind an antiphase boundary (APB) due to a misconfiguration of the atomic stacking order that leads to an increase in the number of high-energy bonds. This comes with an energy penalty that disappears when a second dislocation with the same Burgers vector glides across that area, and so pairs of coupled dislocations are promoted.

The current analysis considers as a first step the evolution of a single dissociated dislocation. Note that segregation assisted stacking fault shearing [244] dominates the creep behaviour at temperatures around 700°C, but this section only considers the athermal prop-

agation of stacking faults. Additionally, a clear distinction can be made between alloys based on their $\gamma\prime$ volume fraction. When this parameter increases to values up to 70%, large cuboidal precipitates develop separated by γ channels with a relatively constant width H, whereas lower volume fractions lead to an array of spherical precipitates with varied radii r and precipitate spacings L. Both cases are analysed here.

Dislocations in a narrow channel

The problem of stacking fault propagation through channels of constant width was treated by Douin [56]. At temperatures where diffusion has no influence in the deformation behaviour, the antiphase boundary energy and the large size of the precipitates restrict most of the deformation to the channels in-between. A schematic diagram of this glide mechanism can be seen in Figure 6.2.

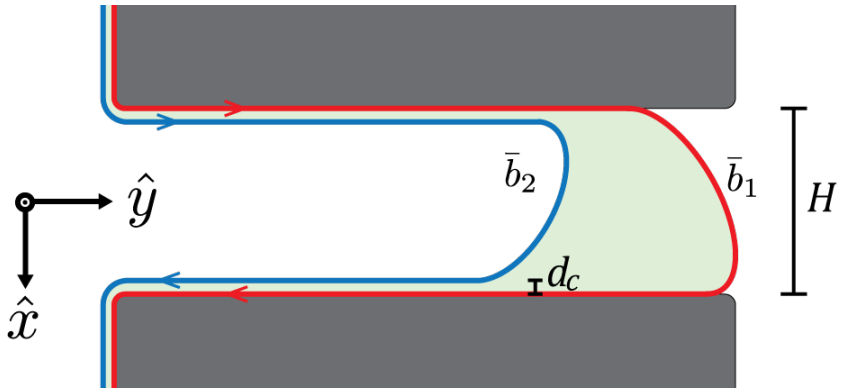

Fig. 6.2 - Schematic diagram of dislocation glide through γ channels.

The required stress for a dislocation to enter a channel of width H is $\tau = 2T/Hb$, which in the current framework becomes a resistance for a perfect dislocation of

$$R_c = \frac{\alpha\mu b^2}{H}, \tag{6.13}$$

or for the leading partial

$$R_{1c} = \frac{\alpha\mu b_p^2}{H}. \tag{6.14}$$

The trailing partial needs to overcome a similar force, with the difference that it will feel a repulsion force from the segments left by the leading partial pushing against the obstacles, which will effectively reduce the channel width.

In the case where both dislocations are already decorrelated and far from each other, the trailing partial will start gliding through the channel when

$$F_{PK2} + \gamma_{ISF} - F_{f2} = R_{2c}. \tag{6.15}$$

Simultaneously, the force balance in direction $\hat{x}$ perpendicular to the glide direction on a straight segment of one of the trailing partials interacting with the other three dislocation segments reads

$$F_{PK2} + \gamma_{ISF} - F_{f2} - \frac{A_s}{d_c} - \frac{A_t}{H-2d_c} - \frac{A_s}{H-d_c} = 0, \tag{6.16}$$

where d_c is the stacking fault width in this direction, A_t/x is the interaction force between two parallel dislocations separated by a distance x on the same slip plane and with the same Burgers vector, and

$$A_t = \frac{4-2\nu-2\nu\sin(\pi/6+2\theta_2)}{8\pi(1-\nu)}\mu b_p^2. \tag{6.17}$$

Note that both A_s and A_t in equation (6.16) must be obtained for a dislocation character $\theta_2 = \theta + \pi/2$ because these segments are perpendicular to the moving end of the partials. Rearranging and solving equations (6.15) and (6.16), with

$$R_{2c} = \frac{\alpha G b_p^2}{H-2d_c}, \tag{6.18}$$

gives two solutions, only one of which has a physical meaning:

$$d_c = \frac{H}{-4+8\pi(1-\nu)+2\nu+2\nu\sin(\pi/6+2\theta_2)}\left(4\pi(1-\nu)-2\nu\cos(2\theta_2)+\nu\sin(\pi/6+2\theta_2)\right.$$
$$\left.-\sqrt{16\pi^2(1-\nu)^2+2(2-\nu)^2-8\pi(2-3\nu+\nu^2)-4(2-\nu)\nu\cos(2\theta_2)+4\nu^2\cos(2\theta_2)^2-(4-8\pi(1-\nu)-2\nu)\nu\sin(\pi/6+2\theta_2)+\nu^2\sin(\pi/6+2\theta_2)^2}\right). \tag{6.19}$$

This means that d_c is proportional to H by a factor that only depends on ν and θ_2, and ranges between 0.07 and 0.139 for a typical value of $\nu = 0.3$. After the critical force has been reached, an increase in the stress applied will result in a reduction of the stacking fault width in the $\hat{x}$-direction, facilitating further glide of the trailing partial.

As the stacking fault width parallel to the channel becomes smaller, the increase in the interaction force on the trailing partial will increase the total stress needed for both dislocations to glide through the channel. Comparing these results to those for a perfect dislocation, it can be seen that $R_c \sim \frac{3}{2}(R_{1c} + R_{2c})$ even ignoring the channel width reduction for the trailing partial. The transition between both regimes is not modelled here as it would involve a line tension approach that considers the curved segments. Nonetheless, it is

theorised here that the actual curve delimiting the region of correlated motion of partials in the stress map would start from point P and then quickly approach the vertical line given by relation (6.11) as the stacking fault width decreases.

Array of spherical $L1_2$ coherent precipitates

The analysis of an array of obstacles constitutes a more difficult challenge than that of individual precipitates due to the variability of the cross sectional areas, precipitate spacings, orientations in which the dislocations must move to surpass them and mechanisms by which this can be done. A number of models have been developed for precipitate hardening by considering their interaction with perfect dislocations [38, 40, 213] but not with individual partials. It is thus the objective of this section to combine the ideas of such models with the orientation framework developed here. The following assumptions are made in this section to attain simplicity. The obstacles in the plane analysed are considered to consist of an array of equally spaced circular precipitate cross sections with a constant radius r. The lattice misfit between the two phases is neglected, which in reality tends to reduce the effective precipitate spacing due to the interfacial dislocations but does not qualitatively affect the results. The elastic modulus mismatch is also ignored as it has been shown that up to a difference of 10% in the resulting internal stress field does not significantly affect the quantitative results [245]. Similarly, the friction force is also assumed to be the same in both phases.

The force balance on a perfect dislocation at the point of maximum particle resistance reads

$$(b\tau_S + F_f)\lambda(b,\gamma_{APB}) - 2r\gamma_{APB} = 0, \tag{6.20}$$

where

$$\lambda(b,\gamma_P) = \left(\frac{\alpha\mu}{2\gamma_P r}\right)^{1/2} \xi bL \tag{6.21}$$

is the Friedel sampling length of a dislocation producing an ordering planar fault with energy per unit area γ_P in the precipitate [53], ξ is a correction parameter and

$$L = \left(\frac{2\pi}{3f}\right)^{1/2} r \tag{6.22}$$

the mean planar distance between precipitates centres. Solving this equation and rearranging it in the form of condition C4 leads to

$$R_s = \frac{2r}{\lambda(b,\gamma_{APB})}\gamma_{APB} = \frac{\gamma_{APB}}{b}\left(\frac{12fr\gamma_{APB}}{\alpha\pi\mu}\right)^{1/2}. \tag{6.23}$$

Equation 6.23 is analogous to that describing weak coupling in precipitate strengthened materials [40, 53, 213], with the difference that an initial configuration of two piled-up perfect dislocations is arbitrarily assumed there, leading to an additional factor of 2 in the denominator. Furthermore, for even bigger precipitates Orowan bowing operates with the same resistance as in the case of fcc channels, *i.e.*

$$R_l = \frac{\alpha \mu b^2}{L - 2r}, \tag{6.24}$$

and the active mechanism is that with the minimum resistance $R = \min(R_s, R_l)$.

The Friedel statistics have been used in this and other yield criteria in an attempt to capture the effect of the microstructure variability on the average effective precipitate spacing λ. This parameter has been analysed in detail in multiple 2D simulations by looking at the evolution of one dislocation gliding along a material with discrete obstacles. This is also the way in which single Shockley partials evolve when fully decorrelated, as out-of-plane glide and pile-ups are not an option. Deviations from equation (6.21) have been systematically studied for different precipitate strengths [246] and ranges of volume fractions [247], all of which are incorporated into ξ. The reader is referred to reference [53] for further details and numerical evaluations of this parameter.

Alternatively, by substituting λ for L in the shearing equations in this section, the description of single precipitate-channels pairs can be obtained, with results similar to those in the literature obtained via phase field modelling [24, 57, 58]. λ is used to give an insight into the effect of the precipitate size variability and volume fraction, whereas it is the critical channel width which actually determines where the partials will be stopped.

Athermal stacking faults in superalloys with arrays of spherical precipitates sometimes show holes in which no planar fault is observed. The origin of such holes can be analysed by accounting for the effect of precipitate size and volume fraction on the glide behaviour of both Shockley partials. The nomenclature used here for the different mechanisms uses the folowing logic: a number indicating which partial it refers to, with subsequent letters referencing the sequence of mechanisms used; *e.g.* (2sl) refers to looping of the trailing partial around a previously sheared precipitate.

Similar to a perfect dislocation, the leading partial should be able to circumvent a precipitate via two possible mechanisms: (1s) shearing and forming a CISF with an energy penalty close to that of the APB, or (1l) Orowan looping around an unfaulted precipitate. In the case of shearing, an approach similar to that of the weak-pair coupling can be followed, accounting for the differences in the Burgers vector, the energy of the planar fault and their effect on the Friedel spacing for the leading partial $\lambda_1 = \lambda(b_p, \gamma_{CISF})$. A force balance leads

then to a resistance

$$R_{1s} = \frac{2\left(\gamma_{CISF} - \gamma_{ISF}\right)}{b_p}\sqrt{\frac{3fr\gamma_{CISF}}{\alpha\pi\mu}}. \tag{6.25}$$

Alternatively, looping in bigger precipitates occurs when the critical bow-out radius is reached, *i.e.*

$$R_{1l} = \frac{\alpha\mu b_p^2}{L-2r}. \tag{6.26}$$

The overall obstacle resistance is then $R_1 = \min\left(R_{1s}, R_{1l}\right)$, and the mechanism that will dominate is the one with the lowest stress threshold. Figure 6.3 shows schematically these mechanisms and those for the trailing partials, showing the defects that are left after each partial bypasses the precipitates.

A variation introduced by Unocic *et al.* [24] for Orowan bypassing of the leading partial considers the elastic contribution of the trailing dislocation pushing via the interaction force. This applies only when both partials are still correlated and for angles $\varphi > -60°$, and the result is a curved boundary rather than a straight line due to the stress contribution on both dislocations. Similarly, this could take place for shearing of precipitates close to or smaller than the dissociation width. These effects are ignored here for simplicity, but adding them is straightforward.

When the trailing partial glides into the precipitate, the force needed to surpass it will depend on which defect it faces. If it runs into a previously sheared precipitate, it can bypass it again via two possible mechanisms: (2ss) shearing it again and transforming the CISF into an APB or (2sl) looping around it leaving behind a $\overline{b_2}$ loop around a CISF within the precipitate. Following the same steps as before yields

$$R_{2ss} = \frac{2\left(\gamma_{APB} - \gamma_{CISF} + \gamma_{ISF}\right)}{b_p}\sqrt{\frac{3fr\left(\gamma_{APB} - \gamma_{CISF}\right)}{\alpha\pi\mu}}, \tag{6.27}$$

and $R_{2sl} = R_{1l}$.

On the other hand, if the trailing partial runs into an unfaulted precipitate with a $\overline{b_1}$ loop around it, it can either be stopped or surpass it via: (2ll) Orowan bowing around it leaving behind a precipitate with two dislocation loops ($\overline{b_1}$ and $\overline{b_2}$) and a stacking fault in-between, or (2ls) inducing the required stress for the loop to collapse and annihilate by shearing the precipitate. The first mechanism would occur in a similar way to gliding of the trailing partial in a γ channel. By analogy with equation (6.18), the resistance force can be approximated by

$$R_{2ll} = \frac{\alpha\mu b_p^2}{L-2r-2d_{ll}}, \tag{6.28}$$

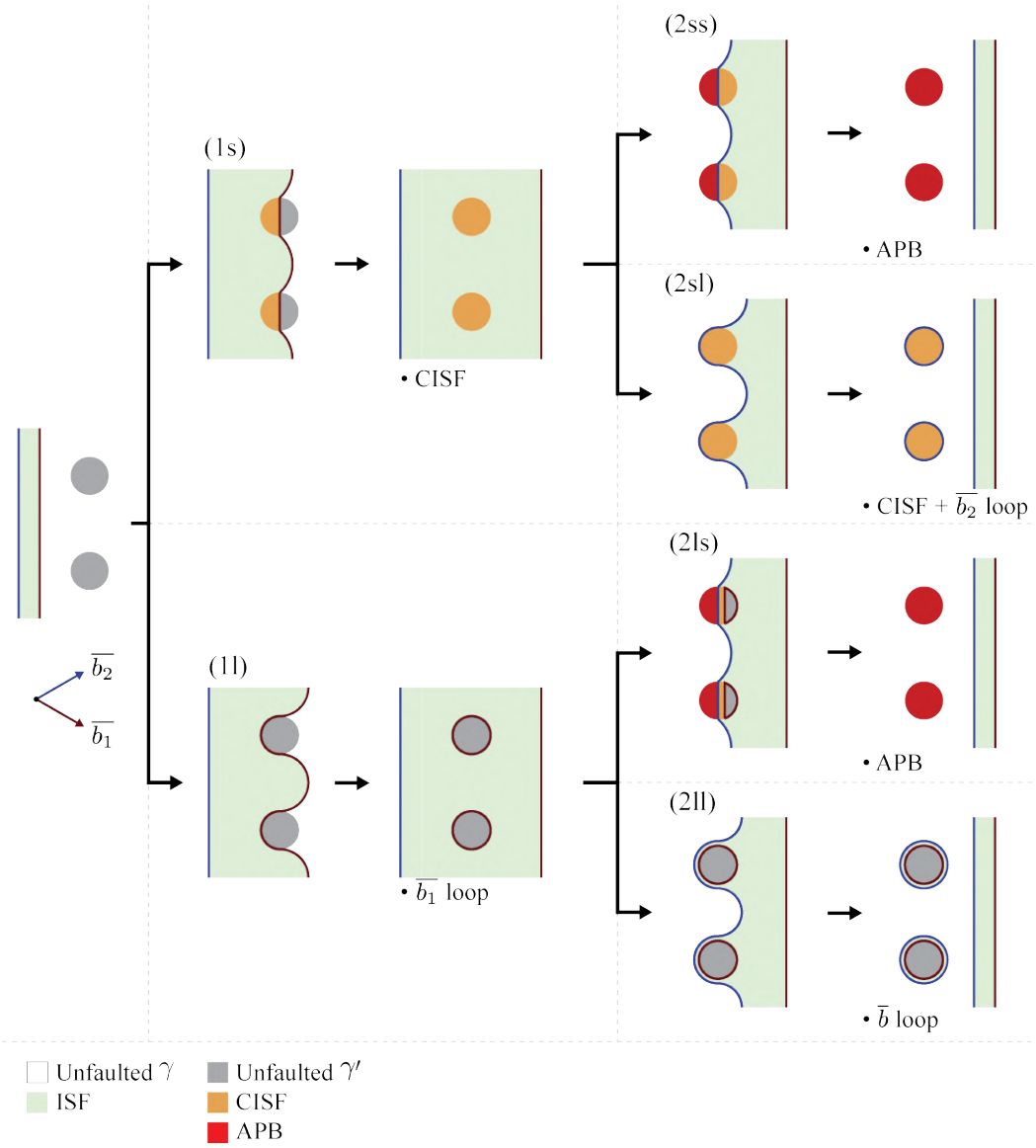

Fig. 6.3 - Schematic diagrams of the mechanisms for Shockley partial precipitate bypassing where dislocations glide from left to right. The defects left after the sweeping of each partial are annotated.

where d_{ll} can be found by substituting H with $(L-2r)$ in the definition of d_c in equation (6.19). Alternatively, shearing provoked by the trailing partial involves the forces felt by both partials. Due to the more complicated geometry of the dislocation configuration, a proper analysis would require a discretised line tension approach, which is skipped here. What can be expected is for the obstacle resistance to have an orientation dependence with an angle different to conditions C1 or C3, as the segments of the partials along which the stress acts

have different lengths. Moreover, if the precipitates were to be sheared this would most likely happen when both partials are still not fully decorrelated.

Among the aforementioned mechanisms, some are not likely to happen. Consider Figure 6.4 calculated for typical parameters of nickel-based superalloys: $\nu = 0.33$, $\mu = 58.6$ GPa, $b = 0.253$ nm, $\gamma_{ISF} = 10$ mJ/m^2 [241], $\gamma_{APB} = 276$ mJ/m^2, $\gamma_{CISF} = 196$ mJ/m^2 [248] and $f = 0.1$, with $\theta = 90°$, $\alpha = 1$ and $\xi = 1$. A parametric analysis for the precipitate size r shows a transition from shearing to looping for the leading partial similar to that of perfect dislocations [213] at $r = r_c$. The trailing partial would then feel a small resistance in the former regime because the energy of a CISF is very similar to that of an APB [249, 250], and no R_{2sl} is to be observed. However, larger precipitates might have to be bypassed via looping of both partials, which generates the large peak in R_2 seen in the plot. Accounting for the variability in precipitate size and spacing within a single material a combination of these mechanisms is expected. This result shows however that propagation of stacking faults will mostly occur for larger precipitates and narrower channels which must undergo Orowan looping, as expected from the analytical result in equation (6.12). In the case of alloys with a bimodal precipitate size distribution, the larger secondaries will be the source of stacking faults as shown by Unocic *et al.* [24].

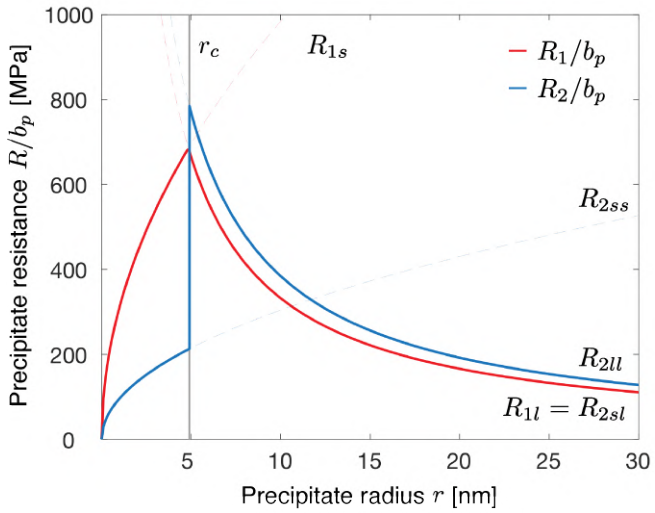

Fig. 6.4 - Precipitate resistance R/b_p for the leading and trailing partial dislocations as a function of mean particle size. The solid lines denote the actual resistance and the dashed lines represent the individual mechanisms. The transition r_c from shearing to looping for the leading partial is marked for reference.

6.3 Thermally assisted stacking fault propagation

At higher temperatures, other mechanisms of stacking fault shearing have been extensively observed in $\gamma\prime$-reinforced nickel-based superalloys. These are superlattice intrinsic stacking faults (SISF), superlattice extrinsic stacking faults (SESF), stacking fault ribbons and microtwins. The planar faults in the matrix that accompany these defects vary considerably too and many of these mechanisms may appear simultaneously during some tests. To the knowledge of the authors no general explanation has yet accounted for all these observed phenomena. Thus, it is it the objective of this section to rationalise the effects of orientation and microstructure underlying the generation of these defects, which include:

- Isolated SISFs
- Extended SISFs + ISF
- Stacking fault ribbons
- Isolated SESFs
- Extended SESFs + ESF
- Extended SESFs + ISF
- Microtwins

The segregation-assisted plasticity theory recently developed by Barba *et al.* [244] has shown that γ-stabiliser elements diffuse towards the aforementioned faults, which has been inferred to reduce their planar energy penalties [251]. Different concentrations are reached in the faults before their leading dislocations may move. In the current framework this constitutes a difficulty as it is hard to pinpoint what the actual energies of the different faults are. The values from the literature used here may be considered upper bounds as the real faults would arise in a more γ-like crystal structure due to elemental segregation. Note that a number of atomistic models consider the unstable energies from the generalised stacking fault energy rather than only the stable points [239, 242, 250, 252]. For simplicity and due to the lack of concentration-dependent data, all the forces from planar defects in this work are assumed to come from the stable energies, but very small adaptations to the equations would be required to account for the unstable points.

An orientation dependence determining which mechanism will dominate is to be expected due to the $\frac{a}{6} < 112 >$ nature of the dislocations involved. Figure 6.5 includes the results of multiple studies on uniaxial creep of single crystals, both in tension and compression,

according to the most frequent mechanism observed in each condition. The results were included when there was a quantitative analysis or when it was clearly stated that a specific mechanism appeared more than others. This description based on the single parameter ϕ unequivocally shows the orientation dependence and the proximities between the mechanisms of SISF and SF ribbon, as well as SESF and microtwinning. Note that most of the studies have been performed in orientations close to $\{001\}$, $\{011\}$ and $\{111\}$; thus, there is insufficient data for loading around $\phi = 0$. Composition, microstructure, stress and temperature are additional variables that may further determine the appearance of these mechanisms.

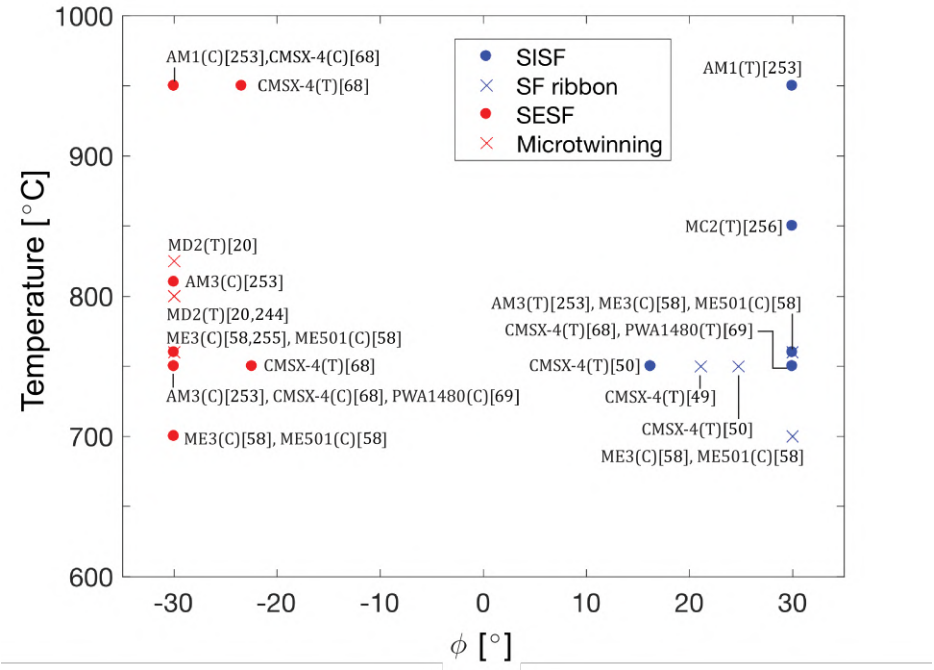

Fig. 6.5 - Map of the most frequently observed stacking fault shearing mechanism as a function of angle ϕ and temperature in a series of uniaxial creep studies [20, 49, 50, 58, 68, 69, 244, 253–256]. Each annotation includes the alloy, loading mode and reference.

Multiple mechanisms have been proposed for the creation of superlattice stacking faults, many of which have no direct experimental validation for the dislocation reactions assumed to occur. Experimental proof via high resolution TEM of the actual dislocation arrangement for SISFs and SESFs was first given by Vorontsov *et al.* [47] and recently validated by Rao *et al.* [257] and Smith *et al.* [258, 259]. These works constitute the basis of the following orientation analysis. The case of cuboidal precipitates is addressed here, but an extension to spherical shapes could be done in a similar manner to that of the athermal mechanisms.

Consider first the case of a SISF. In this model depicted in Figure 6.6 it is envisioned that two coplanar dislocations with different leading but equal trailing partials will first meet

in adjacent planes at a $\gamma/\gamma\prime$ interface. Glide into the precipitate of a full dislocation and an additional leading partial will result in an arrangement such as that in Figure 6.6(b), where a CESF is followed by a an APB. A local diffusive reordering scheme can then transform the latter into a SISF [47, 52].

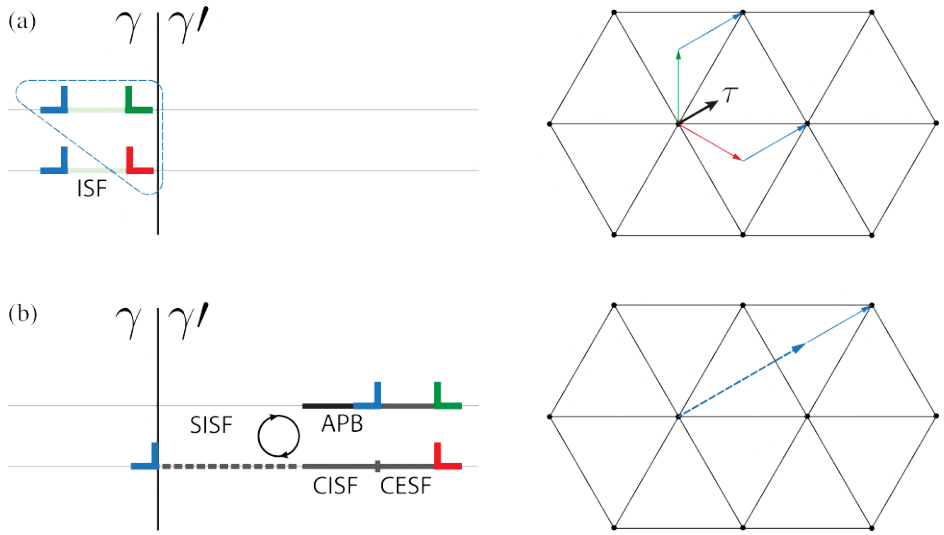

Fig. 6.6 - Dislocation structure of a SISF (a) before and (b) after shearing through the $\gamma\prime$ precipitates. Each figure includes an edge-on view of the slip planes (left) and a top view of the Burgers vectors in a $\{111\}$ plane of the partials involved (right), where the atoms sit on the corners of the triangles. The arrows in (b) correspond to the circled superdislocation and the trailing partial in (a).

A Y-configuration for the stress of a slip plane will result in two equally active slip systems with the same trailing partial, as shown in Figure 6.6(a). How such two dislocations can get to adjacent planes is still unclear, but cross slip of segments stopped at the interface could explain this behaviour. The angle between the Burgers vector of the two leading partials is 120°, meaning that they will attract each other. This gives the leading end of a SISF its extrinsic character observed experimentally. By moving together, the superdislocation formed at the leading end will have a total Burgers vector with the same orientation as the remaining trailing partial and twice its magnitude. This is again the slip direction with the highest resolved shear stress, thus facilitating the viscous motion of the dislocations controlled by the diffusive processes of segregation and reordering.

The CESF formed constitutes a glide barrier upon forming at the interface but not anymore as it moves within $\gamma\prime$. The equilibrium distance between the partials bounding this fault d_{CESF} can be found with a similar derivation to that of equation (6.2). Considering both

ends of the CESF to be stopped by a resisting frontal force, as well as a fully formed SESF,

$$d_{CESF} = \frac{A_t}{\gamma_{CESF} - \gamma_{SISF} + \frac{b}{2}\tau_S + \frac{b}{2\sqrt{3}}\tau_E - F_{f2}}, \tag{6.29}$$

where the character θ is that of the dislocation bounded by a $\overline{b_1}$ and a $\overline{b_2}$ partials. With the values used before, $\gamma_{CESF} = 268$ mJ/m^2, $\gamma_{SISF} = 62$ mJ/m^2 [248] and the stress attained in the high resolution TEM study ($\tau_S = 343$ MPa and $\tau_E = 149$ MPa), the resulting $d_{CESF} = 1.05$ nm is 19% lower than the experimental measurement [47].

For the leading superpartial of a SISF to propagate it must shear through $\gamma\prime$ (1I). The corresponding force balance results in condition $C1_I$

$$C1_I : 2F_{PK2} - \gamma_{SISF} - 2F_{f1} - F_{f2} > 0. \tag{6.30}$$

The contribution of the dislocation pulling from the matrix is ignored here for simplicity. Afterwards, athermal shearing of the trailing partial is not favoured as it would result in a more energetically costly antiphase boundary, but Orowan looping (2Il) may still appear if

$$C2_I : F_{PK2} + \gamma_{ISF} - F_{f2} > R_{1c}. \tag{6.31}$$

This would result in the formation of isolated SISFs within $\gamma\prime$ precipitates. As both conditions have the same gradient, a region where only the trailing partial is blocked will only appear if

$$\gamma_{SISF} + 2\gamma_{ISF} + 2F_{f1} - F_{f2} < 2R_{1c}, \tag{6.32}$$

which is promoted by narrower γ channels. A schematic diagram of conditions $C1_I$ and $C2_I$ can be seen in Figure 6.7. The fault formed will be that where the coordinates of the two coplanar slip systems with the highest Escaig factors fall.

Alternatively, the formation of stacking fault ribbons (2IR) may appear if the stress on the trailing partial is not large enough for athermal looping of the obstacles. In this mechanism the planar fault undergoes the transition SISF-APB-SESF due to the passage of multiple $\frac{a}{6} < 112 >$ dislocations [50]. In this scenario the trailing partial will shear the precipitate followed by an additional pair of dislocations that produce similar transformations in the planar faults, but this time forming a SESF rather than a SISF. Note that again the Burgers vectors of the superdislocation is the one with the highest Schmid factor in configurations with a high value of ϕ. Moreover, a necessary condition for this mechanism will then be for $C2_I$ to be false, also lying in the Extended SISF + ISF region. This explains the different variations of SISF configurations observed.

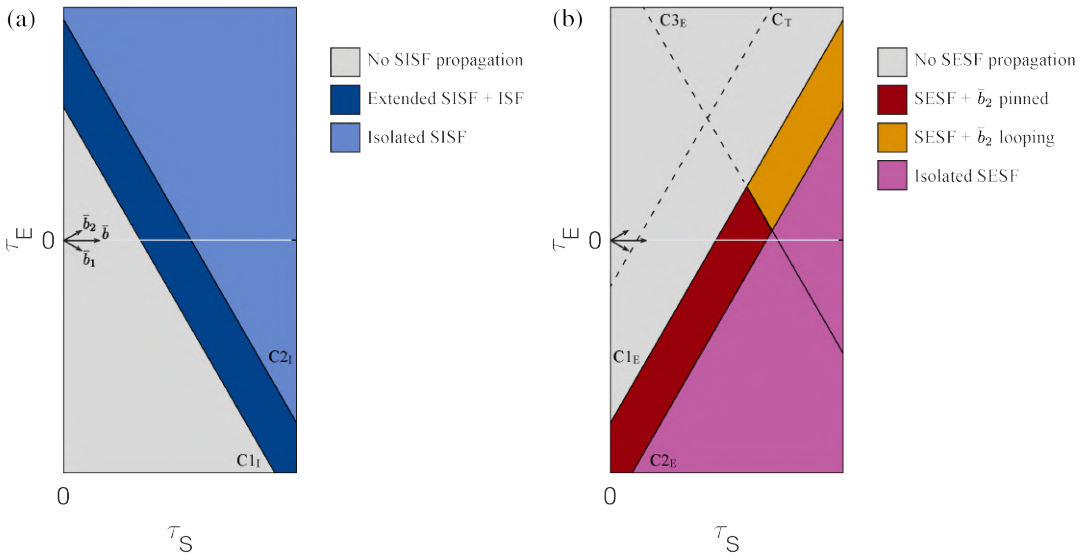

Fig. 6.7 - Schematic plot of the segregation assisted (a) SISF and (b) SESF shearing mechanisms with an aspect ratio of 1:1. The boundaries are labeled for the reference from the conditions that form them.

The dislocation structure of a SESF involves two partials with the same Burgers vector gliding through the precipitates. Elastic interactions in this case provoke these partials to glide separated from each other by a small distance with a CISF in-between. A SESF is then formed after glide of the second partial followed by local atomic reordering [44]. Motion of both leading partials in this scenario is favourable for orientations close to a Λ-configuration.

A condition $\mathrm{C1_E}$ for SESF propagation (1E) based on a force balance reads

$$\mathrm{C1_E}: 2F_{PK1} - \gamma_{SESF} - 2F_{f1} > 0. \tag{6.33}$$

Again, the complex planar fault formed in the front does not impede the propagation of the partials. The repulsive force between the leading partials with equal Burgers vectors results in a CISF of width

$$d_{CISF} = \frac{A_t}{\gamma_{CISF} - \gamma_{SESF} + \frac{b}{2}\tau_S - \frac{b}{2\sqrt{3}}\tau_E - F_{f1}}. \tag{6.34}$$

Evaluating equation (6.34) with $\gamma_{SESF} = 74$ mJ/m^2 this results in $d_{CISF} = 1.76$ nm, a 37% higher than the experimental value [47].

For $\phi = 30°$ there will be two coplanar slip systems sharing the same leading partial but with different trailing dislocations. Analogous to the SISF analysis, the SESF might be

originated by two dislocations with these Burgers vectors pushing against the $\gamma/\gamma\prime$ interface in adjacent planes [258], as shown in Figure 6.8(a). There would be then an attractive force between both trailing partials and their combined Burgers vector would equal that of the leading partial. This is exemplified in Figure 6.8(b).

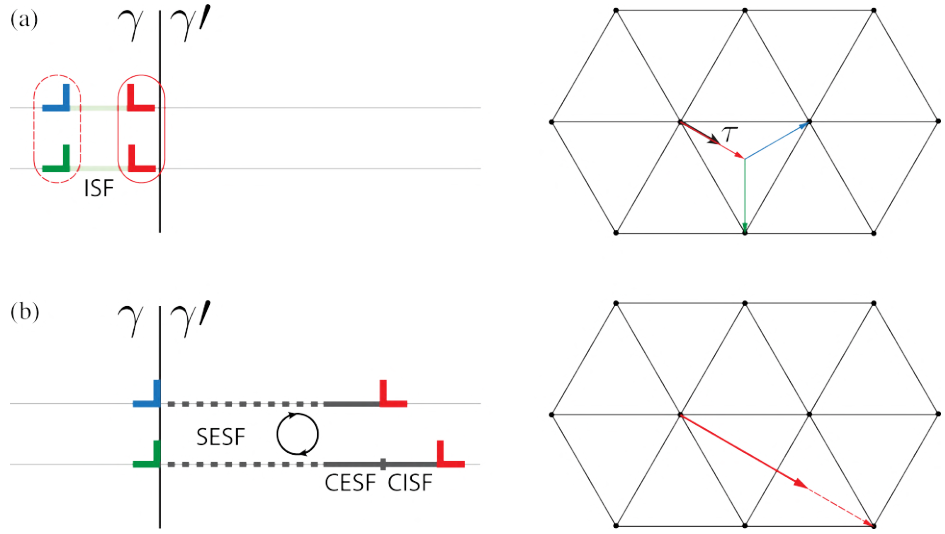

Fig. 6.8 - Dislocation structure of a SESF (a) before and (b) after shearing through the $\gamma\prime$ precipitates. Each figure includes an edge-on view of the slip planes (left) and a top view of the Burgers vectors in a $\{111\}$ plane of the partials involved (right), where the atoms sit on the corners of the triangles. The arrows in (b) correspond to the circled dislocations in (a).

Upon decorrelation and glide of the leading ends, the trailing partials may evolve in three ways. Firstly, both of them could glide together in the matrix bypassing the precipitates via Orowan looping (2Ell), which would occur if

$$\mathrm{C2_E}: F_{PK1} + \gamma_{ESF} - 2F_{f2} > R_{1c}, \tag{6.35}$$

resulting in isolated SISFs. Secondly, looping of a single partial while the other one remains pinned (2El), converting the ISF in the matrix into an ESF with a similar energy penalty [248]. Note that the resulting dislocation structure around the precipitates would be identical to that experimentally observed by Décamps *et al.* [260] in a polycrystalline alloy. Kinetically this mechanism would occur if condition $\mathrm{C2_E}$ is false and

$$\mathrm{C3_E}: F_{PK2} + \gamma_{ESF} - \gamma_{ISF} - F_{f2} > R_{1c}. \tag{6.36}$$

This will happen only if one of the trailing partials experiences a higher force than the other one, which occurs for partial $\overline{b_2}$ as ϕ moves away from $-30°$. These SESF conditions are schematically shown in Figure 6.7(b). A SESF/ISF alternating character would then appear

if the coordinates of only one of the three coplanar slip systems lie in the $\overline{b_2}$ looping region. If the two points with the lowest Escaig stresses fall in this region, then isolated SISFs will appear again. Thirdly, an extended extrinsic fault (SESF/ESF) would be promoted if both of these points are in the region of pinned trailing partials. Note that according to equations (6.33) and (6.35), the second and third options will only be possible for a material in which

$$\gamma_{SESF} + 2\gamma_{ESF} + 2F_{f1} - 4F_{f2} < R_{1c}, \tag{6.37}$$

This covers the different variations of SESF structures observed.

Lastly, segregation assisted microtwinning (2ET) can be seen as a variation of the SESF mechanism in which more leading partials shear the matrix and the precipitates in adjacent planes, with no further glide of the trailing segments. Different pathways for the order in which the planes are sheared have been proposed both in fcc and $L1_2$ structures [261] but the resulting stress orientation dependence is the same. Glide of partials on consecutive adjacent planes is considered here. It is apparent that propagation of the leading partials is promoted for lower values of ϕ, increasing the likelihood for this deformation mechanism to appear. It is not fully clear how microtwins nucleate, but the athermal stopping of the trailing partials may be a necessary condition. This would explain why this mechanism appears at lower stresses than SESFs [20, 58]. Pinned trailing partials would give time for more dislocations to reach planes adjacent to the fault and increase the microtwin thickness as they thermally shear the precipitates (and athermally the matrix).

A leading partial gliding on a plane adjacent to a SESF would transform this fault into a 3-layer microtwin with two corresponding twin boundaries. The force balance reads

$$\mathrm{C_T} : F_{PK1} + \gamma_{SESF} - 2\gamma_{Tp} - F_{f1} > 0, \tag{6.38}$$

where γ_{Tp} is the twin boundary energy in the precipitates. Simultaneously, the ESF in the matrix is replaced by two twin boundaries with energy γ_{Tm}. Studies have shown that the energy difference between a 2- and a 3-layer fault is rather small both in the fcc and the $L1_2$ phases, *i.e.* $\gamma_{ISF} \approx \gamma_{ESF} \approx 2\gamma_{Tm}$ [262, 263] and $\gamma_{SESF} \approx 2\gamma_{Tp}$ [261, 264]. The stress required to activate twinning from equation (6.38) is then expected to be low, as shown in Figure 6.7(b). Upon forming an extended SESF + ESF, microtwinning appearance and thickening may be mostly limited by the diffusion for atomic reordering and to lower the fault energy and not by an additional stress requirement, as long as the leading partials of the SESF are sufficiently separated from that at the third layer.

A summary of the thermal mechanisms described here is shown in Figure 6.9, together with the defects left by the partials when overcoming the precipitates. It is expected that the

thermally activated mechanisms will only occur if no athermal alternative is possible, as this allows the dislocations to push against the obstacles and drive the atomic diffusion process.

A remaining question is: why do multiple types of faults appear during a single test? Looking at Figure 6.7 it is evident that the regions for the SISF and SESF mechanisms overlap for a Schmid stress higher than certain value. This implies that these mechanisms can coexist as long as the appropriate dislocations meet at a $\gamma/\gamma\prime$ interface. The models for both superlattice stacking faults share the $\overline{b_1}+\overline{b_2}$ dislocation, which in an orientation map for a single slip plane corresponds to the point with the highest Schmid factor. The other two coplanar slip systems are then the additional dislocation in each model; the one with the highest Escaig factor for the SISF and that with the lowest for the SESF. The combinations of these two pairs of points determine the faults that will be promoted.

Figure 6.10 shows the superposition of the mechanistic maps for thermal and athermal mechanisms for an alloy with a γ channel of 20 nm. The overlap of the different thermally activated mechanisms is denoted by the striped regions. Just from the geometry of the constraints it can be seen that SISF and SESF propagation will be promoted for positive and negative values of ϕ, respectively. An exception to this is the formation of an extended alternating SESF/ISF, which is more likely to appear with a higher angle. This occurs as the trailing dislocation in the SESF model will tend to split into its two attracting partials under a low Escaig stress. Similar to the case of an infinitely long stacking fault, one of these partials may even be pushed in the opposite direction for an angle close to $\phi = 30$.

Due to the geometric constraints on the slip systems it is only necessary to track one to determine the mechanisms that will dominate in that slip plane. Condensing the orientation dependences via angle ϕ results in smaller maps like those in Figure 6.11 for different channel widths. These maps cover all the possible shear stresses and orientations that a slip plane may experience; they can be related to uniaxial loading by looking at Figure 5.6 but apply for any stress state.

A parametric analysis shows that an increase in the channel width promotes the formation of isolated faults and may even result in the disappearance of regions where extended stacking faults are predicted to appear. This occurs, according to equations (6.32) and (6.32), because athermal dislocation glide along the matrix becomes easier and the trailing partials cannot be pinned anymore. Simultaneously, athermal perfect dislocation glide becomes easier for the same reason. Realistically a wider channel would also decrease the stress required for superlattice fault appearance as the force exerted by the precipitate would increase, but the spatial one-dimensional modelling fails to capture this. It must be noted that all the predictions here refer to the critical channel width and not its mean value, and the statistical

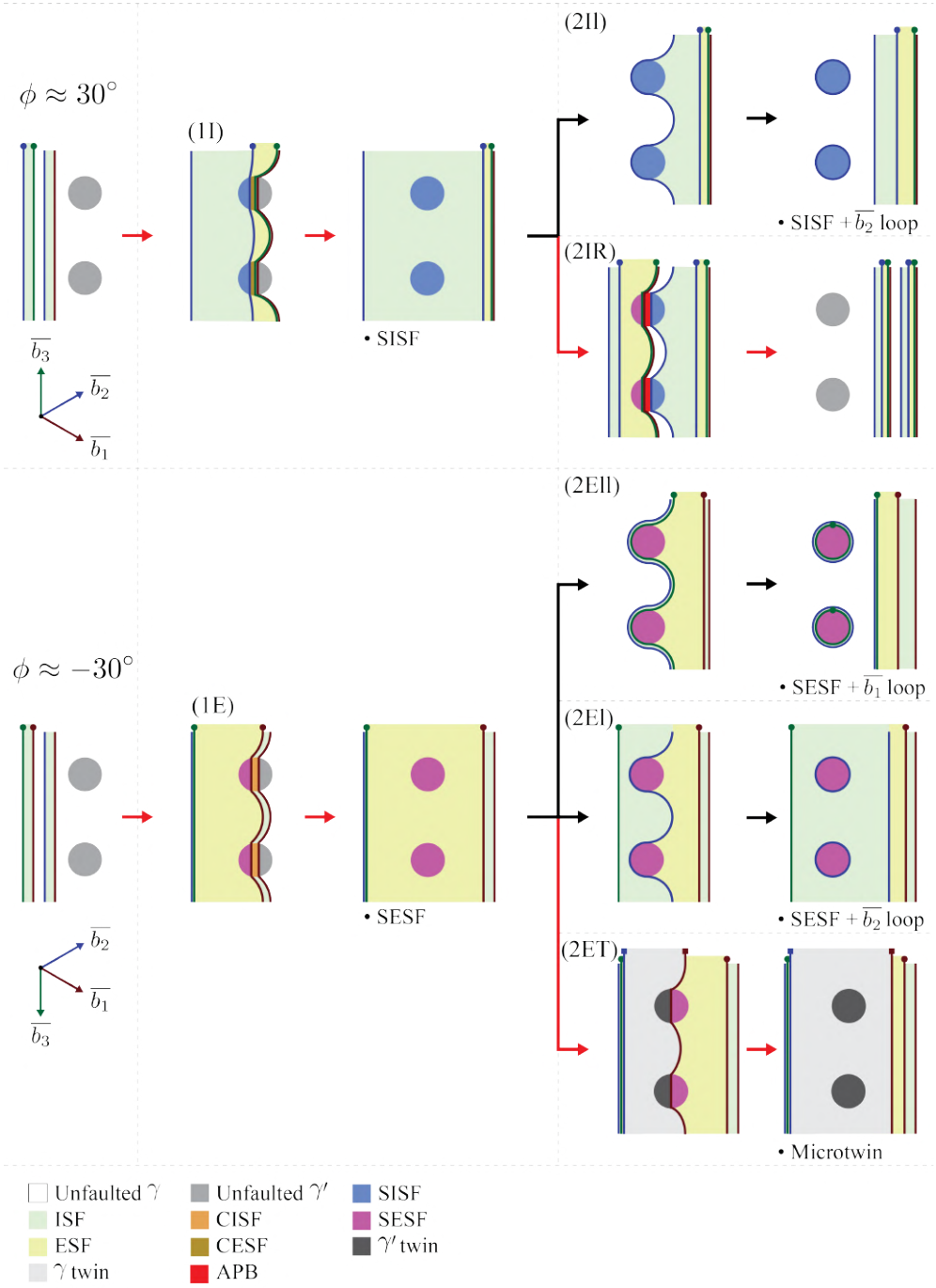

Fig. 6.9 - Schematic diagrams of the segregation assisted stacking fault shearing mechanisms, where dislocations glide from left to right. A dot or square on top of a dislocation indicates that it is gliding on an adjacent plane. Black and red arrows denote the athermal or thermally-assisted nature of the mechanism, respectively. The defects left after the sweeping of each partial are annotated.

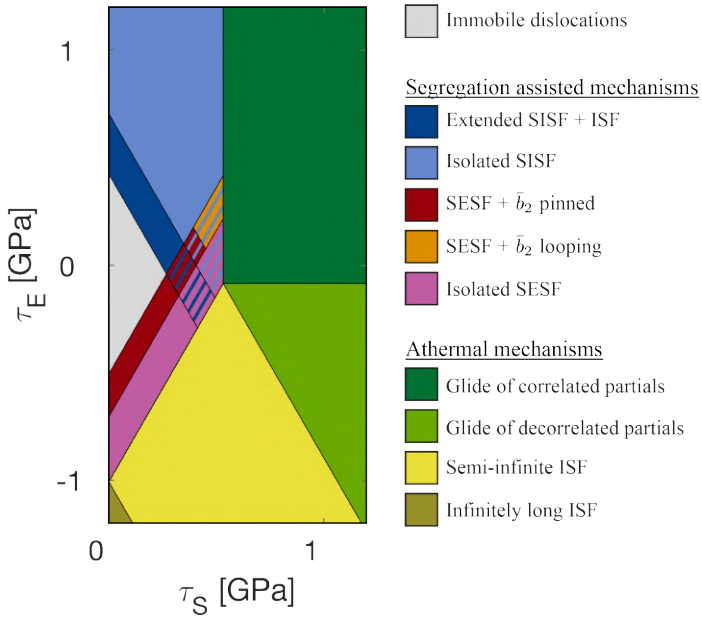

Fig. 6.10 - Regions for the athermal and segregation assisted mechanisms of precipitate bypassing in an alloy with cuboidal precipitates. The striped regions indicate that the mechanisms of both colours are operative. The values used for the calculation are $H = 20$ nm, $\nu = 0.33$, $\mu = 58.6$ GPa, $b = 0.253$ nm, $\alpha = 1$, $\gamma_{ISF} = 10$ mJ/m^2, $\gamma_{ESF} = 10$ mJ/m^2, $\gamma_{APB} = 276$ mJ/m^2, $\gamma_{CISF} = 196$ mJ/m^2, $\gamma_{CESF} = 268$ mJ/m^2, $\gamma_{SISF} = 62$ mJ/m^2, $\gamma_{SESF} = 74$ mJ/m^2.

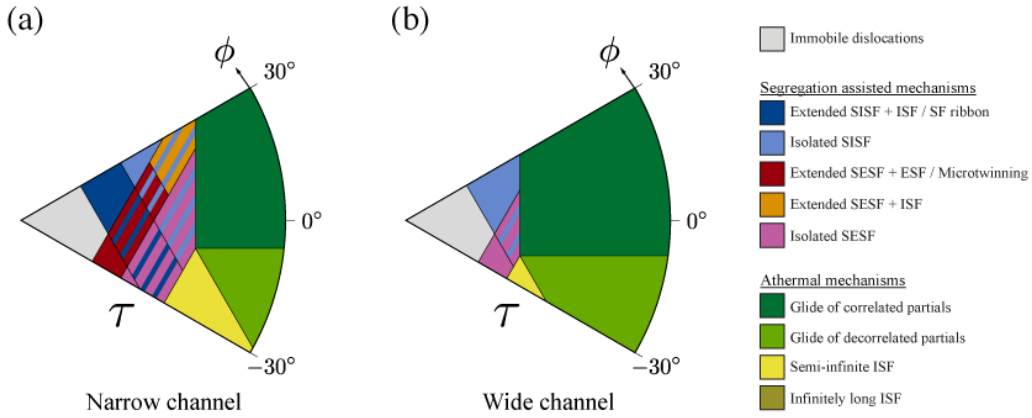

Fig. 6.11 - Stress-orientation maps of athermal and segregation assisted precipitate bypassing mechanisms for alloys with (a) narrow or (b) wide γ channels. The striped regions indicate that the mechanisms of both colours are operative.

variation found in real materials (more predominantly in polycrystals) is the cause for the variety of mechanisms seen in any given sample.

6.4 Conclusions

The current chapter develops a comprehensive theory that explains the orientation dependence for the appearance of planar faults in nickel based superalloys. The rationale behind this involves a sequential analysis of the forces in each Shockley partial that result in orientation dependent conditions for obstacle bypassing. The appearance of each mechanism can then be located at specific regions of a stress orientation map. The main finding are:

- The derivation of athermal stacking fault propagation criteria allows for a clear understanding of the effect of each force involved regardless of the precipitate morphology. The different scenarios proposed in alloys with an array of spherical precipitates derive into the first ever full explanation for the appearance of isolated and continuous ISFs with and without holes.

- The extension of this theory to include thermally assisted stacking fault propagation constitutes a comprehensive description of the orientation effects in creep at intermediate temperatures. The analysis includes the formation of SISFs, SESFs and microtwinning in their respective isolated and extended configurations. Qualitative agreement with experimental results in single crystals found in the literature is observed for the dependence on orientation and stress.

- Mechanistic maps that include stress, orientation and precipitate size have been developed based on the framework developed in Chapter 5. Simultaneously accounting for all the slip systems in a crystal explains the formation of different types of faults for a given test. The orientation dependence described based on angle ϕ allows for the application of these maps for the phenomenological description of creep deformation mechanisms in any stress state, extending the scope of the model beyond uniaxial loading.

The theoretical nature of the analysis developed in this chapter requires further experimental validation. Yet, it may be used as a guide in the search for a full understanding of the creep deformation pathways that develop at intermediate temperatures. A series of predictions that derive from this model and the precise experimentation required to test these ideas is further detailed in Chapter 7.

Chapter 7

Conclusions and future work

The current work sheds new light on different aspects of the plastic deformation behaviour in nickel-based superalloys through a combination of experimental techniques and modelling-based reasoning. This chapter summarises the main findings on the two topics discussed, *i.e.* low cycle fatigue and effects of the stress orientation in the propagation of planar faults. As is common in science, the results found give rise to new questions that will require a big effort to answer, but they also provide the tools necessary to step in that direction. Multiple research lines that derive from the work done during this PhD are also introduced and discussed in this chapter.

Key elements of the evolution of the dislocation structures during low cycle fatigue in RR1000 have been found. Slip band characterisation was performed at a level never achieved before by combining a series of electron microscopy techniques. The distinct nature of discrete closely spaced slip lines within a slip band was resolved and quantified for the first time within the bulk of the material. Instances of the double cross slip mechanism for the activation of nearby slip planes were found. The effect of non-coplanar stacking faults during the first cycles was identified, acting as semi-permeable membranes that hinder dislocation glide and promote the formation of multipoles. The higher spread of slip bands at a higher temperature was observed, in agreement with the literature, but the same behaviour at the level of individual slip lines was quantified here for the first time. These findings offer a more complete description of the evolution of slip bands and their continued degradation effect on the precipitate array.

A possible way of continuing this work is to characterise the slip bands for further temperature or strain amplitude conditions, but of more potential interest is an investigation on the behaviour of cyclic dislocation transmission through stacking faults at the atomic level. The mechanism proposed for dislocations with a 60° character needs validation, which could be obtained via molecular dynamics in a similar way to studies for transmission through

grain boundaries [265]. Fully understanding these interactions and their effect on the stress response and crack initiation processes may give a technological advancement as the stacking fault distribution can be affected with the heat treatments.

The development of a new technique used to quantify the shear step lengths and slip line spacings from γ'-etched micrographs proved valuable in the study of RR1000 due to its large secondary precipitates. Even though this technique can only be used in alloys with relatively large precipitates, the data it produces cannot be matched with other current techniques. The statistical results produced in this way offer a quantitative comparison between samples deformed at different temperatures and number of cycles.

The physics-based cyclic deformation model produced from the previous findings offers an explanation for the cyclic hardening and cyclic softening behaviour observed in coherent precipitate reinforced alloys in a simplistic way. Linking both regimes of the macroscopic response with the formation and evolution of the slip bands in the alloy 718Plus highlights the importance of characterising the dislocation structures. The effects of γ' size and volume fraction on the cyclic softening were reproduced on the sole basis of continued precipitate shearing. Nonetheless, additional factors must be accounted for a full explanation of this behaviour, *e.g.* the evolution of the dislocation structure. A future incorporation of the presented hardening and softening ideas into constitutive equations within a crystal plasticity model is straightforward, although the benefits would be inconsequential; a deeper understanding of the evolution of the dislocation structure is required.

The increased damage and precipitate dissolution observed near the surface cracks provides direct evidence of the effect precipitate shearing can have during cyclic failure. The effect of precipitate size on the localisation of slip must be accounted for in the analysis of crack initiation and early stages of crack propagation.

The framework introduced in Chapter 5 constitutes a novel and unique way of rationalising the effects of stress orientation on dislocation behaviour. Being this a very fundamental analysis, it was preferred to generalise the ideas to all fcc crystals. Exploring the case of uniaxial loading for all possible orientations, a description based on the variation of angle ϕ is used to explain the variation in the behaviours observed, with twin propagation as an example. The explanations given are more comprehensive and intuitive than all the others in the literature. An analysis on the Copley-Kear-Byun and Li's mechanisms for twin nucleation gives results that contradict experimental data, deeming these unrealistic.

The use of this framework for the analysis of stacking fault propagation in nickel-based superalloys further proves the capabilities of this approach. The development of the analytical model for athermal faults matches results produced by simulations from the literature and

expands on the interpretation of how different regimes naturally arise from considering the forces in the individual partials.

The extension of this model onto the segregation assisted superlattice fault propagation is the first one to fully capture the orientation dependence of the multiple types of faults. The development of mechanistic maps based on stress, orientation and microstructure should help as a guide for future research in the area. Additional validation of the model must come in the form of an experimental matrix that focuses mostly on stress and orientation for a given alloy and temperature. Quantification of the types, numbers and lengths of the faults on the two most active slip planes will set the basis for a comprehensive understanding of creep deformation at intermediate temperatures. Coupling EBSD with TEM in polycrystalline alloys could be a fast and reliable way of achieving this, although special care will need to be taken to differentiate between grain boundary effects and bulk deformation behaviour.

The orientation analysis framework is specially valuable due to its generality. Even though this dissertation only covers the propagation of planar faults, other plastic deformation mechanisms could be rationalised with a similar approach. In particular, the study of cross slip related mechanisms would be likely to benefit from the stress orientation maps. The links between conjugate slip systems can be drawn in maps such as that in Figure 7.1, so that the stress in multiple planes can be accounted for. Future work involves developing line tension approaches for the calculation of stress orientation dependent cross slip energy barriers, following a model developed by Kang *et al.* [196].

A good example of such a study is that on the localisation of plastic deformation during low cycle fatigue. This derives from the analysis in Chapter 3 on the spread of slip bands among different grains of the RR1000 samples fatigued at 700°C. As mentioned before, the three grains encountered with homogeneous deformation have a particularly low Schmid factor, but an Escaig factor with a high magnitude. This makes sense considering cross slip will be more likely to happen during either the tensile or the compressive stages due to the narrower stacking fault widths. An orientation analysis considering the cross slip energy barriers for different uniaxial loads may explain this behaviour. Experimental validation could be carried out together with extensive EBSD coupled with ECCI slip band volume fraction characterisation via the FFT filter introduced in Chapter 4. The analysis of the spread of deformation during monotonic loading may be a first step before diving into the fatigue analysis.

Additional potential applications of the orientation analysis framework have been thought through in less detail. Upon linking the orientation framework with cross slip, twin nucleation can be further investigated following the ideas from Section 5.4. More complicated mechanisms can be scrutinised and compared against the extensive data published in the literature.

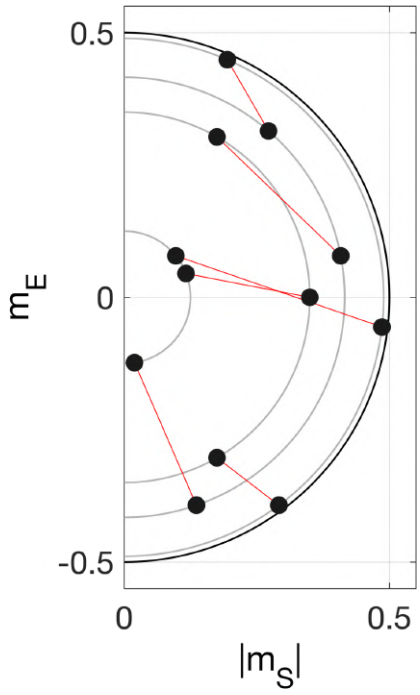

Fig. 7.1 - Orientation map of a uniaxial load along a ⟨124⟩ direction with red lines linking conjugate slip systems.

A more developed line tension model may be able to predict orientation dependent energy barriers for more complex dislocation reactions, such as the formation of Frank partials or stair-rod dislocations, required for mechanisms proposed [65, 236, 266] and observed [267] in the literature.

The study of the effects of lattice rotation for tests with a large deformation (such as those preceding twin nucleation in TWIP steels) may also benefit from the current framework. As shown in Figure 7.2, the trajectory followed by a grain in the fundamental sector can be simultaneously mapped to the stresses on all the slip systems within an orientation map, allowing for a better understanding of the evolution of the dislocations in such a crystal.

The new doors that the orientation analysis framework will open in the study of deformation mechanisms in different alloying systems look promising at the very least. Its generality and applicability in the study of very different deformation mechanisms make it worth extending this model. The incorporation of stresses normal to the slip plane can be attempted, although a three-dimensional map may lose some its intuitiveness. Ways of introducing cubic slip systems may have similar drawbacks, but the benefits if successful would be considerable. Moreover, while this model seems natural for an fcc crystal due to its high symmetry, analogous frameworks in bcc or hcp materials could be developed.

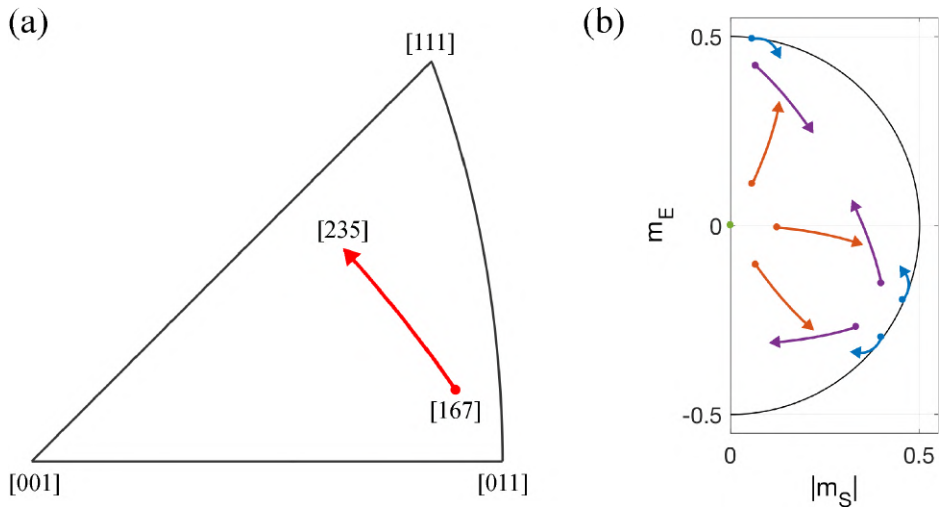

Fig. 7.2 - (a) Arbitrary lattice rotation trajectory in the fundamental sector and (b) its associated evolution of the stresses in all the $\frac{a}{2}\langle 110\rangle\{111\}$ slip systems in an orientation map. Arrows of the same colour correspond to coplanar slip systems.

References

[1] Air Transport Action Group. ATAG: Facts and Figures, 2018.

[2] Rolls-Royce. Market Outlook forecast summary 2014, 2014.

[3] CAVOK a Division of Oliver Wyman and T. Cooper. Global Engine Fleet and Market Forecast 2015-2025, 2015.

[4] J. Verstraete. No Title. Technical report, Hamburg University of Applied Sciences, 2012.

[5] International Air Transport Association. IATA Fuel Fact Sheet. Technical report, IATA, 2019.

[6] Rolls-Royce. *The jet engine*. John Wiley & Sons, Inc, London, 2005.

[7] N. Cumpsty. *Jet propulsion: A simple guide to the aerodynamic and thermodynamic design and performance of jet engines*. Cambridge University Press, Cambridge, 2003.

[8] D. Lambert. *Fatigue damage accumulation in nickel base superalloys*. PhD thesis, University of Sheffield, 1994.

[9] R. Corran and S. Williams. Lifing methods and safety criteria in aero gas turbines. *Engineering Failure Analysis*, 14(3):518–528, 2007.

[10] M. Risbet and X. Feaugas. Some comments about fatigue crack initiation in relation to cyclic slip irreversibility. *Engineering Fracture Mechanics*, 75(11):3511–3519, 2008.

[11] M. Durand-Charre. *The Microstructure of Superalloys*. CRC Press, Florida, 1st edition, 1997.

[12] J. R. Davis. *Nickel, Cobalt and Their Alloys*. ASM International The Materials Information Society, Ohio, 1st edition, 2000.

[13] S. L. Shang, C. L. Zacherl, H. Z. Fang, Y. Wang, Y. Du, and Z. K. Liu. Effects of alloying element and temperature on the stacking fault energies of dilute Ni-base superalloys. *Journal of Physics: Condensed Matter*, 24(50):505403, 2012.

[14] R. Fleischer. Substitutional solution hardening. *Acta Metallurgica*, 11(3):203–209, 1963.

[15] R. C. Reed. *The Superalloys: Fundamentals and Applications*. Cambridge University Press, Cambridge, 2006.

[16] R. A. Ricks, A. J. Porter, and R. C. Ecob. The growth of gamma prime precipitates in nickel-base superalloys. *Acta Metallurgica*, 31(1):43–53, 1983.

[17] E. Pickering, H. Mathur, A. Bhowmik, O. Messé, J. Barnard, M. Hardy, R. Krakow, K. Loehnert, H. Stone, and C. Rae. Grain-boundary precipitation in Allvac 718Plus. *Acta Materialia*, 60(6-7):2757–2769, 2012.

[18] A. S. Wilson. Formation and effect of topologically close-packed phases in nickel-base superalloys. *Materials Science and Technology*, 33(9):1108–1118, 2017.

[19] F. Sun, J. Tong, Q. Feng, and J. Zhang. Microstructural evolution and deformation features in gas turbine blades operated in-service. *Journal of Alloys and Compounds*, 618:728–733, 2015.

[20] D. Barba, E. Alabort, S. Pedrazzini, D. Collins, A. Wilkinson, P. Bagot, M. Moody, C. Atkinson, A. Jérusalem, and R. Reed. On the microtwinning mechanism in a single crystal superalloy. *Acta Materialia*, 135:314–329, 2017.

[21] A. G. Jackson. *Handbook of Crystallography For Electron Microscopists and Others*. Springer-Verlag, New York, 1st edition, 1991.

[22] N. Thompson. Dislocation Nodes in Face-Centred Cubic Lattices. *Proceedings of the Physical Society. Section B*, 66(6):481–492, 1953.

[23] P. M. Anderson, J. P. Hirth, and J. Lothe. *Theory of dislocations*. Cambridge University Press, New York, 3rd edition, 2017.

[24] R. R. Unocic, N. Zhou, L. Kovarik, C. Shen, Y. Wang, and M. J. Mills. Dislocation decorrelation and relationship to deformation microtwins during creep of a γ' precipitate strengthened Ni-based superalloy. *Acta Materialia*, 59:7325–7339, 2011.

[25] H. Mughrabi. Cyclic Slip Irreversibilities and the Evolution of Fatigue Damage. *Metallurgical and Materials Transactions B*, 40(4):431–453, 2009.

[26] P. Lukáš and L. Kunz. Role of persistent slip bands in fatigue. *Philosophical Magazine*, 84(3-5):317–330, 2004.

[27] S. Mahajan. Critique of mechanisms of formation of deformation, annealing and growth twins: Face-centered cubic metals and alloys. *Scripta Materialia*, 68(2):95–99, 2013.

[28] F. Pettinari, J. Douin, G. Saada, P. Caron, A. Coujou, and N. Cle. Stacking fault energy in short-range ordered gamma-phases of Ni-based superalloys. *Materials Science and Engineering A*, 325:511–519, 2002.

[29] A. Pineau and S. D. Antolovich. High temperature fatigue of nickel-base superalloys - A review with special emphasis on deformation modes and oxidation. *Engineering Failure Analysis*, 16(8):2668–2697, 2009.

[30] B. Escaig. Sur le glissement dévié des dislocations dans la structure cubique à faces centrées. *Journal de Physique*, 29(2-3):225–239, 1968.

[31] W. Püschl. Models for dislocation cross-slip in close-packed crystal structures: a critical review. *Progress in Materials Science*, 47(4):415–461, 2002.

[32] R. Madec, B. Devincre, and L. Kubin. Simulation of dislocation patterns in multislip. *Scripta Materialia*, 47(10):689–695, 2002.

[33] G. Ananthakrishna. Current theoretical approaches to collective behavior of dislocations. *Physics Reports*, 440(4-6):113–259, 2007.

[34] J. Kratochvíl and M. Kružík. Statistically motivated model of mechanisms controlling evolution of deformation band substructure. *International Journal of Plasticity*, 81:196–208, 2016.

[35] K. Yashiro, F. Kurose, Y. Nakashima, K. Kubo, Y. Tomita, and H. Zbib. Discrete dislocation dynamics simulation of cutting of γ' precipitate and interfacial dislocation network in Ni-based superalloys. *International Journal of Plasticity*, 22(4):713–723, 2006.

[36] M. Huang, L. Zhao, and J. Tong. Discrete dislocation dynamics modelling of mechanical deformation of nickel-based single crystal superalloys. *International Journal of Plasticity*, 28(1):141–158, 2012.

[37] W. W. Milligan and S. D. Antolovich. Yielding and deformation behavior of the single crystal superalloy PWA 1480. *Metallurgical Transactions A*, 18(1):85–95, 1987.

[38] A. J. Ardell and J. C. Huang. Antiphase boundary energies and the transition from shearing to looping in alloys strengthened by ordered precipitates. *Philosophical Magazine Letters*, 58(May):189–197, 1988.

[39] R. Kozar, A. Suzuki, W. Milligan, J. Schirra, M. Savage, and T. Pollock. Strengthening Mechanisms in Polycrystalline Multimodal Nickel-Base Superalloys. *Metallurgical and Materials Transactions A*, 40(7):1588–1603, 2009.

[40] E. Galindo-Nava, L. Connor, and C. Rae. On the prediction of the yield stress of unimodal and multimodal γ' Nickel-base superalloys. *Acta Materialia*, 98:377–390, 2015.

[41] G. Molenat and D. Caillard. Dislocation mechanisms in Ni3Al at room temperature. In situ straining experiments in TEM. *Philosophical Magazine A*, 64(6):1291–1317, 1991.

[42] E. Conforto, G. Molénat, and D. Caillard. Comparison of Ni-based alloys with extreme values of antiphase boundary energies: dislocation mechanisms and mechanical properties. *Philosophical Magazine*, 85(2-3):117–137, 2005.

[43] Q. Qin and J. L. Bassani. Non-Schmid yield behavior in single crystals. *Journal of the Mechanics and Physics of Solids*, 40(4):813–833, 1992.

[44] M. Kolbe. The high temperature decrease of the critical resolved shear stress in nickel-base superalloys. *Materials Science and Engineering: A*, 319-321:383–387, 2001.

[45] D. Barba, T. M. Smith, J. Miao, M. J. Mills, and R. C. Reed. Segregation-Assisted Plasticity in Ni-Based Superalloys. *Metallurgical and Materials Transactions A*, 49(9):4173–4185, 2018.

[46] G. Viswanathan, R. Shi, A. Genc, V. Vorontsov, L. Kovarik, C. Rae, and M. Mills. Segregation at stacking faults within the γ' phase of two Ni-base superalloys following intermediate temperature creep. *Scripta Materialia*, 94:5–8, 2015.

[47] V. Vorontsov, L. Kovarik, M. Mills, and C. Rae. High-resolution electron microscopy of dislocation ribbons in a CMSX-4 superalloy single crystal. *Acta Materialia*, 60(12):4866–4878, 2012.

[48] R. Unocic, G. Viswanathan, P. Sarosi, S. Karthikeyan, J. Li, and M. Mills. Mechanisms of creep deformation in polycrystalline Ni-base disk superalloys. *Materials Science and Engineering: A*, 483-484(1-2 C):25–32, 2008.

[49] N. Matan, D. Cox, P. Carter, M. Rist, C. Rae, and R. Reed. Creep of CMSX-4 superalloy single crystals: effects of misorientation and temperature. *Acta Materialia*, 47(5):1549–1563, 1999.

[50] C. Rae and R. Reed. Primary creep in single crystal superalloys: Origins, mechanisms and effects. *Acta Materialia*, 55(3):1067–1081, 2007.

[51] G. Viswanathan, P. Sarosi, M. Henry, D. Whitis, W. Milligan, and M. Mills. Investigation of creep deformation mechanisms at intermediate temperatures in René 88 DT. *Acta Materialia*, 53(10):3041–3057, 2005.

[52] L. Kovarik, R. Unocic, J. Li, P. Sarosi, C. Shen, Y. Wang, and M. Mills. Microtwinning and other shearing mechanisms at intermediate temperatures in Ni-based superalloys. *Progress in Materials Science*, 54(6):839–873, 2009.

[53] A. S. Argon. *Strengthening Mechanisms in Crystal Plasticity*. Oxford University Press, Oxford, 1st edition, 2008.

[54] D. Geissler, J. Freudenberger, A. Kauffmann, M. Krautz, H. Klauss, A. Voss, J. Eickemeyer, and L. Schultz. Appearance of dislocation-mediated and twinning-induced plasticity in an engineering-grade FeMnNiCr alloy. *Acta Materialia*, 59(20):7711–7723, 2011.

[55] E. I. Kuprekova, Y. I. Chumlyakov, and I. P. Chernov. Dependence of critical cleavage stresses as a function of orientation and temperature in single crystals of Fe-18% Cr-14% Ni-2% Mo austenitic stainless steel containing hydrogen. *Metal Science and Heat Treatment*, 50(5-6):282–288, 2008.

[56] J. Douin, F. Pettinari-Sturmel, and A. Coujou. Dissociated dislocations in confined plasticity. *Acta Materialia*, 55(19):6453–6458, 2007.

[57] H. Deutchman, P. Phillips, N. Zhou, M. Samal, S. Ghosh, Y. Wang, and M. Mills. Deformation Mechanisms Coupled with Phase Field and Crystal Plasticity Modeling in a High-Temperature Polycrystalline Ni-Based Superalloy. In *Superalloys 2012, Proceedings of the International Symposium on Superalloys*, pages 25–33. TMS, 2012.

[58] T. M. Smith, L. V. Duchao, T. Hanlon, A. Wessman, Y. Wang, and M. J. Mills. Determination of Orientation and Alloying Effects on Creep Response and Deformation Mechanisms in Single Crystals of Ni-Base Disk Superalloys. In *Superalloys 2016, Proceedings of the International Symposium on Superalloys*, pages 579–588. TMS, 2016.

[59] I. Karaman, H. Sehitoglu, Y. I. Chumlyakov, and H. J. Maier. The deformation of low-stacking-fault-energy austenitic steels. *JOM*, 54(7):31–37, 2002.

[60] W. S. Choi, B. C. De Cooman, S. Sandlöbes, and D. Raabe. Size and orientation effects in partial dislocation-mediated deformation of twinning-induced plasticity steel micro-pillars. *Acta Materialia*, 98:391–404, 2015.

[61] S. Cai, X. Li, and N. Tao. Orientation dependence of deformation twinning in Cu single crystals. *Journal of Materials Science & Technology*, 34(8):1364–1370, 2018.

[62] I. Gutierrez-Urrutia, S. Zaefferer, and D. Raabe. The effect of grain size and grain orientation on deformation twinning in a Fe–22wt.% Mn–0.6wt.% C TWIP steel. *Materials Science and Engineering: A*, 527(15):3552–3560, 2010.

[63] I. Gutierrez-Urrutia and D. Raabe. Dislocation and twin substructure evolution during strain hardening of an Fe–22wt.% Mn–0.6wt.% C TWIP steel observed by electron channeling contrast imaging. *Acta Materialia*, 59(16):6449–6462, 2011.

[64] I. Gutierrez-Urrutia and D. Raabe. Study of Deformation Twinning and Planar Slip in a TWIP Steel by Electron Channeling Contrast Imaging in a SEM. *Materials Science Forum*, 702-703:523–529, 2012.

[65] I. Karaman, H. Sehitoglu, Y. Chumlyakov, H. Maier, and I. Kireeva. Extrinsic stacking faults and twinning in Hadfield manganese steel single crystals. *Scripta Materialia*, 44(2):337–343, 2001.

[66] B. C. De Cooman, Y. Estrin, and S. K. Kim. Twinning-induced plasticity (TWIP) steels. *Acta Materialia*, 142:283–362, 2018.

[67] D. Knowles and S. Gunturi. The role of <112>{111} slip in the asymmetric nature of creep of single crystal superalloy CMSX-4. *Materials Science and Engineering: A*, 328(1-2):223–237, 2002.

[68] D. Knowles and Q. Chen. Superlattice stacking fault formation and twinning during creep in γ/γ' single crystal superalloy CMSX-4. *Materials Science and Engineering: A*, 340(1-2):88–102, 2003.

[69] N. Tsuno, S. Shimabayashi, K. Kakehi, C. M. F. Rae, and R. C. Reed. Tension/Compression asymmetry in yield and creep strengths of Ni-based superalloys. In *Superalloys 2008, Proceedings of the International Symposium on Superalloys*, pages 433–442, 2008.

[70] H. Mughrabi. Cyclic slip irreversibility and fatigue life: A microstructure-based analysis. *Acta Materialia*, 61(4):1197–1203, 2013.

[71] H. Mughrabi. Microstructural fatigue mechanisms: Cyclic slip irreversibility, crack initiation, non-linear elastic damage analysis. *International Journal of Fatigue*, 57:2–8, 2013.

[72] L. Brown. Dislocation plasticity in persistent slip bands. *Materials Science and Engineering: A*, 285(1-2):35–42, 2000.

[73] N. Thompson, N. Wadsworth, and N. Louat. The origin of fatigue fracture in copper. *Philosophical Magazine*, 1(July 2014):113–126, 1956.

[74] B. Lerch and V. Gerold. Room temperature deformation mechanisms in Nimonic 80A. *Acta Metallurgica*, 33(9):1709–1716, 1985.

[75] M. Petrenec, K. Obrtlík, and J. Polák. Inhomogeneous dislocation structure in fatigued INCONEL 713 LC superalloy at room and elevated temperatures. *Materials Science and Engineering: A*, 400-401(1-2 SUPPL.):485–488, 2005.

[76] H. Ho, M. Risbet, and X. Feaugas. On the unified view of the contribution of plastic strain to cyclic crack initiation: Impact of the progressive transformation of shear bands to persistent slip bands. *Acta Materialia*, 85:155–167, 2015.

[77] J. C. Fisher, E. W. Hart, and R. H. Pry. Theory of Slip-Band Formation. *Physical Review*, 87(6):958–961, 1952.

[78] A. K. Faradjian, L. H. Friedman, and D. C. Chrzan. Frank-Read sources within a continuum simulation. *Modelling and Simulations in Materials Science and Engineering*, 7:479–494, 1999.

[79] A. Cottrell. LX. The formation of immobile dislocations during slip. *The London, Edinburgh, and Dublin Philosophical Magazine and Journal of Science*, 43(341):645–647, 1952.

[80] J. Friedel. The mechanism of work-hardening and slip-band formation. *Proceedings of the Royal Society of London. Series A. Mathematical and Physical Sciences*, 242(1229):147–159, 1957.

[81] U. Kocks and H. Mecking. Physics and phenomenology of strain hardening: the FCC case. *Progress in Materials Science*, 48(3):171–273, 2003.

[82] M. F. Kanninen and A. R. Rosenfield. Dynamics of dislocation pile-up formation. *Philosophical Magazine*, 20(165):569–587, 1969.

[83] P. Steif and R. Clifton. On the kinetics of a Frank-Read source. *Materials Science and Engineering*, 41(2):251–258, 1979.

[84] L. H. Friedman D. C. Chrzan. Continuum analysis of dislocation pile-ups: influence of sources. *Philosophical Magazine A*, 77(5):1185–1204, 1998.

[85] S. S. Chakravarthy and W. Curtin. Effect of source and obstacle strengths on yield stress: A discrete dislocation study. *Journal of the Mechanics and Physics of Solids*, 58(5):625–635, 2010.

[86] S. Sandfeld, T. Hochrainer, T. E. Simos, G. Psihoyios, C. Tsitouras, and Z. Anastassi. Towards Frank-Read Sources in the Continuum Dislocation Dynamics Theory. In *AIP Conference Proceedings*, volume 1389, pages 1531–1534, 2011.

[87] S. Akarapu and J. Hirth. Dislocation pile-ups in stress gradients revisited. *Acta Materialia*, 61(10):3621–3629, 2013.

[88] F. Pettinari-sturmel, M. Jouiad, H. O. K. Kirchner, N. Clément, and A. Coujou. Local disordering and reordering phenomena induced by mobile dislocations in short-range-ordered solid solutions. *Philosophical Magazine A*, 82(16):3045–3054, 2002.

[89] J. S. Koehler. The Nature of Work-Hardening. *Physical Review*, 86(1):52–59, 1952.

[90] B. Devincre, L. Kubin, C. Lemarchand, and R. Madec. Mesoscopic simulations of plastic deformation. *Materials Science and Engineering: A*, 309-310:211–219, 2001.

[91] C. Déprés, C. Robertson, and M. Fivel. Crack initiation in fatigue: experiments and three-dimensional dislocation simulations. *Materials Science and Engineering: A*, 387-389(1-2 SPEC. ISS.):288–291, 2004.

[92] U. Messerschmidt and M. Bartsch. Generation of dislocations during plastic deformation. *Materials Chemistry and Physics*, 81(2-3):518–523, 2003.

[93] C. Déprés, C. F. Robertson, and M. C. Fivel. Low-strain fatigue in AISI 316L steel surface grains: a three-dimensional discrete dislocation dynamics modelling of the early cycles I. Dislocation microstructures and mechanical behaviour. *Philosophical Magazine*, 84(22):2257–2275, 2004.

[94] Z. Wang, I. Beyerlein, and R. LeSar. Slip band formation and mobile dislocation density generation in high rate deformation of single fcc crystals. *Philosophical Magazine*, 88(9):1321–1343, 2008.

[95] A. M. Hussein, S. I. Rao, M. D. Uchic, D. M. Dimiduk, and J. A. El-Awady. Microstructurally based cross-slip mechanisms and their effects on dislocation microstructure evolution in fcc crystals. *Acta Materialia*, 85:180–190, 2015.

[96] Y. Li and C. Laird. Cyclic response and dislocation structures of AISI 316L stainless steel. Part 2: polycrystals fatigued at intermediate strain amplitude. *Materials Science and Engineering: A*, 186(1-2):87–103, 1994.

[97] R. Stoltz and A. Pineau. Dislocation-precipitate interaction and cyclic stress-strain behavior of a γ' strengthened superalloy. *Materials Science and Engineering*, 34(3):275–284, 1978.

[98] C. Shin, M. Fivel, M. Verdier, and C. Robertson. Dislocation dynamics simulations of fatigue of precipitation-hardened materials. *Materials Science and Engineering: A*, 400-401:166–169, 2005.

[99] C. S. Shin, C. F. Robertson, and M. C. Fivel. Fatigue in precipitation hardened materials: a three-dimensional discrete dislocation dynamics modelling of the early cycles. *Philosophical Magazine*, 87(24):3657–3669, 2007.

[100] A. P. L. Turner. Cyclic deformation behavior of type 304 stainless steel at elevated temperature. *Metallurgical Transactions A*, 10(2):225–234, 1979.

[101] V. S. Srinivasan, R. Sandhya, K. Bhanu, S. Rao, S. L. Mannan, and K. S. Raghavan. Effects of temperature on the low cycle fatigue behaviour of nitrogen alloyed type 316L stainless steel. *International Journal of Fatigue*, 13(6):471–478, 1991.

[102] M. Petrenec, J. Polák, T. Samoril, J. Dluhos, and K. Obrtlík. In-Situ High Temperature Low Cycle Fatigue Study of Surface Topography Evolution in Nickel Superalloys. In *METAL 2014 - 23rd International Conference on Metallurgy and Materials, Conference Proceedings*, pages 1139–1144, Brno, 2014.

[103] C. Huvier, E. Conforto, H. E. Alami, D. Delafosse, and X. Feaugas. Some correlations between slip band emergence and dislocation pattern. *IOP Conference Series: Materials Science and Engineering*, 3:012012, 2009.

[104] B. A. Lerch and V. Gerold. Cyclic hardening mechanisms in NIMONIC 80A. *Metallurgical Transactions A*, 18(12):2135–2141, 1987.

[105] V. Subramanya Sarma, M. Sundararaman, and K. A. Padmanabhan. Effect of γ' size on room temperature low cycle fatigue behaviour of a nickel base superalloy. *Materials Science and Technology*, 14(7):669–675, 1998.

[106] D. Khireddine, R. Rahouadj, and M. Clavel. Irreversibility of strain during low-cycle fatigue experiments of a precipitation-hardened alloy. *Philosophical Magazine A*, 77(6):1555–1566, 1998.

[107] M. Risbet, X. Feaugas, C. Guillemer-Neel, and M. Clavel. Use of atomic force microscopy to quantify slip irreversibility in a nickel-base superalloy. *Scripta Materialia*, 49(6):533–538, 2003.

[108] C. Calabrese and C. Laird. Cyclic stress—strain response of two-phase alloys Part I. Microstructures containing particles penetrable by dislocations. *Materials Science and Engineering*, 13(2):141–157, 1974.

[109] M. Clavel and A. Pineau. Fatigue behaviour of two nickel-base alloys I: Experimental results on low cycle fatigue, fatigue crack propagation and substructures. *Materials Science and Engineering*, 55(2):157–171, 1982.

[110] J. Huang and G. Gray. Microband formation in shock-loaded and quasi-statically deformed metals. *Acta Metallurgica*, 37(12):3335–3347, 1989.

[111] B. A. Lerch, N. Jayaraman, and S. D. Antolovich. A study of fatigue damage mechanisms in Waspaloy from 25 to 800°C. *Materials Science and Engineering*, 66(2):151–166, 1984.

[112] G. Venkataraman, Y. Chung, and T. Mura. Application of minimum energy formalism in a multiple slip band model for fatigue—II. Crack nucleation and derivation of a generalised Coffin-Manson law. *Acta Metallurgica et Materialia*, 39(11):2631–2638, 1991.

[113] V. Gregor, J. Kratochvíl, and M. Saxlová. The model of PSB formation. *Materials Science and Engineering: A*, 234-236(0):209–211, 1997.

[114] V. Gregor and J. Kratochvíl. Internal stress, width, and density of persistent slip bands. *Scripta Materialia*, 40(4):491–496, 1999.

[115] M. Valsan, D. H. Sastry, K. B. sankara Rao, and S. L. Mannan. Effect of strain rate on the high-temperature low-cycle fatigue properties of a nimonic PE-16 superalloy. *Metallurgical and Materials Transactions A*, 25(1):159–171, 1994.

[116] V. Singh, M. Sundararaman, W. Chen, and R. P. Wahi. Low-cycle fatigue behavior of NIMONIC PE16 at room temperature. *Metallurgical Transactions A*, 22(2):499–506, 1991.

[117] M. Sundararaman, W. Chen, V. Singh, and R. Wahi. TEM investigation of γ' free bands in nimonic PE16 under LCF loading at room temperature. *Acta Metallurgica et Materialia*, 38(10):1813–1822, 1990.

[118] F. Humphreys and M. Hatherly. *Recrystallization and related annealing phenomena*. Elsevier, Oxford, 2 edition, 2004.

[119] P. Phillips, R. Unocic, and M. Mills. Low cycle fatigue of a polycrystalline Ni-based superalloy: Deformation substructure analysis. *International Journal of Fatigue*, 57:50–57, 2013.

[120] M. Risbet, X. Feaugas, and M. Clavel. Study of the cyclic softening of an under-aged gamma'-precipitated nickel-base superalloy (Waspaloy). *Journal de Physique IV*, 11(PR4):Pr4–293–Pr4–301, 2001.

[121] C. Calabrese and C. Laird. Cyclic stress—strain response of two-phase alloys Part II. Particles not penetrated by dislocations. *Materials Science and Engineering*, 13(2):159–174, 1974.

[122] P. Zhang, Q. Zhu, C. Hu, C.-j. Wang, G. Chen, and H.-y. Qin. Cyclic deformation behavior of a nickel-base superalloy under fatigue loading. *Materials & Design*, 69:12–21, 2015.

[123] Y. Brechet, F. Louchet, C. Marchionni, and J. L. Verger-Gaugry. Experimental (TEM and STEM) investigation and theoretical approach to the fatigue-induced dissolution of δ' precipitates in a 2.5 wt% Al-Li alloy. *Philosophical Magazine A*, 56(3):353–366, 1987.

[124] A.-W. Zhu. Evolution of size distribution of shearable ordered precipitates under homogeneous deformation: Application to an Al-Li-alloy. *Acta Materialia*, 45(10):4213–4223, 1997.

[125] A.-W. Zhu. Strain localization and formation of heterogeneous distribution of shearable ordered precipitates: application to an Al–10at.%Li single crystal. *Acta Materialia*, 46(9):3211–3220, 1998.

[126] W. Vogel, M. Wilhelm, and V. Gerold. Persistent slip bands in fatigued peak aged Al-Zn-Mg single crystals—I. Development of dislocation microstructure and change of precipitation distribution. *Acta Metallurgica*, 30(1):21–30, 1982.

[127] E. Köhler, E. Bischoff, and V. Gerold. Chemical analysis of persistent slip bands in an age-hardened aluminum-silver alloy by means of eds. *Scripta Metallurgica*, 18(7):699–702, 1984.

[128] Y. Brechet and Y. Estrin. On a pseudo-Portevin-Le Chatelier effect. *Scripta Metallurgica et Materialia*, 31(2):185–190, 1994.

[129] A. H. Cottrell and B. A. Bilby. Dislocation Theory of Yielding and Strain Ageing of Iron. *Proceedings of the Physical Society. Section A*, 62(1):49–62, 1949.

[130] S. D. Antolovich and R. W. Armstrong. Plastic strain localization in metals: origins and consequences. *Progress in Materials Science*, 59(1):1–160, 2014.

[131] R. V. Miner and M. G. Castelli. Hardening mechanisms in a dynamic strain aging alloy, HASTELLOY X, during isothermal and thermomechanical cyclic deformation. *Metallurgical Transactions A*, 23(2):551–561, 1992.

[132] S. L. Mannan. Role of dynamic strain ageing in low cycle fatigue. *Bulletin of Materials Science*, 16(6):561–582, 1993.

[133] G. Chai, P. Liu, and J. Frodigh. Cyclic deformation behaviour of a nickel base alloy at elevated temperature. *Journal of Materials Science*, 39(8):2689–2697, 2004.

[134] P. R. Barrett, R. Ahmed, M. Menon, and T. Hassan. Isothermal low-cycle fatigue and fatigue-creep of Haynes 230. *International Journal of Solids and Structures*, 88-89:146–164, 2016.

[135] R. Ahmed, P. R. Barrett, and T. Hassan. Unified viscoplasticity modeling for isothermal low-cycle fatigue and fatigue-creep stress–strain responses of Haynes 230. *International Journal of Solids and Structures*, 88-89:131–145, 2016.

[136] Z. Zhong, Y. Gu, Y. Yuan, T. Yokokawa, and H. Harada. On the low cycle fatigue behavior of a Ni-base superalloy containing high Co and Ti contents. *Materials Science and Engineering: A*, 552:434–443, 2012.

[137] K. Gopinath, A. Gogia, S. Kamat, R. Balamuralikrishnan, and U. Ramamurty. Low cycle fatigue behaviour of a low interstitial Ni-base superalloy. *Acta Materialia*, 57(12):3450–3459, 2009.

[138] E. W. Ross and C. T. Sims. Nickel-Base Alloys. In C. T. Sims, N. S. Stoloff, and W. C. Hagel, editors, *Superalloys II High Temperature Materials for Aerospace and Industrial Power*, pages 97–134. John Wiley & Sons, Inc, Michigan, 1987.

[139] S. D. Antolovich and N. Jayaraman. Metallurgical instabilities during the high temperature low cycle fatigue of nickel-base superalloys. *Materials Science and Engineering*, 57(1):L9–L12, 1983.

[140] A. Kelly and R. B. Nicholson. Precipitation Hardening. In *Modern Physical Metallurgy*, volume 10, pages 149–391. Oxford : Pergamon Press, 1963.

[141] S. D. Antolovich. Microstructural aspects of fatigue in Ni-base superalloys. *Philosophical Transactions of the Royal Society A: Mathematical, Physical and Engineering Sciences*, 373(2038):20140128–20140128, 2015.

[142] Y. H. He, L. J. Chen, P. K. Liaw, R. L. McDaniels, C. R. Brooks, R. R. Seeley, and D. L. Klarstrom. Low-Cycle Fatigue Behavior of HAYNES HR-120 alloy. *International Journal of Fatigue*, 24:161–931–942, 2002.

[143] J. del Valle, R. Romero, and A. Picasso. Stress saturation in a nickel-base superalloy, under different aging treatments. *Materials Science and Engineering: A*, 319-321:643–646, 2001.

[144] K. Maciejewski and H. Ghonem. Isotropic and kinematic hardening as functions of gamma prime precipitates in a nickel-based superalloy. *International Journal of Fatigue*, 68:123–135, 2014.

[145] E. F. Westbrooke, L. E. Forero, and F. Ebrahimi. Slip analysis in a Ni-base superalloy. *Acta Materialia*, 53(7):2137–2147, 2005.

[146] M. Valsan, P. Parameswaran, K. B. S. Rao, M. Vijayalakshmi, S. L. Mannah, and D. H. Shastry. High-temperature low-cycle fatigue behavior of a nimonic PE-16 superalloy — correlation with deformation and fracture. *Metallurgical Transactions A*, 23A(6):1751–1768, 1992.

[147] P. J. Phillips, R. R. Unocic, L. Kovarik, D. Mourer, D. Wei, and M. J. Mills. Low cycle fatigue of a Ni-based superalloy: Non-planar deformation. *Scripta Materialia*, 62(10):790–793, 2010.

[148] L. Fritzemeier and J. Tien. The cyclic stress-strain behavior of nickel-base superalloys—I. Polycrystals. *Acta Metallurgica*, 36(2):275–282, 1988.

[149] B. H. Choe and H. C. Lee. Cyclic softening and hardening behavior of a nickel-base superalloy. *Scripta Metallurgica et Materialia*, 32(8):1283–1287, 1995.

[150] P. Li, Q. Li, T. Jin, Y. Zhou, J. Li, X. Sun, and Z. Zhang. Comparison of low-cycle fatigue behaviors between two nickel-based single-crystal superalloys. *International Journal of Fatigue*, 63:137–144, 2014.

[151] S. Ganesh Sundara Raman and K. Padmanabhan. Room-temperature low-cycle fatigue behaviour of a Ni-base superalloy. *International Journal of Fatigue*, 16(3):209–215, 1994.

[152] M. Sundararaman, W. Chen, and R. Wahi. Interpretation of fatigue softening at room temperature in a superalloy. *Scripta Metallurgica*, 23(10):1795–1800, 1989.

[153] H.-y. Qin, G. Chen, Q. Zhu, C.-j. Wang, and P. Zhang. High temperature low cycle fatigue behavior of GH4742 alloy. *Journal of Iron and Steel Research International*, 22(6):551–556, 2015.

[154] D. Ye, D. Ping, Z. Wang, H. Xu, X. Mei, C. Xu, and X. Chen. Low cycle fatigue behavior of nickel-based superalloy GH4145/SQ at elevated temperature. *Materials Science and Engineering: A*, 373(1-2):54–64, 2004.

[155] K. Obrtlík, M. Petrenec, J. Man, J. Polák, and K. Hrbáček. Isothermal fatigue behavior of cast superalloy Inconel 792-5A at 23 and 900 °C. *Journal of Materials Science*, 44(12):3305–3314, 2009.

[156] Z. Basinski and S. Basinski. Fundamental aspects of low amplitude cyclic deformation in face-centred cubic crystals. *Progress in Materials Science*, 36(C):89–148, 1992.

[157] S. Henkel, J. Fischer, L. Balogh, T. Ungar, and H. Biermann. Low-cycle fatigue behaviour and microstructure of copper and alpha-brass under biaxial load paths. *Journal of Physics: Conference Series*, 240:012042, 2010.

[158] P. Yang and H. Zhou. Low-cycle impact fatigue of mild steel and austenitic stainless steel. *International Journal of Fatigue*, 16(8):567–570, 1994.

[159] K. Nip, L. Gardner, C. Davies, and A. Elghazouli. Extremely low cycle fatigue tests on structural carbon steel and stainless steel. *Journal of Constructional Steel Research*, 66(1):96–110, 2010.

[160] L. Xiao, D. Chen, and M. Chaturvedi. Shearing of γ' precipitates and formation of planar slip bands in Inconel 718 during cyclic deformation. *Scripta Materialia*, 52(7):603–607, 2005.

[161] L. Xiao, D. L. Chen, and M. C. Chaturvedi. Cyclic deformation mechanisms of precipitation-hardened Inconel 718 superalloy. *Materials Science and Engineering A*, 483-484(1-2 C):369–372, 2008.

[162] A. Banerjee, J. K. Sahu, N. Paulose, C. D. Fernando, and R. N. Ghosh. Micromechanism of cyclic plastic deformation of alloy IN 718 at 600 °C. *Fatigue & Fracture of Engineering Materials & Structures*, 39(7):877–885, 2016.

[163] E. H. Krishna, K. Prasad, V. Kumar, and V. Singh. Low cycle fatigue behaviour of modified and conventional superalloy Inconel 718 at 650°C. *Transactions of the Indian Institute of Metals*, 63(1):63–66, 2010.

[164] J. K. Lee, S. P. Bhat, R. Veaux, and C. Laird. Mechanisms of cyclic softening in precipitation-hardening alloys - A ball model approach and tests at 78 K. *International Journal of Fracture*, 17(2):121–141, 1981.

[165] H. Mughrabi. Cyclic deformation and fatigue of multi-phase materials. In *Deformation of Multi-Phase and Particle Containing Materials, Proceedings of the 4th Riso International Symposium on Metallurgy and Materials Science*, pages 65–82, Roskilde, 1983. Risø National Laboratory.

[166] M. Sundararaman, P. Mukhopadhyay, and S. Banerjee. Deformation behaviour of γ' strengthened inconel 718. *Acta Metallurgica*, 36(4):847–864, 1988.

[167] S. D. Antolovich, E. Rosa, and A. Pineau. Low cycle fatigue of René 77 at elevated temperatures. *Materials Science and Engineering*, 47(1):47–57, 1981.

[168] E. Nes, T. Pettersen, and K. Marthinsen. On the mechanisms of work hardening and flow-stress saturation. *Scripta Materialia*, 43(1):55–62, 2000.

[169] E. Nes, K. Marthinsen, and Y. Brechet. On the mechanisms of dynamic recovery. *Scripta Materialia*, 47(9):607–611, 2002.

[170] U. Essmann and H. Mughrabi. Annihilation of dislocations during tensile and cyclic deformation and limits of dislocation densities. *Philosophical Magazine A*, 40(6):731–756, 1979.

[171] S. Khani Moghanaki and M. Kazeminezhad. Modeling of the mutual effect of dynamic precipitation and dislocation density in age hardenable aluminum alloys. *Journal of Alloys and Compounds*, 683:527–532, 2016.

[172] L. M. Brown and W. M. Stobbs. The work-hardening of copper-silica I. A Model based on Internal Stresses, with no Plastic Relaxation. *Philosophical Magazine*, 23(185):1185–1199, 1971.

[173] L. M. Brown and W. M. Stobbs. The work-hardening of copper-silica II. The Role of Plastic Relaxation. *Philosophical Magazine*, 23(185):1185–1199, 1971.

[174] J. D. Atkinson, L. M. Brown, and W. M. Stobbs. The work-hardening of copper-silica: IV. The Bauschinger effect and plastic relaxation. *Philosophical Magazine*, 30(6):1247–1280, 1974.

[175] M. Kassner, P. Geantil, L. Levine, and B. Larson. Backstress, the Bauschinger Effect and Cyclic Deformation. *Materials Science Forum*, 604-605:39–51, 2008.

[176] Y. Estrin and H. Mecking. A unified phenomenological description of work hardening and creep based on one-parameter models. *Acta Metallurgica*, 32(1):57–70, 1984.

[177] H. Mecking and U. Kocks. Kinetics of flow and strain-hardening. *Acta Metallurgica*, 29(11):1865–1875, 1981.

[178] H. Mecking, B. Nicklas, N. Zarubova, and U. Kocks. A "universal" temperature scale for plastic flow. *Acta Metallurgica*, 34(3):527–535, 1986.

[179] E. Nes and K. Marthinsen. Modeling the evolution in microstructure and properties during plastic deformation of f.c.c.-metals and alloys – an approach towards a unified model. *Materials Science and Engineering: A*, 322(1-2):176–193, 2002.

[180] E. Galindo-Nava, J. Sietsma, and P. Rivera-Díaz-del Castillo. Dislocation annihilation in plastic deformation: II. Kocks–Mecking Analysis. *Acta Materialia*, 60(6-7):2615–2624, 2012.

[181] Y. Estrin, H. Braasch, and Y. Brechet. A Dislocation Density Based Constitutive Model for Cyclic Deformation. *Journal of Engineering Materials and Technology*, 118(4):441, 1996.

[182] Y. Estrin. Dislocation-density-related constitutive modeling. In A. S. Krausz and K. Krausz, editors, *Unified Constitutive Laws of Plastic Deformation*, pages 69–106. Academic Press, Inc., California, 1996.

[183] M. F. Ashby. The deformation of plastically non-homogeneous materials. *The Philosophical Magazine: A Journal of Theoretical Experimental and Applied Physics*, 21(170):399–424, 1970.

[184] J. D. Eshelby. The determination of the elastic field of an ellipsoidal inclusion, and related problems. *Proceedings of the Royal Society of London. Series A. Mathematical and Physical Sciences*, 241(1226):376–396, 1957.

[185] W. Han, A. Vinogradov, and C. Hutchinson. On the reversibility of dislocation slip during cyclic deformation of Al alloys containing shear-resistant particles. *Acta Materialia*, 59(9):3720–3736, 2011.

[186] G. Fribourg, Y. Bréchet, A. Deschamps, and A. Simar. Microstructure-based modelling of isotropic and kinematic strain hardening in a precipitation-hardened aluminium alloy. *Acta Materialia*, 59(9):3621–3635, 2011.

[187] J. da Costa Teixeira, L. Bourgeois, C. Sinclair, and C. Hutchinson. The effect of shear-resistant, plate-shaped precipitates on the work hardening of Al alloys: Towards a prediction of the strength–elongation correlation. *Acta Materialia*, 57(20):6075–6089, 2009.

[188] H. Mughrabi. A two-parameter description of heterogeneous dislocation distributions in deformed metal crystals. *Materials Science and Engineering*, 85(C):15–31, 1987.

[189] W. Schütz. A history of fatigue. *Engineering Fracture Mechanics*, 54(2):263–300, 1996.

[190] F. Braithwaite. On the fatigue and consequent fracture of metals. *Minutes of the Proceedings of the Institution of Civil Engineers*, 13(1854):463–467, 1854.

[191] M. Preuss, P. J. Withers, J. W. L. Pang, and G. J. Baxter. Inertia welding nickel-based superalloy: Part I. Metallurgical characterization. *Metallurgical and Materials Transactions A*, 33(10):3215–3225, 2002.

[192] K. Differt, U. Essmann, and H. Mughrabi. Models of particle destruction in fatigued precipitation-hardened alloys. *Physica Status Solidi (a)*, 104(1):95–106, 1987.

[193] H. S. Ho, M. Risbet, X. Feaugas, and G. Moulin. Damage mechanism related to localization of plastic deformation of Waspaloy: Effect of grain size. *Procedia Engineering*, 10:863–868, 2011.

[194] A. W. Mello, A. Nicolas, and M. D. Sangid. Fatigue strain mapping via digital image correlation for Ni-based superalloys: The role of thermal activation on cube slip. *Materials Science and Engineering: A*, 695(December 2016):332–341, 2017.

[195] Y. Brechet and F. Louchet. On the stability of orowan loops around coherent spherical ordered precipitates. *Acta Metallurgica*, 37(9):2469–2473, 1989.

[196] K. Kang, J. Yin, and W. Cai. Stress dependence of cross slip energy barrier for face-centered cubic nickel. *Journal of the Mechanics and Physics of Solids*, 62:181–193, 2014.

[197] A. Malka-Markovitz and D. Mordehai. Cross-slip in face-centered cubic metals: a general Escaig stress-dependent activation energy line tension model. *Philosophical Magazine*, 98(5):347–370, 2018.

[198] U. Essmann, U. Gösele, and H. Mughrabi. A model of extrusions and intrusions in fatigued metals I. Point-defect production and the growth of extrusions. *Philosophical Magazine A*, 44(2):405–426, 1981.

[199] K. Obrtlík, M. Juliš, J. Man, T. Podrábský, and J. Polák. Extrusion and intrusion evolution in cyclically strained cast superalloy Inconel 738LC using confocal laser scanning microscope and AFM. *Journal of Physics: Conference Series*, 240:012054, 2010.

[200] T. Zhang, J. Jiang, B. Britton, B. Shollock, and F. Dunne. Crack nucleation using combined crystal plasticity modelling, high-resolution digital image correlation and high-resolution electron backscatter diffraction in a superalloy containing non-metallic inclusions under fatigue. *Proceedings of the Royal Society A: Mathematical, Physical and Engineering Science*, 472(2189):1–25, 2016.

[201] T. Edwards, F. Di Gioacchino, H. Springbett, R. Oliver, and W. Clegg. Stable Speckle Patterns for Nano-scale Strain Mapping up to 700 °C. *Experimental Mechanics*, 57(9):1469–1482, 2017.

[202] J. C. Stinville, M. P. Echlin, P. G. Callahan, V. M. Miller, D. Texier, F. Bridier, P. Bocher, and T. M. Pollock. Measurement of Strain Localization Resulting from Monotonic and Cyclic Loading at 650 °C in Nickel Base Superalloys. *Experimental Mechanics*, 57(8):1289–1309, 2017.

[203] F. Bourdin, J. Stinville, M. Echlin, P. Callahan, W. Lenthe, C. Torbet, D. Texier, F. Bridier, J. Cormier, P. Villechaise, T. Pollock, and V. Valle. Measurements of plastic localization by heaviside-digital image correlation. *Acta Materialia*, 157:307–325, 2018.

[204] D. Srinivasan, L. U. Lawless, and E. A. Ott. Experimental Determination of TTT Diagram for Alloy 718Plus®. In *Superalloys 2012, Proceedings of the International Symposium on Superalloys*, pages 759–768. TMS, 2012.

[205] A. Casanova, M. Hardy, and C. Rae. Morphology and Kinetics of Grain Boundary Precipitation in Alloy ATI 718Plus®. In *8th International Symposium on Superalloy 718 and Derivatives*, pages 573–586. John Wiley & Sons, Inc., Hoboken, NJ, USA, 2014.

[206] G. A. Zickler, R. Schnitzer, R. Radis, R. Hochfellner, R. Schweins, M. Stockinger, and H. Leitner. Microstructure and mechanical properties of the superalloy ATI Allvac® 718Plus™. *Materials Science and Engineering: A*, 523(1-2):295–303, 2009.

[207] R. L. Kennedy. ALLVAC® 718PLUS™, superalloy for the next forty years. *Superalloys 718, 625, 706 and Derivatives, Proceedings of the International Symposium on Superalloys 718, 625, 706 and Derivatives*, 718:625–706, 2005.

[208] G. Landini, D. Randell, S. Fouad, and A. Galton. Automatic thresholding from the gradients of region boundaries. *Journal of Microscopy*, 265(2):185–195, 2017.

[209] D. M. Collins and H. J. Stone. A modelling approach to yield strength optimisation in a nickel-base superalloy. *International Journal of Plasticity*, 54:96–112, 2014.

[210] E. I. Galindo-Nava. Modelling twinning evolution during plastic deformation in hexagonal close-packed metals. *Materials & Design*, 83:327–343, 2015.

[211] L. Brown and D. Clarke. Work hardening due to internal stresses in composite materials. *Acta Metallurgica*, 23(7):821–830, 1975.

[212] E. Orowan. Problems of plastic gliding. *Proceedings of the Physical Society*, 52(1):8–22, 1940.

[213] B. Reppich. Some new aspects concerning particle hardening mechanisms in γ' precipitating Ni-base alloys—I. Theoretical concept. *Acta Metallurgica*, 30(1):87–94, 1982.

[214] A. J. Ardell. Precipitation hardening. *Metallurgical Transactions A*, 16(12):2131–2165, 1985.

[215] J. Lemaitre and J. L. Chaboche. *Mechanics of Solid Materials*. Cambridge University Press, Cambridge, 1985.

[216] M. Zecevic and M. Knezevic. A dislocation density based elasto-plastic self-consistent model for the prediction of cyclic deformation: Application to AA6022-T4. *International Journal of Plasticity*, 72:200–217, 2015.

[217] H. Mughrabi. The α -factor in the Taylor flow-stress law in monotonic, cyclic and quasi-stationary deformations: Dependence on slip mode, dislocation arrangement and density. *Current Opinion in Solid State and Materials Science*, 20(6):411–420, 2016.

[218] G. Taylor. Plastic strain in metals. *Journal of the Institute of Metals*, 62:307–324, 1938.

[219] H. Pottebohm, G. Neite, and E. Nembach. Elastic Properties (the Stiffness Constants, the Shear Modulus and the Dislocation Line Energy and Tension) of Ni-AI Solid Solutions and of the Nimonic Alloy PE 16. *Materials Science and Engineering*, 60:189–194, 1983.

[220] W.-D. Cao and R. Kennedy. Recommendations for Heat Treating Allvac® 718Plus® Alloy Parts. Technical report, ATI Allvac, 2006.

[221] ATI Allvac. 718 Plus® Data Sourcebook. Technical report, ATI Allvac, 2008.

[222] A. Manonukul and F. P. E. Dunne. High– and low–cycle fatigue crack initiation using polycrystal plasticity. *Proceedings of the Royal Society of London. Series A: Mathematical, Physical and Engineering Sciences*, 460(2047):1881–1903, 2004.

[223] F. Dunne, D. Rugg, and A. Walker. Lengthscale-dependent, elastically anisotropic, physically-based hcp crystal plasticity: Application to cold-dwell fatigue in Ti alloys. *International Journal of Plasticity*, 23(6):1061–1083, 2007.

[224] D. McDowell and F. Dunne. Microstructure-sensitive computational modeling of fatigue crack formation. *International Journal of Fatigue*, 32(9):1521–1542, 2010.

[225] M. Risbet, X. Feaugas, C. Guillemerneel, and M. Clavel. Damage in nickel base superalloy: Influence of local parameters measured by electron backscattered diffraction and atomic force microscopy. *Scripta Materialia*, 60(5):269–272, 2009.

[226] M. A. Tschopp, D. E. Spearot, and D. L. McDowell. Atomistic simulations of homogeneous dislocation nucleation in single crystal copper. *Modelling and Simulation in Materials Science and Engineering*, 15(7):693–709, 2007.

[227] R. D. Wyman, D. T. Fullwood, R. H. Wagoner, and E. R. Homer. Variability of non-Schmid effects in grain boundary dislocation nucleation criteria. *Acta Materialia*, 124:588–597, 2017.

[228] N. Burbery, R. Das, and G. Ferguson. Mobility of dissociated mixed dislocations under an Escaig stress. *Modelling and Simulation in Materials Science and Engineering*, 25(4):045001, 2017.

[229] T. Byun. On the stress dependence of partial dislocation separation and deformation microstructure in austenitic stainless steels. *Acta Materialia*, 51(11):3063–3071, 2003.

[230] J.-B. Baudouin, G. Monnet, M. Perez, C. Domain, and A. Nomoto. Effect of the applied stress and the friction stress on the dislocation dissociation in face centered cubic metals. *Materials Letters*, 97:93–96, 2013.

[231] A. N. Stroh. Constrictions and Jogs in Extended Dislocations. *Proceedings of the Physical Society. Section B*, 67(5):427–436, 1954.

[232] E. Oren, E. Yahel, and G. Makov. Kinetics of dislocation cross-slip: A molecular dynamics study. *Computational Materials Science*, 138:246–254, 2017.

[233] K.-Q. Li, Z.-J. Zhang, L.-L. Li, P. Zhang, J.-B. Yang, and Z.-F. Zhang. Effective Stacking Fault Energy in Face-Centered Cubic Metals. *Acta Metallurgica Sinica (English Letters)*, 31(8):873–877, 2018.

[234] M. de Koning, W. Cai, and V. V. Bulatov. Anomalous Dislocation Multiplication in FCC Metals. *Physical Review Letters*, 91(2):025503, 2003.

[235] N. Narita and J. Takamura. Deformation twinning in silver-and copper-alloy crystals. *Philosophical Magazine*, 29(5):1001–1028, 1974.

[236] H. Fujita and T. Mori. A formation mechanism of mechanical twins in F.C.C. Metals. *Scripta Metallurgica*, 9(6):631–636, 1975.

[237] S. Sato, E.-P. Kwon, M. Imafuku, K. Wagatsuma, and S. Suzuki. Microstructural characterization of high-manganese austenitic steels with different stacking fault energies. *Materials Characterization*, 62(8):781–788, 2011.

[238] S. Copley and B. Kear. The dependence of the width of a dissociated dislocation on dislocation velocity. *Acta Metallurgica*, 16(2):227–231, 1968.

[239] B. Li, M. Sui, and S. Mao. Twinnability Predication for fcc Metals. *Journal of Materials Science & Technology*, 27(2):97–100, 2011.

[240] R. J. McCabe, I. J. Beyerlein, J. S. Carpenter, and N. A. Mara. The critical role of grain orientation and applied stress in nanoscale twinning. *Nature Communications*, 5(1):3806, 2014.

[241] S. Raujol, M. Benyoucef, D. Locq, P. Caron, F. Pettinari, N. Clement, and A. Coujou. Decorrelated movements of Shockley partial dislocations in the γ-phase channels of nickel-based superalloys at intermediate temperature. *Philosophical Magazine*, 86(9):1189–1200, 2006.

[242] B. A. Szajewski, A. Hunter, D. J. Luscher, and I. J. Beyerlein. The influence of anisotropy on the core structure of Shockley partial dislocations within FCC materials. *Modelling and Simulation in Materials Science and Engineering*, 26(1):015010, 2018.

[243] P. Franciosi and A. Zaoui. Multislip in f.c.c. crystals a theoretical approach compared with experimental data. *Acta Metallurgica*, 30(8):1627–1637, 1982.

[244] D. Barba, E. Alabort, D. Garcia-Gonzalez, J. Moverare, R. Reed, and A. Jérusalem. A thermodynamically consistent constitutive model for diffusion-assisted plasticity in Ni-based superalloys. *International Journal of Plasticity*, 105:74–98, 2018.

[245] P. Zhao, M. J. Mills, Y. Wang, and S. R. Niezgoda. A homogenized primary creep model of nickel-base superalloys and its application to determining micro-mechanistic characteristics. *International Journal of Plasticity*, 110(May):202–219, 2018.

[246] K. Hanson and J. W. Morris. Limiting configuration in dislocation glide through a random array of point obstacles. *Journal of Applied Physics*, 46(3):983–990, 1975.

[247] R. B. Schwarz and R. Labusch. Dynamic simulation of solution hardening. *Journal of Applied Physics*, 49(10):5174–5187, 1978.

[248] V. A. Vorontsov, R. E. Voskoboinikov, and C. M. Rae. Shearing of γ' precipitates in Ni-base superalloys: A phase field study incorporating the effective γ-surface. *Philosophical Magazine*, 92(5):608–634, 2012.

[249] R. E. Voskoboinikov and C. M. F. Rae. A new γ-surface in {111} plane in L12 Ni3 Al. *IOP Conference Series: Materials Science and Engineering*, 3:012009, 2009.

[250] L.-L. Liu, X.-Z. Wu, R. Wang, W.-G. Li, and Q. Liu. Stacking fault energy, yield stress anomaly, and twinnability of Ni 3 Al: A first principles study. *Chinese Physics B*, 24(7):077102, 2015.

[251] A. Breidi, J. Allen, and A. Mottura. First-principles modeling of superlattice intrinsic stacking fault energies in Ni3Al based alloys. *Acta Materialia*, 145:97–108, 2018.

[252] A. Hunter, R. F. Zhang, I. J. Beyerlein, T. C. Germann, and M. Koslowski. Dependence of equilibrium stacking fault width in fcc metals on the γ -surface. *Modelling and Simulation in Materials Science and Engineering*, 21(2):025015, 2013.

[253] B. Décamps, A. J. Morton, and M. Condat. On the mechanism of shear of γ' precipitates by single (a/2)<110> dissociated matrix dislocations in Ni-based superalloys. *Philosophical Magazine A*, 64(3):641–668, 1991.

[254] B. Décamps, J.-M. Pénisson, M. Condat, L. Guétaz, and A. J. Morton. High resolution imaging of shearing configurations of γ' precipitates in Ni-based superalloys. *Scripta Metallurgica et Materialia*, 30(11):1425–1430, 1994.

[255] T. Smith, Y. Rao, Y. Wang, M. Ghazisaeidi, and M. Mills. Diffusion processes during creep at intermediate temperatures in a Ni-based superalloy. *Acta Materialia*, 141:261–272, 2017.

[256] M. Benyoucef, A. Coujou, F. Pettinari-Sturmel, S. Raujol, B. Boubker, and N. Clément. Dynamics of micromechanisms controlling the mechanical behaviour of industrial single crystal superalloys. *Sadhana*, 28(1-2):129–146, 2003.

[257] Y. Rao, T. M. Smith, M. J. Mills, and M. Ghazisaeidi. Segregation of alloying elements to planar faults in γ'-Ni3Al. *Acta Materialia*, 148:173–184, 2018.

[258] T. Smith, B. Esser, N. Antolin, G. Viswanathan, T. Hanlon, A. Wessman, D. Mourer, W. Windl, D. McComb, and M. Mills. Segregation and η phase formation along stacking faults during creep at intermediate temperatures in a Ni-based superalloy. *Acta Materialia*, 100:19–31, 2015.

[259] T. M. Smith, B. D. Esser, B. Good, M. S. Hooshmand, G. B. Viswanathan, C. M. F. Rae, D. W. Ghazisaeidi, D. W. Mccomb, and M. J. Mills. Segregation and Phase Transformations Along Superlattice Intrinsic Stacking Faults in Ni-Based Superalloys. *Metallurgical and Materials Transactions A*, 49A:4186–4198, 2018.

[260] B. Décamps, S. Raujol, A. Coujou, F. Pettinari-Sturmel, N. Clément, D. Locq, and P. Caron. On the shearing mechanism of γ' precipitates by a single (a/6)<112> Shockley partial in Ni-based superalloys. *Philosophical Magazine*, 84(1):91–107, 2004.

[261] S. Y. Yuan, Z. H. Jiang, J. Z. Liu, Y. Tang, and Y. Zhang. Nano-twinning in a γ' precipitate strengthened Ni-based superalloy. *Materials Research Letters*, 6(12):683–688, 2018.

[262] M. Chandran and S. K. Sondhi. First-principle calculation of stacking fault energies in Ni and Ni-Co alloy. *Journal of Applied Physics*, 109(10):103525, 2011.

[263] S. Kibey, J. Liu, D. Johnson, and H. Sehitoglu. Predicting twinning stress in fcc metals: Linking twin-energy pathways to twin nucleation. *Acta Materialia*, 55(20):6843–6851, 2007.

[264] J. Wang and H. Sehitoglu. Dislocation slip and twinning in Ni-based L12 type alloys. *Intermetallics*, 52:20–31, 2014.

[265] M. D. Sangid, T. Ezaz, H. Sehitoglu, and I. M. Robertson. Energy of slip transmission and nucleation at grain boundaries. *Acta Materialia*, 59(1):283–296, 2011.

[266] J. Cohen and J. Weertman. A dislocation model for twinning in f.c.c. metals. *Acta Metallurgica*, 11(8):996–998, 1963.

[267] H. Idrissi, K. Renard, L. Ryelandt, D. Schryvers, and P. Jacques. On the mechanism of twin formation in Fe–Mn–C TWIP steels. *Acta Materialia*, 58(7):2464–2476, 2010.

Appendix A

Differt model of precipitate shearing

Differt *et. al.* [192] proposed a model for the precipitate shearing phenomenon that accounts for the dislocation irreversibilities in a probabilistic way. The total number of irreversible slip steps Z within a slip band of width w evolves with the number of cycles N as

$$Z = 4N\frac{w}{b}p\left(\frac{\Delta\gamma_{SB,p}}{2}\right), \tag{A.1}$$

where p is an irreversibility factor which can vary from 0 to 1, and $\frac{\Delta\gamma_{SB,p}}{2}$ is the localised plastic strain amplitude, assumed to remain constant. The model considers the following assumptions:

(i) The probability P that there are n^+ positive slip steps in a glide plane within a region of thickness t is given by a Poisson distribution

$$P(n^+) = \frac{z^{n^+}}{n^+!}\exp(-z), \tag{A.2}$$

where $z = Za/2t$ and a is the mean slip line spacing.

(ii) There is an equal distribution of positive and negative slip steps n^-, thus $P(n^+) = P(n^-)$.

(iii) The same number of dislocations travel the same distance along the multiple slip lines.

(iv) The probability of getting a new positive (or negative) slip step is history-independent.

Then, to calculate the probability of finding a number $\Delta n = n^+ - n^-$ of slip steps in a slip plane, a sum over the products of the probabilities $P(n^+)P(n^-)$ is done; *i.e.*

$$P(\Delta n) = \sum_{n^-=0}^{Z/2} P(\Delta n + n^-)P(n^-), \tag{A.3}$$

and substituting equation (A.2) into (A.3):

$$P(\Delta n) = \sum_{n^-=0}^{Z/2} \frac{z^{\Delta n+2n^-}}{(\Delta n+n^-)!\,n!} \exp(-2z). \tag{A.4}$$

Considering the infinite summation of the n^- values, equation (A.4) takes the form of the modified Bessel function of the first kind I_α, so that

$$P(\Delta n) = \exp(-2z)\, I_{\Delta n}(2z). \tag{A.5}$$

This is a reasonable assumption given that Z takes very large numbers. Equation (A.5) being the discrete probability distribution, the mean number of steps per plane can be calculated from the absolute value Δn as

$$\overline{|\Delta n|} = \sum_{\Delta n=-\infty}^{\infty} |\Delta n| P(|\Delta n|) = 2\sqrt{\frac{z}{\pi}}. \tag{A.6}$$